IN SITU ULTRAFAST SYNCHROTRON X-RAY IMAGING STUDIES OF THE DYNAMICS OF ULTRASONIC BUBBLES IN LIQUIDS

Dongyue Tan

University of Hull

August 2015

THE UNIVERSITY OF HULL

IN SITU ULTRAFAST SYNCHROTRON X-RAY IMAGING STUDIES OF THE DYNAMICS OF ULTRASONIC BUBBLES IN LIQUIDS

A Thesis submitted for the Degree of

Doctor of Philosophy, School of Engineering
in the University of Hull

by

Dongyue Tan

MEng, (Northwest A & F University, China)

August 2015

Abstract

The research studies the highly dynamic and transient behaviour of ultrasonic bubbles in liquids of different physical properties, including water, silicone oil, and liquid metals. A novel ultrasound solidification apparatus as well as the special sample containers and the relevant control systems were designed, built and commissioned for this research.

Systematic in situ experiments were conducted using this novel apparatus at the ultrafast synchrotron X-ray imaging (271,554 fps) beamline, the sector 32-ID-B of Advanced Photon Source (APS) and the high speed X-ray imaging beamline, I12 of Diamond Light Source (DLS) in 2011-2015.

A huge amount of real-time images were obtained in this research, a procedure and the relevant in-house Matlab code were developed to analyse those images and extract the key information for understanding the highly dynamic behaviour of the nucleation, oscillation, implosion, coalescence of ultrasonic bubbles and bubble cloud. The ultrasound induced acoustic flows coupled with bubbles and particles were also investigated, and their effects on liquid-solid interface during the solidification of a Bi-8%Zn were analysed and quantified.

The experiments were complemented by the modelling and simulations of the acoustic pressure field, the bubble dynamics using the classical Helmholtz Equation and Gilmore model, providing more quantitative understanding for the interactions of ultrasonic waves and bubbles with the liquids and the solid phases in the liquids.

The key research findings are:

- For bubble implosion: For the first time, bubble implosion in liquid metal was captured in real-time and in situ. In both water and liquid Bi-8%Zn, compressed gas cores were found at the centre of the imploding bubble with shock waves emitted outwards from the centre.

- For bubble oscillations at quasi-steady state condition, the measured bubble radii agree well with the predictions made by Gilmore model for all liquids studied in this research.

- For bubble coalescence, the time needed for liquid Bi-8%Zn cannot be predicted using either the no-slip or the free interface model. A new power law model is developed and the prediction made using this new model agrees well with the experiments.

- For the first time, in metal alloys, the in situ and real-time studies proved that the ultrasonic bubbles and the acoustic flows are capable of fracturing and detaching the solid phases from the liquid-solid interface.

- Temperature fluctuations caused by applying ultrasound in Bi-8%Zn during solidification is capable of detaching the solid phases from the liquid-solid interface. However, it is less important and slower than acoustic flows and ultrasonic bubbles.

- Ultrasound power is a dominant parameter for the interactions of ultrasonic bubbles, acoustic flows, temperature fluctuations with liquid-solid interface.

Dedication

This thesis is dedicated to my loved mom Li Li, dad Zhongping Tan, and sister Na Tan, for their love and support throughout my PhD research.

Acknowledgements

I would like to acknowledge gratefully the PhD Studentship awarded jointly by the China Scholarship Council and University of Hull for me to conduct this very advanced research project in the past 4 years.

I also would like to express my sincere gratitude to my supervisor, Dr Jiawei Mi for his persistent support and encouragement, academic advice and guidance throughout the PhD project. I am a MEng student with civil engineering background. The knowledge and equipments needed for this project are completely new to me, and I went through a steep learning process at the very beginning of my PhD study. His patience guidance, encouragement and advice helped me to overcome the very difficult period in my PhD research, and finally achieved what I have now.

Special thanks go to the academic staff in the School of Engineering , University of Hull, including Prof. Ron Patton, Prof. Jim Gilbert, Dr Sergey Rybchenko, Prof. Michael Fagan and Dr Michael McGuire for their support and encouragement; and the technical staff, Miss Julia Malle for making the quartz sample containers for the in situ ultrasound experiment, Mr Garry Robinson, Mr Tony Sinclair for assistance on the microstructure characterisation using optical microscopy, scanning electron microscopy, Mrs Sue Taft for X-ray imaging and tomography, and Mr Peter Lobo-Kazinczi and Mr Steve Coopland for helping on designing and building the relay system for the ultrasound experimental apparatus.

The awards of the synchrotron X-ray beam time (EE8542-1) by the Diamond Light Source, UK, and those (GUP 23649 and GUP 26170) by the Advanced Photon Source, Argonne National Laboratory, US are also gratefully acknowledged. I am also very grateful for the guidance and support given by the beamline scientists Dr Thomas Connolley at I12, Diamond Light Source, UK and Dr Kamel Fezzaa at 32-ID-B, Advanced Photon Source, Argonne National Laboratory, US during the in situ experiments and the analyses of the data afterwards. Use of the Advanced Photon Source, an Office of Science User Facility operated for the U.S. Department of Energy (DOE) Office of Science by

Argonne National Laboratory, was supported by the U.S. DOE under Contract No. DE-AC02-06CH11357.

Last but not least, I would like to thank my colleagues and friends for the many stimulating technical discussions with them, including Mr Jia Chuan Khong, Mr Tung Lik Lee, Dr Theerapatt Monuwang, Mr Wei Zhang, Dr Chuangnan Wang, Mr Wenjia Du, etc just name a few.

Publications, prize and awarded beam time

The research papers published in the peer reviewed journals and the contributions to the conference proceedings and those in preparation are listed below:

1. Journal papers:

- **D. Tan** and J. Mi, "High speed imaging study of the dynamics of ultrasonic bubbles at a liquid-solid interface," *Materials Science Forum*, vol. 765, pp. 230–234, 2013.
- J. Mi, **D. Tan**, and T. L. Lee, "In Situ Synchrotron X-ray Study of Ultrasound Cavitation and Its Effect on Solidification Microstructures," *Metallurgical and Materials Transactions B*, pp. 1-5, 2014/12/11 2014.
- **D. Tan**, T. L. Lee, J. C. Khong, T. Connolley, K. Fezzaa, and J. Mi, "High-Speed Synchrotron X-ray Imaging Studies of the Ultrasound Shockwave and Enhanced Flow during Metal Solidification Processes," *Metallurgical and Materials Transactions A*, pp. 1-11, 2015/03/31 2015.

2. Conference papers:

- C. Wang, **D. Tan**, W. Zhang, W. Du, T. Connolley, J. Mi, "High speed synchrotron x-ray imaging of ultrasonic bubble cloud in liquid metal", Journal of Physics: Conference series, 2015.

3. Manuscripts in preparation

- Manuscript titled "Ultrafast synchrotron X-ray imaging studies of ultrasonic bubble implosion in water and liquid metal" is preparing for submission.

- Manuscript titled "In situ synchrotron X-ray imaging studies of the dynamics of ultrasonic bubbles and streaming flow at liquid-solid interface during metal solidification" is in process.

4. **Awarded synchrotron X-ray beamtimes**

- The awarded beamtime for proposal titled "Ultrafast synchrotron X-ray phase-contrast imaging study of ultrasound cavitation and its effect on nucleation and dendritic grain evolution: phase 2 investigation on metallic alloys" (GUP 23649 and GUP 26170, totally 10 days), from Advanced Photon Source, Argonne national laboratory, USA.

- The awarded beamtime for proposal titled "In situ study of processing conditions to deliver embryonic nuclei for grain self-refinement in clean metals under ultrasound cavitation " (EE8542-1), and " In situ study of ultrasound cavitation clouds in liquid metals" (NT12131-1), totally 8 days, from Diamond Light Source, UK.

5. **Posters and awards:**

- Poster prize with the poster named "Synchrotron X-ray Imaging Studies of the Dynamics of Ultrasonic Bubbles in Liquid Metals" was awarded in the UK Solidification Workshop 2014 supported by EPSRC, and hosted by Brunel University, in 9-10, April.

- Poster named "High Speed Synchrotron X-ray Imaging Studies of Metal Solidification Under Ultrasonic Waves" was presented at the 4th International Conference on Advances in Solidification Processes, 8-11th July 2014, Beaumont Estates, Old Windsor, UK

Contents

Chapter 1: Introduction

1.1 The background of the research

Ultrasonic waves, and their transmission and attenuation in a solid medium and the interactions with the constituents inside the solid are well understood. Built upon those well-developed understandings and theories, ultrasound-based imaging, non-destructive testing techniques and the relevant instruments have been well developed and widely used in human society and industry [1-4].

Similarly, theories regarding the propagation of ultrasonic waves in a single phase liquid medium are also well developed. However, above a certain acoustic pressure threshold – the Blake's threshold [5], ultrasound can generate bubbles in a liquid medium. The bubbles, driven by the alternating acoustic pressure field in the liquid, oscillate, grow, coalesce, and split, and under certain conditions collapse violently. This is a process commonly known as ultrasonic cavitation and bubble implosion [6] which has found very diverse applications in ultrasonic cleaning, chemical synthesis and medical treatments [3, 6-14].

Most of the previous research on studying the dynamics of ultrasonic bubbles were carried out in visible-light transparent liquid media such as water, or water based solution illuminated using visible light. For example, the physics of bubble oscillation in water were intensively studied in the past 50 years as reviewed by Lauterborn and Kurz [6]. Previous studies in the field of sonochemistry [8, 9, 15, 16] revealed that bubble implosion can generate a shockwave with an extremely high pressure (>1000 atm) and temperature (>5000 K) immediately adjacent to the bubble surface, leading to complicated sonochemical reactions. Ohl and Ikink [17] also reported that, when bubble implosion occurs near a rigid interface, microjets with extremely high velocity can be created near the interface. Although very high imaging acquisition rate, i.e. up to two million frames per second, was used in the imaging studies, visible light illumination often suffer the light absorption, reflection and multiple scattering problems, especially at the bubble boundaries, i.e. the air-liquid interface. Therefore the boundaries of the bubbles are often blurred, making it difficult to study the details of the oscillation, coalescence, violent implosion of the bubbles. For example, in the bubble coalescence process, visible light illumination cannot "see" though the details of the breaking up and then joining of the two touching boundaries of two bubbles, and therefore misinterpretation were often found in previous papers. [6, 14, 18-27].

Furthermore, visible light is not suitable for none-transparent materials, such as opaque polymers, liquid metals, etc. For example, Tischer, *et al* [28] found that ultrasound treatment of polymer materials leads to the formation of different nanostructures that is suitable for making new scaffolds for tissue engineering. Huang , et al [29] also reported that ultrasound treatment of a resin liquid with impregnated fibres enhance the interfacial interactions between a carbon fibre and the epoxy matrix. However, due to the opacity of those materials, the mechanisms of how ultrasonic waves interact with those viscous liquids are not fully understood.

Ultrasound has been long found to be beneficial in metallurgical processes such as liquid metal degassing, grain refinement, welding, etc. Laboratory-based research in ultrasound treatment of metallic alloys started in 1930s, and a wide range of fundamental and applied research on ultrasonic processing of metal alloys had been conducted in Russia from the 1960s to the 1980s as comprehensively reviewed in the new book by Eskins [5]. However, almost all previous research were conducted using post-mortem microstructural characterisation of the solidified alloys and the empirical correlation between the measured grain size and the input ultrasonic power [5, 30]. This is mainly because of the opacity of metallic alloys and the difficulty in conducting any sensible real-time observation of the effect of ultrasound in a high temperature alloy melt. Hence, many in situ solidification studies have been made using organic transparent alloys instead [31-33], and then applied the findings obtained from the organic transparent alloys to real metal alloy systems. However, compared with metal alloys, organic transparent alloys often have huge difference in density, viscosity, surface tension, heat/mass transfer coefficient, and sound velocity which will lead to different behaviors in solidification, especially for the phenomena when an ultrasound is present [6]. Hence real-time and in situ studies of the solidification of metal alloys at the presence of an ultrasound are very necessary for understanding the complex and transient physical phenomena during the ultrasound processing of metal alloys.

In the past 20 years or so, the worldwide advances in the third generation synchrotron X-ray facilities and the associated development of a vast number of experimental devices and scientific instruments made the in situ and real-time investigations of metal solidification under conventional condition become possible [34-37]. Funded by the Royal Society, Dr Mi's group (where I am one of the researchers) came the first in using Synchrotron X-rays to study the dynamics of ultrasound cavitation and bubbles in liquid metals [38]. The 1st experiment was conducted in 2-4 July 2011 using the ultrafast synchrotron X-ray imaging facility (up to 271,554 frame per second) at sector 32ID-B of Advanced Photon Source (APS), Argonne national laboratory, USA. I am one of the key researchers heavily involved in the in situ experiments conducted since September 2011 after I joined Dr Mi's group. This thesis reported the key research findings obtained from those experiments with the details listed in Table 3.1 of Chapter 3.

1.2 The objectives of the research

Considerable progress has been made in studying the mechanism and effectiveness of using ultrasonic waves to manipulate liquid or semisolid alloys; However, uncertainties remain in both the underlying physics of how ultrasonic waves interact with liquid and semisolid metals, and the solidifying microstructures, and the best technological approach to control the final microstructure to achieve the optimal mechanical properties.

The objectives of this research are:

1. To design, build and commission a laboratory scale experimental apparatus and the sample environments for studying in situ and in real time the solidification of metal alloys under the applied ultrasonic waves.

2. To carry out a series of in situ experiments and study systematically the underlying mechanisms of how ultrasonic waves interact with the liquids or semi-solid metals during the solidification.

3. To analyse the huge amount of image data set and use the modeling and simulation tools to interpret and explain the multiphysic phenomena found in the experiments, providing more insight on understanding quantitatively the dynamics of ultrasound bubbles in liquids of very different physical properties, including during the solidification process of metals under ultrasound.

1.3 The structure of the thesis

The thesis consists of 8 chapters as detailed below.

Chapter 1 is a brief introduction of the research background, the objectives and the structure of the thesis.

Chapter 2 reviews the literatures that are directly relevant to the research, and they are grouped into five sections as detailed at the very beginning of Chapter 2.

Chapter 3 describes, in details, the design, making and commissioning of the in situ experimental apparatus and the sample environment, as well as the capability of the X-ray beamlines used in the research, and how the experiments were carried out at APS and DLS.

Chapter 4 presents the X-ray images obtained from different liquids (water, silicone oil, and liquid metals) for ultrasound bubble nucleation, oscillation, implosion, coalescence and bubble cloud.

Chapter 5 describes the effects of ultrasound bubbles and acoustic flows on the liquid-solid interface of a metal alloy.

Chapter 6 presents the modelling and simulation of the acoustic pressure field, the dynamics of single bubble in a acoustic pressure field for the cases of water, silicone oil, and metallic alloys.

Chapter 7 discusses, in details, the bubble dynamics in different liquids with an emphasis on the bubble implosion and coalescence, and the effect of ultrasound induced multiphase flows, and temperature fluctuations on the liquid-solid interface during the solidification process of metallic alloys.

Chapter 8 summarise the major findings and contributions of the research to this important research field. Possible future directions to continue this work are also briefly discussed.

Chapter 2: Literature Review

In this chapter, the literatures that are directly relevant to this research are critically analysed and reviewed. It consists of five parts: (1) the basic theory of ultrasonic waves and its propagation in liquids, (2) ultrasound induced cavitation and the dynamics of ultrasonic bubbles, including bubble nucleation, oscillation, implosion, bubble coalescence and multi-bubble cloud, (3) ultrasound induced acoustic flows in the presence of ultrasonic bubbles and solid particles, (4) ultrasound treatment of metallic alloys, and (5) the X-ray imaging techniques for in situ studies of metal solidification processes and the methods for processing those images.

2.1 Ultrasound, the intensity and pressure field

Sound wave is a mechanical wave of pressure and displacement that propagates through a medium (gas, liquid, solid) in periodic compression and expansion (rarefaction) cycles [39]. The numbers of the wave periods counted in a second is called frequency, *f*. Fig. 2.1 shows the frequency range for the sound waves commonly found in nature and used in industries. That of a frequency > 20 kHz is often called ultrasound because it is beyond the detection capability of a human ear. However, in nature, some animals, e.g. bats and dolphins use ultrasound (about 14-100 kHz and 40-150 kHz, respectively) to navigate their environment.

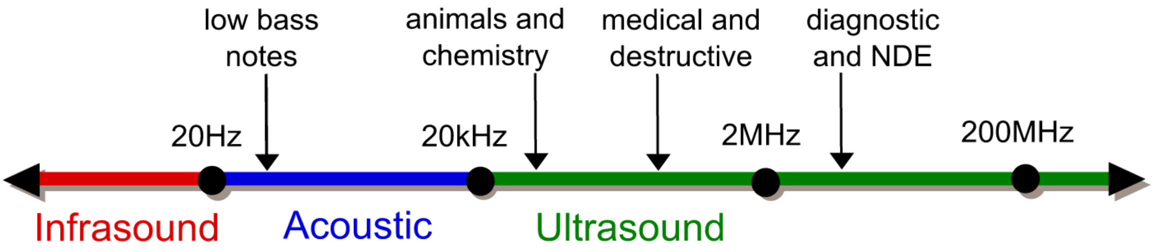

Fig. 2.1. *The approximate frequency range for different sound waves, and the typical sources or applications [40].*

The energy density of an ultrasound travelling in a medium is defined as the ultrasound intensity (I, W/m^2). For a simplest plane wave that is passing through a given section in one direction, I can be calculated by [41]:

$$I = \frac{N_{ac}}{S} = \frac{1}{2}\rho C v^2 = \frac{1}{2}\rho C (A_m \omega)^2 \qquad (2.1)$$

where Nac is the power flux of ultrasound, S is the area, ρ and C are the density and speed of sound of the liquid medium. v is the maximum value of oscillation velocity. A_m is the amplitude of the ultrasound vibration, $\omega = 2\pi f$ is the angular frequency and f is the frequency of ultrasound.

Dependent on the level of intensity, ultrasound falls into three categories [41]: (1) low intensity ultrasound ($I < 10^4$ W/m^2), (2) middle intensity ultrasound ($10^4 < I < 10^5$ W/m^2), and (3) high intensity ultrasound ($10^5 < I < 10^6$ W/m^2). The ultrasound used in this research is high intensity ultrasound. In Eq. 2.1, the product of ρ and C (ρC) is called the wave, or acoustic, impedance of the given medium.

Assuming a time harmonic vibration and ignoring the effect of cavitation flow, the cyclic ultrasonic acoustic pressures can be calculated using the Helmholtz equation [33, 42].

$$\frac{(\omega/C)^2}{\rho} P_a + \nabla \cdot \left(\frac{1}{\rho} \nabla P_a \right) = 0 \qquad (2.2)$$

$$P_a = P_A \cos(\omega t) \qquad (2.3)$$

$$P_A = \sqrt{2\rho C W/A} \qquad (2.4)$$

Where P_a is the alternate pressure at the sonotrode wave emitting surface, P_A is the amplitude of the pressure wave, W is the input ultrasound power, and A is the area of the ultrasonic wave emitting surface.

2.2 Cavitation, ultrasound cavitation and bubbles in liquids

Cavitation is the formation of vapour cavities (bubbles or voids) in a liquid when the liquid is subjected to rapid changes of pressure. Cavities often form at relative low pressure, but may collapse (implode) at higher pressure, generating an intense local shockwave surround the cavities [43].

2.2.1 A brief history on cavitation research

The phenomena of cavitation in liquids were reported as early as in the end of 19th century. In 1894, the British torpedo boat destroyer "HMS Daring" achieved a top speed of 24 knots, despite the theoretically designed speed of 27 knots [44]. Barnaby [44] led the investigation of the problem, and concluded that the limit of the propeller speed is related to the maximum tensile strength of water, beyond which the propeller inflow broke down, creating discontinuity of the flow. In 1895, Froude proposed the term "cavitation" for such a phenomenon, derived from the Latin word "cavus, -a, -um" – "hollow". Between 1908 and 1924, cavitation studies became essential for the design and testing of propeller for fast boats, and cavitation tunnels were built in 1911 to facilitate the photographic observation of cavitation. However those early experiments had not been able to address the central question on "how cavitation is actually corroding the propeller surfaces".

It was not until 1917 when Lord Rayleigh published "The theory of sound" [45], the theoretical framework for cavitation began to be established.

In 1920's, Boyle and others [46, 47] were probably the first to identify acoustic cavitation in water produced by ultrasound. Since then, cavitaiton in ultrasound fields had become an intensive research field because the very diverse and exponential growth in applications of ultrasound technologies in modern society and industries.

Since 1920's, numerous technologies had become available for studying a single bubble in liquids in a very precisely controlled manner. For example, (1) electrically induced sparks from electrode immersed into liquids in the 1940's, (2) pulsed laser beams in the 1960's, (3) single bubble sonoluminescence phenomenon found in 1980's. Huge scientific advances have been made in cavitaiton research, and those directly relevant to the research in this thesis are reviewed in the following sections in this chapter.

2.2.2 Ultrasound cavitation and bubble nucleation

When the applied acoustic intensity in liquids is above a certain level (the cavitation threshold) [5], bubbles or cavities are created, and this is a process commonly known as bubble nucleation [3] which occurs either homogeneously or heterogeneously.

Homogeneous nucleation of cavitation arises from microscopic voids in liquids due to thermal fluctuations [48] (Fig. 2.2a). Under ultrasonic irradiation the growth of the nucleated bubbles in a liquid can occur through the following mechanisms [49, 50]: (1) with high-intensity low frequency ultrasound (20 kHz), cavitation nuclei may grow rapidly through inertia effects and (2) with low-intensity high frequency ultrasound (> 50 kHz) a cavity may also grow, but slowly, this process is called rectified diffusion. This occurs because the cavities surface area is slightly greater during expansion than during compression. The cavity can reach a critical size where it can no longer efficiently absorb energy from the sound field to sustain itself [3]. This size is determined by the frequency of the ultrasound. For instance, the critical size in water is around 170 μm in diameter at 20 kHz.

In contrast, heterogeneous nucleation of cavitation (Fig. 2.2b) originates from the presence of sub-microscopic air pockets at the solid/ liquid interface on the wall of the substrate or on particles present in the liquid [51]. Theoretically, liquids can resist pressures of 3×10^4 Pa to 3×10^5 Pa. In reality, however tensions of just 100 times less can induce cavitation because the imperfections or “weak points” [52] present inside the liquids which provide the point for nucleating cavitation heterogeneously. For example, pre-existing bubbles present in liquids, impurities or particulates (may contain gases) that cause discontinuity or liquid-solid interfaces in the medium. Other possible sources for cavitaiton nucleations is electromagnetic radiation, which may be mediated by ionisation, or thermal motion of the molecules [53].

In summary, the most common sites for heterogeneously nucleating cavitation are: boundaries and surface (particularly structural defects such as cracks, crevasses and debris material), suspended particles, small pre-existing bubbles (nanobubbles) and external electromagnetic radiation, such as lasers [53].

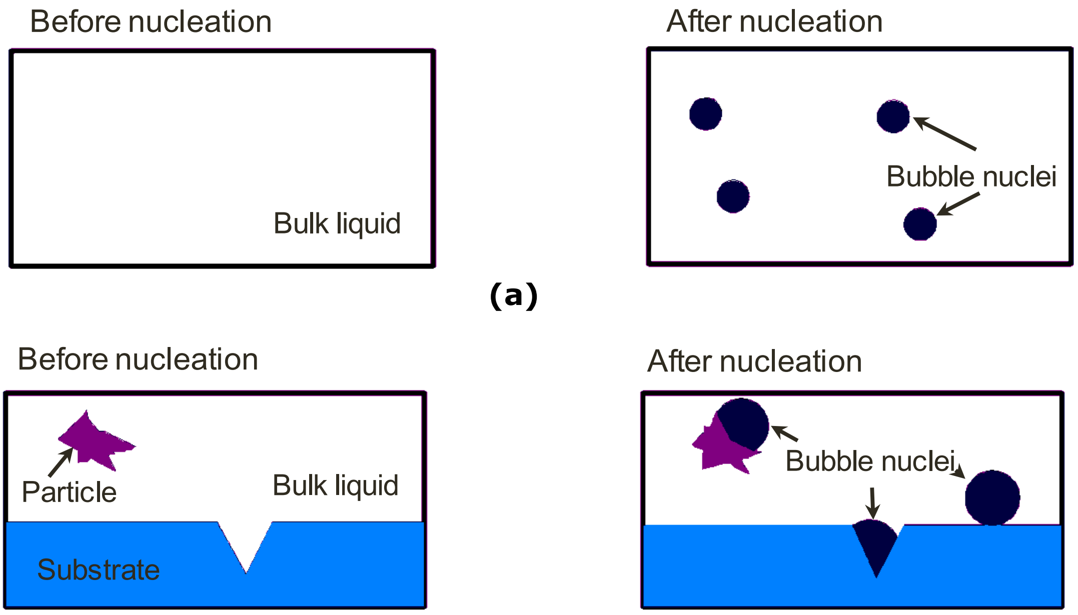

(a)

(b)

Fig. 2.2. *Schematic diagrams, showing (a) homogenous and (b) heterogamous nucleation of bubbles in liquids [54].*

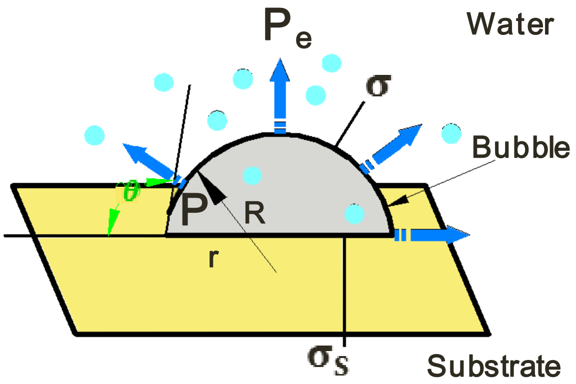

Fig. 2.3*. A sketch, showing the balance of energy for a bubble nucleated at the substrate inside a liquid [3].*

Fig. 2.3 schematically illustrates a bubble nucleated at a wettable surface if the surface tension of the solid-vapour interface (σ_s) is smaller than the surface tension of the vapour-liquid interface (σ) [55], because, for small contact area, the free energy reduction of the nucleus due to the contact with the surface is larger than the loss in free energy due to cutting off of the otherwise spherical cap of a non-contacting nucleus. For this reason cavitation occurs exclusively at the surface. Mossop *et al*. [56] and Turnbull [57] assumed that the heterogeneous nucleus is a spherical cap of the nucleating phase on a flat substrate (Fig. 2.3). The energy E(R) of a growing vapour bubble of radius R can be computed in the same way as that for the homogeneous case except that the interface-creating work is comprised of two parts: the gas-liquid part and gas-solid part. Therefore, E(R) is the sum of the work for volume expansion, gas-liquid interface creation and gas-solid interface creation. The volume of the spherical cap (V_b), the interfacial area of gas-liquid (A_{GL}) and that of gas-solid (A_{GS}) can be obtained as follows:

$$V_b = \frac{1}{3}\pi R^3(2 + 3cos\theta - cos^3\theta) \tag{2.5}$$

$$A_{GL} = 2\pi R^2(1 + cos\theta) \tag{2.6}$$

$$A_{GS} = \pi R^2(1 - cos^2\theta) \tag{2.7}$$

By combining these equations, the critical radius $r*$ and the corresponding critical energy $E(r*)$ can be calculated by:

$$E(r^*) = \frac{16\pi\sigma^3 g}{3(P-P_e)^2} \tag{2.8}$$

and

$$g = \frac{1}{4}(2 - cos\theta)(1 + cos\theta)^2 \tag{2.9}$$

The parameter g is a shape factor of the gas bubble on the surface, and P and P_e are the pressure inside and outside the bubble, respectively. Critical sizes in different solvents can be calculated from their cohesion energy [3].

For a bubble formed under an ultrasound, the pressure P has to perform work on the gas with volume V_b. Thus the pressure P includes the difference from the outside hydrostatic pressure of the liquid resulting from possible entrapped gas with partial pressure P_G, vaporized liquid with partial pressure P_V, the largest contribution being the acoustic pressure upon rarefaction P_A:

$$P = P_A + P_G + P_V \tag{2.10}$$

According to Flynn’s criterion [58], the partial pressure of gas in the cavity equals the vapour pressure of the cavitating media at the operating temperature at the adiabatic collapse phase.

Furthermore, an addition of the chemicals can enhance the bubble nucleation by promote the heterogeneous nucleation. For example, presence of surface active materials or polymers can influence the cavitation process at the surface. For instance, Nanjo *et al*. showed that the forms and processes of the cavitation damage pits in specimens in a polymer solution are totally different from those in water [59]. Oblique and pot-shaped damage pits are formed on a flat, smooth surface of a specimen in a polymer solution. If the specimen has artificial pits such as small conical or cylindrical holes, the parts with small radius of curvature are apt to be damaged, although the smooth surfaces are not.

Experimental studies on bubble nucleation were also conducted by many researchers. for example, in 2007, Mettin [54] captured bubble nucleation from a single bubble to bubble clusters under a continuous acoustic field.

2.2.3 Bubble oscillation, implosion and coalescence

2.2.3.1 Bubble oscillation

Once a bubble is nucleated and grows bigger than the critical size, the nucleus becomes a mature bubble, and its size and shape oscillate in response to the periodic sound field. At relatively low acoustic pressures (P_a) where the pressure wave oscillates in a sinusoidal waveform between compression and rarefaction cycles, the radial motion of the bubble responds linearly [8] to the pressure field, characterised by nearly equal rates of expansion and contraction with no shift in phase relative to the pressure field. In fact, under this condition, bubble expansion is slightly larger than bubble compression, simply because the surface area of the bubble on expansion (gas flow in) is slightly larger than the surface area on compression (gas flow out). This growth process for long-lived bubbles is called rectified diffusion [43, 60]. For example, the well-known degassing of liquids by ultrasound is actually based on the rectified diffusion processes [54].

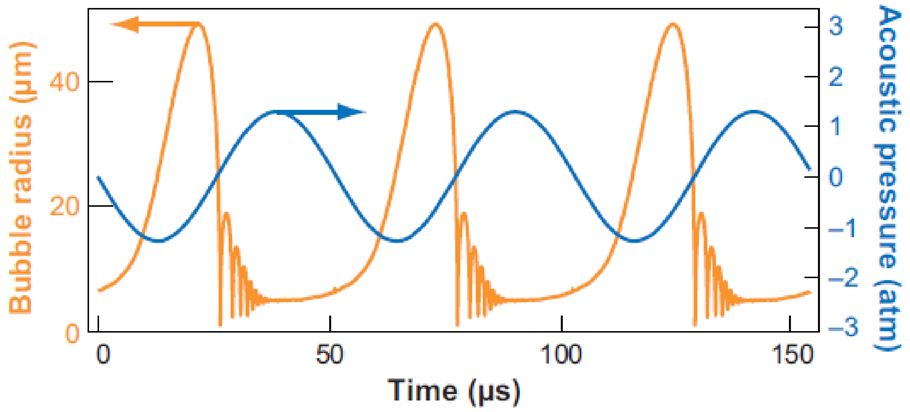

Fig. 2.4. *The calculated radial response of a bubble driven by a sinusoidal acoustic field. The bubble is assumed to be in equilibrium with respect to mass transport across the interface (i.e., no net change in intra-cavity mass over any single acoustic cycle). Thus, the bubble maintains the same spatial parameter space and shows no phase shift from one cycle to the next [8].*

At a higher P_a, bubble motion becomes highly nonlinear [43, 60, 61] in response to the cyclic acoustic pressure. Fig. 2.4 shows a bubble of a radius of R_n at rest, and this is at ambient conditions. As the acoustic pressure wave enters the rarefaction phase, the bubble begins a relatively slow volume growth, essentially a linear growth, lasting for roughly half the cycle. As the acoustic pressure wave enters its compression phase, the bubble motion starts to deviate from the linear compression. However, at a lower compressive P_a, the bubble continues to expand inertially, resulting in an energetically unfavourable situation until the bubble growth is quickly arrested at a higher compressive P_a, i.e. the maximum bubble radius, R_{max}, is reached. The bubble then begins a very rapid and eventually a catastrophic collapsing or imploding event. The velocity of the implosion at the last stage can be enormous and in some instances can be several times the speed of sound in gas at ambient temperature and pressure conditions [62]. As the compression phase continues, the bubble rapidly passes through R_n on its way to R_{min}, the minimum bubble radius. The gas and vapour trapped inside the bubble are then strongly compressed at R_{min}, making the bubble to rebound and expand quickly. The bubble then goes through a series of secondary compression and expansion cycles until finally coming to rest again at R_n.

For a bubble that is in equilibrium with respect to mass transport (Fig. 2.4), the same radial motion is repeated almost exactly from one cycle to the next for an isolated bubble far from any surface or interface.

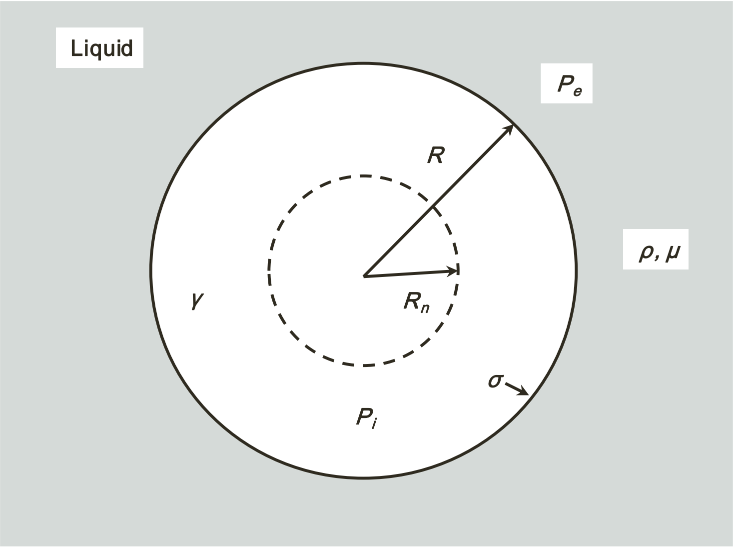

Fig. 2.5. *A sketch of the bubble oscillation in liquid with its parameters.*

For a spherical bubble, the variables to describe its size and shape can be reduced to just one, the bubble radius, R. The time-evolved bubble radius, $R(t)$, can then be calculated by the Rayleigh model [6]:

$$\rho R\ddot{R} + \frac{3}{2}\rho\dot{R}^2 = p_i - p_e \tag{2.11}$$

Where p_e is the external pressure in the liquid, p_i is the pressure inside the bubble. ρ *is* the density of liquid. The overdot ($\dot{R}$) means differentiation with respect to time. The pressure difference, ($p_i - p_e$) is the driving force for the bubble motion.

The form of the inertial terms on the left-hand side is due to the spherical 3-D geometry that is transformed to one radial dimension in the differential equation. Both, p_i and p_e are functions of radius R and time t, when gas and vapour fill the bubble, and when surface tension σ, liquid viscosity μ and a sound field, *p(t)*, are taken into account. With these considerations, the Rayleigh model takes the form [63, 64]:

$$\rho R\ddot{R} + \frac{3}{2}\rho\dot{R}^2 = p_{gn}\left(\frac{R_n}{R}\right)^{3k} - p_v - p_{stat} - \frac{2\sigma}{R} - \frac{4\mu}{R}\dot{R} - p(t) \qquad (2.2)$$

and

$$p_{gn} = \frac{2\sigma}{R_n} + p_{stat} - p_v \qquad (2.3)$$

p_gn is the gas pressure inside the bubble at rest, p_stat the static pressure and p_v the (here constant) vapour pressure. The pressure *p(t)* is an external pressure applied at the bubble wall. In the case of a single frequency ultrasonic excitation of the bubble, it can be written in the form of

$$p(t) = -p_a \sin(2\pi f t) \qquad (2.14)$$

It varies sinusoidally with frequency f and has a pressure amplitude p_a. The '–' sign is convenient for starting the oscillation at t = 0 with an expansion of the bubble at rest.

This model and some variants are called Rayleigh–Plesset models. A more advanced model is the Gilmore model [23] that incorporates sound radiation into the liquid from the oscillating bubble, whose surface acts like the membrane of a spherical loudspeaker. For strong oscillations, i.e. strong compression of the gases inside the bubble, the model is further augmented by a van der Waals law to account for a non-compressible volume of the inert gas inside the bubble [65]. This bubble model reads:

$$\left(1 - \frac{\dot{R}}{C}\right)R\ddot{R} + \frac{3}{2}\dot{R}^2\left(1 - \frac{\dot{R}}{3C}\right) = \left(1 + \frac{\dot{R}}{C}\right)H + \frac{R\dot{R}}{C}\left(1 - \frac{\dot{R}}{C}\right)\frac{dH}{dR} \qquad (2.15)$$

$$C^2 = \frac{n(P+B)}{\rho}\left(\frac{P+B}{P_0+B}\right)^{-\frac{1}{n}} \tag{2.16}$$

$$H = \frac{n}{n-1}\frac{(P_0+B)^{\frac{1}{n}}}{\rho}\left[(P+B)^{\frac{n-1}{n}} - (P_\infty + B)^{\frac{n-1}{n}}\right] \tag{2.17}$$

$$P = \left(P_0 + \frac{2\sigma}{R_0}\right)\left(\frac{R_0}{R}\right)^{3\gamma} - \frac{2\sigma}{R} - \frac{4\mu\dot{R}}{R} \tag{2.18}$$

where *R*, *P*, *H* and *C* is the radius, pressure at the bubble wall, enthalpy and sound speed of the liquid, respectively; R_0 is the initial bubble radius, *B* and *n* are empirical constants that depend on the particular liquid, P_0 is the liquid ambient pressure at 1 atm and $P_\infty = P_0 + P_a$ is the pressure at infinite distance from the bubble.

Another model is the Keller–Miksis model [66] that also incorporates sound radiation from the oscillating bubble, but features a retarded time $t - R/c$ in the equations, and *c* is the sound velocity in the liquid, and dispensing with the retarded time, it reads as [67]:

$$\left(1 - \frac{\dot{R}}{C}\right)R\ddot{R} + \frac{3}{2}\dot{R}^2\left(1 - \frac{\dot{R}}{3C}\right) = \left(1 + \frac{\dot{R}}{C}\right)\frac{p_1}{\rho} + \frac{R}{\rho C}\frac{dp_1}{dt} \tag{2.19}$$

and

$$p_1 = \left(\frac{2\sigma}{R_n} + p_{stat}\right)\left(\frac{R_n}{R}\right)^{3\gamma} - p_{stat} - \frac{2\sigma}{R} - \frac{4\mu}{R}\dot{R} - p(t) \tag{2.20}$$

$$p(t) = -p_a \sin(2\pi f t) \tag{2.21}$$

The connection between the different bubble models has been explored by Prosperetti and Lezzi [68, 69].

The radius of the bubble at rest, R_n, is applicable to a wide range of bubble radius (from sub-micrometre to microbubbles to millimetre bubbles). It may be also useful for large bubbles found in underwater explosions, either by underwater sparks or by explosions. The frequency, *f*, can take values from a few hertz to a few megahertz. While the pressure, p_a, may vary between zero (no sound field) and several MPa.

The three basic bubble models (Rayleigh–Plesset; Gilmore; Keller–Miksis) have given astonishing precise descriptions of most experiments on spherical bubble oscillations. Among them, Gilmore model is the most commonly used in the studies of bubbles in the past decades, and has been proved to be valid in water and water solutions [6, 18, 64, 70-72]. For instance, Geisler [70] has validated the Gilmore model by comparing it with the experimental results of the bubble oscillation. The experiment was conducted by using a simple arrangement consists of a rectangular glass cuvette with just one piezoelectric transducer glued to the bottom for producing the ultrasound, as shown in Fig. 2.6a. The thin platinum wire sticking into the cuvette from the upper right side produced bubble via a current pulse. A stably trapped bubble was seen by its bluish-white light emission.

The bubble can be photographed with high resolution in time and space [73] by the use of a long distance microscope, a short exposure time and sampling the oscillation by shifting the phase at which the picture is taken with respect to the driving ultrasound. Fig. 2.6b shows one cycle of a bubble oscillation driven at 21.4 kHz and taken in backlight conditions [70]. The time interval between frames is 500 ns. The spherical bubble is black on a brighter background as the illuminating light is scattered at bubble surface. A slow expansion of the bubble and a fast collapse with several bounces afterwards was observed and captured.

Fig. 2.6c is the comparison of the bubble sizes measured from Fig. 2.6b with the modelled ones by using the Gilmore model (see [72] for more details). The measured and modelled radius agreed well. However, the event of bubble collapsing or implosion occurs in such a short time scale, even the 500 ns exposure time cannot resolve the highly transient event.

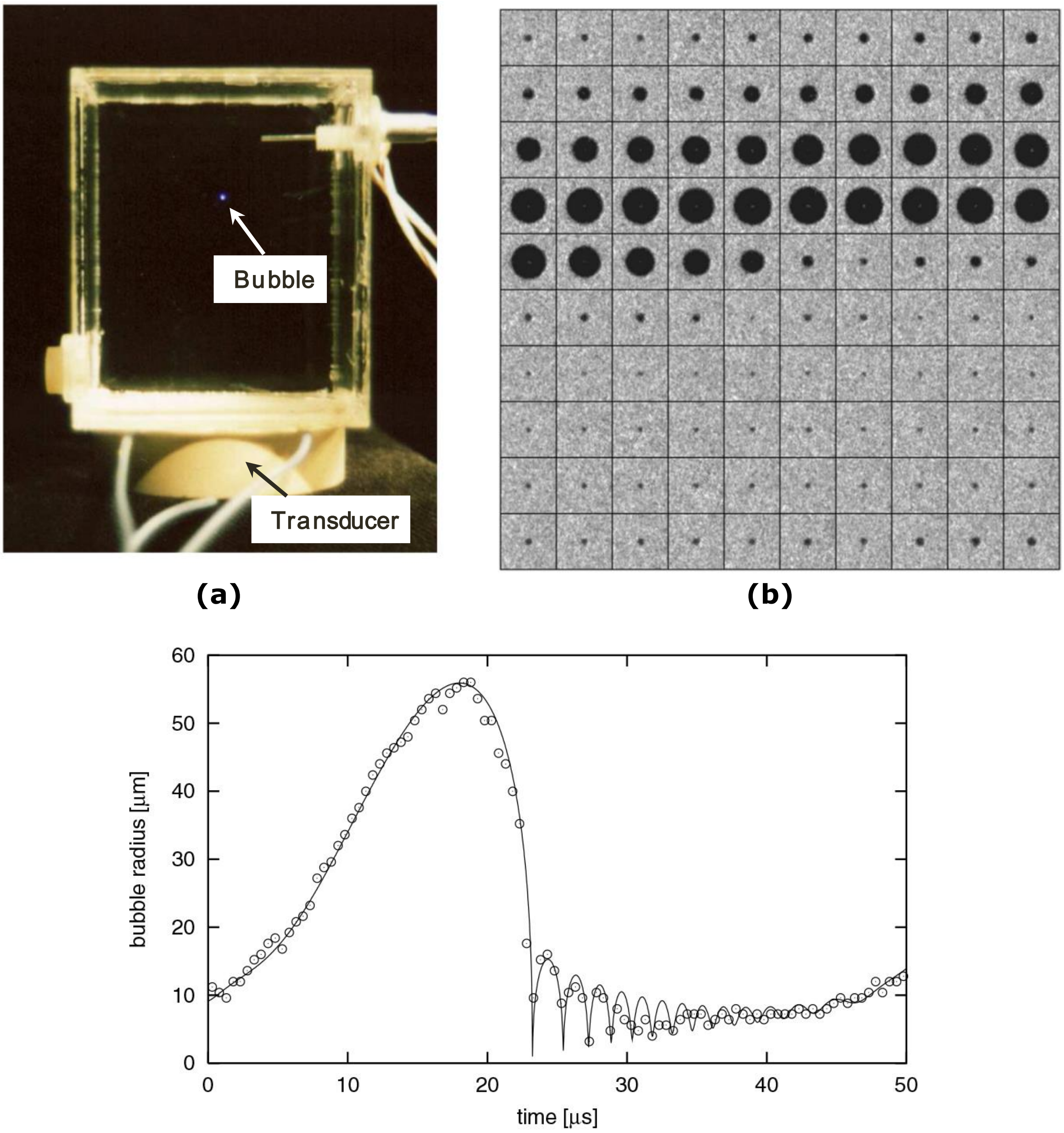

(a) **(b)**

(c)

Fig. 2.6. *(a) A photo of a bubble trap with a transducer glued to the bottom. The bluish-white spot in the middle of the upper part of the water filled cuvette (cube with an inner edge length of 5 cm) is the light emitted by a stably oscillating bubble. (b) Image sequence of a trapped bubble driven at 21.4 kHz in one acoustic cycle (500 ns interframe time, frame size 160μm × 160μm). (c) the oscillation curve (solid line) of a trapped bubble calculated using the Gilmore model with the experimental data (circular marker) measured from the images showed in b. [70].*

2.2.3.2 Bubble implosion

For any growing bubble inside an acoustic field, if the surface tension of the liquid is no longer able to support the pressure difference under the compression wave, the bubble collapses or implodes as schematically illustrated in Fig. 2.7.

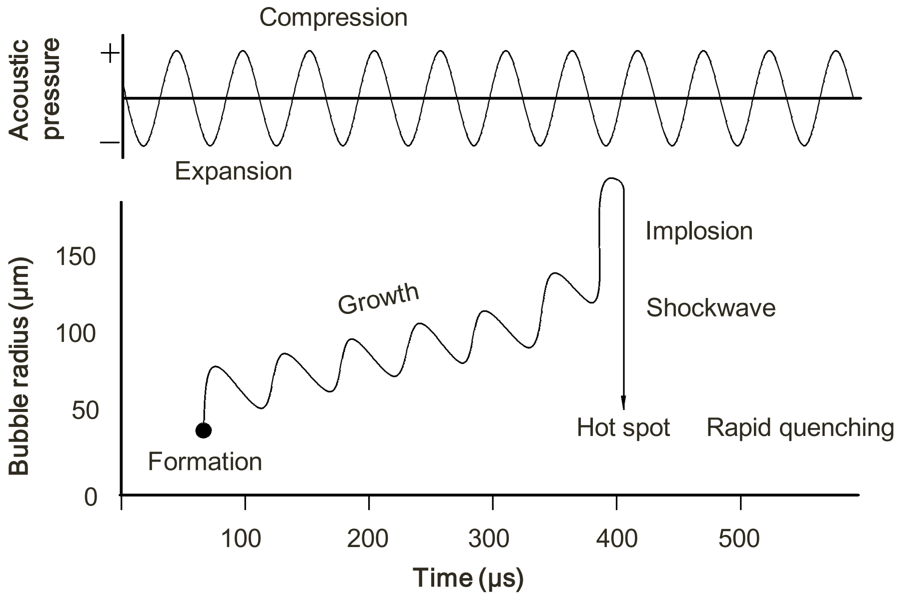

Fig. 2.7. *The formation, growth and implosion of a bubble under a cyclic acoustic pressure field [74].*

Many previous studies [8, 9, 16, 75, 76] had confirmed that, at bubble implosion, a shockwave is produced by the gas trapped inside the bubble because the gas is compressed so rapidly, and the heating due to the rapid compression is nearly adiabatic with no time to flow out, resulting in the formation of a localized, transient hot spot companied by an extreme pressure. Suslick, *et al* [8, 76, 77] argued that the pressure is in a range of a few thousands bars occurring in a few nanoseconds, responsible for driving a wide variety of reactions in chemistry and physics, and producing products not typically accessible by other standard means. This is typically known as the sonochemistry domain as illustrated in Fig. 2.8 where extreme conditions (heat and high pressure) lead to a new type of interactions or reactions between energy and matters at nano or sub-nanosecond scale [8].

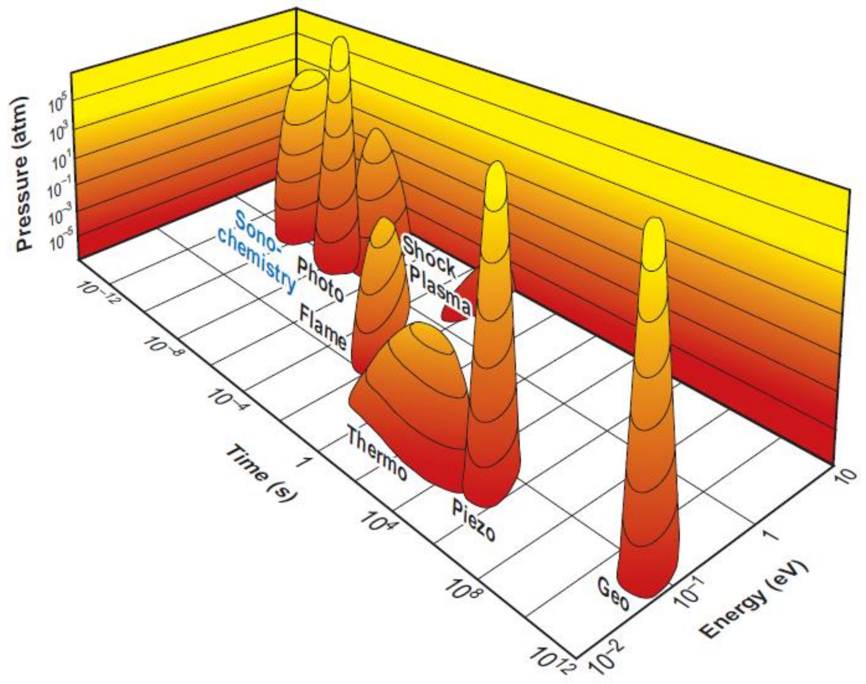

Fig. 2.8. *A schematic diagram of the distinct domains of chemistry, showing that acoustic cavitation and the corresponding sonochemistry method provide an unusual means to access a unique parameter space for exploring new and interesting chemistry and physics [8].*

Currently, the highly transient events occurring at the last stage of bubble implosion is not well understood, and this is still the centre of bubble physics research. Generally two methods were often used in the studies on bubble implosion: (1) high speed optical imaging under the illumination of a visible light [6, 14, 18, 19, 21, 24, 33], and (2) spectroscopic measurement of the light emission spectrum due to the sonoluminescence effect at bubble implosion [8, 9, 16, 75] or measurement of the chemical reaction rate [9]. All reported experiments were conducted in a transparent liquid media such as water or water based solutions under visible light illumination.

Using the first method, Lauterborn and Ohl [17, 18, 78] captured the shockwave emitted at bubble implosion in a view field of about few square millimetres as showed in Fig. 2.9 using an exposure time of 10 ns.

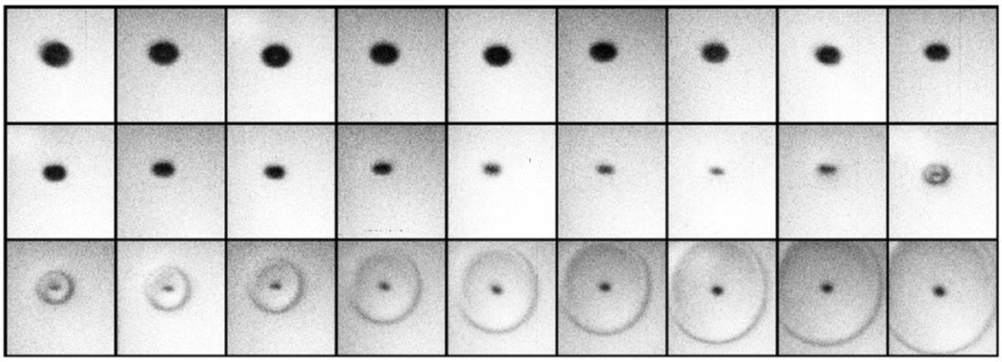

***Fig. 2.9**. A series of photographs (1.5×1.8mm^2) captured using 20.8 million fps (interframe time of 48 ns, exposure time of 10 ns), showing the dynamics of a laser produced bubble in water and the shock wave produced at implosion. The bubble reaches its maximum radius of 1.1 mm at 99.5 μs before the first frame [78].*

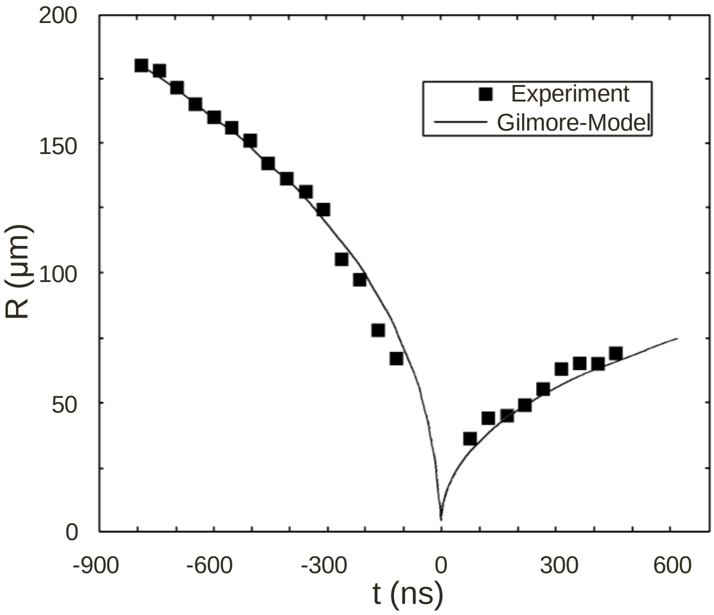

***Fig. 2.10.** The comparison of the measured bubble radius (from the images in **Fig. 2.9**) with that calculated using the Gilmore model. The bubble radius around implosion (around t = 0) cannot be not obtained [6].*

Fig. 2.10 shows that the measured bubble radius from the images (Fig. 2.9) agreed well with the Gilmore model calculation. However, at the very instant of bubble implosion, clear images of the bubbles were not able to be captured because the shock wave deflects the light and does not give an undisturbed view on the bubble surface. Therefore the key radius information at bubble implosion is missing.

Although the shockwave has been captured, the intra-cavity condition cannot be analysed because the illumination often suffers strong light absorption, reflection and multiple scattering problems, resulting in general two problems in the obtained images: (1) cannot "see" through the bubble, therefore the dynamic event occurring inside the bubble cannot be revealed; (2) often have a blurred bubble boundary, hence any dynamic events involving the movement of boundaries, such as the breaking up or coalescence of bubbles cannot be studied in great details [6, 14, 18, 19, 21, 24, 33]. The above two problems can be avoided if the synchrotron X-ray is used as the light source as detailed later.

In liquids other than water [79], the bubble behaviour will be, of course, different due to the different liquid properties. Comparison of experiment and theory of bubble oscillation in the silicone oil with a viscosity of 0.485 Pa·s have been done and a fairly good fit was obtained [6, 18]. However, the fit for even higher viscosity silicone oils (higher than 1 Pa·s) [80] is not good, as viscoelastic properties come into play during the fast motion [81].

When a bubble is collapsing in a non-spherically symmetric environment, e.g. near a rigid boundary, the collapsing behaviour are remarkably different [78], and this is generally categorised as bubble-boundary interactions which is the fundamentals for ultrasound cleaning/erosion, and medical applications, e.g. drug delivery.

Both experiments and simulations illustrated that the bubble implosion near a rigid boundary produce a microjet towards the boundary [82-84], and the morphology of the microjet is linked to the distance between the bubble and the boundary [71, 85, 86]. The distance is usually defined as a normalized distance, i.e. the distance from the bubble centre to the boundary over the maximum bubble radius during oscillation [6].

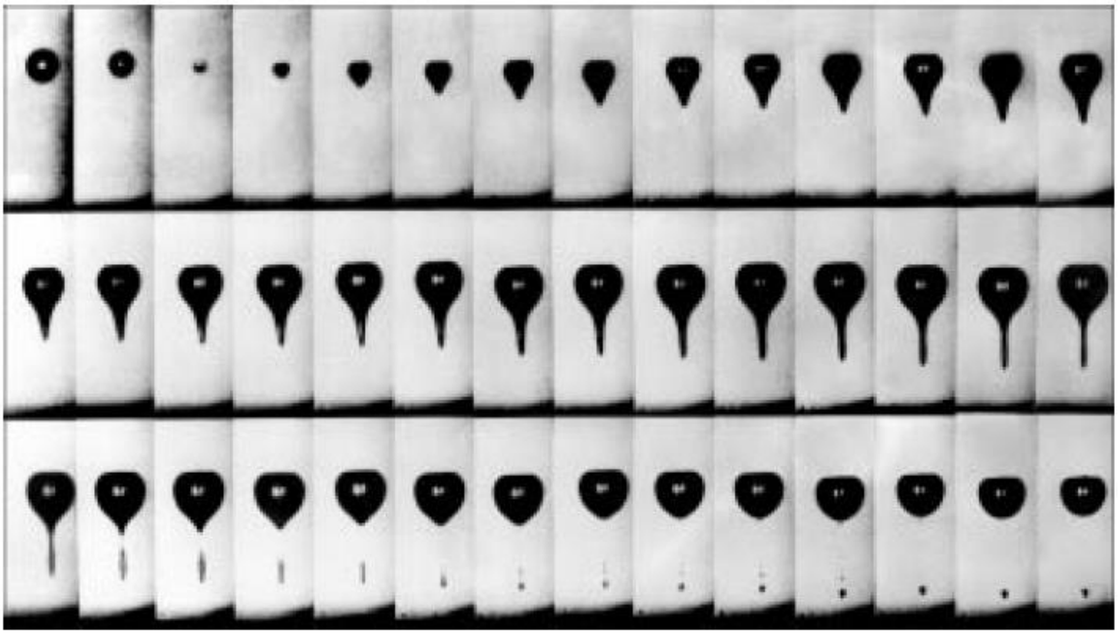

Fig. 2.11. *The microjet of a laser-generated spherical bubble in water in the vicinity of a plane solid boundary at the bottom, observed at 300, 000 fps. The frame size is 6.7 × 2.7 mm^2 [78].*

Fig. 2.11 shows a typical image sequence [78] of a laser-generated bubble collapsing near a plane boundary. Immediately after the collapsing and in the first rebound phase, a funnel-shaped protrusion pointing downwards the boundary was observed. It is actually the elongated bubble wall containing a high-speed liquid jet. The momentum of the liquid jet drives the funnel-shaped protrusion into a tube-shaped bubble until its energy is used up. Then the tube becomes unstable and decays into many tiny bubbles, while the main bubble surface snaps back to its former spherical shape.

However, laser beam has, in general, an elongated conical shape, larger in the longitudinal direction than in the transverse direction. So whether the laser-generated bubble is spherical in 3-D are still subject to active debating and investigation [78]. This uncertainty, however, can be removed if an ultrasound sonotrode is used to generate the spherical bubbles, as described in details in the experiment in this research later.

To measure the pressure and temperature created at bubble implosion, Flamnnigan and Suslick [8, 16] analysed the sonoluminescence spectrum produced from a single bubble imploded in an aqueous solution of a modest acoustic pressure of ($P_a \approx 1.5$ bar). The calculation indicated that a shockwave with a pressure of >4000 bar and temperature of >5000 K was created, leading to complicated sonochemical reactions. They argued that an optically opaque plasma core is formed at implosion. However, it is very difficult to reveal the intra-cavity [16] event occurs at bubble implosion, especially under visible light illumination.

Suslick, *et al* used the "comparative-rate chemical thermometry" technique [9] to determine the effective temperature reached during bubble implosion. The sonochemical ligand substitutions of volatile metal carbonyls were used as the comparative rate probes (Eq. 2.22).

$$M(CO)_X \overset{)))}{\rightarrow} M(CO)_{X-n} + nCO \overset{L}{\rightarrow} M(CO)_{X-n}(L)_n \qquad (2.22)$$

where M = Fe, Cr, Mo, W; L represents a substituting ligand; and the symbol $\overset{)))}{\rightarrow}$ represents ultrasonic irradiation of a solution.

These kinetic studies revealed that there are in fact two sonochemical reaction sites as shown schematically in Fig. 2.12: the first (dominant site) is the bubble's interior gas-phase. While the second is an initially liquid phase. The latter corresponds either to the heating of a shell of liquid around the collapsing bubble or to the injection of liquid droplets into the hot spot by surface wave distortions of the collapsing bubble [87].

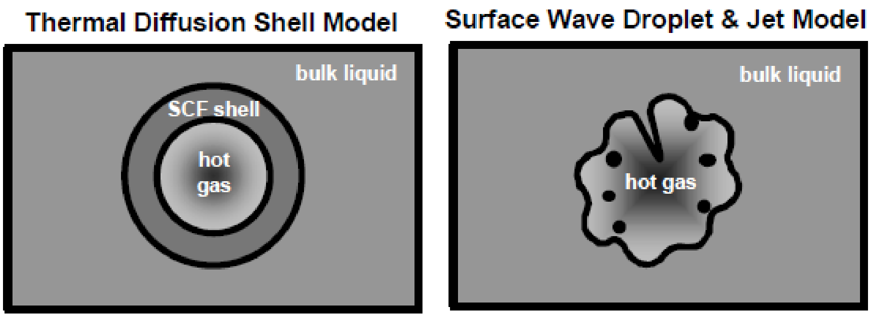

Fig. 2.12. *Two-site models for sonochemical reactions [87].*

The effective local temperatures in both sites were determined by combining the relative sonochemical reaction rates for Eq. 2.22 with the known temperature behavior of these reactions. The effective temperatures of these hot spots were measured at about 5200 K in the gas-phase reaction zone and around 1900 K in the initially liquid zone [9]. This two-site model has been confirmed by other reactions [88].

2.2.3.3 Bubble coalescence

The extensive studies on the dynamic behaviour of a single bubble in the past few years have provided much insight into the underlying physics of bubble nucleation, oscillation and implosion. However, in reality, many ultrasonic bubbles appear in liquid simultaneously, and evolve collectively. When two or more bubbles make contact with each other, they may join together to form bigger bubbles, a process commonly known as bubble coalescence. It plays an important role in the formation of cavitation patterns, and consequently the heat transfer, gas-liquid or liquid-liquid mass transfer in the liquids [24, 89].

Bubble coalescence is of great significance in industrial applications, such as multiphase reactors in chemical and biochemical processes [90, 91], degassing of liquid metals during melting, as well as in separation processes like absorption and distillation. Ultrasound induced bubble coalescence has potential clinical applications in harmonic imaging, non-invasive blood pressure measurements and targeted drug delivery [21].

To understand quantitatively the process of bubble coalescence, the basic theories and models are reviewed and discussed here.

In 1969, Marrucci [92] proposed that bubble coalescence occurs in 5 steps:

(1) **Approaching**: two bubbles in the liquid approach to each other.

(2) **Flattening of contact surfaces**: the approaching bubbles come in contact, forming a thin film (a quasi equilibrium film of an initial typical thickness of 1-10 μm) between the two bubbles in contact. This step is driven by the hydrodynamics of the bulk liquid.

(3) **Liquid film drainage**: this is a process of thinning of the film by draining away of the liquid trapped inside the film. The process is driven by the combined effects of (i) capillary pressure, (ii) plateau border suction, and (iii) disjoining pressure [93]. The process is also influenced by the properties of the liquid, such as surface tension and viscosity.

When the thickness of the film is reduced to ~100 nm, Van der Waals attraction increases the draining rate, while the electrostatic double layer repulsive force decreases the draining rate. On further thinning to a thickness of 50-10 nm, some films may collapse, while others may become metastable dependent on the balance among the border suction, Van der Waals attraction and double layer repulsive forces. Instability occurs when the attraction forces predominate [94].

(4) **Rupture of the film**: when the film is reduced to below 10 nm, it ruptures, leading to coalescence. Unstable films (often called transient films) rupture spontaneously at the 'critical thickness'. However, if the contact time is less than the time needed for a complete film drainage, film rupture does not occur, and the bubbles will bounce off each other and separate [89].

(5) **Spherical recovery**: the new bubble formed by coalescence may inherit the shape from the parent bubbles. It tends to become spherical driven by surface tension, especially when it continually grows bigger under the expansion cycle of the acoustic pressure. Fig. 2.13 demonstrates the coalescence process schematically. The liquid film drainage step is highlighted in Fig. 2.14, showing two modelled bubbles (R_1 and R_2, with the internal pressure of p_1 and p_2 respectively), and the liquid film (h) in between the two bubbles.

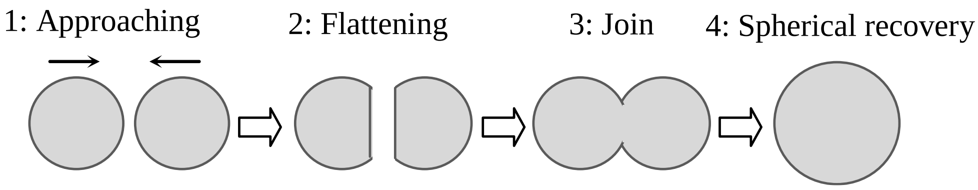

Fig. 2.13. *A schematic diagram, illustrating the process of bubble coalescence.*

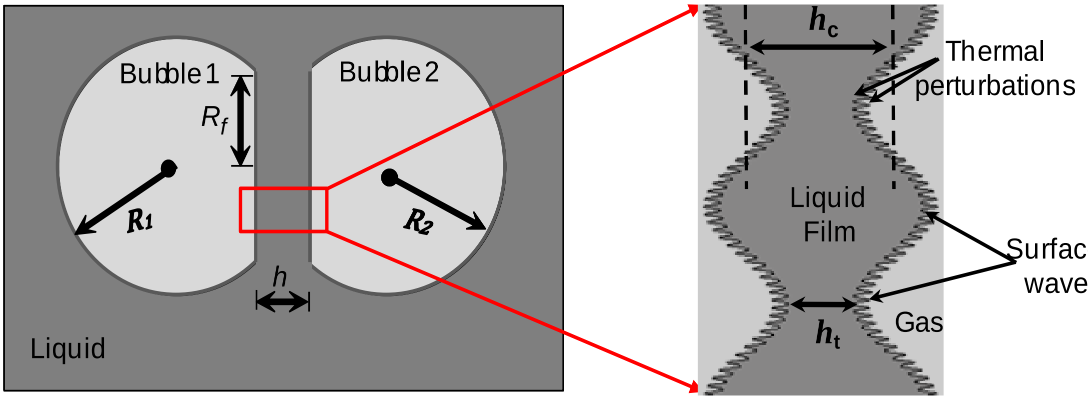

Fig. 2.14. *The model and parameters for calculating film drainage during bubble coalescence.*

(i) Flattening of the bubble surfaces and liquid film

For the two colliding bubbles (Fig. 2.14), flattening of the contacting surfaces occurs when the liquid inertia overcomes the capillary pressure, and this can be assessed by the Weber number for two colliding bubbles which is defined as the ratio of inertial force relative to the surface tension force:

$$We = \frac{\rho v^2}{\frac{\sigma}{R_e}} \tag{2.23}$$

where v is the relative approach velocity of the bubble walls, ρ is the fluid density, σ is the surface tension. R_e is the mean bubble radius calculated by:

$$\frac{2}{R_e} = \frac{1}{R_1} + \frac{1}{R_2} \tag{2.24}$$

For bubbles with a constant center-to-center distance, the relative approach velocity of bubble wall is given by:

$$v = \dot{\mathrm{R}}_1 + \dot{\mathrm{R}}_2 \tag{2.25}$$

When $We < 0.5$, bubble coalescence always occur without flattening of the adjacent surfaces prior to contact [95]. However, when $We \geq 0.5$, surface flattening occurs and a thin layer of residue liquid, i.e. a liquid film, forms in between the contacting surfaces [95]. Coalescence is then controlled by the mechanisms and the time needed to completely drain out the liquid film - the film drainage process.

(ii) Film drainage

The driving force for draining the liquid film is the difference between the film pressure, $p_f = \frac{1}{2}(p_1 - p_2)$, and the liquid ambient pressure,p_0. At equilibrium, the pressure difference is balanced by surface tension (by ignoring the disjoining pressure [88]):

$$p = p_f - p_0 = \sigma\left(\frac{1}{\mathrm{R}_1} + \frac{1}{\mathrm{R}_2}\right) \tag{2.26}$$

Two models had been proposed to calculate the time needed for film drainage: (a) no-slip (rigid) bubble interface where a laminar flow is assumed for the film drainage. The typical examples are the liquids with surfactant or electrolytes [96]; (b) Free (mobile) bubble interface where and a plug flow (no boundary layer near the boundary) is assumed for the film drainage, e.g. for pure water.

No-slip interface assumes zero tangential velocity for the interface and the plug flow contribution is zero [97]. The velocity for film drainage can be calculated by using the laminar flow model given by the Reynolds equation [98] :

$$-\frac{\partial \mathrm{h}}{\partial \mathrm{t}}=\frac{2\mathrm{ph}^3}{3\mu\mathrm{R}_\mathrm{f}^2} \tag{2.27}$$

where μ is the viscosity and R_f is the radius of the film surface.

The drainage time, t_d, between the initial film thickness h_i and the critical film thickness h_c (the film thickness at the instant of rupture as shown in Fig. 2.14 can be determined by integration of Eq. 2. 27,

$$\int_{h_i}^{h_c}-\frac{dh}{h^3}=\int_0^{\tau_d}\frac{2p}{3\mu\mathrm{R}_\mathrm{f}^2}dt \tag{2.28}$$

$$t_d=\frac{3\mu R_f^2}{4ph_c^2}\left(1-\frac{h_c^2}{h_i^2}\right) \tag{2.29}$$

Furthermore, if assuming $h_c^2 \ll h_i^2$, then:

$$t_d\approx\frac{3\eta\mathrm{R}_\mathrm{f}^2}{4ph_c^2} \tag{2.30}$$

Substituting Eq. 2.26 into 2.30:

$$t_d\approx\frac{3\eta\mathrm{R}_\mathrm{f}^2}{4\sigma\left(\frac{1}{\mathrm{R}_1}+\frac{1}{\mathrm{R}_2}\right)h_c^2} \tag{2.31}$$

Apparently, viscosity is taken into account in this case [99, 100], which means any surfactant can affect the process [21, 98, 101, 102]

Free interface assume that the drainage is inertial [103]. The velocity for free radial surfaces is given by the equation below regardless of viscosity [104]:

$$-\frac{\partial \mathrm{h}}{\partial t}=\sqrt{\frac{8p}{\rho}\frac{h}{R_f}} \tag{2.32}$$

Assuming a quasi-static condition for p and R_f, the drainage time can be calculated by [21]:

$$t_d \approx R_f \sqrt{\frac{\rho}{8p}} log\left(\frac{h_i}{h_c}\right) \tag{2.33}$$

(iii) Film rupture

For the plane-parallel configuration with tangential immobility, the drainage time can be predicted well using the no-slip interface model at room temperature and pressure of 1 atmospheric pressure [89]. However, at micro level, the bubble surface adjacent to liquid film is non-flat surface (Fig. 2.14), composing of a combination of hydrodynamic surface wave (low frequent, large amplitude) and thermal perturbation (high frequent, small amplitude) [93].

Sheludko Angarska *et al* [105] measured the thicknesses and radii of liquid films of different surfactant concentration, and found that, for film radii of 60 μm < R_f < 160 μm, the critical thicknesses is in the range of 20 nm< h_c < 40 nm.

Many efforts have been made to study the bubble coalescence in different liquids [89], for example, water, water solution of electrolytes or surface active agents (surfactant solution), and even non-Newtonian fluid of high viscosity [106]. A major emphasis has been on understanding the influence of electrolytes and/or surfactants on the time for coalescence and bubble size. For example, Postema *et al* [21] studied the ultrasound (0.5 MHz) induced microbubble coalescence in water with electrolytes by using a microscope coupled with a high speed camera.

Very recently, Bi, *et al*. [107] studied the bubble coalescence affected by the nucleation site arrangement and spacing, and Fig. 2.15 illustrates that bubble coalescence on three nucleation sites in a triangular pattern. In most pure solvents, bubbles tend to coalesce faster, while the additions of electrolytes or surfactants lead to suppression of bubble coalesecence, resulting in lower average bubble size, higher gas hold-up and interfacial area. Similarly, temperature and pressure have a significant influence on the bubble size, the gas hold-up and the associated flows as reported in [90, 108].

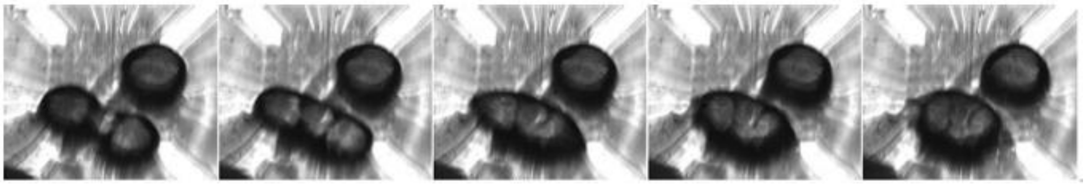

Fig. 2.15. *Bubble coalescence on three nucleation sites in a triangular pattern [107]. The interframe time is 1 ms.*

However, quantitative predictions on the bubble size, its distribution, coalescence time, turbulence structure, interfacial area, and gas hold-up as a function of operating conditions and properties of a system are still very difficult, especially in the field of design of multiphase reactors involving bubbles. This is largely due to the lack of quantitative understanding of the mechanisms of bubble break-up and coalescence and the physical processes involved in it [89], especially for the case of liquid metals.

2.2.4 Bubble cloud and cavitation zone in liquids

Cavitation in liquids starts at relatively low acoustic pressures, forming a cavitation region or zone, typically close to the vibrating source.

The size and geometry of the cavitation zone is not a very well-studied subject. The average dimensions of the cavitation zone are on the same scale as the diameter of the sonotrode. The dimensions of the cavitation zone can be estimated by observing cavitation erosion of a thin foil placed under the sonotrode, or by measuring the loss of mass of special samples immersed into the liquid. When cavitation is established, the cavitation region has a volume with the cross section ranging approximately from $\lambda/4$ to $\lambda/2$. For example, 20–40 mm for water, and 50–100 mm for aluminium melts [109, 110].

Fig. 2.16 illustrates a typical cavitation region generated by a cylindrical horn (the type that is frequently used in metallurgical applications). Evidently, there is a very densely cavitating zone close to the face of the sonotrode, which then develops into a cone-like structure with blur boundaries. Dubus et al. [111] suggest that the thin and concentrated cavitation bubble layer close to the surface of the sonotrode grows in thickness with the amplitude of the source until it reaches the acoustic half wavelength (estimated to be on order of 1-2 mm at 20 kHz for a sound velocity in the bubbly medium of 60 m/s). As soon as the resonance thickness is reached, the pressure field inside and outside the layer dramatically increases, leading to the formation of the cone of bubbles. With further thickening of the dense cavitating layer, it goes out of the resonance conditions; the pressure and bubble density decrease; and the layer becomes thinner, going back to the resonance thickness. The process eventually stabilizes with the layer thickness oscillating around the resonance size. In addition, the dense bubble layer is not uniform across the surface of the radiating face of the sonotrode. It is thicker in the centre, where the acoustic intensity is maximum and thinner at the periphery of the sonotrode. As a result, the cavitation bubble layer forms a lens-like structure, focusing the acoustic field at a short distance.

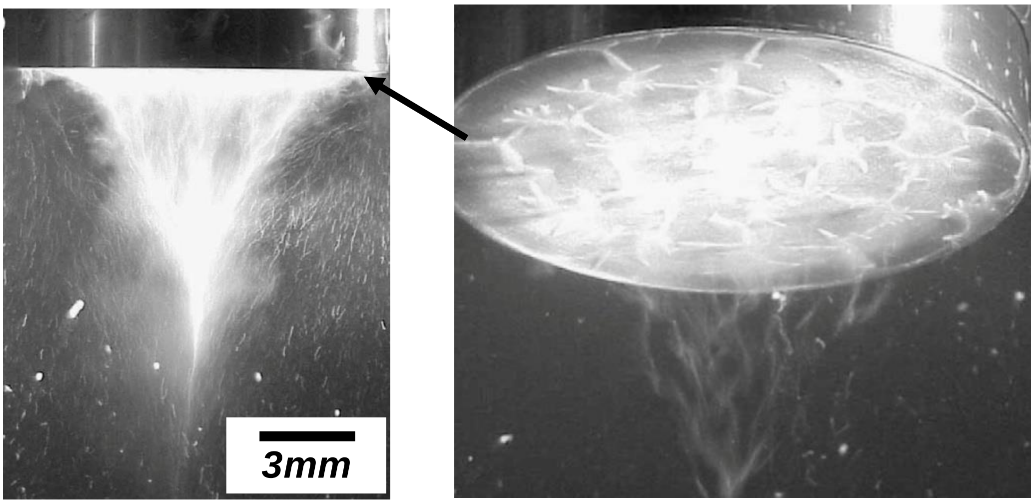

Fig. 2.16. *A typical cavitation-zone found in water, the sonotrode diameter is 120 mm and acoustic intensity is 8.2 W/cm^2 [112].*

Another interesting phenomenon that has consequences for the formation of the cavitation cone is the development of so-called streamers [112]. The insert in Fig. 2.16 shows the netlike pattern at the surface of the sonotrode, reflecting the bubble trajectories before they leave the surface. The bubbles that are formed unevenly at the radiating surface self-organize in several streamers. The bubbles in the streamer will propagate into the bulk liquid under the acoustic force, *i.e.*, the interaction of the bubble and acoustic pressure, defined as p*rimary Bjerknes forces,*

$$F_B = -\langle V(t)\nabla p(x,t)\rangle_T \tag{2.34}$$

where the bubble volume *V* and pressure *p* is a function of time *t* and bubble position *x*. The symbol $<>_T$ means the net force on a bubble depends on the time average in a period *T*.

These streamers are not stable in time and space, and they tend to rotate around the axis of the sonotrode. Upon increasing the acoustic intensity, the streamers multiply and merge, forming the macroscopically stable cone structure. The bubbles in the cavitation zone also interact under the acoustic pressure, *i.e.* the attractive or repulsive force, which is termed the secondary Bjerknes force [113] and defined as:

$$F_{B2}^{1,2} = -\frac{(x_2-x_1)}{|x_2-x_1|^3}\left(\dot{V}_2(t) - \dot{V}_1(t)\right) \tag{2.35}$$

where $F_{B2}^{1,2}$ is the force of bubble 1 on bubble 2, and the time average is over the time derivatives of the product of both bubble volumes V_1 and V_2. Under secondary Bjerknes force, the bubbles with similar size will attract each other while the bubbles with different size are repulse.

In generally, the Bjerknes forces lead to a spatial concentration of bubbles. Primary forces drive the cavitation bubbles towards pressure antinodes in standing waves and larger (degassing) bubbles to nodes. Neighbouring bubbles tend to cluster due to secondary forces. Furthermore, acoustically hard object surfaces can attract bubbles due to secondary Bjerknes forces from reflections (virtual mirror bubbles) [113, 114]. Driven by these forces, bubbles tend to move to their favourable positions and finally results in the specific cavitation pattern and structure of the bubble cloud.

The experimental observations show that the cone structure is more pronounced with wide radiating faces [112], narrow sonotrodes produce more turbulent and disturbed jet-like cavitation structure [114] and fixed transducer (standing wave emitted) always generate the bubble structure in a filamentary streamer, or a double layer structure [54]. Moussatov, Granger, and Dubus [112] relate the origin of cavitation cones to the formation of high-pressure repulsive zone under the sonotrode, with increasing distance under the sonotrode, the high-pressure zone becomes narrower and then disappears, transforming to the attractive zone. A cone of bubbles and then a narrow downward jet of bubbles are thus created. The entire cavitation cone is an active zone where the intensification of processes and liquid phase treatment occur.

2.3 Acoustic flow and multiphase flow

2.3.1 The characteristics of acoustic flow

Acoustic flow results from the attenuation of the acoustic wave in a medium [115]. In reality, the streaming of the liquid is always companied with the presence of cavitation bubbles, and sometimes solid-semisolid particles, such as when ultrasound introduced into a metallic alloy during solidification, i.e. multiphase flows. Acoustic streaming has been shown to enhance both thermal convection and mass transport, where convective transport is added on top of diffusive transport [116]. Thus the study of the acoustic streaming is very important for various ultrasound applications in liquids.

The ultrasound induced flows are represented by (1) acoustic streams that originate from the pressure wave caused by high-frequency vibration of the sonotrode and pulsation of the cavitation region and (2) secondary, forced convective flows. A typical flow pattern induced by an ultrasonic horn in a limited volume is shown in Fig. 2.17 [5].

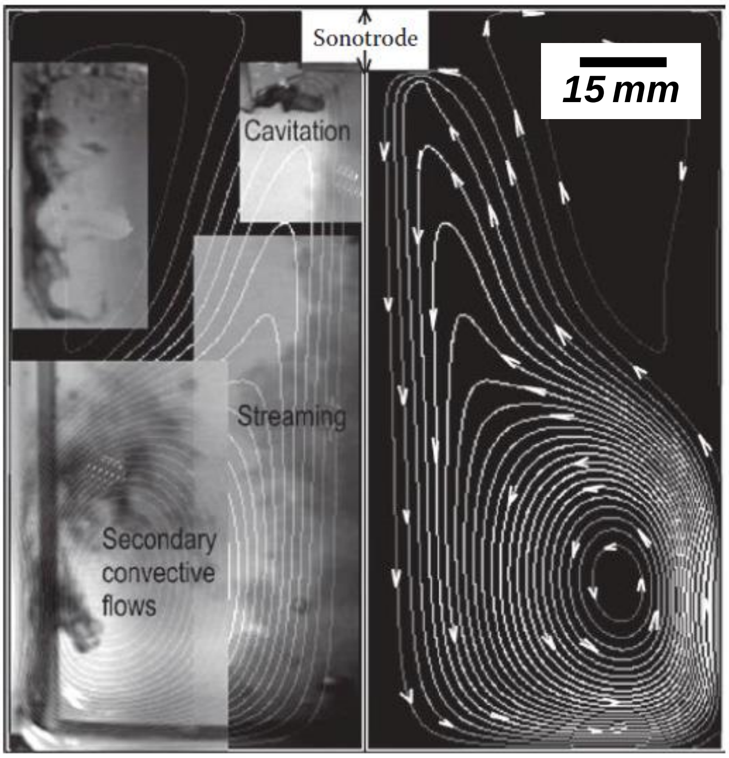

Fig. 2.17. *Typical flow pattern in water induced in a limited volume by an ultrasonic horn: (left) flow pattern visualized by dye injection; (right) streamlines obtained by computer modelling [5].*

The origin of streams relates to the momentum acquired by the liquid when it absorbs the wave. Therefore, the velocity of acoustic streams increases with the ultrasonic intensity and the sound absorption, and inversely proportional to the bulk viscosity and the speed of sound in the medium. Generally, there are three types of acoustic streams [117]:

The first is the flows in viscous boundary layers near the solid boundaries or at the phase interface. The second originates in the field of standing waves. Finally, the third type originates from the absorption of wave momentum of an inhomogeneous sound field in the bulk liquid. Most of the experimental and modelling work on acoustic and induced convective flows has been done using water or transparent liquids. Particle Image Velocimetry (PIV), laser Doppler anemometry (LDA), and high-speed filming of liquids with dye, tracers, or immiscible liquids have been widely used since the 1960s [117] and most intensely in the last fifteen years [118-120].

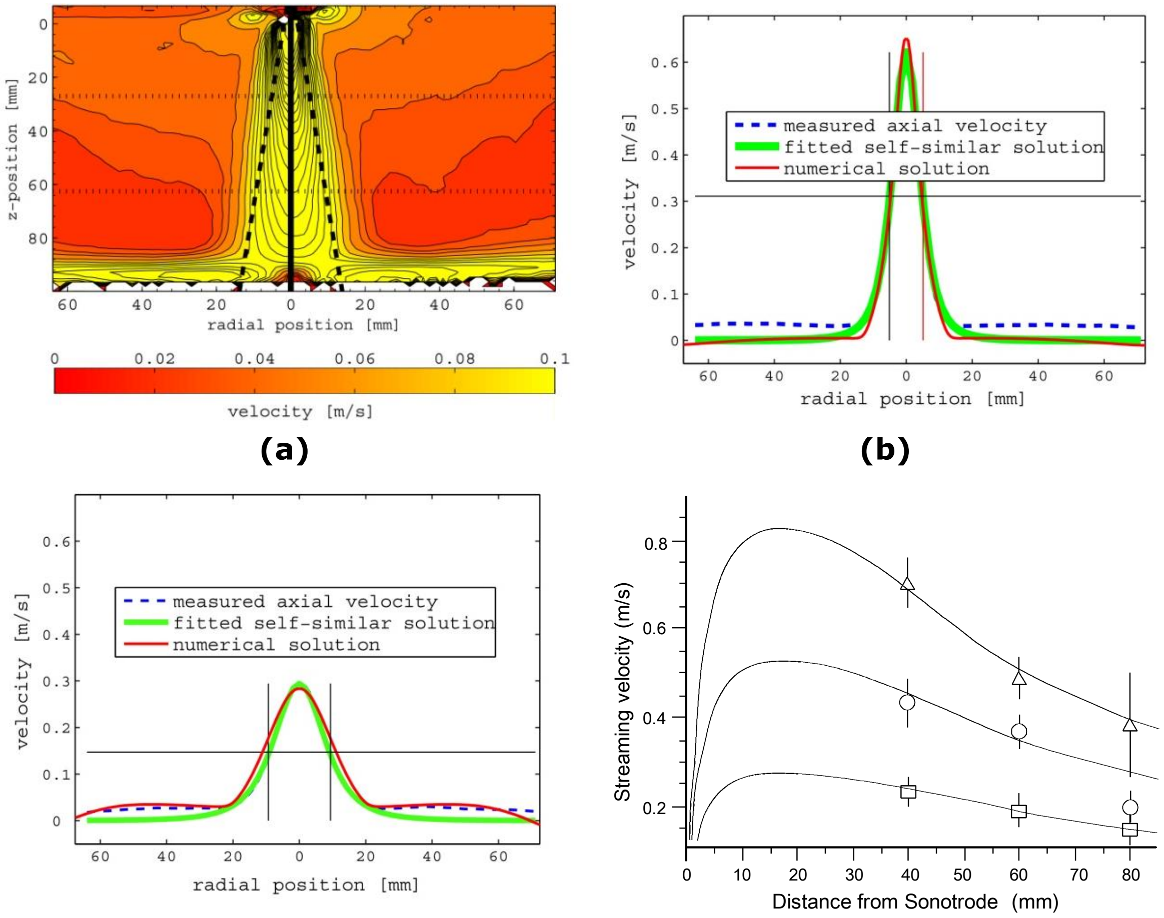

(a) (b)

(c) (d)

***Fig. 2.18**. Acoustic stream velocity distribution: (a) velocity magnitude of the time-averaged flow; thin dashed horizontal lines drawn in (a) represent the downstream positions for the velocity profiles showed in (b, c) [120]; (d) The measured velocities in liquid aluminium with the amplitudes of: (1) 12 μm; (2) 18 μm; (3) 24 μm) [121]. The sonotrode tip is at the centre of the top edge of (a), and (a-c) were obtained by using PIV method in water while (d) is using probe sensor method to measure the velocity in liquid aluminium.*

A combination of PIV and computer modelling nowadays allows researchers to get accurate data on the velocity profile and magnitude outside the cavitation zone. Fig. 2.18a-c demonstrates the velocity distribution in a water volume excited by an 18 kHz, 4 kW magnetostrictive transducer with a Ti horn of 20 mm in diameter. The linear flow velocity reaches approximately 1 m/s and then rapidly attenuates with the distance from the sonotrode tip. Secondary flow velocities are in the range of cm/s. These results agree well with earlier estimates of streaming velocities of 2-3 m/s close to the cavitation region [122]. The pressure measured in water ahead of a 20 mm horn working at 20 kHz frequency is from 0.6 to 0.15 MPa over the distance of 40 mm from the horn surface [123]. Recent measurements of acoustic pressure in liquid aluminium gave concurring results [121]. Fig. 2.18d shows the results on the streaming velocity, recalculated from acoustic pressure. These data demonstrate very similar velocities to those measured and calculated in water, and also illustrate the dependence of the flow velocity on the ultrasound intensity (amplitude of vibrations).

Abramov, Astashkin, and Stepanov [124] studied acoustic flows in an undercooled transparent analogue of melts, i.e., a 35% naphthalene–65% camphor eutectic alloy. The sonication was carried out at frequencies of 45-250 kHz in order to minimize the effects of cavitation. Fig. 2.19 shows schematically the streaming flows in the undercooled transparent melt. Within a few seconds of sonication with the amplitude above the cavitation threshold, solidification nuclei (crystals) start to form near cavitation bubbles. The analysis of the motion of bubbles and crystals allowed the observer to trace the development of the acoustic flow. These investigations show that the crucial factors determining the nature, velocity, and scale of streaming are the ultrasonic intensity, the melt temperature, and viscosity.

2.3.2 Bubbles and particles in acoustic flow

Bubbles in an ultrasonic filed are driven by the Bjerknes force, and understanding of the bubble movement is very important for the applications, such as drug delivery, material processing, etc.

Luther, *et al* imaged (2250 fps) the ultrasound induced bubbles in a relatively big view field ~1 x 1 cm^2 [125], and the bubbles' trajectories are showed in Fig. 2.20. Results showed that, under the 20 kHz ultrasound with an acoustic pressure of 200 kPa, the bubbles move in a ‘Y’ pattern, and the velocity of the cavitation bubbles reaches ~1 m/s. The average speed is ~0.3 m/s, an order of magnitude faster than the average drift velocity of the liquid (~1 cm/s) [125]. The results are in consistency with the previous results obtained using different techniques [126].

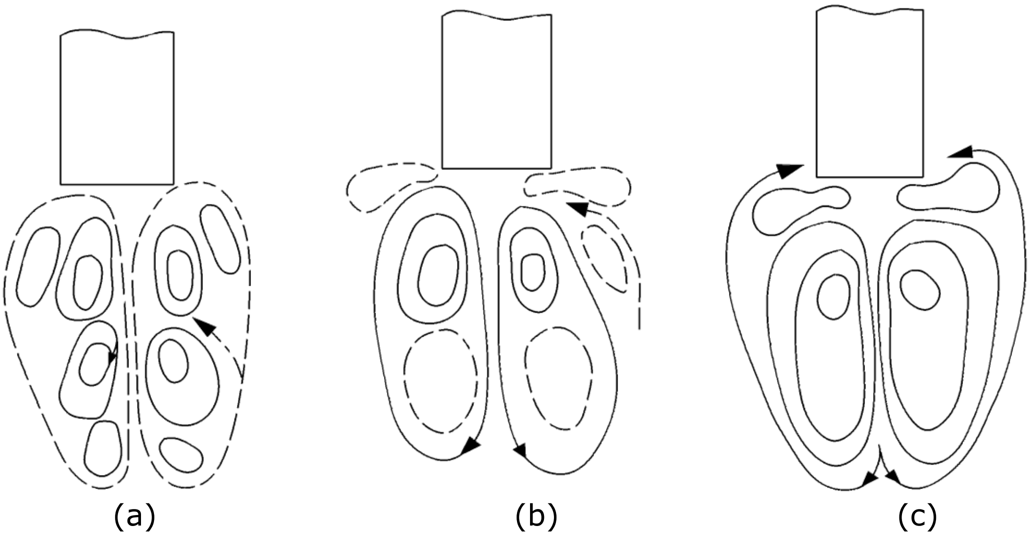

Fig. 2.19. *The development of acoustic streams in an undercooled ($\Delta T = 4°C$) transparent material: (a) 10 s, (b) 20 s, and (c) 30 s after onset of sonication at 139 kHz with amplitude of oscillation velocity = 5 cm/s [124].*

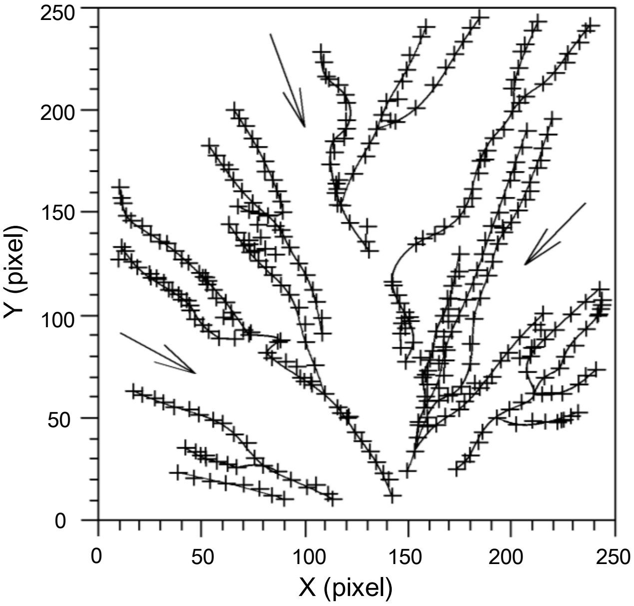

Fig. 2.20. *Bubble trajectory in water [125]. The image centre is about 2.5cm below the sonotrode and the image size is 1 x 1 cm^2.*

There are many studies conducted on the fluid-particles interactions. For example, Suslick studied the effect of high intensity ultrasound field on the particles (Ni, Cu, Fe powders) in water [127, 128], and found that the ultrasound induced multiphase flow will lead to violent collisions of the particles, creating substantial surface damage to the powders, and increasing surface areas significantly, and sometimes causing increased particle aggregation.

The particle behaviour under ultrasound in a liquid or a semi solid is extremely important for the studies of ultrasound treatment of liquid metals and the alloys during solidification, however, until now, there are no report on the in situ observation of the interactions between ultrasonic bubbles, flows with the solidifying metals, which is the central part of this research.

2.4 Ultrasound processing of metallic alloys

2.4.1 Ultrasound degassing

Gas porosity is one of the major defects in aluminium ingots or castings. The presence of porosity is detrimental to the mechanical properties, notably the fatigue resistance and the pressure tightness of a casting [129]. The removal of the porosity (mainly due to the dissolved hydrogen in the molten aluminium) alloy is critical for the production of high-quality castings.

Several methods are currently in use to degas aluminium. These methods include lance degassing using argon or nitrogen, rotary degassing, tablet degassing using hexachloroethane (C_2Cl_6); and vacuum degassing. Rotary degassing is the most widely used method for degassing in aluminium alloys. The process is efficient but the use of chloride and moving part such as the graphite rotor are drawbacks. Vacuum degassing and lance degassing are slower processes compared to rotary degassing. None of these methods are capable of degassing particulate-reinforced metal matrix composites.

Ultrasonic degassing [129-131], an environmentally clean and relative inexpensive technique, uses high intensity ultrasonic vibrations to remove hydrogen in molten aluminium. An ultrasonic wave propagating through a liquid metal generates alternate regions of compression and rarefaction. When the intensity of the ultrasonic vibration is high enough, a large number of tiny vacuum cavities are generated in the melt. The dissolved gas diffuses into these vacuum bubbles and is removed out of the melt as the bubbles escape from the melt surface [132]. Ultrasound degassing can be combined with the traditional lane degassing together to bright the benefits of 1) a reduction of dross formation during degassing, 2) much reduced use of inert gases and no use of chlorine since the alternating pressure induced by ultrasound creates fresh metal/bubble interfaces on the bubbles, and 3) removal of trace elements such as Na and Li.

2.4.2 Ultrasound grain refinement

The mechanical strength of metallic alloys is predominantly governed by the size of the grains as described by the Hall-Petch relation [133, 134]:

$$\sigma_y = \sigma_0 + k_m d^{-\frac{1}{2}} \tag{2.36}$$

where σ_y is the yield strength, σ_0 is a material constant for the starting strength, k_m is a material constant and *d* is the diameter of grain.

Therefore, reducing grain size normally increase the strength of materials [134].

In the past few decades, extensive laboratory results have demonstrated that applying ultrasound waves into solidifying liquid alloys can lead to the refinement of alloy microstructures [5, 135, 136] as typically showed in Fig. 2.21 below. Furthermore, the soundness of castings can also be improved due to the reduction in shrinkage, hot tearing, and more uniform distribution of refined secondary phases and/or microporosity [137].

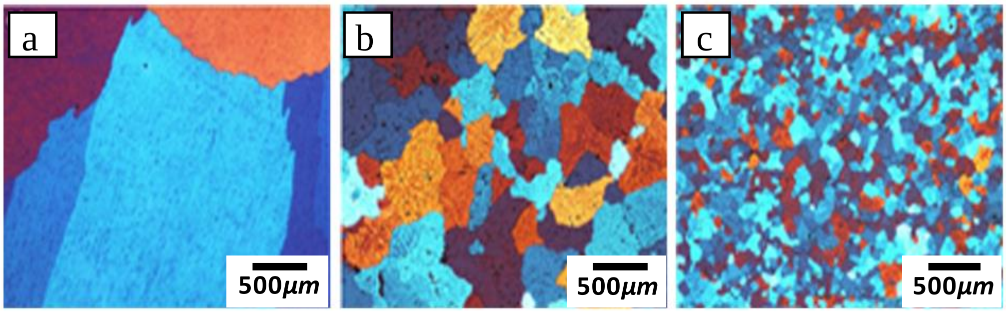

Fig. 2.21. *(a) Pure Al grains without grain refiner; (b) with grain*

refiner, and (c) after ultrasound processed [138].

Many worldwide researches have been carried out to study the relationship between the solidified microstructure and the ultrasound parameters (power, frequency, duration, and the melt temperature) applied during the solidification of metal alloys, including Al [135], Mg [20, 139], Sn [140], Fe [141] based alloys. Eskin, *et al* also [138] found that the primary phases such as the Al_3Zr in Al-Zr-Ti alloy can be also refined by using ultrasound (Fig. 2.22a-b) [142]. Han [143] also confirmed that the eutectic phase can be effectively refined by high intensity ultrasound treatments (Fig. 2.22c-d).

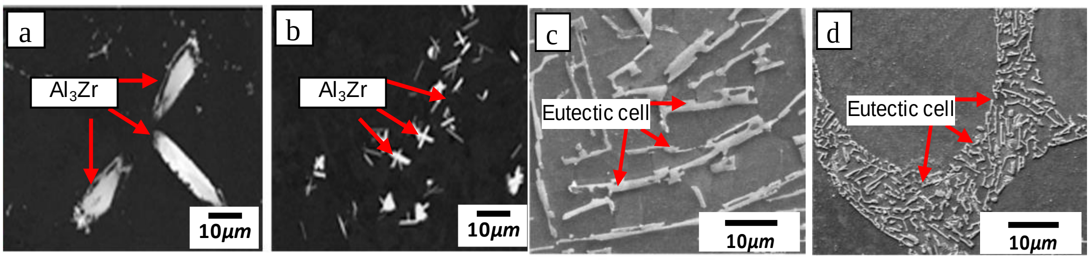

Fig. 2.22. *Typical morphologies of primary Al_3Zr particles in an Al–Zr alloy: (a) cast without ultrasound, (b) with ultrasound [142], and typical morphologies of eutectic phases in A356 alloy: (c) cast without ultrasound, (d) with ultrasound [143].*

The effectiveness of grain refinement using ultrasound has been demonstrated in almost all alloy systems [5, 30]. Generally, three mechanisms have been proposed for the underlying physics of grain refinement: (1) enhancement of homogeneous nucleation because of bubble implosion induced high pressure that effectively increases the melting point of the metal alloy at the region very close to the bubble and therefore increase the level of undercooling for nucleation [144, 145]; (2) activation of potential inoculating particles for heterogeneous nucleation [5, 141], and (3) grain multiplication due to dendrite fragmentation [32, 33, 146, 147].

However, almost all previous research has been based on post-mortem microstructure analysis made on the solidified samples. There have been hardly any systematic studies on in situ observation of the dynamic interaction between the ultrasound bubbles and the solidifying liquid and phases, apart from a very limited work on organic-transparent alloys [32, 33]. Hence the relevant importance of the above grain refinement mechanisms has never been fully clarified. From industry application perspective, there are two basic problems: (1) the erosion of the sonotrode in the high temperature melt prevents ultrasound from being used for long time and continuous operations, i.e. DC casting; (2) the localisation of ultrasound treatment (limited to the cavitation zone) make it difficult to be used for large volume mass production.

To tackle the above problems, very recently, Komarov, *et al* have developed [148] sonotrodes made by Si_3N_4-based ceramics (Fig. 2.23a) which have a working life time longer than 700 hours in DC casting of Al-Si alloy ingots [149]. They also designed a controlled cavitation zone as showed in Fig. 2.23b and force the liquid metal to flow through this zone to maximise the cavitation effect. These new developments make ultrasound processing of light metal alloys a very promising technology for manufacturing DC casting ingots of light alloys without the need of adding of external grain refiners. Other emerging and novel technologies include the use of electromagnetic coupling to generate ultrasound in the liquid metal in a contactless manner to solve sonotrode erosion problems [150].

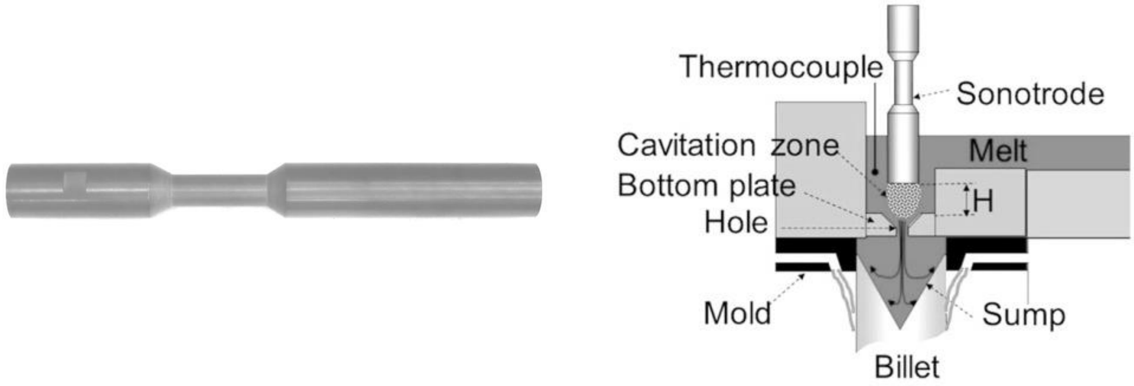

(a) **(b)**

Fig. 2.23. *(a) A barbell-shaped Si_3N_4-based ceramic sonotrode. (b) A schematic, showing the controlled cavitation zone designed for ultrasonic treatment of a Al-Si alloy in DC casting [149].*

Of course, ultrasound is also used in welding, manufacturing of nanomaterials, and many other materials processing related fields as well, which is outside the scope of this research and therefore those materials are not covered here in this literature review.

2.4.3 Real-time imaging of solidification processes

Metallic alloys are opaque to visible light, hence, the in situ observations of solidification processes were historically conducted using a number of organic transparent alloys [6, 18]. Jackson [151] defined a dimensionless parameter in order to select the organic transparent alloys to mimic metal alloys as below,

$$\alpha = \frac{L\epsilon}{RT_E} \tag{2.37}$$

where L is the latent heat, R the gas constant, T_E the equilibrium melting temperature and ϵ is a crystallographic factor which depends on the growing face but is always $<\frac{1}{2}$. Jackson and Hunt [152] investigated several transparent organic materials with $\alpha < 1$, including camphene, succinonitrile, and NH_4Cl water solution, and found that they behaved very similar to metals during solidification. Among these, camphene and succinonitrile are very good working materials since they are readily available, safe, and have low melting temperature of 320 K and 331.23 K, respectively.

Fig. 2.24 shows the typical optical images of the growing dentritic phases observed in a NH_4Cl water solution [31]. Similar approach had been widely used by numerous researchers to investigate the dendrite evolution under different thermal conditions [153], including mechanical stirring and/or shearing [31, 154], etc., mimicking the conditions often found in the processing of metallic alloys.

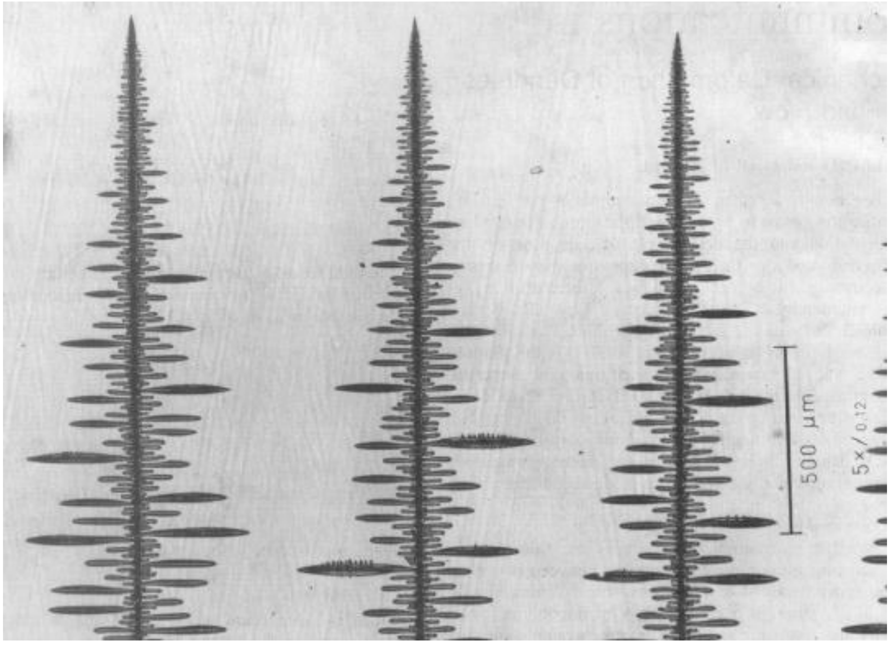

Fig. 2.24. *NH_4Cl dendrites growing from aqueous solution under steady state conditions on a gradient stage: growth rate 28 μm/s and temperature gradient 5.5 K/mm. Minimum secondary arm necks are of diameters 5 to 10 μm [31].*

In 1985, Swallowe, *et al.* [32] reported firstly the in situ imaging study of the effect of ultrasound treatment on the solidification of a transparent metal analogue. The ultrasound was transmitted via a glass strip attached to an ultrasonic soldering iron working at 35 kHz. Both nucleation of the solid phase in the ultrasonic field and fragmentation of growing dendrites by oscillating cavitation bubbles were observed, as illustrated in Fig. 2.25. Chow *et al* [147, 155] investigated the effect of ultrasound on nucleation of a 15 wt% water solution of sucrose. A commercial 20 kHz transducer was used as shown in Fig. 2.26. Ice nuclei were formed at a distance from the sonotrode almost immediately after an ultrasonic pulse, and they grew to equiaxed crystals.

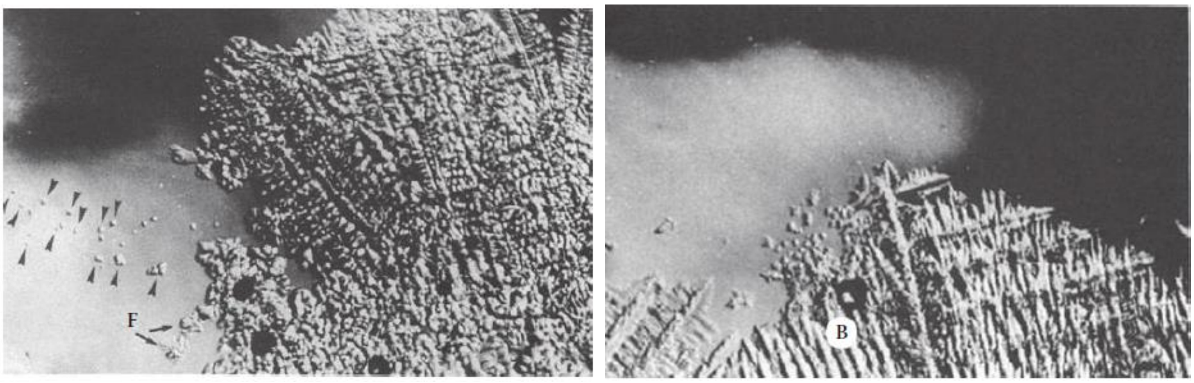

(a) **(b)**

Fig. 2.25. *Effect of ultrasonic processing in a camphene solution on (a) dynamic nucleation, where the smaller particles on the left are those nucleated in the liquid, while larger particles shown as F are fragments; and (b) fragmentation, where B is a cavitation bubble inside the dendrite that causes fragmentation by oscillations. [32]*

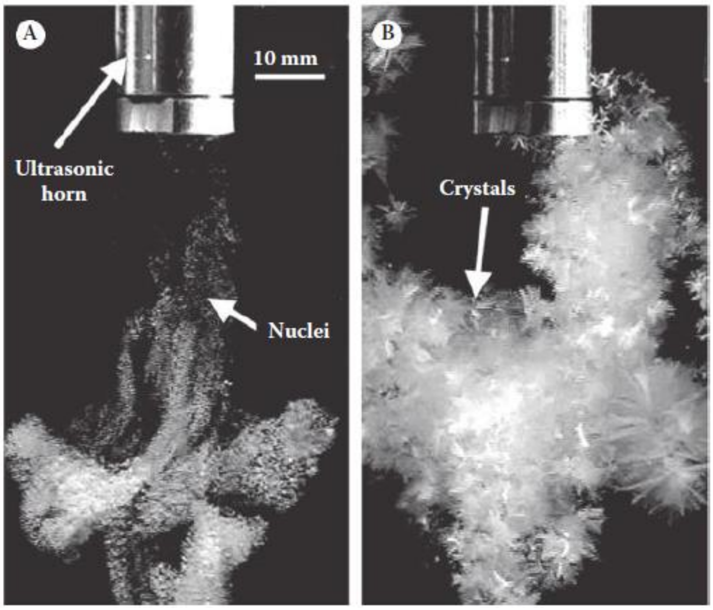

Fig. 2.26. *The dynamic nucleation of ice ahead of a sonotrode: (a) immediately after ultrasonic pulse and (b) after 5 s. [147]*

The fragmentation of the solid phase under dynamic action was suggested by many researchers as the main mechanism of structure refinement [4, 32, 156, 157]. Mechanical fracture and liquid-metal embrittlement [4, 31] and solute redistribution and local dendrite branch re-melting [158-160] were considered as the main mechanisms. Acoustic and secondary flows assist in transporting the formed fragments to the solidification front and in the melt bulk.

A detailed study of fragmentation of dendrites by single cavitation bubble had been demonstrated by Shu, *et al*. [33]. A cold ultrasonic probe working at 20 kHz with an amplitude of 4 μm was used to induce individual cavitation bubble in a transparent succinonitrile–1 wt% camphor solution. Fig. 2.27 shows a quasi-steady state bubble of a diameter ~0.2 mm oscillating or 'pulsating' at a primary dendrite tip and created a "cleavage" at a secondary dendrite arm after 279 wave periods (13.93 ms). This whole sequence occurred over 315 wave periods, equivalent to 15.77 ms.

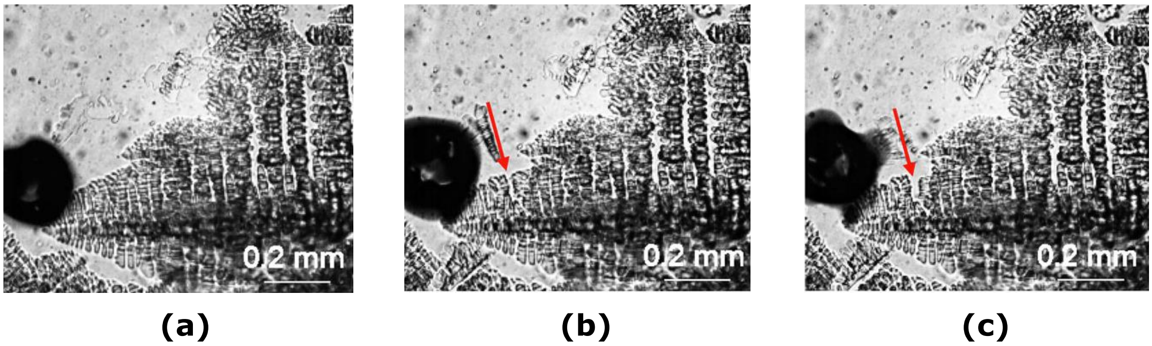

Fig. 2.27. *The process of fracturing a secondary dendrite arm by a quasi-steady state bubble pulsing on the tip of a dendrite at (a) t = 0, the start; (b) t = 13.93 ms, after 279 periods; and (c) t = 15.77 ms, after 315 periods. The images were recorded at 8,113 fps [5].*

The findings in transparent metal analogue provide very valuable data to understand the mechanism of ultrasound induced refinement in the metallic alloys. However, (1) there are only several tens of plastic crystals found among millions of organic compounds can be used as proper metal analogue, and the melting and boiling point of many metal analogues are too low to be suitable for experimental research on solidification processes [152]; (2) the liquid property of the metal analogue is very different from the liquid metal, such as the surface tension, density, sound velocity, thermal conductivity, etc., which are the most dominant parameters for the ultrasound induced caviation bubble behaviour and fluid flow. For example, the density of organic alloy, succinonitrile-1% of camphor, is 0.97g/cm^3 which is much lower than Al alloys (2.7 g/cm^3 of pure Al), while the thermal diffusivity of organic alloy (1.15×10^{-7} m^2/s) is more than 100 times lower than Al alloys (8.418×10^{-5} m^2/s), and the mass diffusivity coefficient (10^{-5} cm^2/s) at least 25 orders of magnitude higher than Al-Cu alloy (10^{-30} cm^2/s) [161]; (3) the third reason comes from another fact that the enthalpy of transparent alloys and real metals are dramatically different when the temperature over a specific level [162].

2.5 X-rays and the imaging techniques

Hence, an in situ observation in the real metals is critically important for revealing the underlying physics of ultrasound treatment of metals. Nowadays, X-ray or neutron beam are the standard methods to “see” through an optically opaque materials, such as liquid metals. In the following sections, the principle of lab based X-rays and synchrotron X-rays are described in details, with an emphasis on the difference between synchrotron X-rays and lab based X-rays, and why it is so important to use synchrotron X-rays with phase contrast imaging capability in the research.

2.5.1 A brief history of X-rays

In November 1895, Rontgen discovered X-rays firstly in his laboratory at the University of Würzburg, Germany. Commercial X-ray instruments became available in 1912 after Coolidge developed a practical X-ray tube at General Electric Research Laboratories in New York. The Coolidge tube served as the standard X-ray tube for many decades with only marginal improvements in the design and making, and a gradual increase in the X-ray flux until the arrival of synchrotron X-rays that provide the exponential changes in the capability of the X-ray source (brilliance, flux, coherence, spatial resolution, etc.) and the associated experimental devices and instruments. As illustrated in Fig. 2.28, the first generation synchrotron light source – the electron-positron colliding machine – became available in 1970s. The second generation with the use of large storage ring and bending magnets started from 1980s. Nowadays, the third generation of synchrotron radiation facilities have a remarkable improvement in flux and intensity of the X-rays produced, and are available for research in almost all disciplines of sciences [163].

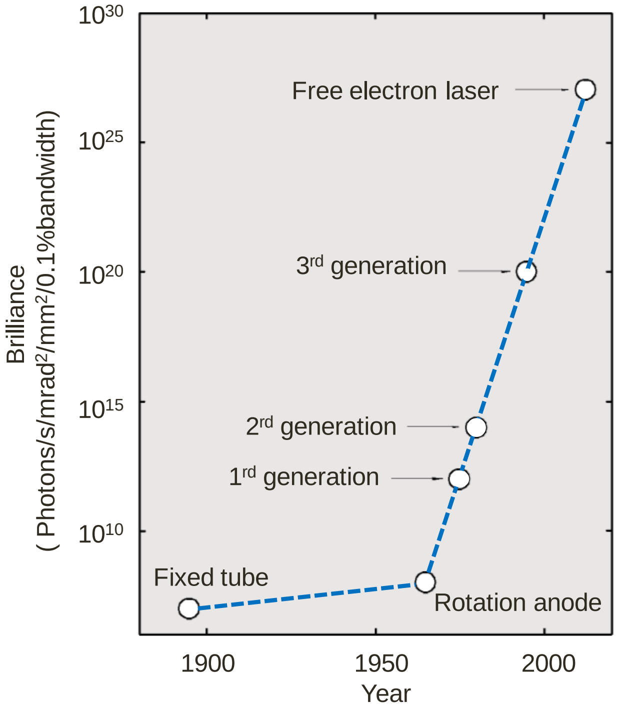

Fig. 2.28. *The brilliance of X-ray sources as a function of time. Source brilliance is defined by Eq.2.38 [164].*

2.5.2 X-ray sources and imaging techniques

2.5.2.1 Lab based X-ray tube

Fig. 2.29a illustrates the principle of generating X-ray from the Coolidge tube. When a filament, also called cathode, is heated up by using a high voltage normally in the range of 20-150 kV, electrons are emitted and then accelerated in a vacuum by a high electric field towards to a metal target, such as W, Cu, Mo, Ag, etc., which being positive is called the anode and it is normally cooled by using a circulation of water. In medical X-ray tubes, the target is usually tungsten or a more crack-resistant alloy of rhenium (5%) and tungsten (95%), but sometimes molybdenum for more specialized applications, such as when softer X-rays are needed as in mammography. In crystallography, a copper target is most common [165]. In 1960s, rotating anode generator was invented with the use of a higher power as the heat could be dissipated over a much larger volume than in a standard tube (Fig. 2.29b).

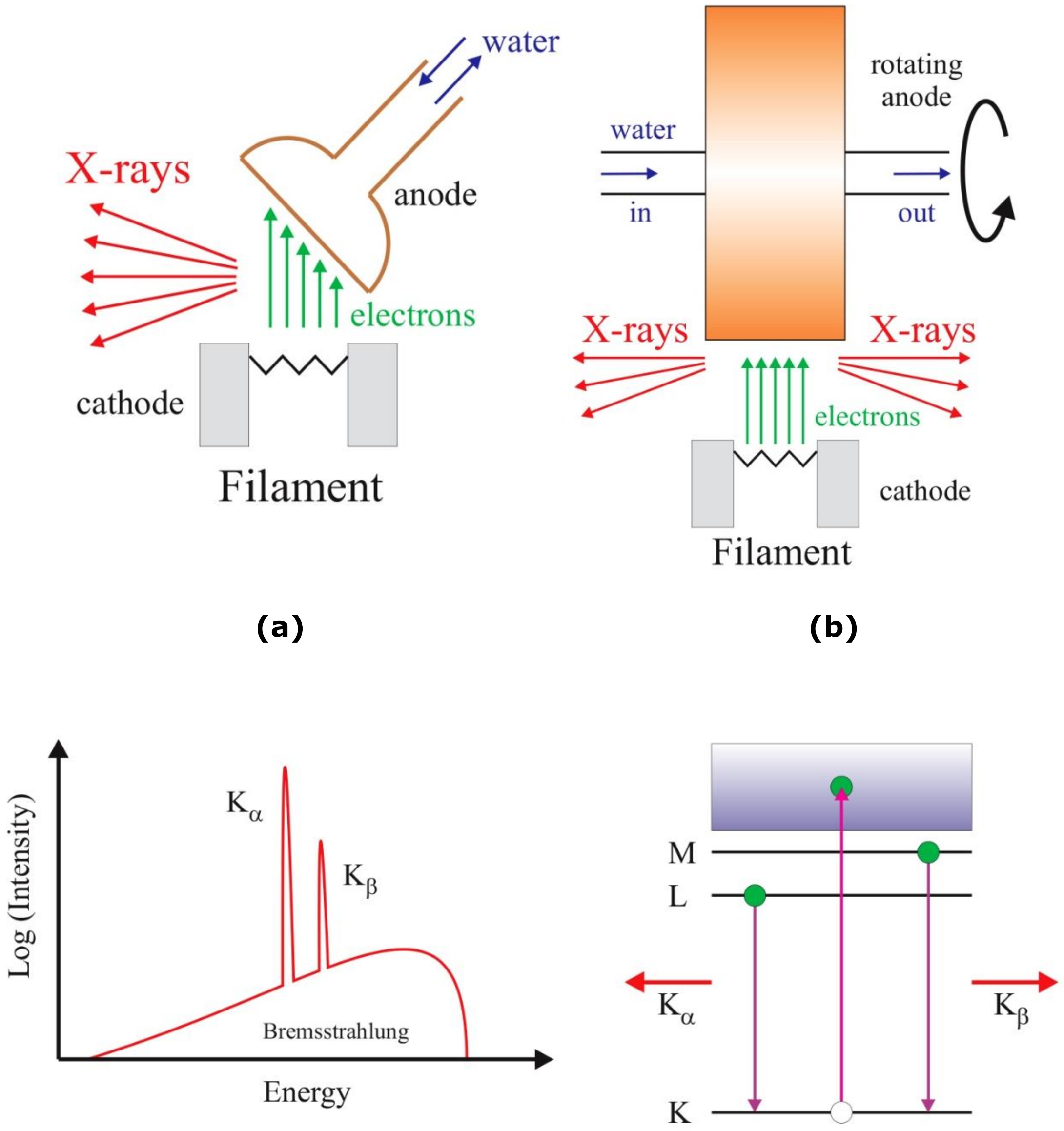

(a) **(b)**

(c) **(d)**

Fig. 2.29. *(a) The standard X-ray tube developed by Coolidge around 1912. (b) X-ray tube with a rotating anode. (c) The spectrum from an X-ray tube with discrete fluorescent lines superimposed on the continuous Bremsstrahlung radiation and characteristic X-ray (K_α and K_β). (d) Schematic atomic energy level diagram: the K_α line results from transitions between an L and K shell, whereas the K_β comes from an M to K transition [164].*

Fig. 2.29c shows that the spectrum of X-rays generated from electrons impinging on a metal anode has two distinct components. The first is a broad and continuous spectrum, commonly known as Bremsstrahlung radiation. It has a maximum energy that corresponds to the high voltage applied to the tube. The second is sharp line spectra with characteristic energies superimposed on top of the broad spectrum. The sharp line spectra are produced by the collisions of the incident electrons with the atoms in the target material. When an incident electron collides onto an atom, it may also cause an electron to be removed from one of the inner shells of the atom, creating a vacancy. The subsequent relaxation of an electron from an outer shell into this vacancy produce an X-ray with a characteristic energy equal to the difference in energy between the two shells. For example, Fig. 2.29d shows that the electrons at K shell are knocked off and then the vacancies is filled by the electrons from L and M shell. During this process, the extra energy of the electrons on L and M shells will be released in the way of emitting X-ray with the energy at K_α and K_β with an intensity few orders higher than the Bremsstrahlung spectrum (especially K_α), and this is called characteristic X-ray. For experiments requiring a monochromatic beam, the K_α line is often used, which is several orders of magnitude more intense (bright) than the Bremsstrahlung spectrum. The energy of characteristic X-ray mainly depends on the atomic structure of the target materials, and some of the commonly used targets are listed in Table 2.1.

Table 2.1. The common anode materials [166] and characteristic X-rays

Anode material	**Atomic number**	**Photon energy (keV)**		**Wavelength (nm)**	
		K_α	K_β	K_α	K_β
W	74	59.3	67.2	0.0209	0.0184
Mo	42	17.5	19.6	0.0709	0.0632
Cu	29	8.05	8.91	0.157	0.139
Ag	47	22.2	24.9	0.0559	0.0497
Ga	31	9.25	10.26	0.134	0.121
In	49	24.2	27.3	0.0512	0.455

2.5.2.2 Synchrotron X-rays

All the third generation synchrotron X-ray facilities around the world are operated in the same principles, therefore the Advanced Photon Source (APS) as shown in Fig. 2.30a is used here as an example to explain briefly the basic theory, essential configurations and functions.

As shown in Fig. 2.30b, an X-ray beam at the APS begins with electrons emitted from a cathode heated to ~1100° C, and they are accelerated by high-voltage alternating electric fields in a linear accelerator (linac). Selective phasing of the electric field accelerates the electrons to 450 million volts (MeV). At 450 MeV, the electrons are traveling at >99.999% of the speed of light, which is 299,792,458 meters/ second (186,000 miles/second).

Electrons are injected into the booster synchrotron, a racetrack-shaped ring of electromagnets, and accelerated from 450 MeV to 7 billion electron volts (7 GeV) in one-half second. (By comparison, the electron beam that lights a TV screen is only 25,000 electron volts.) The electrons are now traveling at >99.999999% of the speed of light. The accelerating force is supplied by electrical fields in four radio frequency (rf) cavities. In order to maintain the orbital path of the electrons, bending and focusing magnets are used to increase the electron field strength in synchronization with the rf field.

The 7 GeV electrons are injected into the 1104-m-circumference storage ring, a circle of more than 1,000 electromagnets and associated equipment, located in a radiation-proof concrete enclosure inside the experiment hall. A powerful electromagnetic field focuses the electrons into a narrow beam that is bent on a circular path as it orbits within aluminium tube vacuum chambers running through the centres of the electromagnets.

(a)

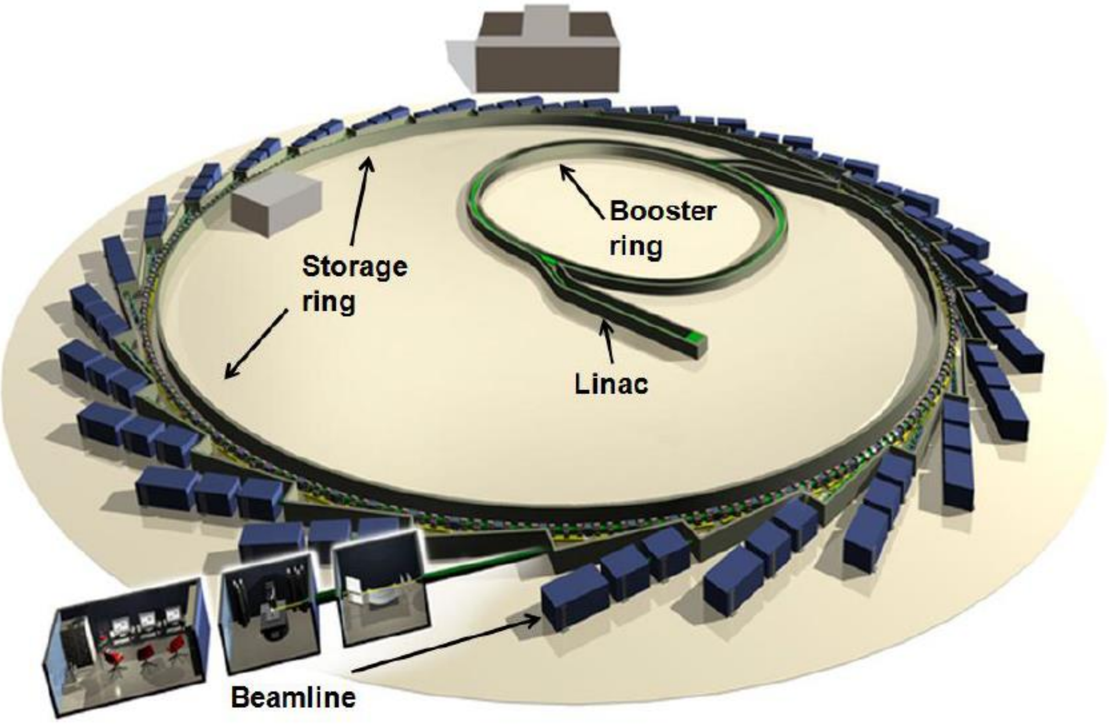

(b)

Fig. 2.30. *(a) The aerial view of Advanced Photon Source, Argonne National Laboratory, USA. (b) A schematically diagram of a typical third generation synchrotron radiation source which is composed of (1) an electron gun, (2) a linear accelerator (Linac), (3) a booster ring, (4) a storage ring with insertion devices, (5) beamlines [167].*

Insertion devices (commonly used are wiggler and undulator), consisting of periodic magnetic structures, are added in the straight section of storage ring to extend the spectral range and increase the ‘brilliance’ of X-rays by optimizing the ring. When the electrons pass through the device, they are undergo a transverse oscillation under the alternating magnetic fields, and the bend and acceleration of electrons associated with this movement result in the emission of synchrotron radiation. Brilliance is a quantity determines the quality of the X-ray beam, and it is defined as the number of photons per second pass through per unit area (mm^2) of the radiation source per unit solid angle ($mrad^2$) of the radiation cone per unit spectral bandwidth (0.1%BW) as shown below.

$$\text{Brilliance} = \frac{\text{Photons/second}}{(\text{mrad})^2(\text{mm}^2\,\text{source area})(0.1\%\text{BW})} \qquad (2.38)$$

It uses the $mrad^2$ to describe how much the beam diverges, or spreads out as it propagates. Usually the collimation of the beam is given in milli-radian, both for the horizontal and for the vertical direction and uses 0.1%BW to illustrate the brilliance at a specific energy range and because the accuracy of monochromator used to filter a specific energy is relatively to 0.1%.

Wiggler and undulator are similar in terms of the structure and principle of producing synchrotron radiation. However, in a wiggler, the period and the strength of the magnetic field is not tuned to the frequency of radiation produced by the electrons. Thus every electron in a bunch radiates independently, and the resulting radiation bandwidth is broad. While, in an undulator, the radiation produced by the oscillating electrons interferes constructively with the motion of other electrons, causing the radiation spectrum to have a relatively narrow bandwidth. The intensity of radiation is in direct proportion to the second power of the number of poles in the magnet array. Thus, the undulator performs better in terms of brilliance than Wiggler. Fig. 2.31 is the energy spectrum of X-rays produced by different sources. The brilliance (flux) of X-ray produced by an undulator (10^{21}) is higher than that from a wiggler (10^{18}), and both produce X-rays with much higher brilliance than those produced by traditional lab-based X-ray tube (up to 10^{11}) and bending magnet (10^{16}). However, due to the narrow bandwidth of the radiation spectrum, the energy spectrum from an undulator is not continuous, while the X-ray from wiggler has a continuous energy.

After the insertion device, a series of crystal and/or mirror optics are put in place to tailor the X-ray beam [168, 169] and to direct the beam into a specific experimental hutch or station (commonly known as beamlines) that is purposely built for housing the specific experimental instruments for any specific type of experiments.

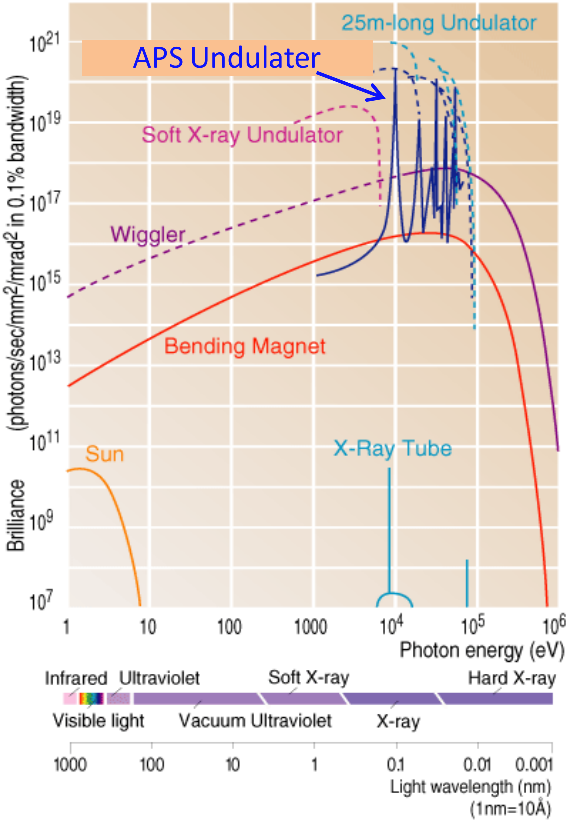

Fig. 2.31. *The X-ray energy (wavelength at the bottom) spectra for different light sources [170].*

Synchrotron radiation has a huge range of applications including chemistry, cultural heritage, earth science, engineering, environmental science, life science and material science. Currently, about 90 the third generation synchrotron radiation facilities around the world have been built to serve users, for example, the Advanced Photo Source (APS), Diamond Light Source (DLS), European Synchrotron Radiation Facility (ESRF), Super Photon Ring - 8 GeV (Spring-8).

The European Synchrotron Radiation Facility (ESRF) in Grenoble, France, is the first third-generation hard X-ray sources in operation, coming on line for experiments with a 6-GeV storage ring and commissioned beamlines in 1994. The ESRF was followed by the Advanced Photon Source at Argonne National Laboratory (7 GeV) in late 1996, and SPring-8 (8 GeV) in Harima Science Garden City in Japan in late 1997. These machines are physically large (850 to 1440 meters in circumference) with a capability for 30 or more insertion devices, and a comparable number of bend-magnet, beamlines. DLS is the UK national synchrotron facility, having 31 beamlines with the range of energy from 1.2 eV to 150 keV [171, 172]. Some important information and configurations for these outstanding synchrotron radiation sources are listed in Table 2. 2.

Many other third-generation synchrotron radiation facilities have been built as users all over the world increasingly demand X-ray sources and on-line instruments of different capabilities for research in different scientific disciplines.

Table 2. 2 *The specification of some synchrotron radiation sources.*

Facility	Advanced Photon Source (APS)	Super Photon Ring-8GeV (SPring-8)	European Synchrotron Radiation Facility (ESRF)	Diamond Light Source (DLS)
Location	Argonne, USA	Hyogo, Japan	Grenoble, France	Didcot, UK
Energy Number of Beamlines Circumference	7 GeV 68 1104 m	8 GeV 62 1436 m	6 GeV 56 844 m	3 GeV 31 561.6 m
Preparation Construction User Operation	1986-1988 1989-1994 1996-	1987-1989 1991-1997 1997-	1986-1987 1988-1994 1994-	1998-2001 2001-2007 2007-

2.5.2.3 X-ray absorption imaging

When X-rays pass through materials, its energy is absorbed or scattered. These absorption and scattering are called attenuation. The number of photons transmitted through a material depends on the thickness (distance travelled), density and atomic number of the material, and the energy of individual X-ray photon. The photon flux passing through materials can be calculated by Beer-Lambert law [173]:

$$I = I_0 e^{-\mu l} \tag{2.39}$$

where I_0 is the original intensity of the beam, I is the intensity of the beam at the distance l into the materials, e = 2.718, is Euler's number, μ is the linear attenuation coefficient.

μ describes the fraction of an X-ray beam that is absorbed or scattered per unit thickness of the absorber. μ is dependent on the density of a material, and those for the typical metal elements are showed in Fig. 2.32.

Another useful term is the so called mass attenuation coefficient, which measures the intensity of X-rays travelling through per unit mass material, and is defined as (μ/ρ) with the unit of cm^2/g.

To convert a mass attenuation coefficient (μ/ρ) to a linear attenuation coefficient (cm^{-1}), simply multiplying it by the density ρ. The data of the mass attenuation coefficients of the elements from Z =1 to 92 are available on the National Institute for Standards and Technology website [174]. For an alloy containing multiple elements, the linear or mass attenuation coefficients can be calculated using a mix rule based on the weight ratio of each element:

$$\mu_{mix} = (w_1 \times \mu_1) + (w_2 \times \mu_2) + \cdots + (w_n \times \mu_n) \tag{2.40}$$

where w is the weight percentage of each constituent element of the alloy and μ_n is attenuation of each element.

Using linear attenuation coefficients, the attenuation or often called absorption contrast of the different constituent elements and/or phases in a metal alloy can be calculated for the purpose of choosing the suitable alloy composition and selecting the appropriate X-ray energy range to achieve the best absorption contrast for imaging studies [37]. This is particularly important for achieving the best imaging conditions to study the evolutions of the different phases during solidification, because the composition of the phases change continuously with temperature changes during solidification.

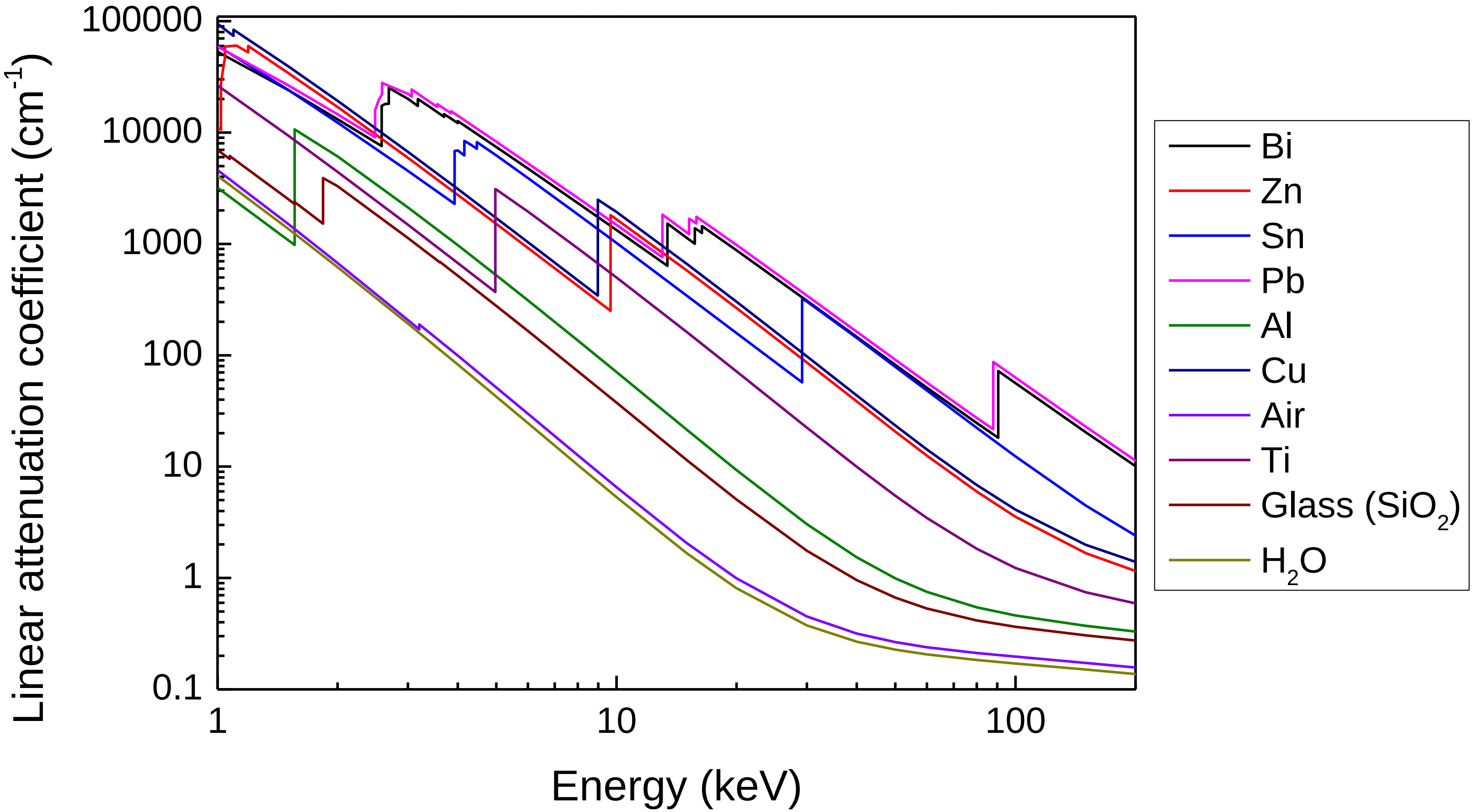

Fig. 2.32. *The X-ray linear attenuation coefficients of typical metal elements in the X-ray energy range of 1-200keV (Data from NIST database).*

The other important factor in X-ray absorption is the sample thickness [175, 176], the thickness of the sample (X) can be calculated by:

$$X = \frac{-1}{\mu_{mix}} \ln \frac{I}{I_0} \qquad (2.41)$$

To have sufficient X-ray transmission through a sample for imaging, normally, the attenuation length needs to be considered. The attenuation length of a specific material is the distance (thickness) where about $\frac{1}{e}$ (about 37%) of the X-rays are not absorbed by the sample as described by Eq. 2.42.

$$\ln \frac{I}{I_0} = \frac{1}{e} \qquad (2.42)$$

Thus, at a specific X-ray energy, the higher, the attenuation length, the lower, the linear attenuation coefficient for the material.

2.5.2.4 X-ray phase contrast imaging

In addition to absorption contrast due to attenuation, synchrotron X-rays can create phase contrast [177] and it is very useful for imaging materials with very similar X-ray absorption coefficients simply because the absorption difference cannot provide enough contrast for imaging.

The contrast is produced when a coherent X-ray beam refracts from two materials or structures of different refraction indices because the difference in the refractive index causes a phase shift.

Fig. 2.33 depicts an incident X-ray wave interacting with two objects at P and O. Due to the different refractive index of the two objects, at an appropriate sample-to-detector distance, both are projected at the point D on the detector. At the detection point D, there will be a phase difference due to the different path lengths experienced by the spherical waves. In the far-field limit both spherical waves can be approximated as plane waves of wavevector k'. The phase difference in this case is simply Q · r, where $Q = k' - k$, and r is the vector connecting the two points. In Fig. 2.33a, k is perpendicular to r, so that the phase difference in the far-field limit is $k' \cdot r$.

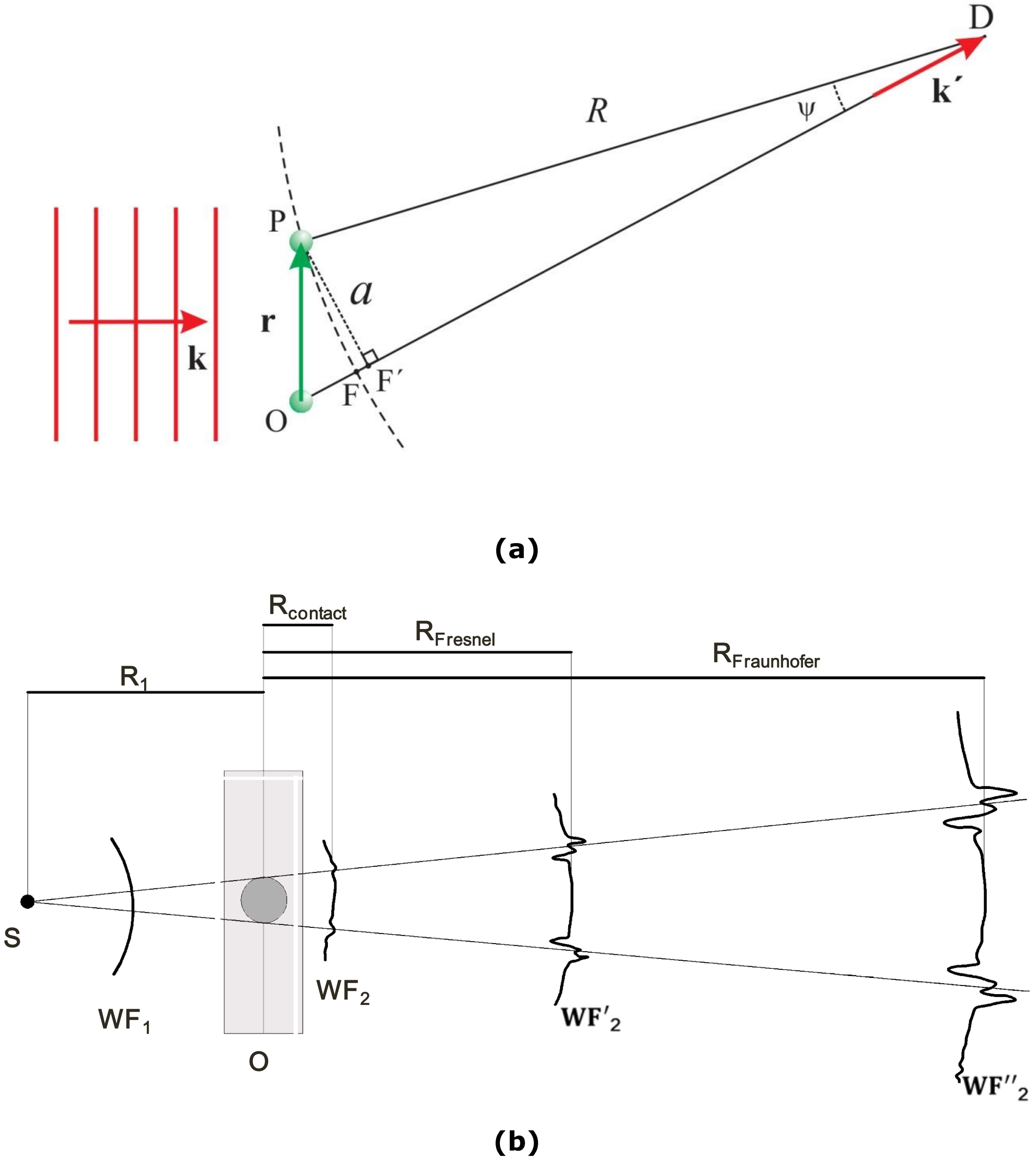

Fig. 2.33. *Schematically diagram of (a) phase contrast imaging technique, showing that O and P are two objects with different refractive index and vector k is the X-ray source, at a proper sample-to-detector distance, due to the different refractive indexes, both of the refracted waves are projected at D, with an angle of ψ, while for the vector of k′ are travelled longer than R, resulting in the phase different to the refracted waves at the detection D, thus the contrast of the image, and (b) phase contrast effect at the phase boundaries when the detector positioned in different region [164].*

The far-field limit is also called the Fraunhofer regime. If the detection point is closer to the scattering objects, because the path length difference is shortened by an amount given by $\Delta = OF' - OF$ in Fig. Fig. 2.33a, with $\Delta \approx a^2 / (2R)$, a more accurate algorithm is required to calculate the phase difference. If Δ is of order λ (wavelength of the X-ray waves) then the far-field approximation breaks down and we are in the so-called Fresnel or near-field regime. As the detector is brought closer to the sample it becomes meaningless to consider the phase difference between the refracted waves. This is the contact regime where imaging contrast arises from differences in absorption between O and P only. Fig. 2.33b shows that different regions exist determined by a, R and λ,

Fraunhofer region : $R >> a^2/\lambda$
Fresnel region : $R \approx a^2/\lambda$
Contact region : $R << a^2/\lambda$

Fig. 2.34 shows an example of the images at different regions from a simple model of discs of diameter 5 μm. Two types of idealised discs are considered: perfect absorbers (red), and perfect phase objects (blue). In the contact region imaging arises from absorption contrast only, so only the read particles can be revealed. Moving to the near field (Fresnel regime) and beyond, the phase objects become visible without any effect on the absorbers due to the refraction index difference at the materials contact interface. Once the distance from object to detector is well beyond the Fresnel region, the shape of the diffraction image does not change any more, although it gets weaker in intensity per unit area of detector as the inverse square of the distance and correspondingly covers more detector area.

In summary, phase contrast technique can be used to enhance the contrast of hard X-ray absorbing image especially for the low density constituent phases within sample. The gradient in the transmitted beam arising from refractive index variations in the sample leads to contrast in image. This technique is necessary and crucial for our research to reveal the bubbles in water (also silicone oil) due to the similar X-ray absorption between air bubble and water.

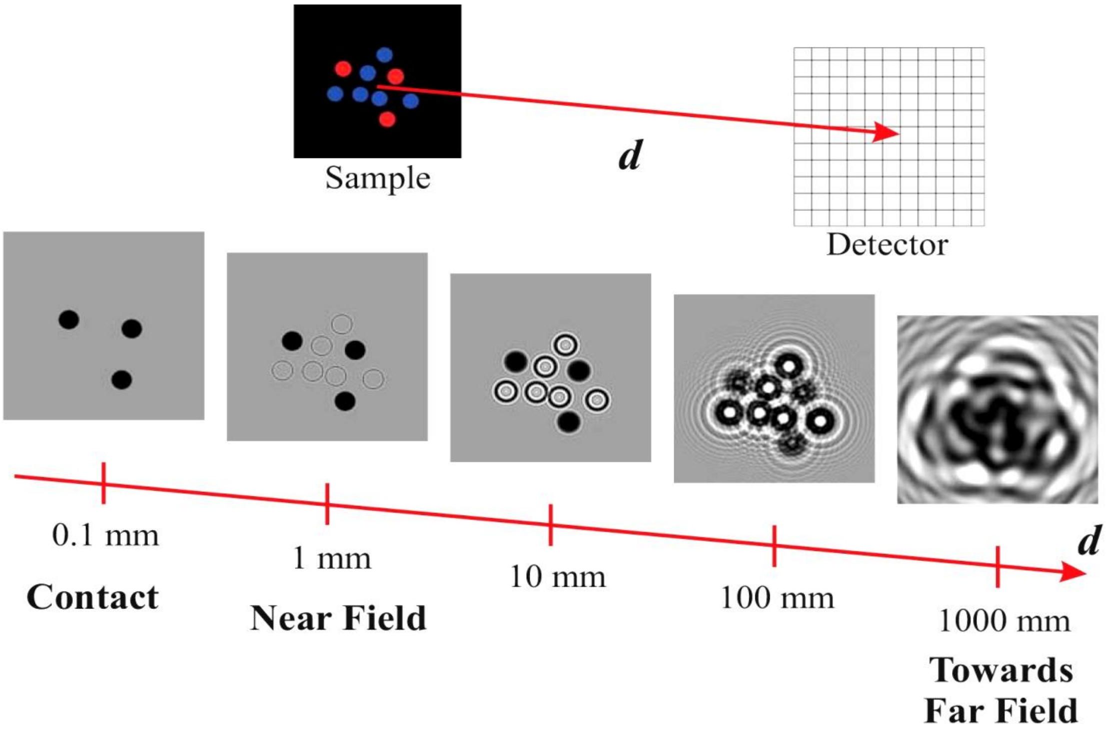

Fig. 2.34. *X-ray radiographs simulated to illustrate the transition from pure absorption contrast (in the contact regime) via edge enhancing phase contrast (near field) to stronger phase contrast (Fresnel region) and towards the far-field (near Fraunhofer) regime. The phantom object used in this simulation is an ensemble of small disk-like objects, some of which are taken to be ideal absorbers (red: zero transmission) and the rest ideal phase objects (blue: no absorption). The diameter of each disk is 5 µm. The grey scale images show simulated radiographs of the phantom, for illumination by a monochromatic X-ray plane wave of wavelength 1 A, at different distances between sample and detector (0.1, 1, 10, 100, and 1000 mm) [178].*

2.5.2.5 Lab based X-rays versus synchrotron X-rays

Using a special anode (target), lab-based X-rays can also achieve an X-ray energy of few hundred keV which is capable of penetrating thick metals. However, the brilliance of the best lab based X-ray is at least 10^{10} and 10^{7} lower than the synchrotron X-rays produced at APS and DLS, respectively (Fig. 2. 31), hence an image captured with exposure time of 1 s at APS would take 10^{10} s if a lab based X-rays is used.

In order to observe in real-time any ultrasound cavitation and bubbles in metallic alloys, which is a highly transient and dynamic phenomenon occurs in few tens of nanoseconds as discussed in ***Section 2.2****, the ultrafast synchrotron X-rays at APS is the only suitable light source for such a research.*

In addition, the synchrotron X-rays is a highly coherent source of parallel beam, and can be monochromatized using dedicated X-ray optics, while the lab based X-rays are always in a cone shape (Fig. 2.29a-b) which lead to the fast divergence of photons after emitting form the targets.

Hence, since synchrotron X-rays become available for researchers in materials and engineering in the early 1990s, the in situ imaging studies of the solidification dynamics have been mostly conducted using synchrotron X-rays as briefly reviewed in the next section.

2.5.3 In situ X-ray imaging studies of metallic alloys

Mathiesen, *et al* [37] firstly used synchrotron X-ray radiography to study in situ the solidification of metallic alloys using the beamlines ID22 and ID18 at ESRF. Fig. 2.35a shows schematically the experiment design and set-up with the thin metal samples of 200 μm thickness put in the X-ray path. Fig. 2.35b shows the real-time X-ray images of the solidified dendrites of a Sn-10%Pb alloy. The monochromatic beam of synchrotron X-rays produce much clearer images than those by using lab-based X-rays.

Since then, many researchers used the similar set-up and synchrotron X-rays at different facilities to study the directional solidification of aluminium alloys [160], the 3-D equiaxed dendrites of Al–Cu alloys [160, 179], etc. Very recently, some researchers started to impose external fields onto the samples during solidification, for example, Liotti, *et al* [171] studied the effect of pulsed electromagnetic field on the solidification microstructure and dendrite fragmentation in an Al–15Cu alloy. By using a similar design as Mathiesen, Wang [180] investigated the effect of electricity current on the solidification microstructure of Al alloys as well. Attempts to use synchrotron X-ray to study ultrasound induced cavitation and bubbles in metallic alloys were firstly made by Mi's [38, 42, 172] research group in 2012. Some of the key information and findings are presented in this thesis.

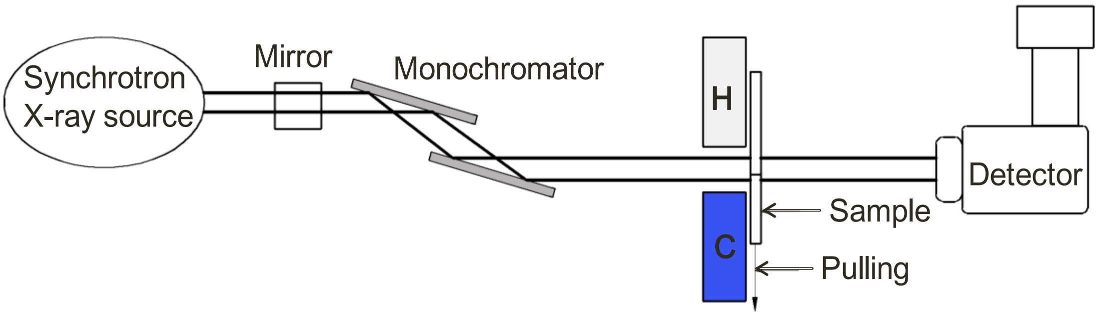

(a)

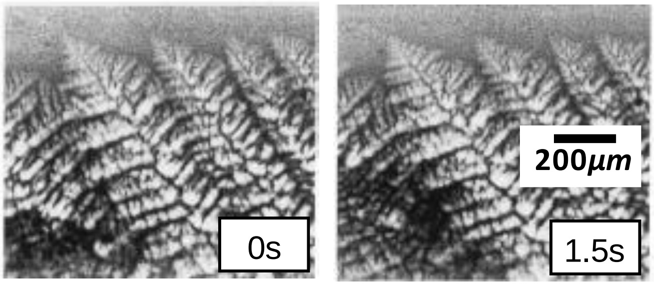

(b)

Fig. 2.35. *(a) A schematic diagram of the experimental set-up at a synchrotron X-ray beamline, and (b) the real time X-ray images of the columnar dendrites [37].*

Very recently, a few other researchers have also made similar attempts using Al-Cu alloys, for example, Huang, et al.[181] of Shanghai Jiao Tong University, and Wu, et al [182] of Manchester University. They used a very slow imaging rate, i.e. 2 fps, and 13 fps respectively, which actually cannot reveal any of the dynamic behaviour of the ultrasound bubbles in liquid metals.

In summary, synchrotron X-rays for metal research have the unique advantages of:

(1) Very high brilliance (very high photon flux), making it possible to do time-resolved research in situ to visualise the dynamic events of materials in a time scale down to microsecond

(2) Monochromatic beam and nano or micro focusing focusing capability, allowing images of micron or even submicron features to be captured for high spatial resolution work.

(3) Phase contrast capability, allowing materials containing different phases or interfaces (such as air-liquid interface of bubbles, solid-liquid interface during solidification) to be resolved with great details.

2.5.4 X-ray image processing and analyses

2.5.4.1 The processing of X-ray images

This section describes the image processing procedures for enhancing the quality of the X-ray images or video captured by using synchrotron X-rays.

Images acquired from synchrotron X-ray often contain defects, noises, or speckeles due to the imperfection of the X-ray optics (scintillator, lens camera, etc), and the non-uniformity of the X-ray beam.

The most common image enhancement techniques used for image processing are removal of noises, despeckle, edge sharpening, softening, gamma correction, contrast and brightness adjustment. The procedure illustrated by Eq. 2.43 and Fig. 2.36 is used for processing the X-ray images. There are 8 steps, including (1) converting video into image sequence, normally in a 'tif' format; (2) averaging the flat field images, and then despeckle the original images and averaged flat field images; (3) subtracting the flat field images from the original image using the equation below:

$$\text{Result image} = (\text{original image} - \text{noise}) - (\overline{\text{flat field image}} - \text{noise}) \quad (2.43)$$

(4) removing the outliers of the image by choosing a proper threshold and pixel size, the choose of threshold should be follow the rules of avoiding remove any useful information (particle or bubbles) from the image; (5) Fourier transformation to reduce the periodical noise in the images; (6) Inverse Fourier transformation; (7) improving the image quality by using

different band pass filters, and enhancement, e. g. adjust contrast and brightness, image sharpening; (8) converting the processed image sequence back to a video.

2.5.4.1.1 Flat field correction

In our experiments, the flat field images are actually the X-ray images of the sample when it becomes a full liquid inside the quartz containers. While the original images are the images of the samples inside the sample container when it starts to solidify or when an ultrasound is applied. Hence using Eq. 2.43, the features found during the solidification or those found when ultrasound is applied can be enhanced greatly [183].

In order to remove the most significant noises from the raw images, we have to average the flat field images into one image. The averaging of the flat field images is the averaging of the pixel value of the flat field images after despeckle of both the original and averaged flat field image to remove the small noises and defects such as salt and pepper noise, the averaged flat field image was then subtracted from the original image.

2.5.4.1.2 Fourier transformation of images

For periodical noise reduction, Fourier transform is used to decompose an image into its sine and cosine components. The output of the transformation represents the image in the Fourier or frequency domain, while the input image is the spatial domain. In the Fourier domain image, each point represents a particular frequency contained in the spatial domain image.

For the raw image f(x, y) with image size of M x N, the 2-D Discrete Fourier Transform is given by [184]:

$$F\,(u,v) = \frac{1}{MN}\sum_{x=0}^{M-1}\sum_{y=0}^{N-1} f(x,y)e^{-i2\pi\left(\frac{xu}{M}+\frac{yv}{N}\right)} \qquad (2.44)$$

Where f(x, y) is the image in the spatial domain and the exponential term is the basis function corresponding to each point F(u, v) in the Fourier space.

The equation can be interpreted as: the value of each point F(u, v) is obtained by multiplying the spatial image with the corresponding base function and summing the result.

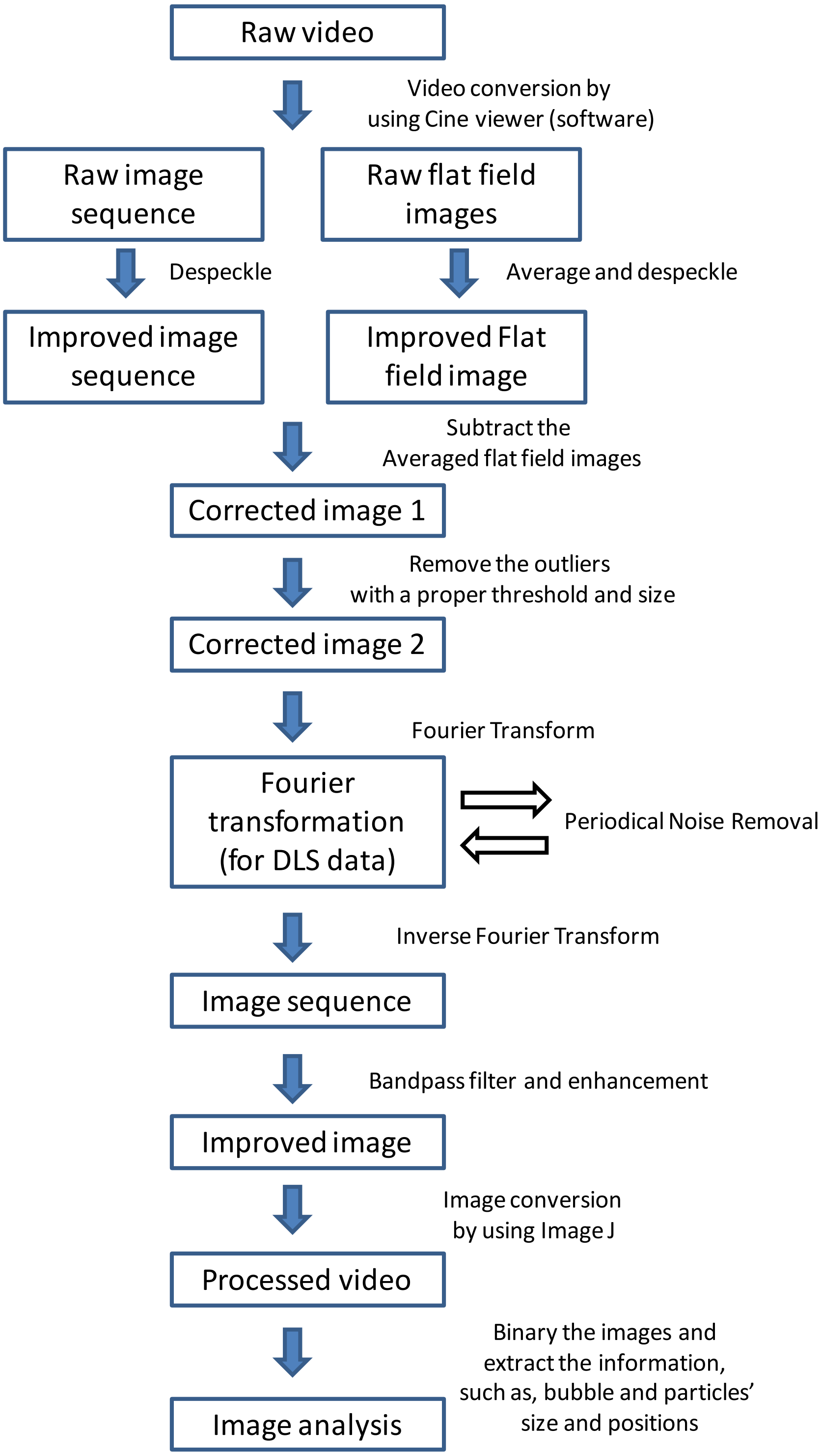

Fig. 2.36. *The flow chart of the procedure of image processing.*

Note that $\frac{1}{MN}$ is the normalization term in the forward transformation. This normalization is also applied to the inverse transform instead of the forward transform, but it should not be used for both.

After the image is converted to the Fourier domain image, the periodical noise positions have to be identified. The periodic noise signal always appears as a paired high intensity pattern along the vertical axis in the Fourier domain as some of the small brighter dots near the centre spot in Fig. 2.37d. But it should be very careful to test which of them is the periodic noise and which of them is the useful information from the image by compare the image with periodic noise and without periodic noise. Once the noise position is identified, the bandrejected filter or bandstop filter [184] (fill up the brighter spots by using a black patch) is then used to replace the noise pixel as showed in Fig. 2.37e.

The Fourier domain image is then converted back to spatial image using inverse Fourier transform, the periodical noise is therefore reduced. The inverse Fourier transform operation is given by:

$$f\,(x, y) = \sum_{u=0}^{M-1} \sum_{v=0}^{N-1} F\,(u, v) e^{i2\pi\left(\frac{xu}{M}+\frac{yv}{N}\right)} \tag{2.45}$$

2.5.4.1.3 Example of image processing

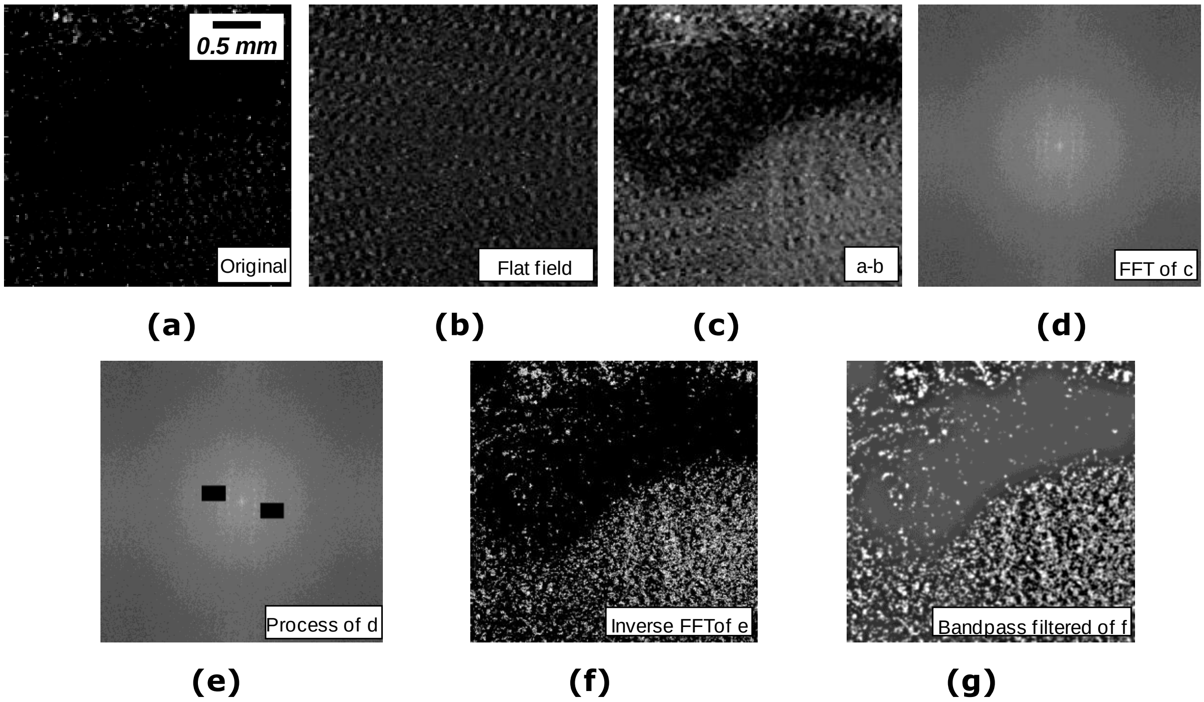

Fig.2.37. *(a) The original image (despeckled), (b) the flat filed image (averaged and despeckled), (c) image of* ***a-b****, (d) Fourier domain image of* ***c****, (e) Fourier transform with bandrejected filter on the periodical noise, (f) inverse Fourier transformed image of* ***e*** *and (g) bandpass filtered and enhanced image of* ***f****. The original image is captured at I12 of DLS, 1500 fps, 660ms exposure time.*

Fig. 2.37 shows the image processing procedure I developed by using ImageJ and Matlab® image processing tool box. All the images are applied to subtract the image of empty quartz container. The salt and pepper noises from the scintillator and also the image of fully liquid alloys with a camera noises at high frame rate, then, spot and strip noises are removed from the images first. In order to enhance the contrast of the images, we use the band-pass filter to process the area of interesting by separating the images into many sub-images and then combining them back together. For each sequence of images, the same parameters are used, e.g. the minimum and maximum processing scale and frequency, so that they are consistent and comparable before and after processing. While for different image sequence, we may choose the different parameters to achieve the best image contrast.

2.5.4.2 Bubbles and particles tracking

After obtaining a clear image, the key information such as the size, morphology, velocity and distribution of the particles and bubbles can be extracted using a in-house code developed using Matlab® as detailed in **APPENDIX 4**.

Fig. 2.38 shows the processing of a typical image extracted from an image sequence acquired at APS using 5413 fps. After subtracting the flat field image, bandpass filtering, and enhancement, the image is clear enough for statistical analysis. The particle and bubble tracking follows the following procedure: (1) inputting the image or image sequence into Matlab; (2) converting the image from greyscale into binary image; (3) removing the noise and filling the holes of the image; (4) Finding out the centre position, shapes and size of each particle; (5) tracking the particles and finding out the trajectory and velocity of particles.

As Fig. 2.39 shows that the processed image in Fig. 2.38d was binaried by using a proper threshold, and then the shape and centre location of particles can be found (Fig. 2.38f), trajectory and velocity of each bubble and particle. For example, five particles marked P1, P2, P3, P4 and P5 in Fig. 2.38e were selected, and their trajectories were calculated using the standard 4 frame tracking algorithm [39] (open source of Matlab® code) based on the time-resolved locations of the target objects in the consecutive images by estimating their most probable path and plotted in Fig. 2.38g.

Due to the low X-ray absorption and oscillation of bubbles, we can distinguish the bubbles which are brighter and with varied volume from particles.

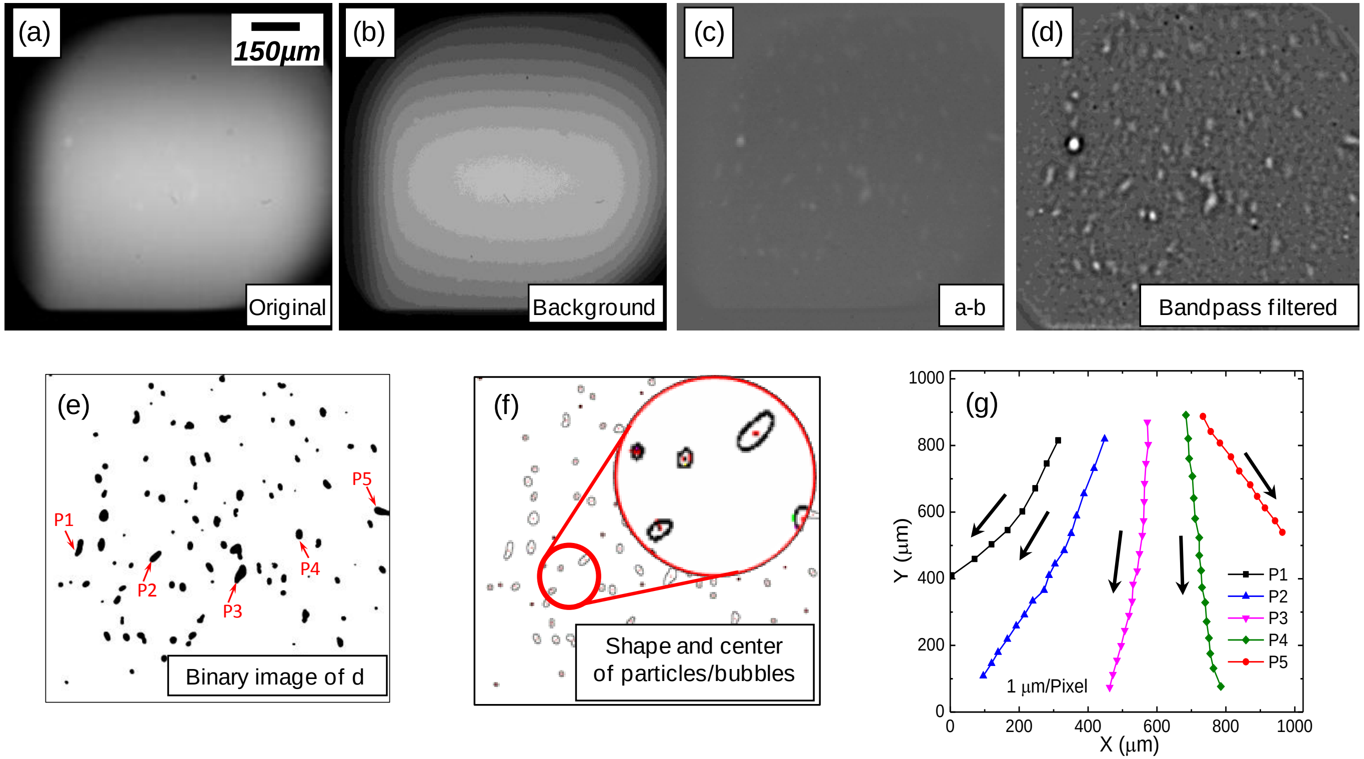

Fig. 2.38. *(a) A typical raw X-ray image acquired at APS using 5413 fps, (b) a typical background image acquired from a pure liquid Bi–8%Zn, (c) the image obtained by subtracting **b** from **a**, (d) the image after applying the band-pass filter on **c**, (e) the binarised image of **d**, (f) the shape profiles and centroids of the particles and bubbles, and (g) the trajectory of five typical particles for the image sequence acquired at 2.5mm below the sonotrode tip using an ultrasound input power of 20W. The arrows indicate the direction of movement.*

Fig. 2.39a-d shows that the cavitation bubbles captured in water at the position 1.2 mm below the sonotrode, at 5413fps. The contrasts of bubbles in water are very similar as the background (water), so the position findings cannot be achieved by using thresholding and convert them into binary images. However, owing to the phase contrast imaging technique, the bubble surface is obviously reveal the shapes and sizes of bubbles, so a very useful function in Matlab- 'imfindcircles', was found and proved to be suitable to reveal the bubble size and position:

$$[\text{centers, radii, metric}] = \text{imfindcircles (Ix, [a,b], 'sensitivity', c)} \quad (2.46)$$

where Ix is the image name (name of the image matrix) read into the Matlab, a and b are the minimum and maximum circle radius we are looking for, respectively. Sensitivity means that the circles in the image might not in a perfect circular shape. c is the tolerance of the distorted circles to a perfect circle, and it is ranged from 0-1. The sensitivity parameter is very useful here because many bubbles are distorted due to the strong fluid flow or acoustic waves, e.g. the bubbles in Fig. 2.39d.

Fig. 2.39e-h are the resulting images by circling the bubbles detected from original images, Fig. 2.39a-d, respectively. The blue and black circles stand for bubbles in the different range of size, where blue-line circled bubbles are bigger than 10μm while black-line circled bubbles are smaller than 10μm in radius. The comparison of the result images and original images shows that by using this function in matlab, almost all (>95%) the bubbles in Fig. 2.39a-d can be find correctly.

After obtaining the bubble positions, the tracking of bubbles are followed the same method as those in metallic alloys, however, because they oscillate, most of the time manually tracking and checking are necessary to make sure that the bubbles tracking are correctly performed.

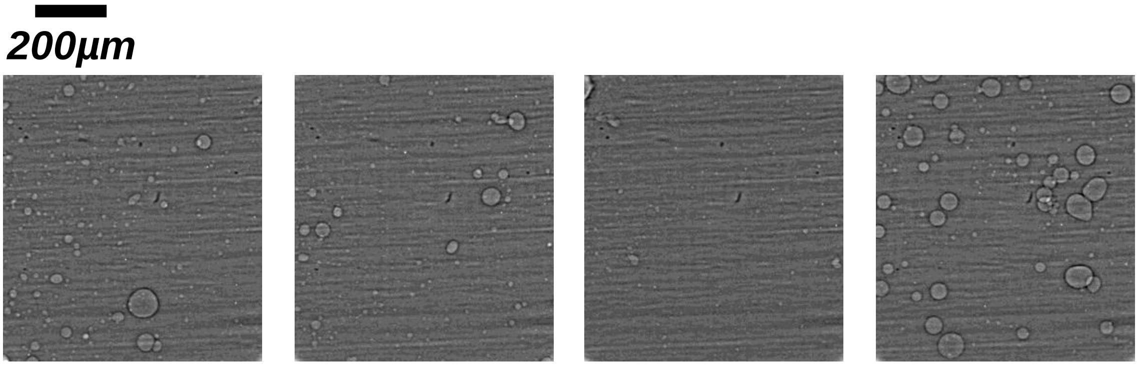

(a) 0 µs (b) 185 µs (c) 369 µs (d) 739 µs

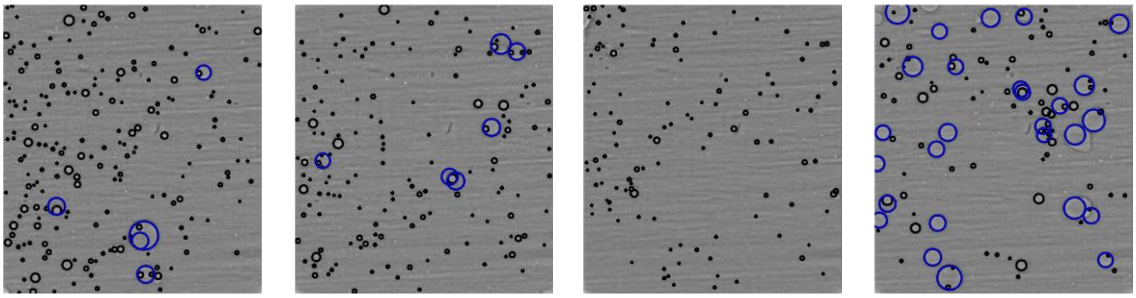

(e) 0 µs (f) 185 µs (g) 369 µs (h) 739 µs

Fig. 2.39. *a-d are the images of ultrasonic bubbles in water at the position 1.2 mm below the sonotrode. (e-h) The bubbles found for images of a-d, respectively. The blue-line and black circle stand for the different bubble range, where blue circled bubbles are bigger than 10µm while black-line circled bubbles are smaller than 10µm in radius. (Images are captured at APS with 5413fps)*

The bubbles or particles velocities can be calculated by using the translation distance over the time interval between the consecutive images. However, any movement in the thickness direction cannot be obtained because of the nature of the 2-D images. Actually the geometrical design of the thin channel ensure that the ultrasound wave and the associated fluid move downward directly without any noticeable movement in the thickness direction, therefore the relative movement of the particles and the bubbles in the thickness direction can be ignored. The Matlab in-house code can be found in **APPENDIX 4**.

2.6 Summary

In this chapter, the literatures that are directly relevant to this research are critically analysed and reviewed as already summarised at the very beginning of this chapter.

Chapter 3: Synchrotron X-ray beamlines and in situ imaging experiments

This chapter describes the synchrotron X-ray beamlines used, and the in situ synchrotron X-ray imaging experiments that were conducted at the sector 32-ID-B of Advanced Photon Source (APS), Argonne national laboratory, USA, and the Joint Environmental, Engineering and Processing (JEEP) beamline (I12) of Diamond Light Source (DLS), UK. The information in this chapter is directly relevant to the results described in chapter 4 and 5, modelling in chapter 6 and the discussion in chapter 7.

3.1 Fundings and the awarded X-ray beam time

The in situ experimental studies are parts of the key research agenda defined in the projects led by Dr Jiawei Mi, my supervisor, including two Royal Society projects, and one EPSRC project as detailed below:

- The Royal Society Research Grant – "*Development of a novel sonication solidification process for advanced materials (£15 k, 01/05/2011-30/04/2012)*". It provides the essential fund for the purchase of an ultrasound processor, UP100H from Hielscher Ultrasonics GmbH (100W, 30 kHz), the design and building of an in situ ultrasound solidification experimental apparatus.

- The Royal Society Industry Fellowship (for Dr Jiawei Mi) – "*Development of a sonication solidification technology for Ni superalloys (£97.8 k, 01/02/2012 - 31/01/2016)*". It funds partially the relevant travels, consumables and shipping cost for conducting the experiments at APS.

- The EPSRC project (EP/L019965/1, £308.7 k 01/09/2014 - 31/08/2017) – "*Development of efficient and scalable ultrasound-assisted solidification technologies for manufacturing advanced metallic alloys*". It provides further fund to support the continuous research on the fundamental studies and technological development concerning the ultrasound-assisted solidification processes and technologies.

Dr Mi is the principal investigator of the above projects and he also authored four successful research proposals, winning 24 shifts (1 shift = 8 hours) of synchrotron X-ray beam time from APS and 21 shifts from DLS in year 2011 - 2015 as detailed in Table 3.1. I participated in three of the five experiments during my PhD study (the one on 01-05 March 2013 at APS, and the two at DLS in 20-25 June 2013 and 11-13 Feb 2015, but missed the one at APS in 29 Feb - 03 March 2012, because of a visa issue).

Table 3.1. The proposals and synchrotron X-ray beam times awarded by Advanced Photon Source and Diamond Light Source

Proposal code	**Proposal title**	**Beamline & X-ray facility**	**Dates to do Experiment**
GUP 23649	Ultrafast synchrotron X-ray phase-contrast imaging study of ultrasound cavitation and its effect on nucleation and dendritic grain evolution	32-ID-B APS	02-04/07 2011
GUP 26170	Ultrafast synchrotron X-ray phase-contrast imaging study of ultrasound cavitation and its effect on nucleation and dendritic grain evolution: phase 2 – investigation on metallic alloys	32-ID-B APS	29/02-03/03 2012
			01-05/03 2013
EE8542-1	In situ study of optimal processing conditions to deliver embryonic nuclei for grain self-refinement in clean metals under ultrasound cavitation	I12 DLS	20-25/06 2013
NT12131	In situ, high speed radiography of the interactions between ultrasound bubbles and nucleating particles in solidifying metal alloys	I12 DLS	11-13/02 2015

The sector 32-ID-B of APS provides the ultrafast X-ray imaging capability (upto 271, 554 fps), while the I12 of DLS provides a high speed imaging capability of upto a few thousands of frames per second. Both are the key research instruments for the in situ experimental studies. Hence, in this chapter, the functionalities of the beamlines are described first, followed by a detailed description on the ultrasound solidification apparatus developed, and the sample environment; and how they were integrated with the beamlines to conduct the in situ experiments.

3.2 The synchrotron X-ray beamlines

Firstly, the electron filling mode in the storage ring of APS, the specification, capabilities and characteristics of the ultrafast synchrotron X-ray imaging beamline, the sector 32-ID-B are described in this section.

3.2.1 The sector 32-ID-B of APS

At APS, the electrons circulating inside the storage ring can be operated in two modes: the conventional uniform filling mode or hybrid filling mode as schematically showed in Fig. 3.1a. In the conventional uniform filling mode, the electrons circulating inside the storage ring consists of 24 uniformly spaced electron bunches (singlets) with the total current of 102 mA equally distributed in each singlet (4.25 mA/singlet). While in the hybrid filling mode, there are two uneven bunches of electrons, one is a single short electron bunch containing 16 mA, and the other is a long-and-fat bunch train of electrons consisting of 8 electron bunches with the remaining current of 86 mA. The total time span of the long-and-fat electron bunch train is only 500 ns, and the X-ray created by this fat, closely packed electron bunches is 6 times brighter than those obtained from the uniformly filling model [177, 185].

The sector 32-ID-B is an undulator insertion device. The X-rays are produced by the mechanism schematically showed in Fig. 3.1b as described here. The undulator has 72 magnetic periods (144 poles) in a total length of 2.4 m with each period having a period length of 3.30 cm. The gap of the undulator (gap between the poles) can be adjusted from 1 cm to 3.5 cm.

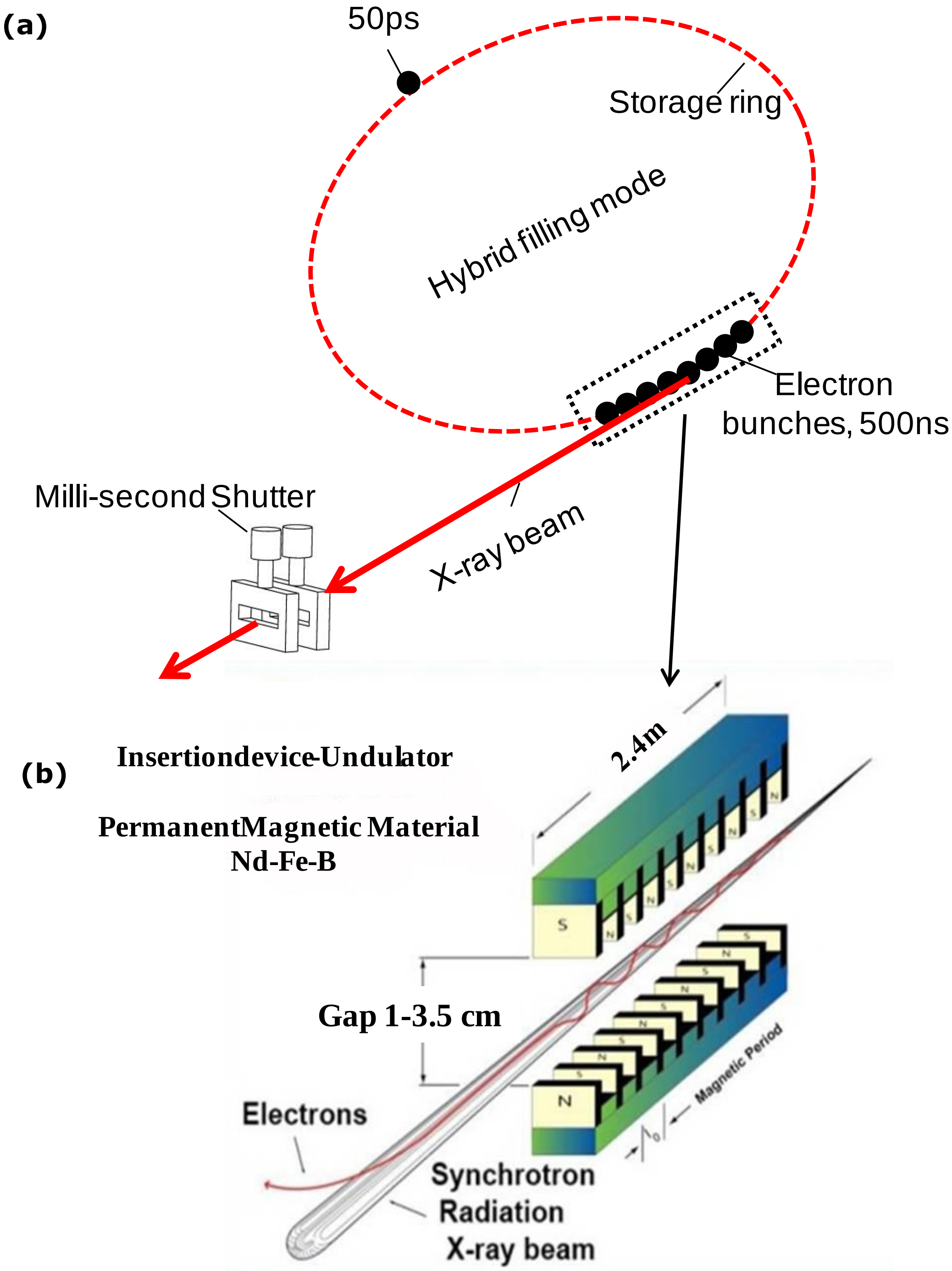

Fig. 3.1. *(a) A schematic diagram, showing the electron bunches in the hybrid filling mode inside the storage ring of APS. (b) The undulator inserted at the position marked by the dash line in **a** for sector 32-ID-B [168].*

When the electrons travelling in the storage ring pass through the device, they are subject to a transverse oscillation under the alternating magnetic fields. The bending and acceleration of electrons associated with this movement result in the emission of synchrotron X-rays. Normally, the gap between the undulator is smaller and magnetic power is higher than other insertion device such as wiggler, so the oscillation amplitude of the electrons in undulator is smaller, and thus the X-rays produced by the oscillating electrons interferes constructively with those from other electrons, causing the X-rays spectrum to have a relatively narrow bandwidth. For example, every time the long-and-fat electron bunch train of 500 ns duration passes the undulator, an X-ray pulse of 500 ns duration is emitted. At 32-ID-B, when the undulator is set at different gaps to generate different magnetic fields, different characteristic X-ray spectra are produced as showed in Fig. 3.18 later for the typical energy spectra at different gaps.

Sector 32-ID-B is designed to fully utilise the 500 ns electron bunch train by synchronizing the X-ray pulse from the undulator with the X-ray shutter and the camera on the beamline using a Stanford DG535 delay generator fed with the radio-frequency signal from the storage ring. The 500 ns electron bunch train is circulating in the storage ring and comes around in every 3.68 μs (1104m / light speed ≈ 3.6825 μs), delivering an X-ray pulse of the duration of 500 ns in every 3.6825 μs. Hence, the maximum effective image acquisition rate is 271,554 fps (theoretically calculated by: 10^6 / 3.6825 = 271,554). The synchronization ensures that the image of an object is taken within the 500 ns exposure time, providing an image temporal resolution of 500 ns regardless of the frame acquisition rate. Currently, this is the fastest imaging capability among the Synchrotron X-ray based imaging beamlines around the world, only inferior to the X-ray free electron laser based imaging technique, such as the Coherent X-ray Imaging (CXI) instrument at the Linac Coherent Light Source at Stanford University [186, 187]. Sector 32-ID-B can be operated in white beam or monochromatic beam in the energy range of 8 - 35 keV for imaging and diffraction studies.

3.2.2 The JEEP beamline (I12) of DLS

Fig. 3.2 shows the layout of the X-ray optics and the experimental hutch 1 of the Joint Environmental, Engineering and Processing beamline (I12) at DLS. It has three different sections: (1) two optics hutches where the X-ray is filtered and focused; (2) the experimental hutch 1 and 2 (hutch 2 is not showed here) where the samples sit and the experiments are carried out; and (3) the control room where the scientists control the experiments. I12 is a dedicated high energy instrument on a 4.2 T wiggler source.

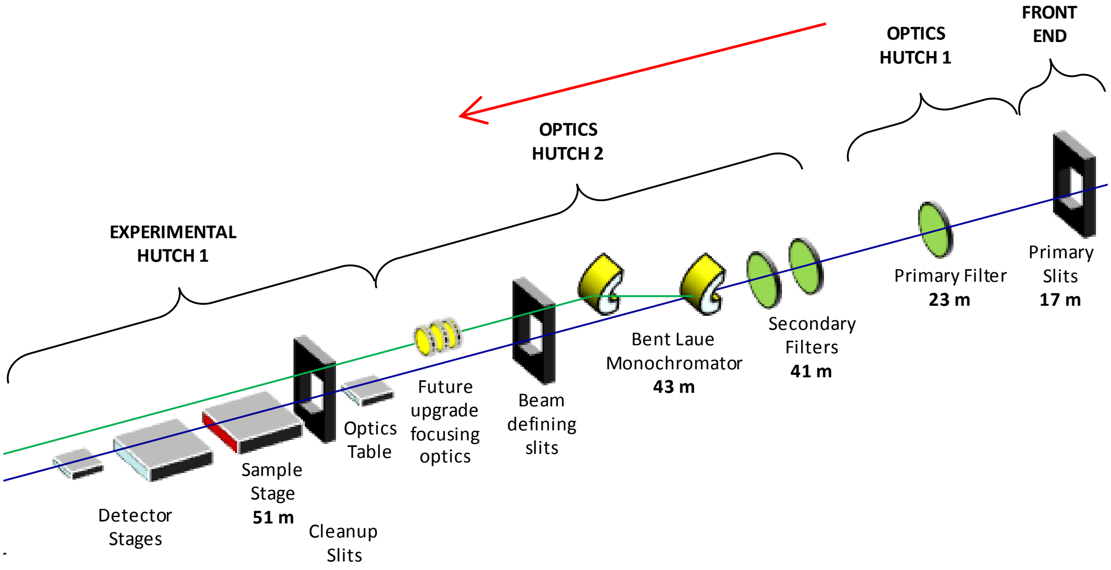

(a)

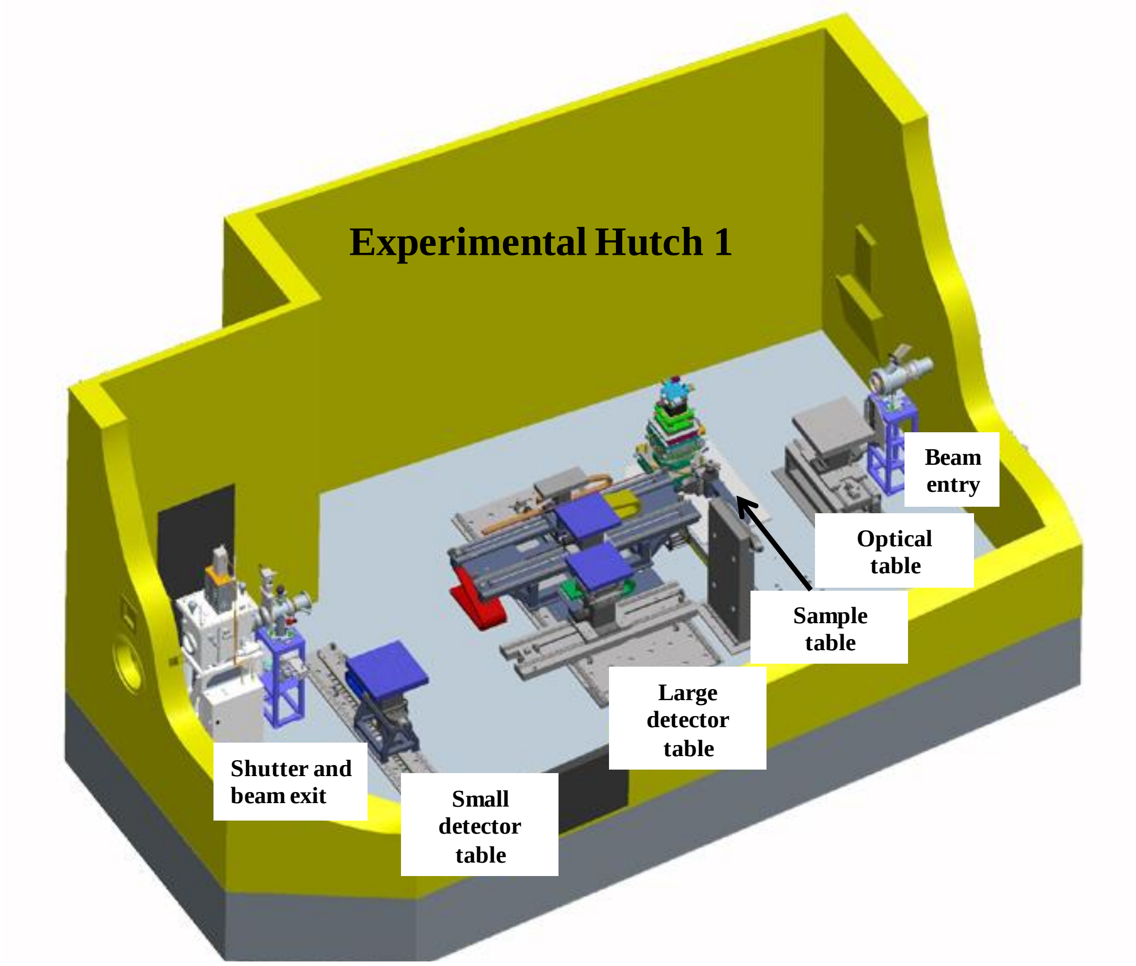

(b)

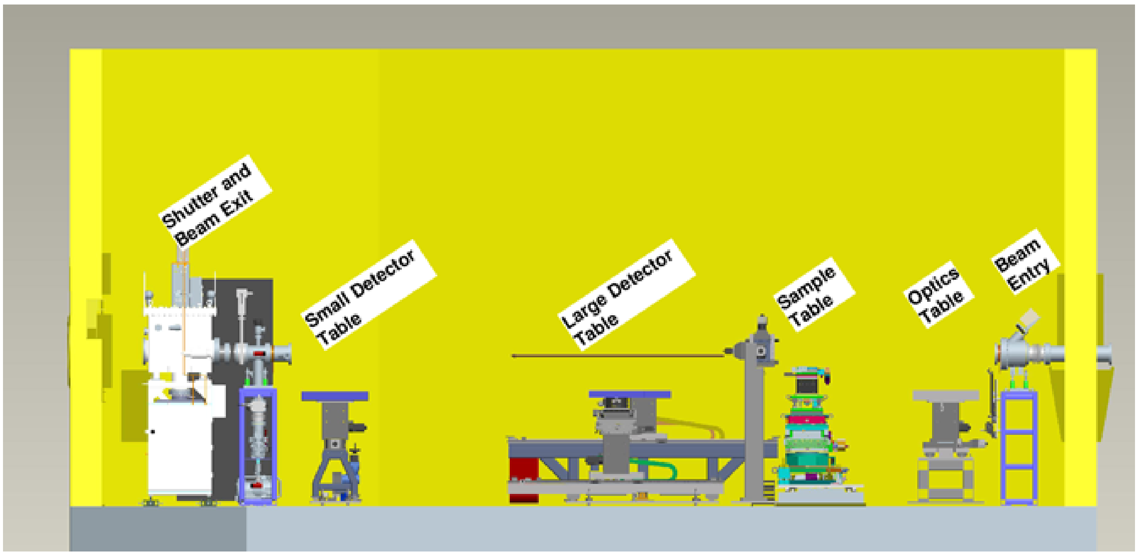

(c)

Fig. 3.2. *(a) The layout of the X-ray optics, (b) a 3-D top view and (c) a side view of the experimental hutch 1 of I12 at DLS [167].*

A wiggler is also an insertion device commonly used in a synchrotron storage ring. Similar to an undulator, it also consists of a series of magnetic dipoles that produce high flux X-rays by enhancing the oscillation of the electrons. However, because of the fixed gap between the magnetic dipoles in wiggler [164], the period and strength of the magnetic field is not tuned to the frequency of radiation produced by the electrons, thus every electron in a bunch radiates independently and the resulting X-ray radiation bandwidth is broader, the beam size is bigger and the X-ray flux is lower than those from an undulator source as schematically explained by Fig. 3.3 [164].

I12 can be operated in white beam condition or monochromatic beam in the energy range from 50 to 150 keV for imaging, diffraction and tomography experiments. I12 has a large beam size (up to 50 mm × 12 mm in Experimental Hutch 1) and an X-ray imaging system with interchangeable objective lenses. The imaging system allows users to flexibly select different image magnifications and hence fields of view. The relative bigger field of view is therefore suitable for studying the collective behaviour of bubble clouds and their interactions with the metal flow and semisolid phases.

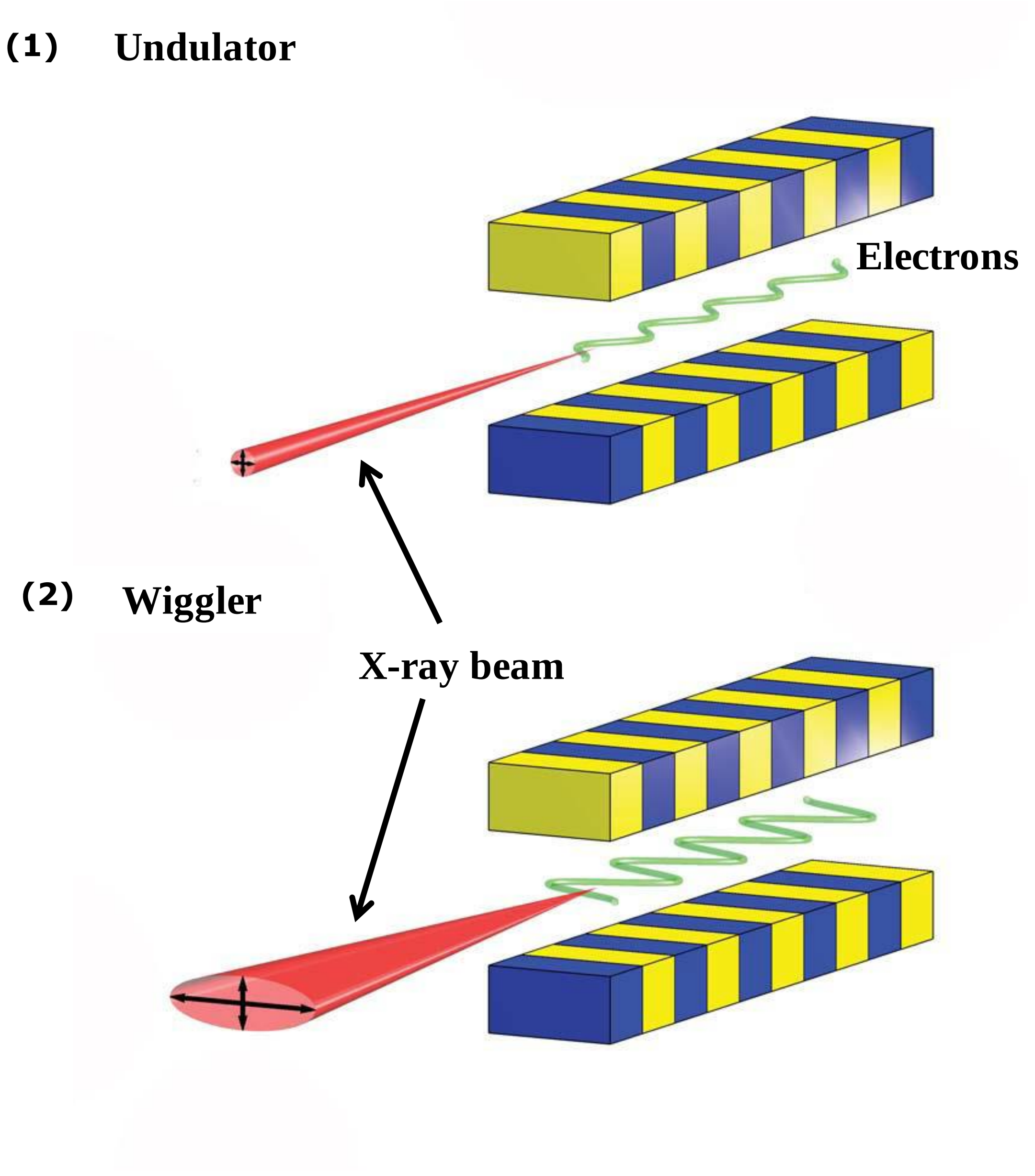

Fig. 3.3. *The characteristics of the X-ray radiation generated by (1) an undulator and (2) a wiggler. The difference in the performance of the two devices arises from the differences in the maximum angles of the electron oscillations in the horizontal plane* [164].

3.3 The experimental apparatus

3.3.1 Sample containers and materials

For the in situ X-ray imaging experiments, the samples and the containers for the samples have to be thin enough to allow sufficient X-ray flux to pass to form images with sufficient contrast. However, in order to observe the dynamic behaviour of ultrasonic waves inside liquid metal, the samples need to be thick enough to accommodate the sonotrode tip (the wave emitting surface), and then allow the ultrasonic waves to be transmitted into the samples. Finally, the material of the sample containers need to withstand high temperature (~1000 K) and with lowest possible X-ray absorption. Hence, the thin foil samples (those of a typical thickness of 100 ~ 200 μm sandwiched between two carbon plates or Alumina plates) used in the previous in situ solidification research as described the literature review [34-37] are not suitable for this research.

In order to accommodate the typical sonotrode tips of 0.5 ~ 2 mm in diameter (these are the smallest commercially available sonotrodes provided for the UP100H ultrasound processor manufactured by Hielscher), and also allow a sufficient volume of melt to be around the sonotrode tip for transmitting ultrasonic waves, at first, a special miniature liquid metal container (actually a special casting mould) was designed. The detailed information and 3-D views of the key components and the assembly are showed in Fig. 3.4, which has 3 main functional parts:

1. An upper reservoir to hold liquid metals with a cylinder-shape recess to accommodate a sonotrode for transmitting ultrasonic waves down wards.
2. A thin channel below the upper reservoir to allow the liquid metal to flow into and form a thin section for X-ray imaging. At either side of the thin channel, a circular recess is designed to reduce the thickness of the mould wall to facilitate the penetration of X-rays.
3. A lower reservoir to hold any liquid metal flowing down from the thin section and also accommodate a brass rod as a chill to create a desired thermal gradient within the thin section.

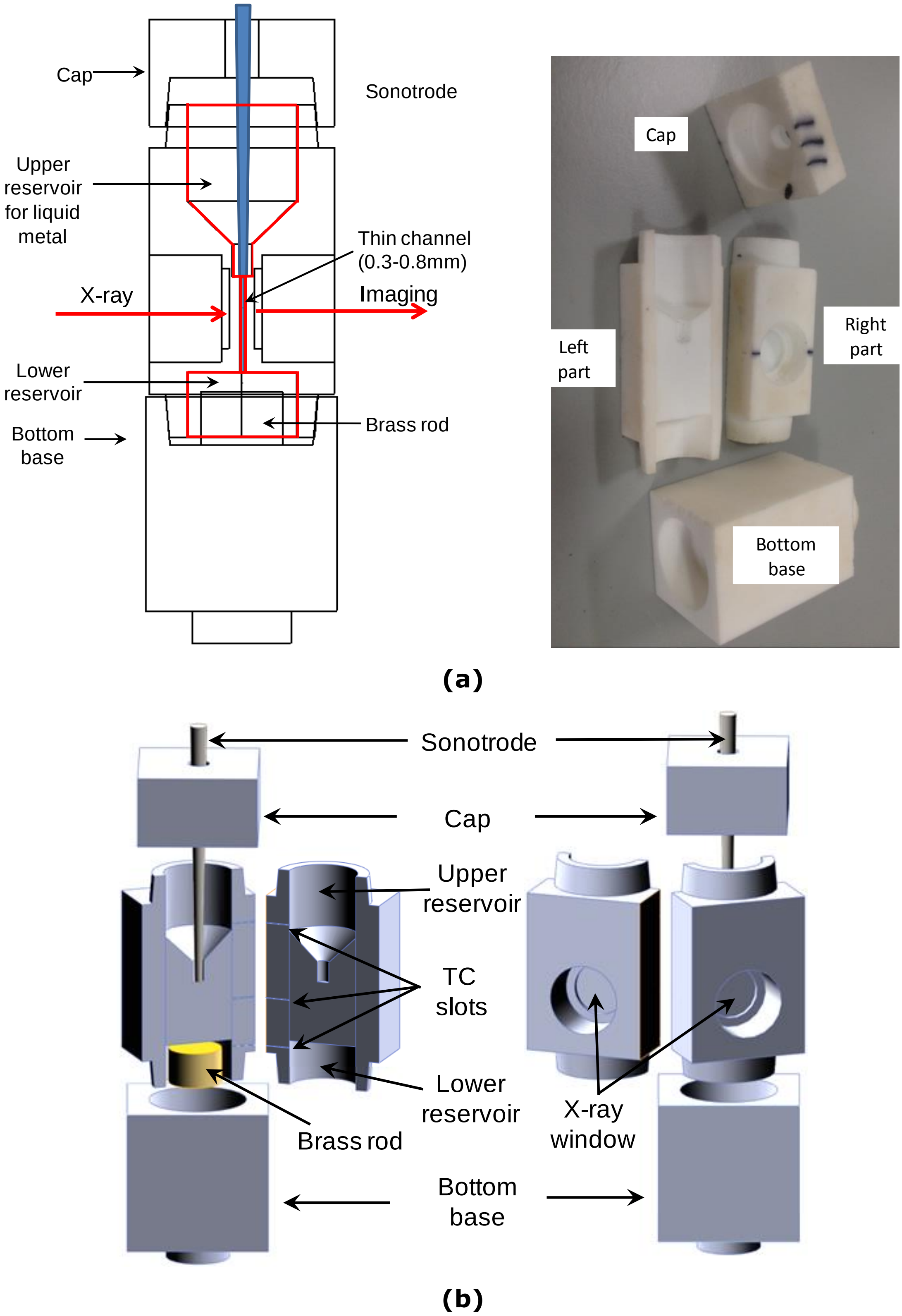

Fig. 3.4. *(a) left: a sectional view of the outline of the designed sample container assembly, right: a photo, showing the machined container using either Duratec 750 or Marcor. (b) The container assembly in 3-D viewed from different directions (open to show the inside). The CAD drawings for all components are in* ***Appendix 1****.*

The container is designed as a casting mould with the partition line in the middle. So after each solidification experiment, the sample can be simply taken it out by opening the mould (Fig. 3.4b), and then the mould can be used repeatedly for following experiments. In addition, a cap is also designed to cover the upper reservoir to reduce the heat loss during experiments and also help to lock the two half moulds together.

Two materials, Duretec 750 and Macor (purchased from RS component UK®, with stock No.248-4630 for Duratec 750 and 158-3203 for Macor) were selected because they are machinable ceramics and designed for working in high temperature environment. The properties of Duratec 750 and Macor can be found in Table 3.2.

Initially, we used a low melting point alloy, Sn-13%Bi to study the effects of the sample thickness on the quality of the X-ray images obtained, and tested different thicknesses of the thin channel, i.e. 0.2, 0.3, 0.5, and 0.8mm. The X-ray attenuation length of Duratec (Ca_2SO_4) [188], and that of Sn-13%Bi [189] are showed in Fig. 3.5a and b, respectively. Theoretical calculations indicate that at a thickness of 0.5 mm, the X-rays with the energy lower than 95 keV are absorbed completely by the alloy, and the image obtained is very dark (Fig. 3.6c), containing virtually no useful information at all. At the thickness of ~0.3 mm, the X-rays of the energy higher than 70 keV can penetrate the alloy sample and ultrasonic bubbles were apparently captured and showed more clearly on the images (Fig. 3.6b). At the thickness of ~0.2 mm, more X-ray will penetrate the sample, however, it is too thin to allow the ultrasonic bubbles to move freely into the thin channel (Fig. 3.6a). Hence, based on the theoretical calculations and the experimental trials, the samples with the thickness of 0.3 mm (sample container with 0.3 mm thin channel) are used in the subsequent in situ experiments.

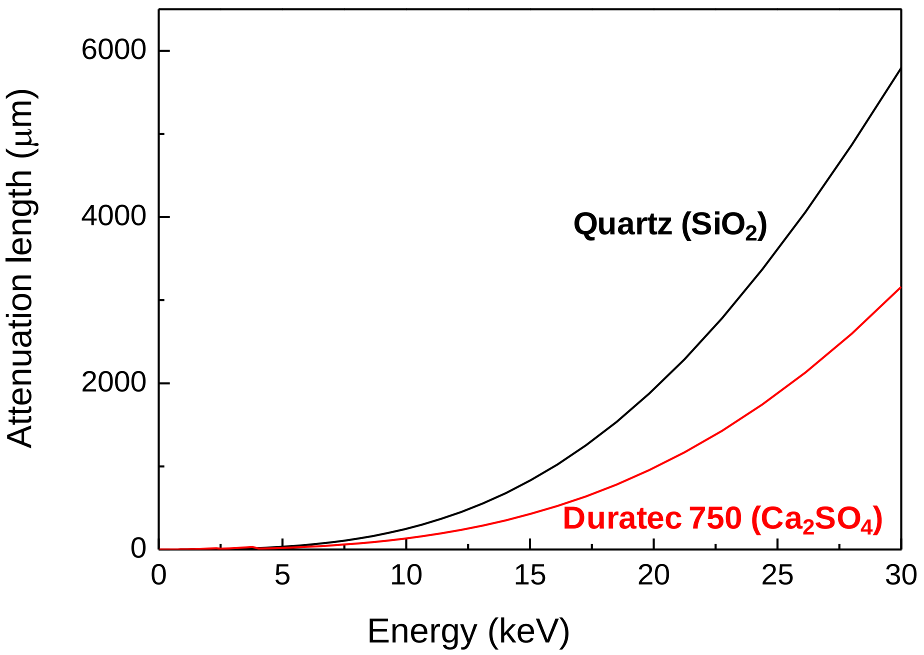

(a)

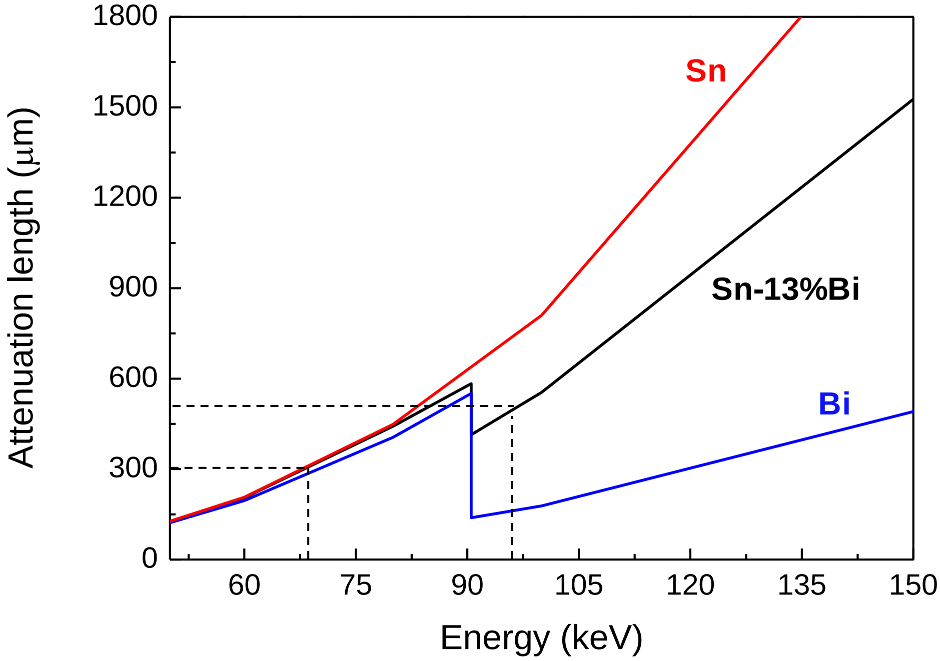

(b)

Fig. 3.5. *The X-ray attenuation lengths for (a) Quartz and Duratec 750 at the energy range of 3-30 keV [188], and those for (b) Sn, Bi and Sn-13%Bi at the energy range from 50 to 150 keV (Sn-13%Bi is calculated using the mix rule from pure Sn and Bi) [13].*

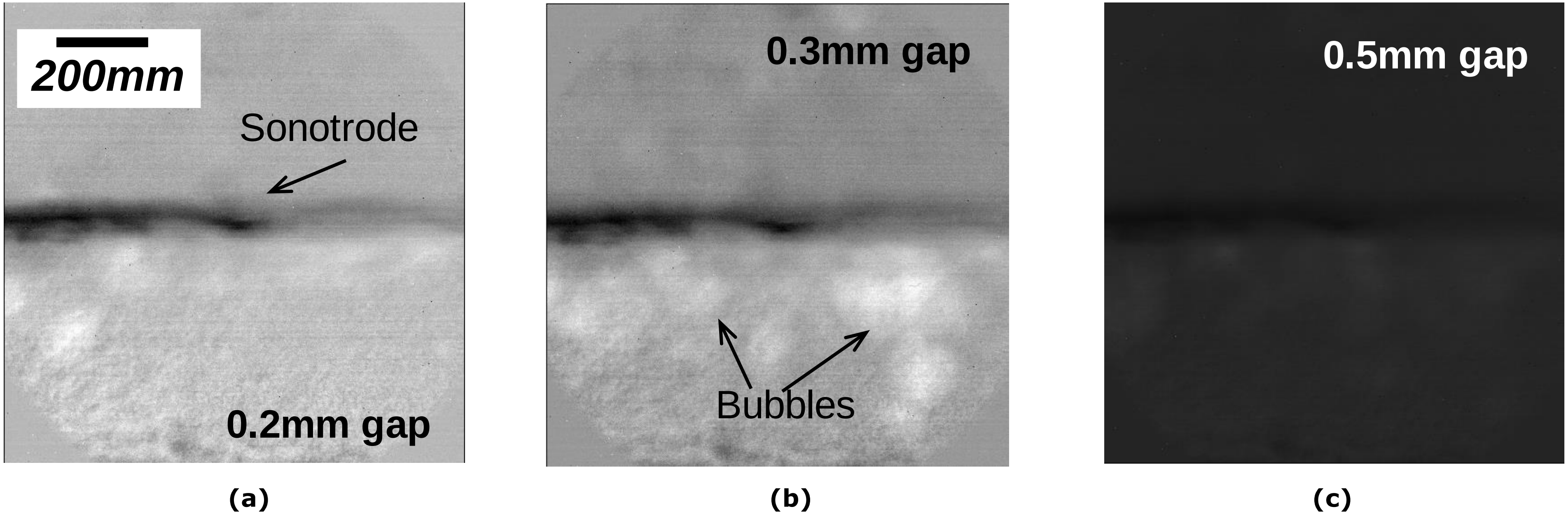

Fig. 3.6. *The real time X-ray images of the sonotrode tip and the ultrasonic bubbles captured in a liquid Sn-13%Bi alloy at APS by using the sample containers with the thin channel thickness of (a) 0.2 mm, (b) 0.3 mm and (c) 0.5 mm. All the images are taken by using 20 W ultrasound under white beam.*

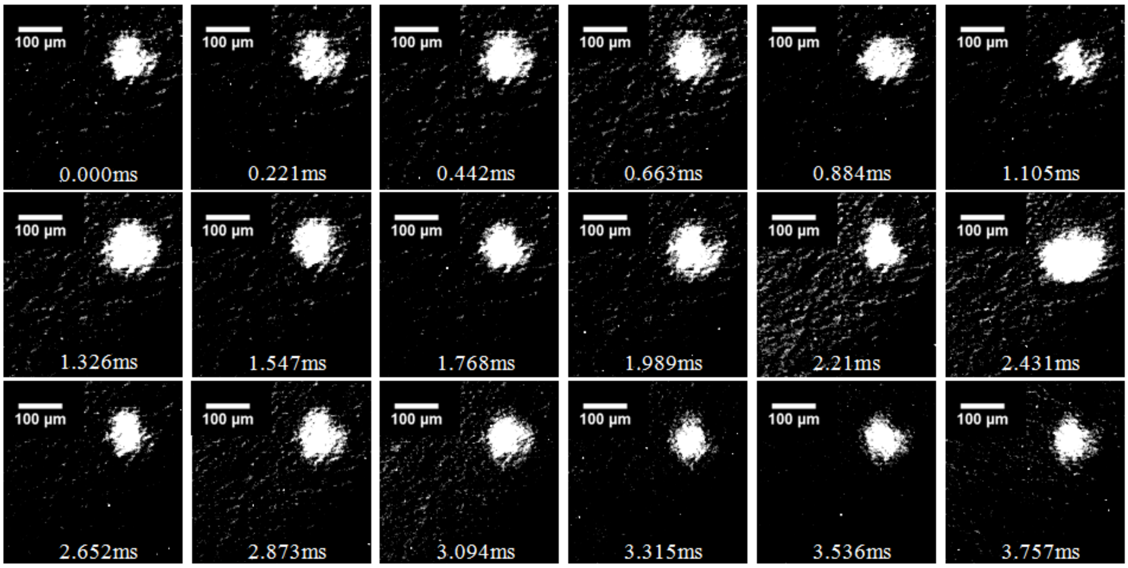

Fig. 3.7. *A quasi-steady state ultrasonic bubble captured using 4526 fps in a Sn-13%Bi alloy melt contained inside a Duratec mould at 3 mm below the sonotrode tip. The inter-frame time is 0.221 ms.*

A series of experiments were carried out using the Duratec mould as the sample container. Fig. 3.7 shows the typical X-ray images obtained. The images were found to have backgrounds with high level of noises because Duratec is a relative porous material and its density is not uniform. Similar phenomenon was found in the case of using Macor as the sample containers. The high level of background noises causes difficulties in processing the images, for example, it blurs the boundary of bubbles, causing error in calculating the size of the bubbles (Fig. 3.7).

The CAD drawings for all components of the Duratec and Macor sample containers are in **Appendix 1**.

Because of the above problems, we then studied the possibility of using quartz (SiO_2) as the sample containers. Quartz has very low X-ray absorption (about half of Duratec 750 as shown in Fig. 3.5a) and is uniform in density. Fig. 3.8 shows a series of X-ray images for a K-type thermocouple of 0.25 mm in diameter covered by quartz plates (20 x 20 mm, from Robson Scientific^{TM}) of 0, 0.5, 1, 1.5, 2, 2.5, 3, 3.5 mm in thickness respectively. The images were taken using a lab based X-ray CT scanner (HMX 160CT from X-TEK Corporation$^{®}$) operated at 35 kV and 38 µA (a Tungsten target was used in the X-ray tube). Clearly, the image is getting darker as the thickness of the quartz plate increases. However, the background is very uniform and even at 3.5 mm, the absorption of X-ray is much lower than that by Durtec (Fig. 3.5a).

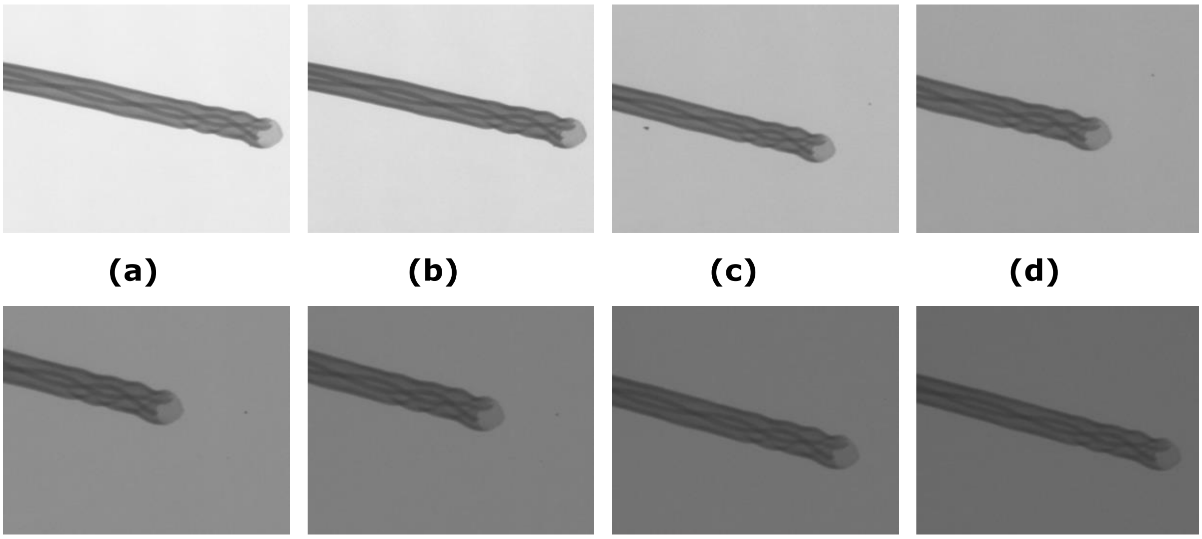
(a) (b) (c) (d)

(e) (f) (g) (h)

Fig. 3.8. *A series of X-ray images of a K-type thermocouple of Ø 0.25mm (with stainless steel sheath) covered by a quartz plate of the thickness of (a) 0, (b) 0.5 mm, (c) 1 mm, (d) 1.5 mm, (e) 2 mm, (f) 2.5 mm, (g) 3 mm, (h) 3.5mm, respectively.*

However, the problem with quartz is that it is non-machinable, and a dedicated glass workshop is needed to form it into the container with the geometry similar to the mould machined by using Duratec (Fig. 3.4).

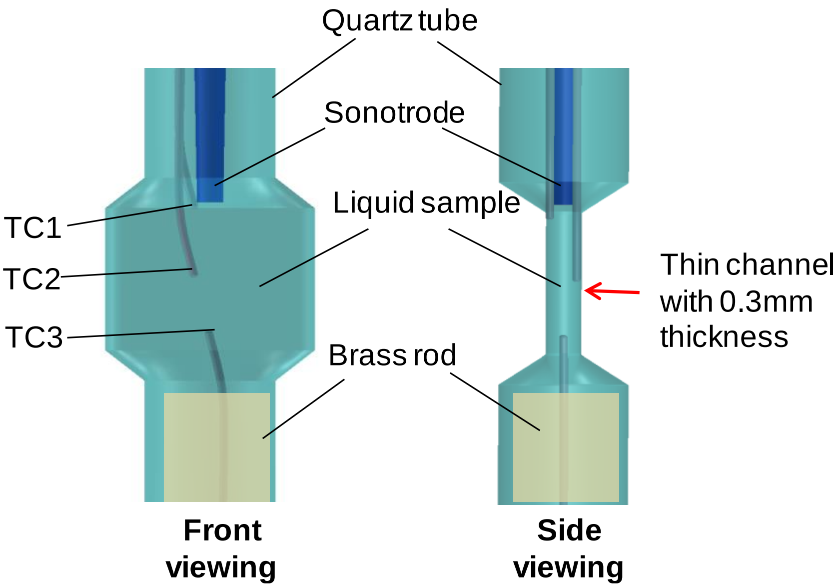

(a)

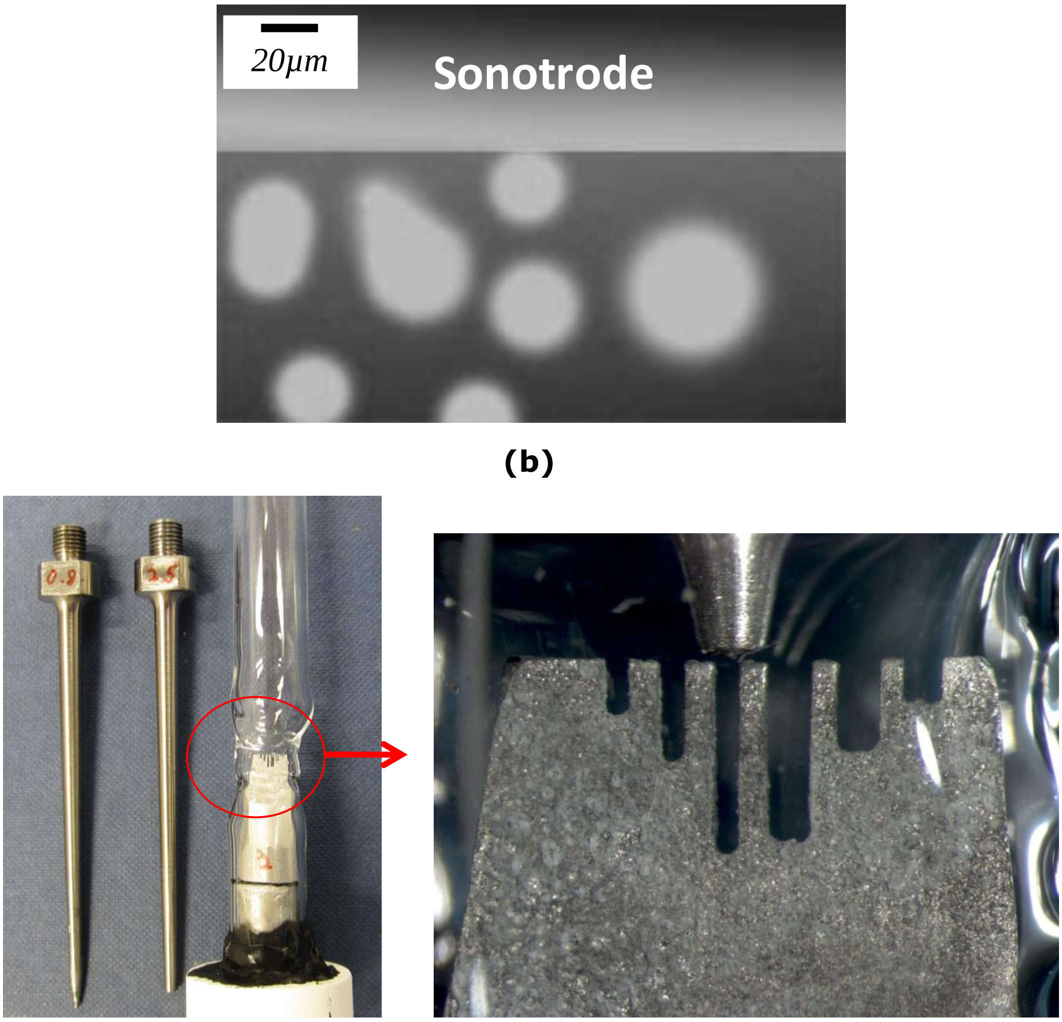

(b)

(c)

Fig. 3.9. *(a) A sketch, showing the design of the quartz sample container with a thin channel of ~300 μm in the middle section. Three thermocouples (TC1, TC2, TC3) are set at the top, middle and bottom of the thin channel. (b) The X-ray image captured by using the quartz sample container with Sn-13%Bi alloy at APS (20 W ultrasound power and 135,780 fps). (c) The left is a photo of quartz container with a ~ 250 μm thick Al-20%Cu slot sample inserted inside the thin channel area. The right is an enlarged photo of the circled area, showing the details of the slot sample and the sonotrode tip on top.*

We therefore designed a similar sample container (with ~300 μm thin channel in the middle) and made it using quartz tubes and plates by the following procedure:

1. Firstly, two rectangular thin quartz sheets (15 × 10 × 1.2 mm) were put in parallel together with a gap of ~300 μm in between.

2. Secondly, the edges along the 10 mm side of the two sheets were welded together using a gas torch to form the thin channel of ~300 μm internal gap.

3. Finally, the two openings of the thin channel along the 15 mm side were linked and welded onto two 40 mm long quartz tubes (13 mm outside diameter and 1.5 mm wall thickness from Robson Scientific™). Careful operations were carried out in the quartz softening temperature range to deform one end of the quartz tubes into a wedge-shaped transition area in order to fit smoothly and then welded together with the thin channel.

Fig. 3.9a shows the design of the quartz sample containers with the thin channel in the middle. The real quartz sample containers are typically showed in Fig. 3.9c, and they were made by a specialist, Ms. Julia Malle in the Glass Workshop at the Department of Chemistry, University of Hull.

Tests of the quartz sample containers with Sn-13%Bi alloy were conducted at 32-ID-B, and Fig. 3.9b shows that the ~300 μm internal gap in the thin channel area is wide enough to allow the ultrasonic bubbles generated immediately under the sonotrode tip to pass through the channel, while thin enough to allow X-rays to penetrate the metal alloy held inside the channel with enough photon flux to form images at an acquisition rate of up to 135, 780 fps. All the experimental results concerning metal alloys present in this thesis are obtained by using such quartz sample containers.

3.3.2 Selection of sample materials

Different materials, including water, silicone oil (~50 mPa·s, 1.062 g/mL at 20 °C, from Dow Corning®), water mix with 2mg/ml Ge particles (from Goodfellows®, 99.999% purity, with maximum particle size of 150 μm), and three metallic alloys, Bi-8%Zn, Sn-30%Cu and Sn-13%Bi (weight percentage). The materials properties are listed in Table. 3.2. The different materials were chosen because:

1. water (including water mixed with particles) is the most common Newtonian fluid and has been always used as the typical liquid for studying the physics of cavitation and fluid flow [6].

2. Silicone oil has similar surface tension and density as water, but, it has a very different viscosity and therefore has been always used as the typical liquid in the studies of non-Newtonian fluid, owing to its transparency. It has been also used as the typical polymer material in the in situ experiment [3].

3. The metal alloys were chosen because of their low melting temperature (their phase diagrams are shown in Fig. 3.10), and the adequate X-ray absorption contrast, especially between Bi and Zn, for high speed synchrotron X-ray imaging. Furthermore, Bi-Zn alloy has a typical eutectic reaction while Sn-Cu alloy has a typical peritectic reaction as shown in Fig. 3.10, facilitating the studies of different microstructures affected by the applications of ultrasonic waves. Furthermore, Sn-Cu system is also the base materials systems for soldering [190] and anodes for lithium batteries [191]. Therefore any research findings will have direct industry application relevance.

Fig. 3.11 shows that Bi and Sn are heavy X-ray absorption materials. If any cavity or bubble (may contain vapour or gas inside the cavity or bubble) present in the liquid Bi and Sn. The big absorption contrast will give a clear image for the cavity or bubble as clearly seen in Fig 3.9b. Hence Bi and Sn based low temperature alloys are ideal systems for studying ultrasonic bubbles in liquid metals. Furthermore, the relatively big X-ray absorption difference between Bi and Zn (Fig. 3.11a) makes the Bi-Zn alloy a very good (clear X-ray image contrast) system to study the interaction of ultrasonic waves with the primary phase, in this case the primary Zn phase, during solidification. In addition, the relatively big X-ray absorption difference between Sn and Cu (Fig. 3.11b) is useful for us to study the solidification process with and without ultrasound treatment of the typical peritectic alloy.

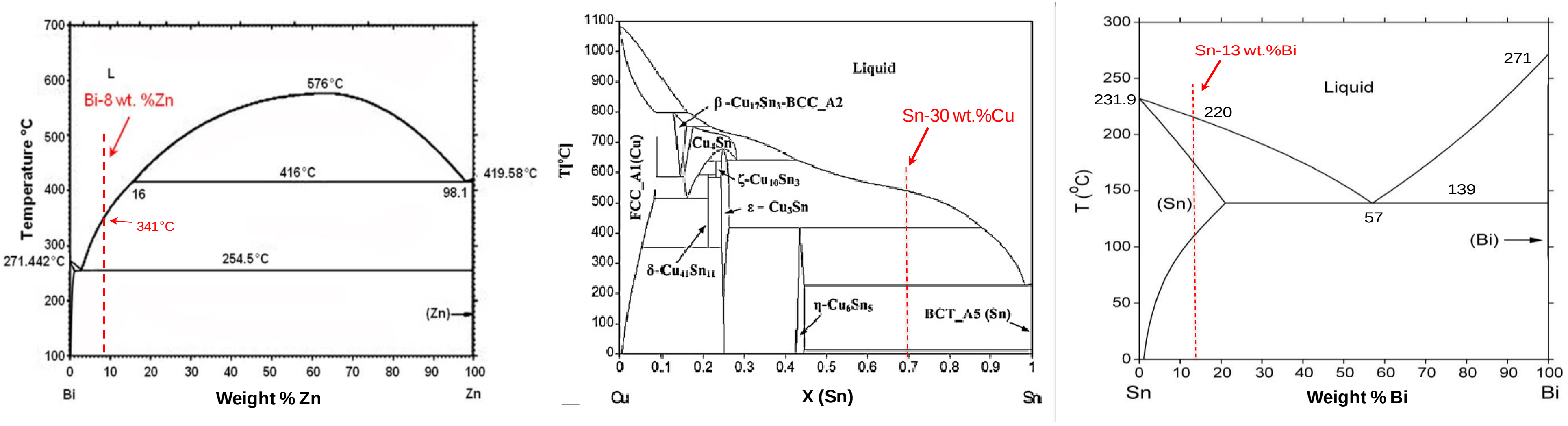

(a) **(b)** **(c)**

Fig. 3.10. *The binary phase diagram of (a) Bi-Zn [192, 193], (b) Sn-Cu [194], and (c) Sn-Bi [194] with the dashed line marking the Bi-8%Zn, Sn-30%Cu and Sn-13%Bi alloys used in the experiments.*

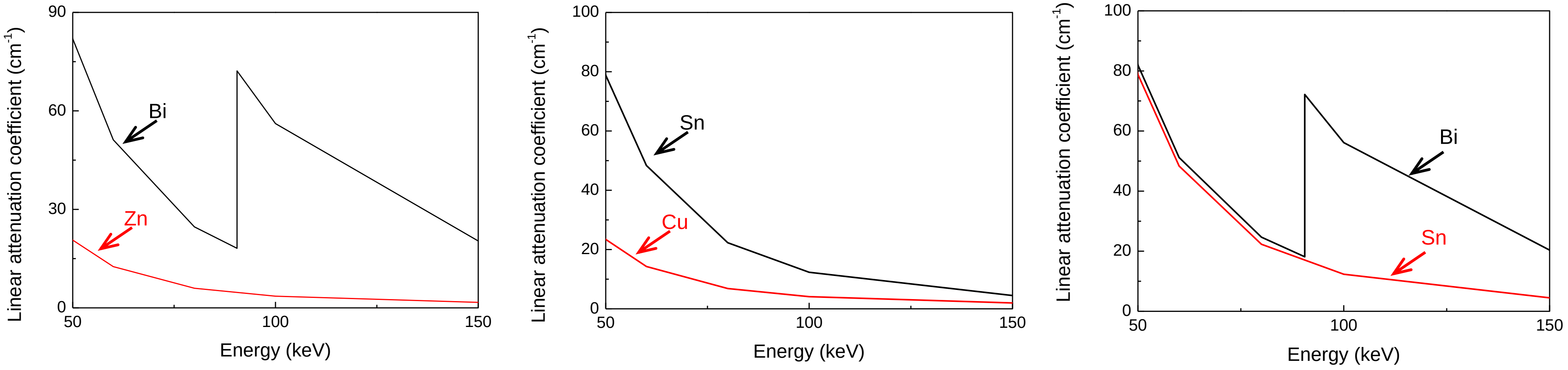

(a) **(b)** **(c)**

Fig. 3.11. *The linear attenuation of (a) Bi-Zn, (b) Sn-Cu, and (c) Sn-Bi in the X-ray energy range of 50-150 keV.*

3.3.3 Making of the alloys and samples

The alloys were made in the Advanced Materials Laboratory at the School of Engineering, Hull University using high purity elemental Bi (99.999%), Zn (99.99%), Sn (99.99%) and Cu (99.999%) purchased from Goodfellows®. Firstly, the correct weights of the pure metals were prepared. Secondly, the prepared pure metals were melted in an electrical-resistance heating furnace. Finally, the alloys were cast into quartz tubes of 9 mm inner diameter (the diameter is 1 mm smaller than the tubes used in the in situ experiments) by using a small counter-gravity casting system.

When liquid metal is poured into a casting mould under gravity without control the mould filling process, surface turbulence always occurs, causing air bubbles and/or oxide films to be entrained into the solidified samples [195-197], and forming bubbles, micro-porosity, cracking, etc. inside the samples. These should be avoided as much as possible in our dedicated in situ experiments. We designed and made a dedicated small counter-gravity filling apparatus [198] to flow the liquid metal alloys against the gravity into the quartz tubes and produced a very clean alloy ingots for the subsequent in situ experiments.

Fig. 3.12a-b shows a 3-D diagram and a photo of the counter-gravity filling apparatus. Basically a vacuum pump is used to firstly pump the air out from a desiccator which acts the negative pressure reservoir to subsequently “suck” the liquid metal into a quartz tube that is connected to the reservoir. Careful operation is needed to adjust the pressure via a ball valve during the “suck” operation in order to flow the liquid metal quiescently into the quartz tube and solidify as a clean rod ingot subsequently.

To avoid the possibility of sucking the liquid metal into the desiccator due to any unexpected operation, a one metre tall borosilicate tube is inserted between the quartz tube and ball valve. The low vacuum of the negative pressure reservoir cannot provide enough hydrostatic pressure to draw the liquid metal up over 1 m high, preventing the liquid metal from entering the desiccator.

Table. 3.2. The properties of the sample materials and sample containers, and the parameters used for the simulations

Sample properties					
Samples	Water	Silicone oil	Bi-8%Zn (700K)	Sn-30%Cu (950K)	Sn-13%Bi (500K)
Density, ρ_0 (kg m^{-3})	1000	960	9561	7793	7631
Viscosity, μ (Pa s)	1.002×10^{-3}	50×10^{-3}	1.5×10^{-3} [199]	1.35×10^{-3} [199]	1.5×10^{-3} [199]
Surface tension, σ (N m^{-1})	7.2×10^{-2}	3×10^{-2}	0.376 [200]	0.4 [199]	0.5 [199]
sound speed, C (m s^{-1})	1484	980	1790 *	2730*	2730*

Sample container properties			
Material	Duratec 750	Macor	Quartz
Composition	Ca_2SiO_4	SiO_2 (46%), MgO (17%), Al_2O_3 (16%), K_2O (10%), etc.	SiO_2
Density, ρ_0 (kg m^{-3})	1400	2520	2203
Thermal conductivity (W/mK)	0.49	1.46	1.38
Maximum service temperature (K)	1273	1073	1873
sound speed, C (m s^{-1})	4431*	4431*	5300

Other parameters	
Frequency of ultrasound, f (kHz)	30
Ultrasound power, W (W)	20
Diameter of the sonotrode tip, d (m)	2×10^{-3}
Gas polytropic exponent, γ	1.4
Empirical constant, B (bar)	3046 *[10]
Empirical constant, n	7.025*[10]

*Due to lack of data, the speed of sound in pure Bi was assumed for Bi-8%Zn and pure Sn was used for Sn-30%Cu and Sn-13%Bi, respectively. Speed of sound in Duratec and Macor was empirically estimated. The values of empirical constants, B and n for water were used.

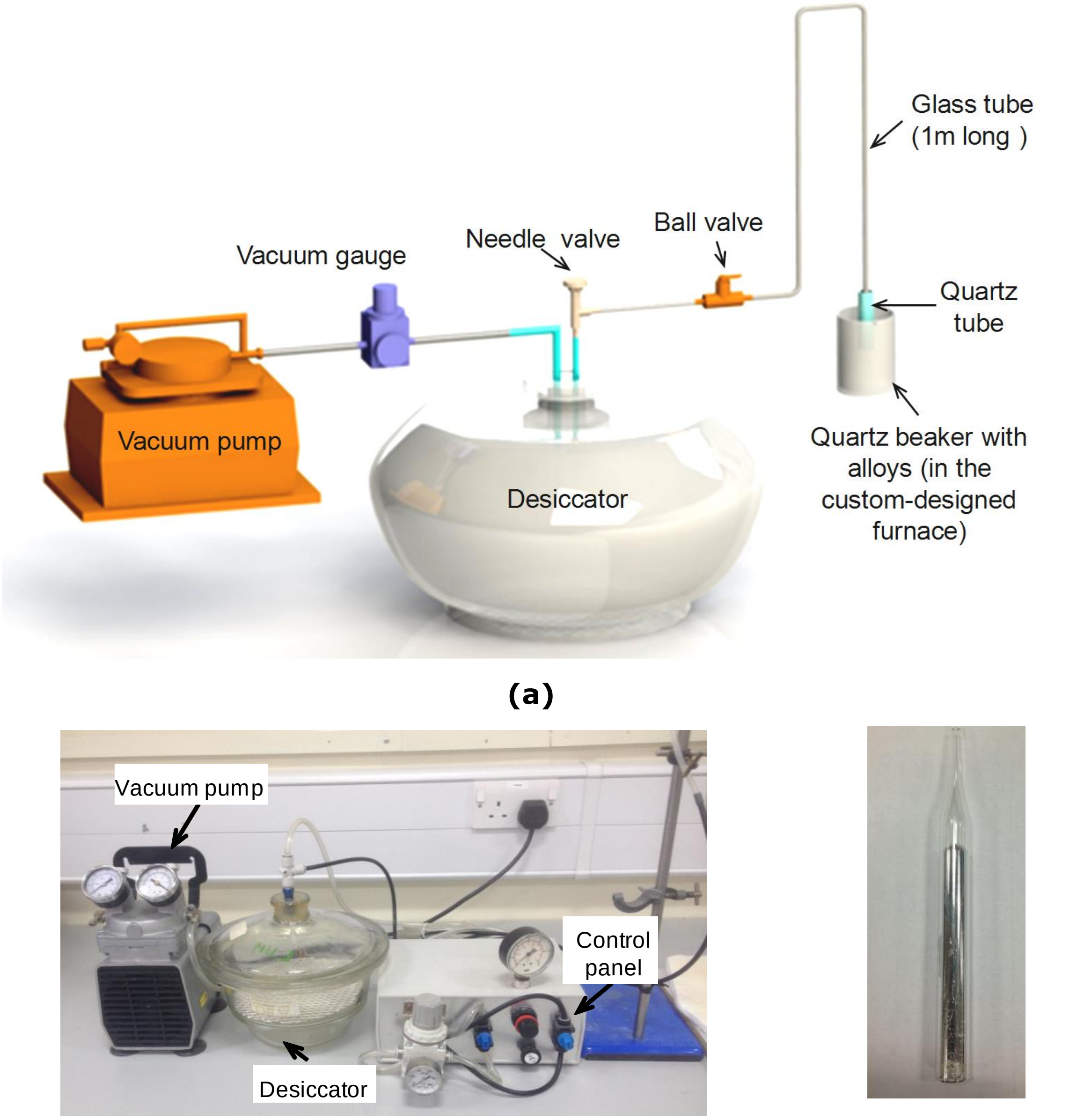

(a)

(b) **(c)**

Fig. 3.12. *(a) A 3-D diagram and (b) a photo of the counter-gravity filling system, (c) the sample alloy ingot cast in a quartz tube (inner diameter of 9 mm, 110 mm length).*

The melting of the alloys was carried out inside the furnace as showed in Fig. 3.13. The furnace was built based on a cylinder-shaped furnace (CRFC-412, from Omegalux®, 100 mm I.D., 200 mm O.D., with the maximum working temperature of 1000°C). The furnace is held inside an aluminium tube (5 mm wall thickness) casing with stainless steel cap and bottom plate. Ceramic fibres were filled into the gap between the furnace and the aluminium tube casing for insulation. A Duratec plate set on top of a Duratec rod was used to hold a small crucible (a quartz beaker in this case) for melting the metal alloys. The furnace is mounted onto a stainless steel jack, and therefore it is convenient to lift up the furnace to melt the alloy in the centre of the furnace, and then move the furnace down to expose the crucible and allow the quartz tube to be immerged into the melt within crucible for sucking the liquid metal via the vacuum filling system.

After casting, the rod bars (~110 mm long) were cut into 50 mm long and a 4 mm diameter hole was drilled along the centre of the bars to allow the sonotrode to go through the rod bars to facilitate the setting up of the rod bars inside the quartz tubes during the in situ experiments.

3.3.4 Cartridge heater furnace

A special cartridge heater furnace was designed and made for melting the rod bars contained inside either the Duratec or quartz sample containers during the in situ experiments.

Fig. 3.14a-c shows the furnace assembly, the sample containers and the sonotrode for the in situ experiments. The furnace consists of six plates machined from the Duratec 750 materials, including 1 front plate and 1 back plate with the same dimension of 120 mm (width) × 120 mm (height) × 20 mm (thickness); and 2 side plates with the same dimension of 35 mm (width) × 120 mm (height) × 20 mm (thickness) on each side. Holes of 10 mm in diameter were drilled through the thickness of the plates to accommodate six cartridge heaters with 2 seated inside the front plate, 2 inside the back plate, and 1 inside each of the side plates. Each cartridge heater is 9 mm in diameter and 52 mm long with a heating power of 300 W. The plates can be flexibly assembled around the sample containers (either a Duratc mould or a quartz tube) to form a rectangular enclosure to act as a furnace. The six cartridge heaters can deliver a heat power of 1.8 kW and heat the samples to 1073 K without difficulty. Two slot windows (5 mm wide and 30 mm long) were machined along the central symmetrical lines of the front and back plates to allow X-ray to pass through the furnace and focus onto the liquid alloys held inside the sample containers.

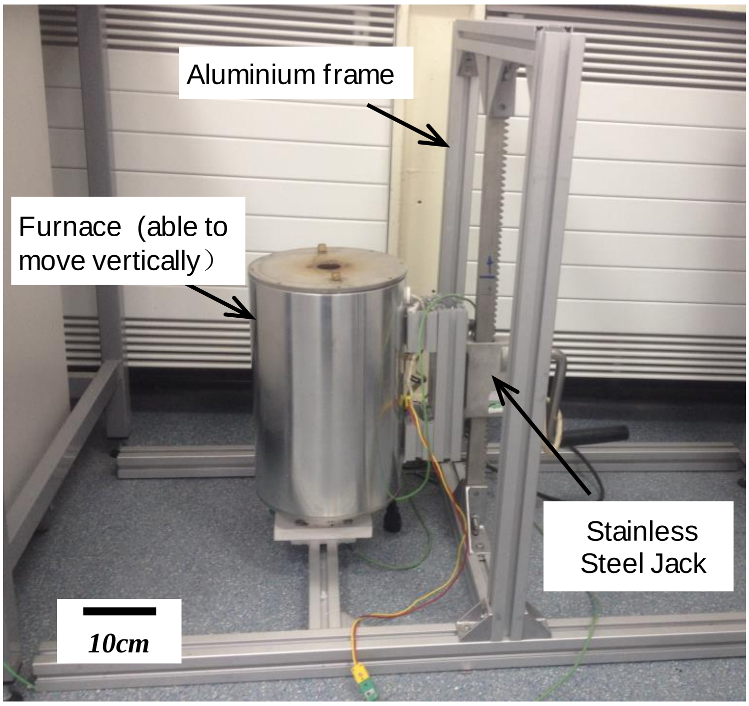

(a)

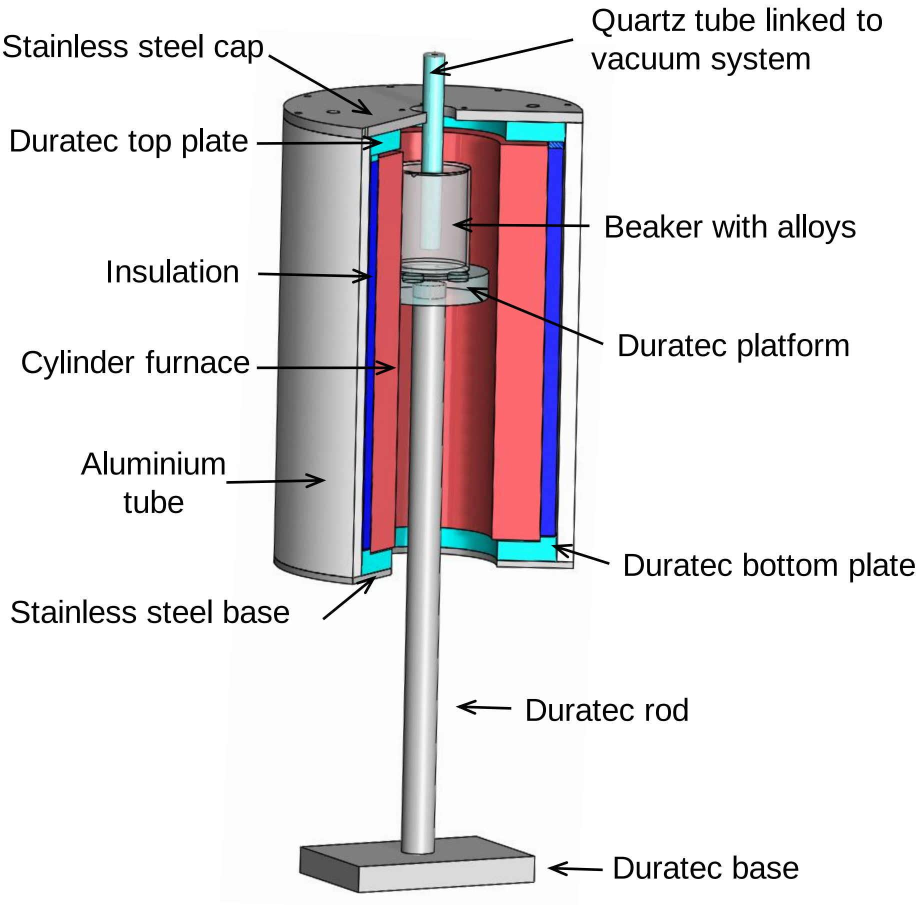

(b)

Fig. 3.13. (a) A photo of a custom designed and made furnace (b) a sectional view of the furnace.

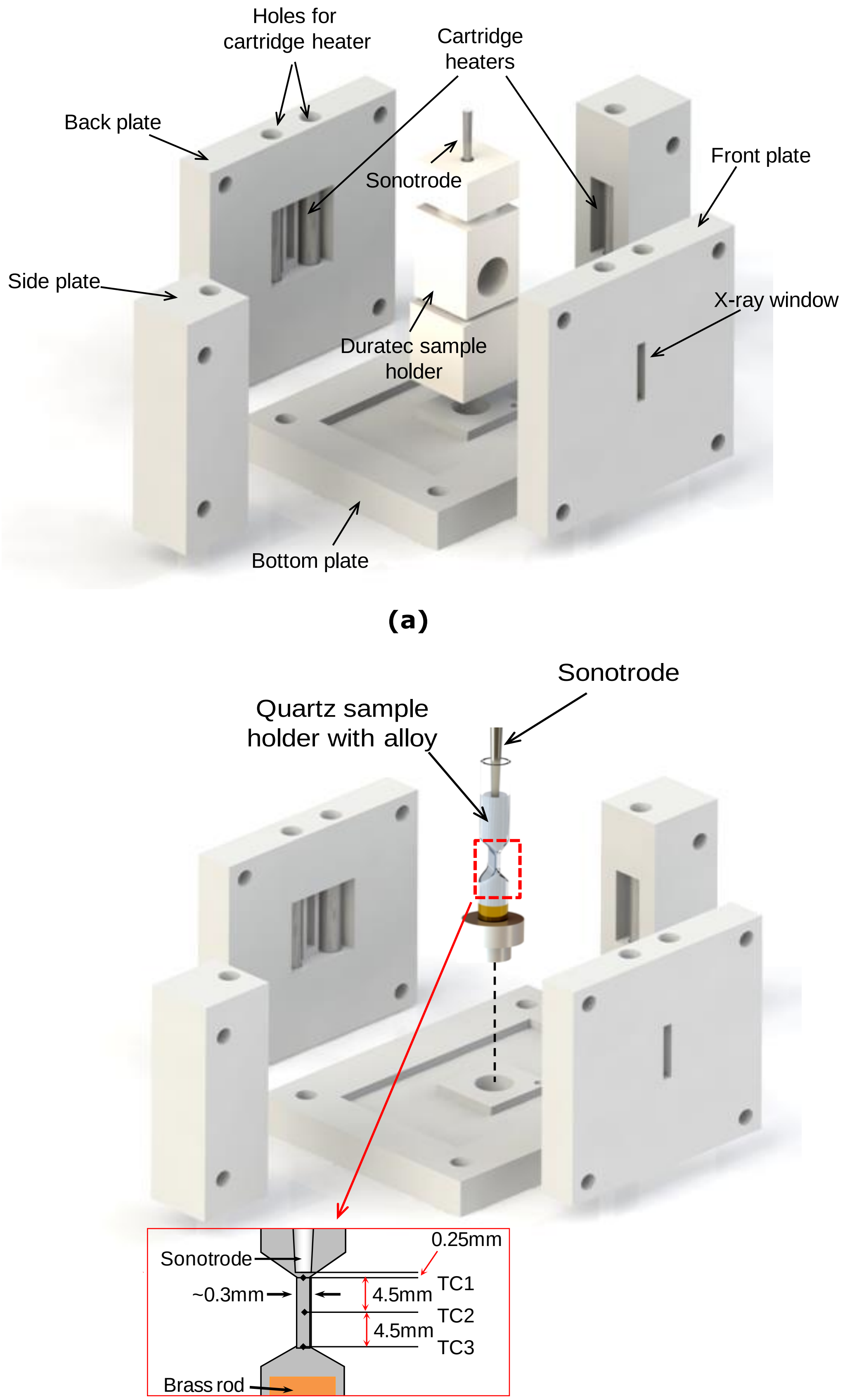

(a)

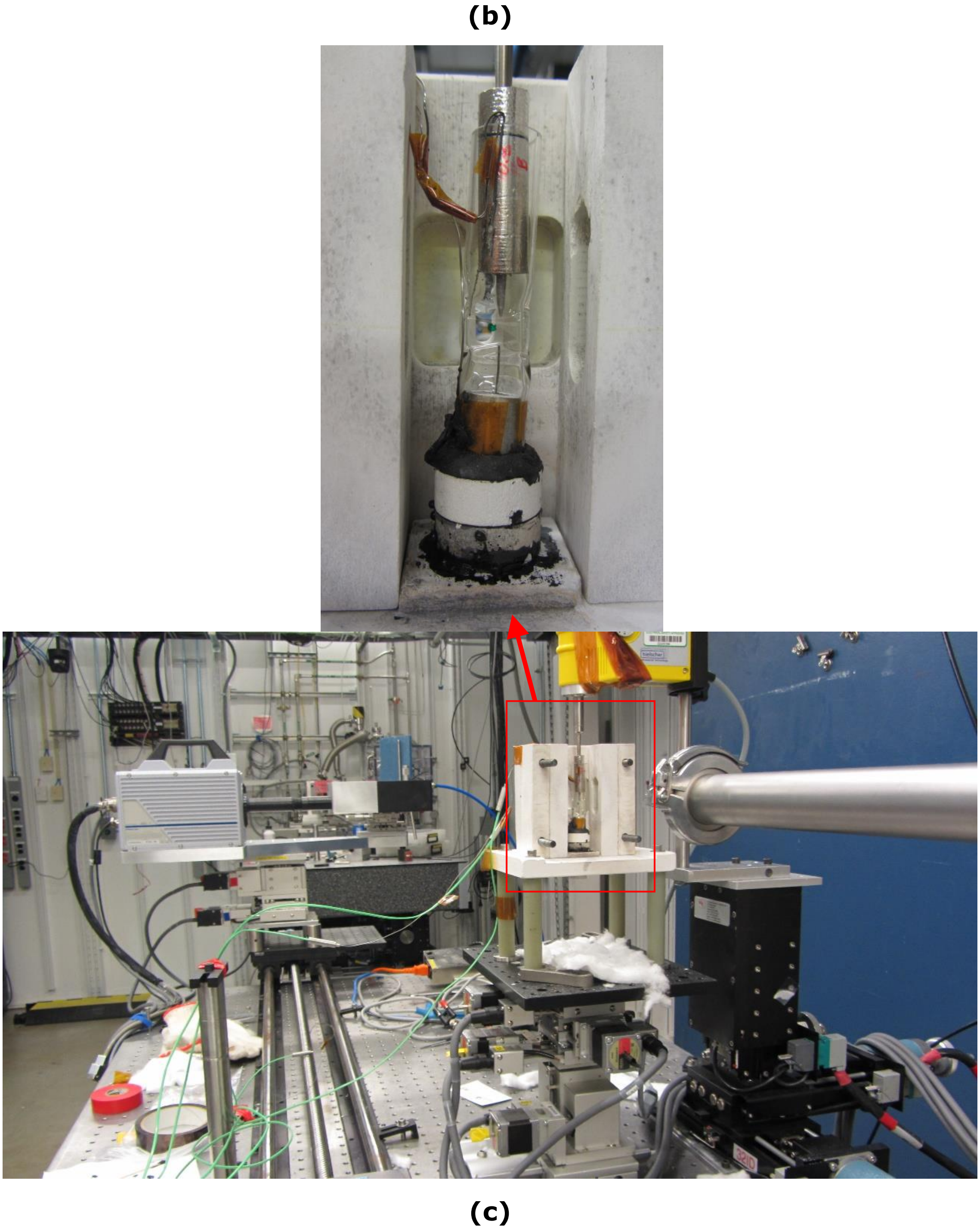

Fig. 3.14.** 3-D drawings of the furnace with (a) the Duratec sample container or (b) the quartz sample container, and the insert is a 2-D sketch, highlighting the quartz sample container and the 300 μm thin channel in the middle. Three K-type thermocouples (TC1, TC2, and TC3) were positioned at the top, middle and bottom of the thin channel to measure the temperatures of the liquid metal during melting and solidification. (c) A photo of the assembled furnace, sample container and sample on the stage at APS. The detailed dimension of each part of the furnace is **in Appendix

2.

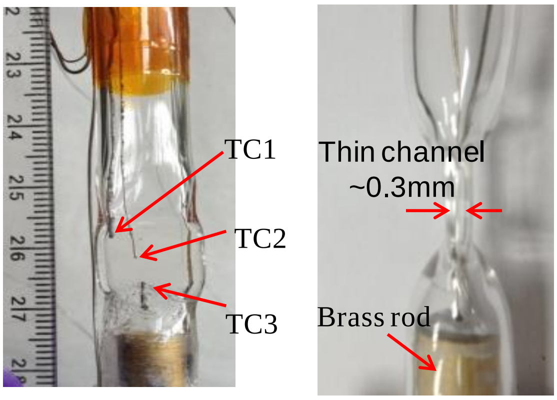

Fig. 3.15. *Photos of the front view (left) and side view (right) of the quartz sample container with a thin channel of ~300 μm in the middle section. Three thermocouples (TC1, TC2, TC3) are set at the top, middle and bottom of the thin channel.*

The cartridge heaters accommodated in the furnace was controlled by using a temperature controller (Engineering CN8201-DC1 Temperature & Process Controller, from Omega$^{®}$), with an accuracy of 1°C. In order to obtain the accurate temperature distribution of the sample, three K-type thermocouples (Ø 250 μm or Ø 500 μm sheathed by stainless steel, from Omega$^{®}$) were placed at the top (TC1, Ø250μm), middle (TC2, Ø250μm) and bottom (TC3, Ø500μm) positions of the thin channel (Fig. 3.15) to monitor and record the temperatures of the alloys during melting and cooling operations. The data was logged into an 8-channel Pico data logger, and recoded into a laptop computer. The time intervals for data acquisition used were either 1 ms or 1 s. The desired temperature gradient in the alloy inside the thin channel was controlled by (1) adjusting the position of the quartz container relative to the cartridge heaters, and (2) placing a cold brass rod (ф9 × 15 mm) below the thin channel as a heat sink (Fig. 3.15).

The detailed dimension of each part of the furnace is **in Appendix 2**.

3.3.5 Ultrasound processor and sonotrodes

An UP100H ultrasound processor (Fig. 3.16a) made by Hielscher^{TM} was used in the experiment. It has a fixed frequency of 30 kHz, and adjustable input power of 0 – 100 W with a maximum acoustic power density of 600 W/cm^2. Sonotrodes of 74 mm long with different tip diameter of 0.5, 1, 2 (Fig. 3.16b) were used and positioned at the wedge area above the thin channel (Fig. 3.14c insert) to transmit ultrasonic waves into the liquid metal held inside the thin channel. The detailed specification of the UP100H ultrasonic processor and the sonotrodes are listed in Table. 3.3.

(a) **(b)**

Fig. 3.16. *(a) A photo of the UP100H ultrasound processor (from Hielscher Ultrasonics GmbH) used in the experiments, and (b) the sonotrode with 0.5 mm, 1 mm, and 2 mm tip diameters.*

Table. 3.3. *The specification of the UP100H ultrasonic processor and the sonotrodes.*

Sonotrode	**Power (W)**	**Max. submerged depth (mm)**	**Tip diameter (mm)**	**Max. amplitude (µm)**	**Acoustic power density (W/cm^2)**
MS0.5 Micro tip 0.5	20-100W	5	0.5	140	125
MS1	20-100W	5	1	140	125

Micro tip 1					
MS2 Micro tip 2	20-100W	30	2	220	600

3.4. In situ synchrotron X-ray imaging experiments

3.4.1. Set-up of the experimental apparatus

The set-up of the experimental apparatus (the furnace with Cartridge heaters, the quartz container holding metal alloy, the sonotrode and ultrasound processor) on the sample table of the sector 32-ID-B of APS is shown in Fig. 3.17a. The quartz sample container with the sontorde is highlighted in the schematic diagram below (Fig. 3.17b). The furnace was supported by 4 ceramic pillars that were mounted onto the sample table, and this arrangement prevents any possible overheating of the sample table. The table is driven by multiple precision motors and can travel in x, y, z directions with a spatial resolution of 1 μm. The ultrasound processor with the sonotrode was mounted on a precision linear stage (T-LSR075A, 75mm travel, ± 12 μm accuracy, from Zaber), and its vertical movement is independent to that of the sample table, facilitating the focus of the X-ray beam either at the tip of the sonotrodes or at the area of interest within the thin channel.

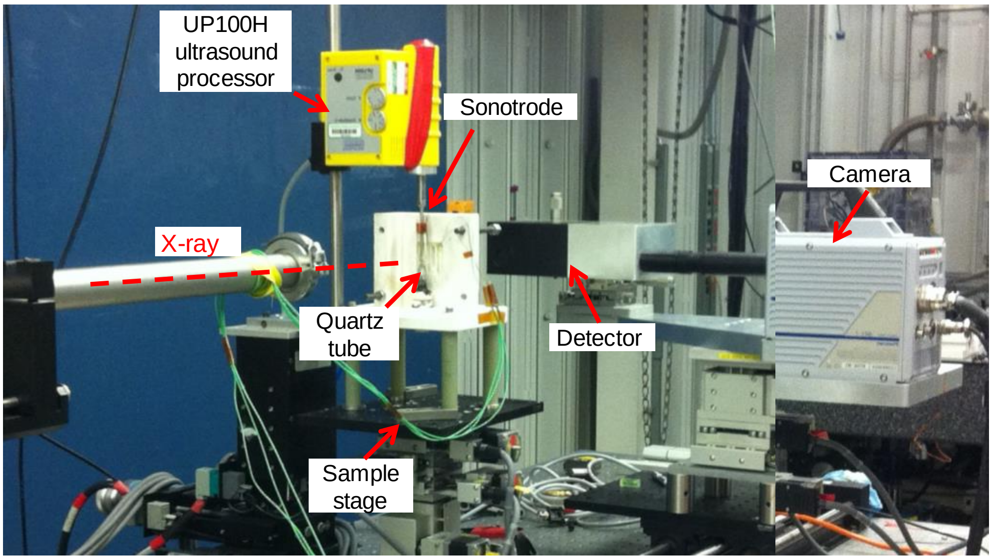

(a)

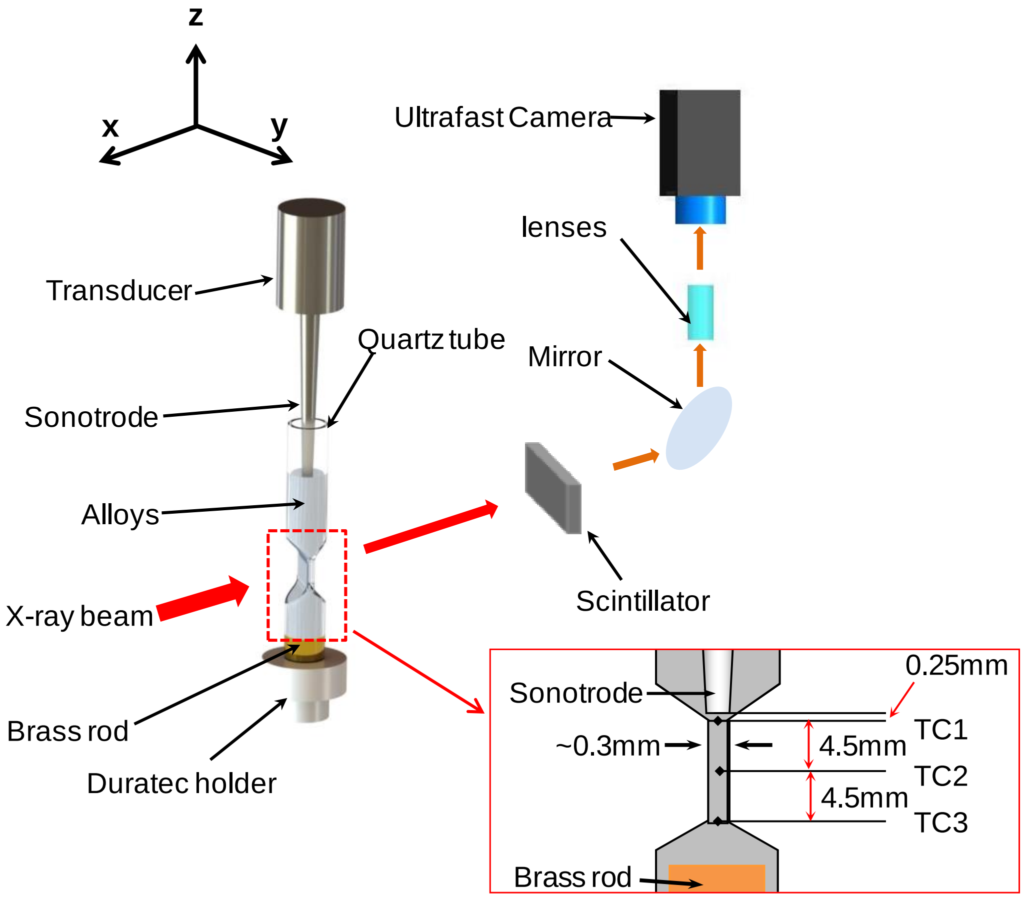

(b)

Fig. 3.17. *(a) A photo and (b) a 3-D schematic diagram, showing the experimental set-up at the sector 32-ID-B of APS. The insert is a 2-D sketch, highlighting the quartz sample container and the 300 μm thin channel in the middle. Three K-type thermocouples (TC1, TC2, and TC3) were positioned at the top, middle and bottom of the thin channel to measure the temperatures of the liquid metal during melting and solidification.*

3.4.2. The X-rays and optimal parameters for imaging

3.4.2.1 The X-rays and ultrafast imaging at sector 32-ID-B

At sector 32-ID-B, the X-ray energy and flux are controlled by the undulator gap as explained in section 3.1.1. Table 3.4 lists the commonly used undulator gaps and the resulting X-rays in terms of the peak irradiance, the most intensive X-ray energy, its bandwidth and its harmonic number. Fig. 3.18

shows the full X-ray spectra of four different undulator gaps, i.e. 11, 18, 27, 31 mm. Clearly, the X-ray spectrum from the 18 mm undulator gap is very different to that of the 27 mm gap. For the 18 mm gap, most of the X-ray intensity is located within the first harmonic around 7.7 keV with the peak irradiance of 3.4 × 10^{14} photon/s/mm^2/0.1%bw, and a bandwidth of 0.4 keV full-width at half-maximum (FWHM). While for the 27 mm gap, the most intensive X-ray occurs at the first harmonic around 12.2 keV. Its peak irradiance is 1.45 × 10^{14} photon/s/mm^2/0.1%bw, and the bandwidth is 0.35 keV FWHM.

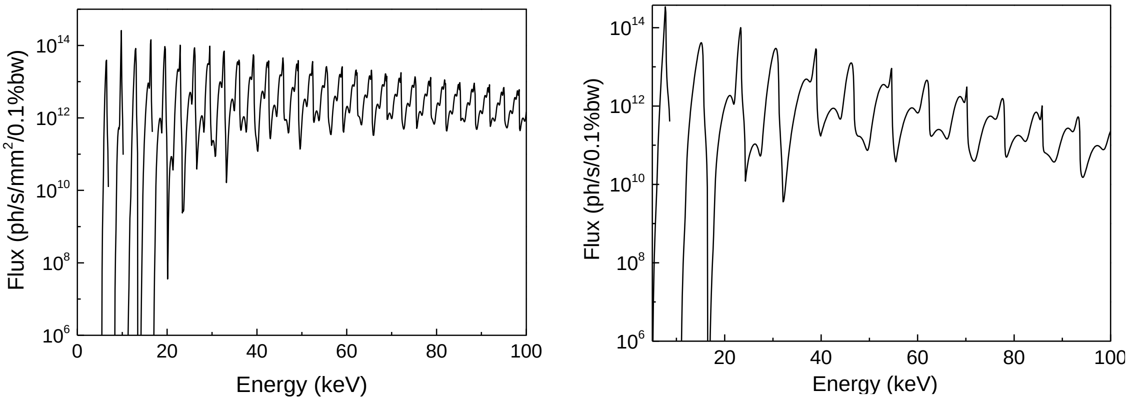

(a) 11 mm undulator gap

(b) 18 mm undulator gap

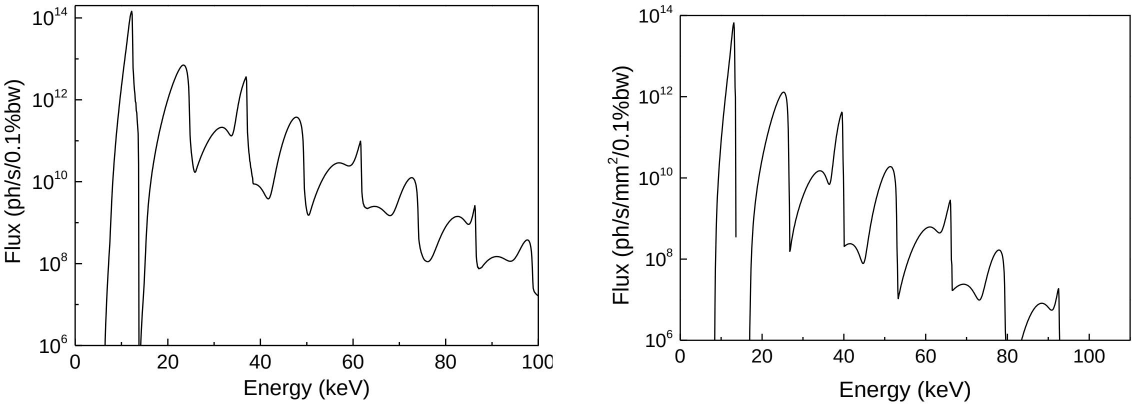

(c) 27 mm undulator gap

(d) 31 mm undulator gap

Fig. 3.18. *The X-ray spectrum produced by the undulator gap of (a) 11 mm, (b) 18 mm, (c) 27 mm and (d) 31 mm at sector 32-ID-B of APS.*

Table.3.4. *The characteristics of the X-rays (white beam) produced by the different undulator gaps at sector 32-ID-B of APS*

Undulator gap (mm)	Peak irradiance (10^{14} ph/s/mm^2/0.1%bw)	Peak Energy (keV)	Peak Harmonic No.	Bandwidth at FWHM (keV)
11	2.59	9.8	2nd	0.2
14	4.22	5.04	1st	0.3
17	3.59	7	1st	0.35
18	3.4	7.7	1st	0.4
19	3.52	8.4	1st	0.35
20	3.47	9	1st	0.3
25	1.9	11.5	1st	0.4
27	1.45	12.2	1st	0.35
31	0.7	13.3	first	0.3

The white beams produced by the undulator gaps from 14 to 28 mm were tested for imaging the liquid Bi-8%Zn, water and silicone oil samples. Based on these tests, it was found that the optimal images were obtained for Liquid Bi-8%Zn using 18 mm gap, for water and silicon oil using 27 mm gap; and the full spectra of the white beams for both gaps are showed in Fig. 3.18b and c. Both were used in the subsequent experiments, and they are very intense and powerful X-rays. Hence, a millisecond fast shutter was placed upstream of the X-ray path to manage the intense heat load generated by the white beam, allowing only few tens of milliseconds exposure of the white beam onto the samples when acquiring images to avoid overheating the samples [177, 185].

Fig. 3.19 shows that, using a view field of 1 × 1 mm (1024 × 1024 pixels), the spatial resolution is calibrated at ~1 μm / pixel. The images sequences were acquired using a fast scintillator crystal (LYSO:Ce) detector and recorded by a Photron FASTCAM SA1.1 camera (Fig. 3.17b). In order to achieve the best spatial resolution and phase contrast, the sample-to-detector distance (the distance between the sample and scintillator as showed in Fig. 3.19b) was tested for the different sample materials used in the experiments. Table. 3.5 summaries the optimised sample-to-detector distances for those materials used. The objective lens used at sector 32-ID-B is 10x. Calibration of the images made by using the standard calibrant (Fig. 3.19) indicates that the spatial resolution of 1μm/pixel in a view field of 1024×1024 μm can be achieved at the image acquisition rate of 5413 fps. The field of view becomes smaller when a higher image acquisition rate is used due to the limited data readout speed of the camera. The size of the field of view (the image size), exposure time and resolution under the different image acquisition rates are listed in Table. 3.6 for the imaging experiments at APS and DLS.

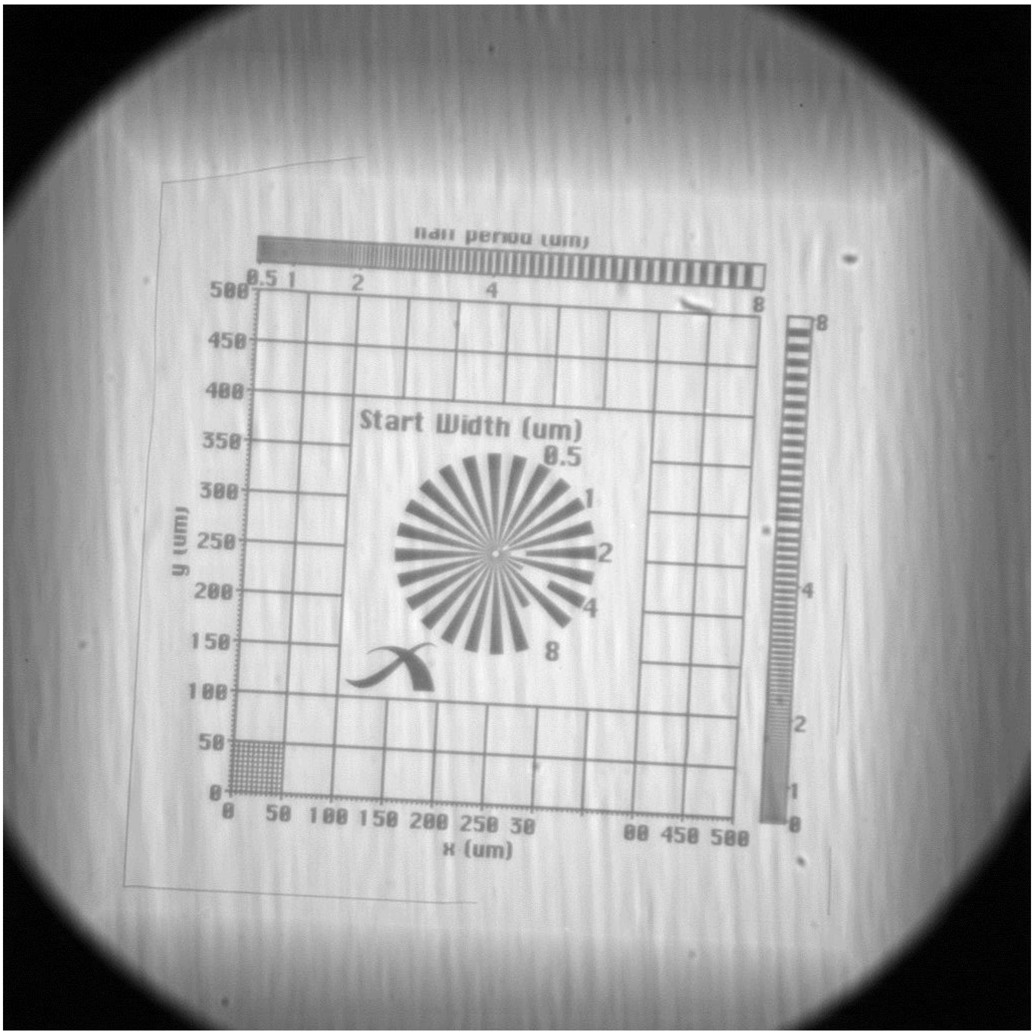

Fig. 3.19. *A calibration of the X-ray image made using a standard calibrant for the ultrafast imaging experiments at sector 32-ID-B of APS. The image is captured by using white beam with a 10x optical objective lens.*

Table. 3.5. *The optimised sample-to-detector distance (SDD) for imaging the different sample materials in the experiments at APS and DLS*

Beamline	X-ray beam	Sample materials	Sample-to-detector distance (mm)
32-ID-B APS	White	Water	200
		Water mixed with Ge particles	150
		Silicone oil	200
		Sn-13%Bi	980
		Bi-8%Zn	980
I12 DLS	Monochromatic	Bi-8%Zn	900
		Sn-13%Bi	
	White	Bi-8%Zn	
		Sn-13%Bi	

3.4.2.2 The X-rays and high speed imaging at I12

At I12, both white beam and monochromatic beam were used. The white beam contains the full spectrum of the X-rays delivered by the storage ring as showed in Fig. 3.20a (with 6mm Cu filter). Theoretically, the X-ray energy used in our experiment is from 50 keV to 3 GeV, but in reality, the energy from 50 keV to 300 keV is useful because the flux of the X-rays with the energy > 300 keV is too low to penetrate the samples. Compared to sector 32-ID-B, different method is used at I12 to manage the heat load produced by the white beam. In addition to the fixed filters (one 2.2 mm diamond plus one 5.5 mm SiC filters) along the X-ray path, 6 mm thick Cu filters (2 mm + 4 mm) were added upstream to reduce the intensity of the white beam to be projected onto the samples, allowing longer exposure times to be used without heating and damaging the samples [169]. The white beam energy spectrum after filtered by 6 mm Cu plate is shown in Fig. 3.20a, and compared to the energy spectra of the X-rays at 32-ID-B (Fig. 3.18), the wiggler insertion device at I12 delivers X-rays of continuous energy profile. Monochromatic beam was also used in the imaging experiments, and its beam energy profile is shownin Fig. 3.20b.

Table. 3.6. *The objective lenses and the imaging parameters used in the experiments at APS and DLS*

Beamline	X-ray beam	The objective lens	Acquisition rate (fps)	Field of view (pixel)	Exposure time (μs)	Resolution (μm/pixel)
32-ID-B APS	White	10x	271,554	128 x 64	0.5	1
		10x	135,781	192 x 128		
		10x	30,173	448 x 384		
		10x	5,413	1024 x 1024		
I12 DLS	Monochromatic	5x	30	800 x 600	33000	12.2
	White	5x	1000	544 x 440	990	
	White	5x	1500	544 x 440	660	

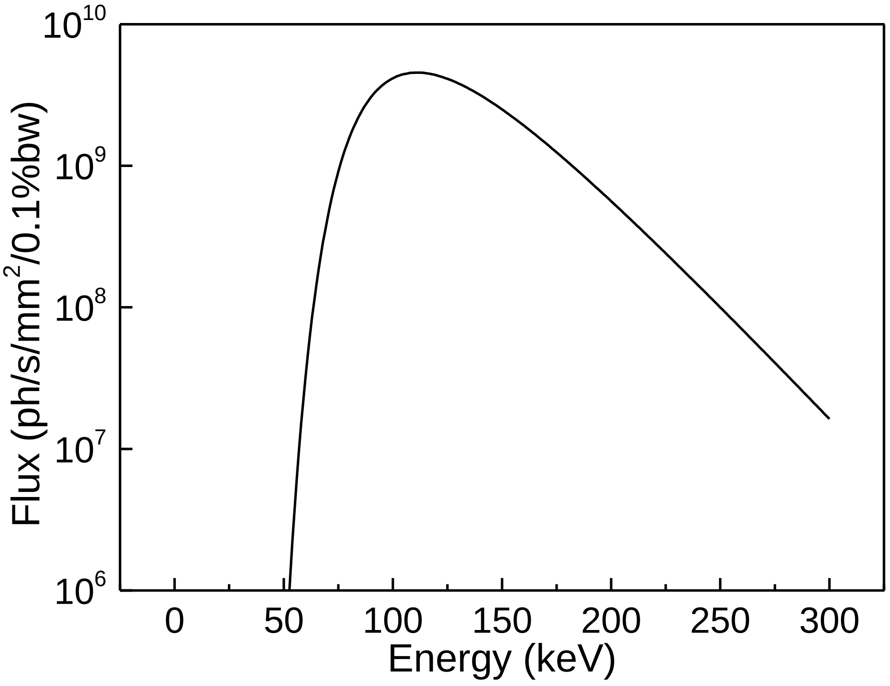

(a)

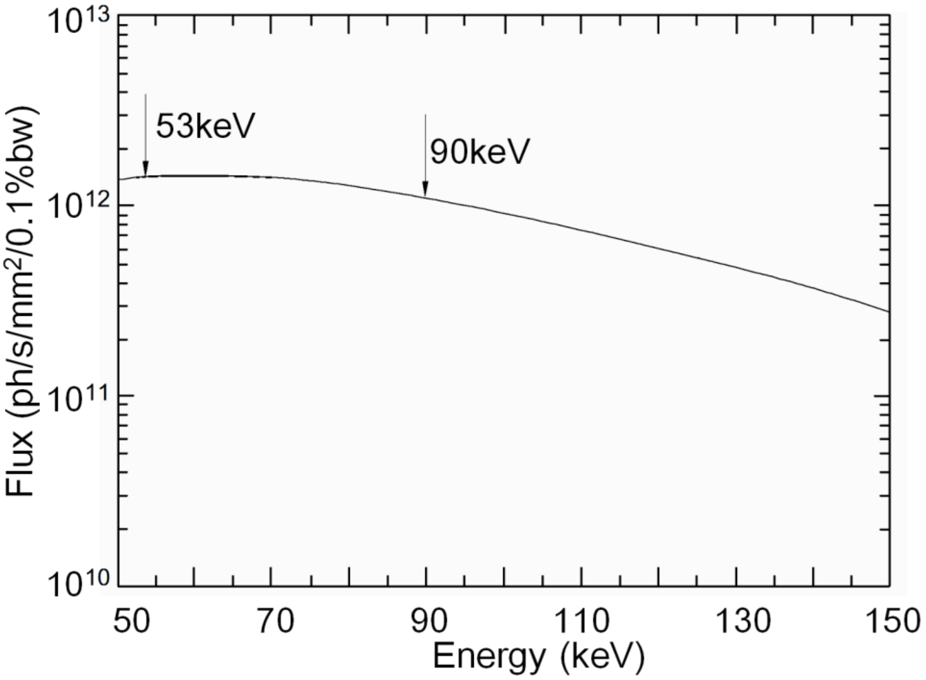

(b)

Fig. 3.20. *(a) The calculated white beam intensity profile at I12 after filtered by 6mm Cu plate (the electron current in the storage ring is 300 mA). (b) The calculated monochromatic beam intensity profile at the sample position with 1x1 mm beam size.*

Because the sample thickness is fixed at 300 μm, we can use the linear attenuation coefficients of the different elements in the alloys to select the optimal energy to achieve the maximum absorption contrast for imaging. For example, Fig. 3.21 shows the linear absorption coefficients for Bi and Zn in the energy range of 50-150 keV. Apparently, the biggest difference in the linear attenuation coefficient of Bi and Zn occurs at around 50 keV (~62 cm^{-1}), and ~90 keV (~68 cm^{-1}) where the absorption edge of Bi occurs.

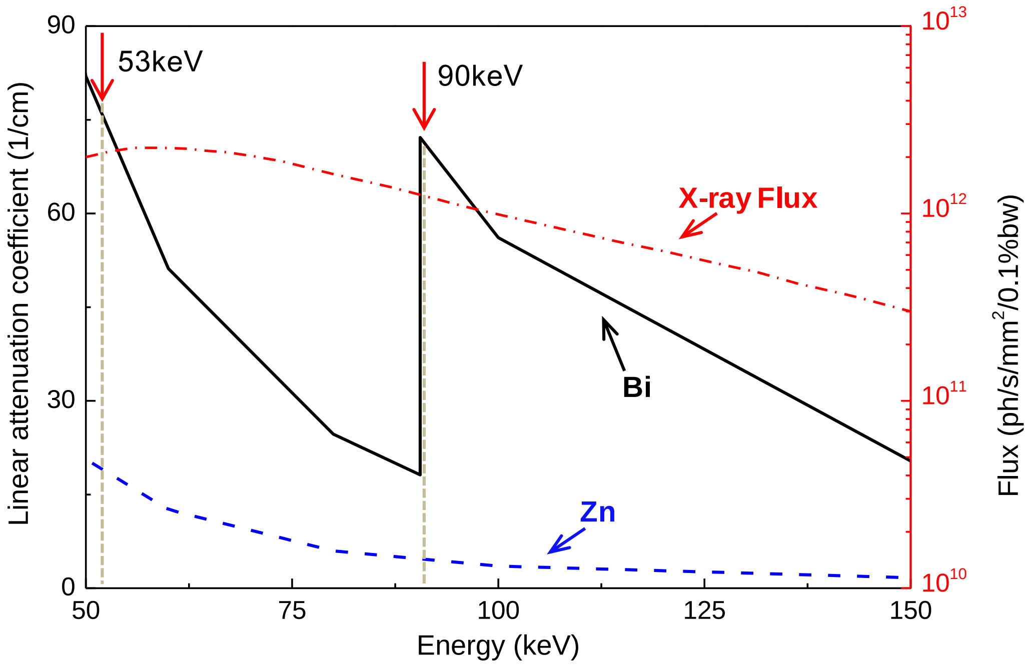

Fig. 3.21. *The X-ray absorption coefficient of Bi and Zn, and the X-ray flux of the monochromatic beam at I12 in the energy range of 50 to 150 keV.*

Hence, X-ray energy of 50 keV, 53 keV, 90 keV were chosen to image a Bi-8%Zn sample of the thickness of 0.3mm. The sample was double-side polished to minimize the surface artifacts. Fig. 3.22 shows that monochromatic beam of 53 KeV give an image with the best contrast. Hence, when monochromatic beam is used in the subsequent experiments, 53 KeV was chosen for imaging. More importantly, at around 53 KeV, the maximum X-ray flux (~2 x 10^{12} ph/s/mm^2/0.1%bw) is reached, a condition desired for imaging at high speed. At I12, the image detector is a 700 μm thick Lutetium Aluminium Garnet detector, doped with Cerium (LuAG:Ce). A Phantom^{TM} V7.3 high speed camera was used to record the images. The sample-to-detector distance was set at 900 mm. The flexible swap between different viewing fields (from 23 mm × 12 mm to 1.8 mm × 1.3 mm with a spatial resolution from 29.7 to 2.2 μm/pixel) at JEEP made it a suitable system to study the behaviour of fluid flow and their interactions with the solid and semisolid phases during solidification.

3.4.3 Synchronisation of ultrasound and image acquisition

At 32-ID-B, the synchronisation of the switching (on or off) and the duration of the ultrasound with the open or close of the X-ray shutter and the high speed camera is made via the trigger signals generated using a Stanford DG535 delay generator. The ultrasound was switched on 7 ms after the solenoid shutter was fully opened, and switched off 4 ms before the shutter started to close. In this way, the images before switching on ultrasound and those after switching off can be captured. In each acquisition, images sequences of ~33 ms duration were captured.

At I12, the synchronisation was controlled by a custom-made relay apparatus (designed and made by the electrical technician, Mr. Peter Lobokazinczi of School of Engineering, University of Hull) operated from the control room (the photos of the relay apparatus are showed in Fig. 3.23a). The trigger signals to the high speed camera and ultrasound generator is shown in Fig. 3.23b. Two time delay periods, D1 and D2 were used. D1 is the duration when ultrasound is switched on at t_2 after the camera is turned on at t_1, and D1 can be adjusted in the range from 0 to 1000 ms. D2 is the duration after the ultrasound is off at t_3 and before the camera is turned off at t_4. D2 can be adjusted between 0 and 100 sec. Using these trigger signals, the synchronization of ultrasound and the imaging acquisition can be achieved.

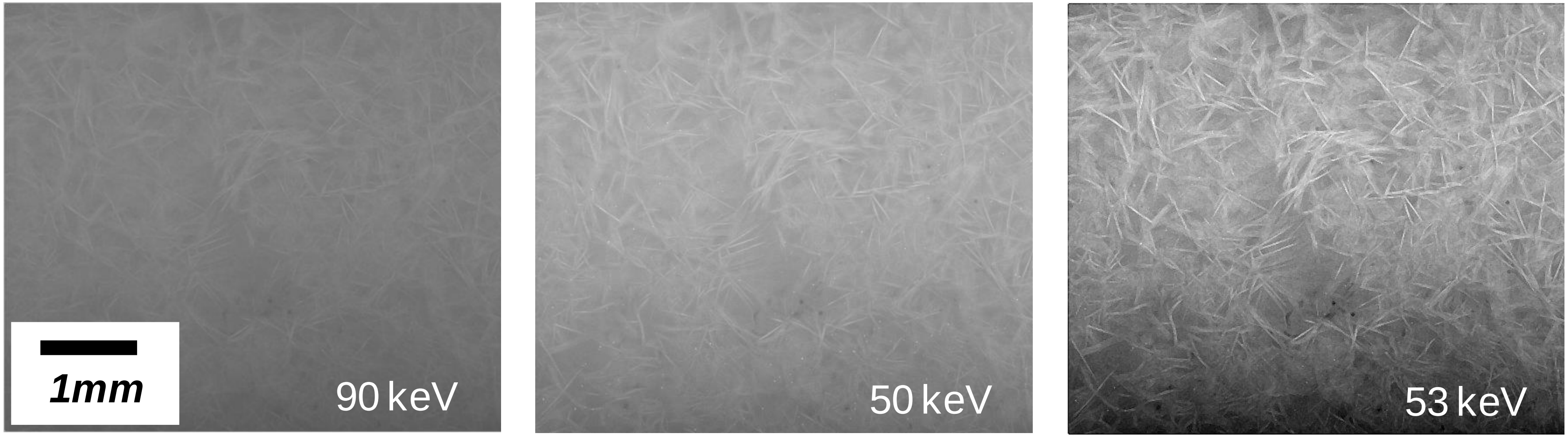

(a) **(b)** **(c)**

Fig. 3.22. *X-ray images of a double-side polished Bi-8%Zn sample with 0.3 mm thickness taken using monochromatic beam of the energy of (a) 90 keV, (b) 50 keV and (a) 53 keV at I12 of DLS. All the images were taken at 1000 fps.*

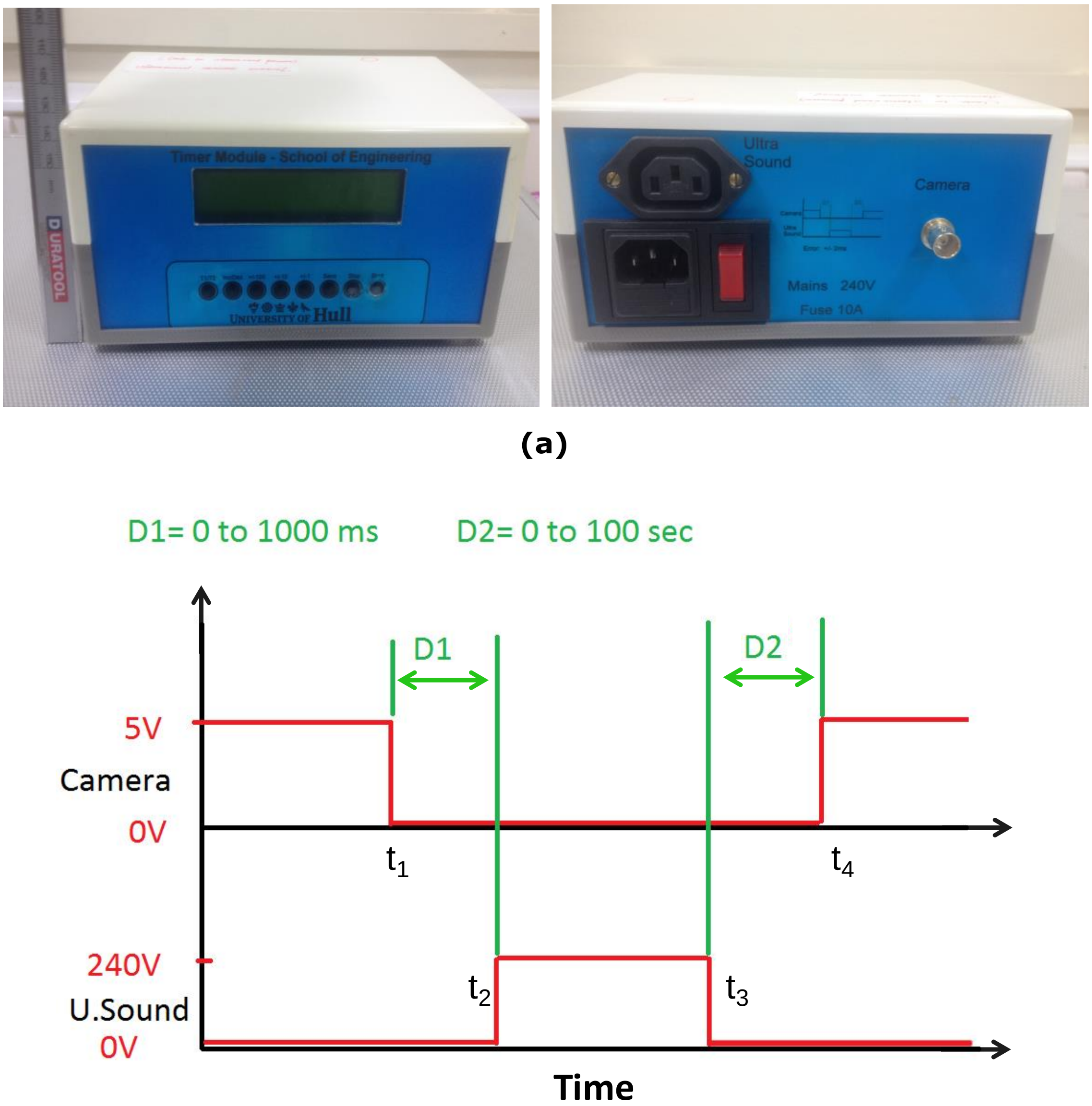

(a)

(b)

Fig. 3.23. *(a) photos of the front view (left) and back view (right) of the relay box, and (b) time sequence of the trigger signals for the synchronisation of the ultrasound and the imaging.*

3.5 Summary

This chapter describes the synchrotron X-ray beamlines used and the experimental apparatus developed for the in situ imaging experiments. The characteristics of the X-rays produced at sector 32-ID-B of APS and I12 of DLS are presented and analysed. The design, commissioning and set-up of the experimental apparatus and the optimal conditions for acquiring high speed images at both beamlines are also described in great details.

Chapter 4: The dynamics of ultrasonic bubbles

This chapter presents the real-time synchrotron X-ray images obtained from the in situ experimental studies of the highly dynamic behaviour of ultrasonic bubbles, including the nucleation, growth, oscillation, coalescence and violent implosion of a single bubble and the collective behaviour of many bubbles, i.e. a bubble cloud. Different liquids were used in the experiments, including water (a typical Newtonian fluid), silicone oil (a typical viscous polymer-type material), and liquid metals. The differences in densities, viscosities, surface tensions and sound velocities of the chosen materials (as listed in Table 3.2) allow the effects of the dominant physical properties on the dynamic behaviour of the ultrasonic bubbles to be investigated in great details. The images presented in this chapter were obtained at sector 32-ID-B of APS in 2011, 2012 and 2013 during the experiments detailed in Table 3.1, except that those for the Sn-30%Cu alloy were acquired at I12 of DLS in 2015.

4.1 Real-time observation of sonotrode tip vibration

When focusing the X-ray beam onto the sonotrode tip, the vibration of the sonotrode tip can be “seen” clearly using the ultrafast X-ray imaging capability at sector 32-ID-B of APS. For the fixed 30 kHz ultrasound in this research, using the fastest image acquisition rate, i.e. 271,554 fps, 9 images can be acquired in one wave period. Hence the up-and-down movement of the sontrode tip can be tracked with sufficient details. Fig. 4.1a shows 20 consecutive images for the sonotrode tip captured in water in two wave periods. From these images, the micrometre scale vibration (the up-and-down movement) of the sonotrode tip can be extracted (the numbered squares plotted in Fig. 4.1b). A sine wave function was used to fit those squares and the correlation coefficient is $R^2=0.9876$, confirming that the sonotrode tip vibrates exactly according to sine wave. These measured vibrating distances and the amplitude are very important for validating the Helmholtz equation (as described in Chapter 6) used for calculating the acoustic pressure which has a dominant effect on the dynamic behaviour of the ultrasonic bubbles as explained later in this and the following chapters. In some cases (especially for the cases in liquid metals), the view field (128 × 64 μm^2) at 271,554 fps is too small to capture the whole phenomena occur, hence the second fastest acquisition rate, 135,781fps, were used to give a bigger view field of 192 ×

128 μm^2. Fig. 4.2a shows a typical image series for the liquid metal containing the sonotrode tip. Although the data points that can be measured from the images in one wave period is reduced to a half, the comparison between the measurement and the sine wave (Fig. 4.2b, R^2=0.9892) indicates that, at this acquisition rate, the data points obtained are still enough for tracking the highly dynamic vibrating behaviour of the sonotrode tip. Fig.4.3 shows that the pressure wave follows a sine function as well, but has a phase shift of 180 compared to the tip mechanical movement, i.e. the lowest pressure P_{min} is at the highest tip position, while the highest pressure P_{max} is at the lowest tip position.

4.2 Nucleation of ultrasonic bubbles

Fig. 4.4a, b, d show three series of consecutive X-ray images, showing the nucleation and growth of ultrasonic bubbles. Fig. 4.4a and b are for water and silicone oil (271,554 fps), and the measured sonotrode positions are plotted in Fig. 4.4c together with the acoustic pressure wave. Fig. 4.4d is for Bi-8%Zn, and 135,781 fps was used to obtain a bigger view field because the bubbles in liquid metal are bigger; and the corresponding sonotrode positions and acoustic pressure wave are plotted in Fig. 4.4e.

From the 2nd image (a-2, b-2 and d-2) of each image sequence (Fig. 4.4), it clearly shows that a tiny bubble (pointed by the white arrow) appears at the sonotrode tip. The size of the bubble is measured as approximately 2 μm (in water), 3 μm (in silicone oil), and 8 μm (in Bi-8%Zn) in radius respectively. Because the spatial resolution of the imaging is 1 μm/pixel, these are the smallest possible features that the images can resolve. It is therefore logically to assume that the tiny bubbles showed in images a-2, b-2 and d-2 are actually growing out of the even smaller bubble nuclei occurred in the 1st images (a-1, b-1, d-1) which cannot be seen at the sonotrode tip due to the 1 μm/pixel spatial resolution. By observing many such videos and images, it is very confident to conclude that the sonotrode tip surface is a site for nucleating ultrasonic bubbles.

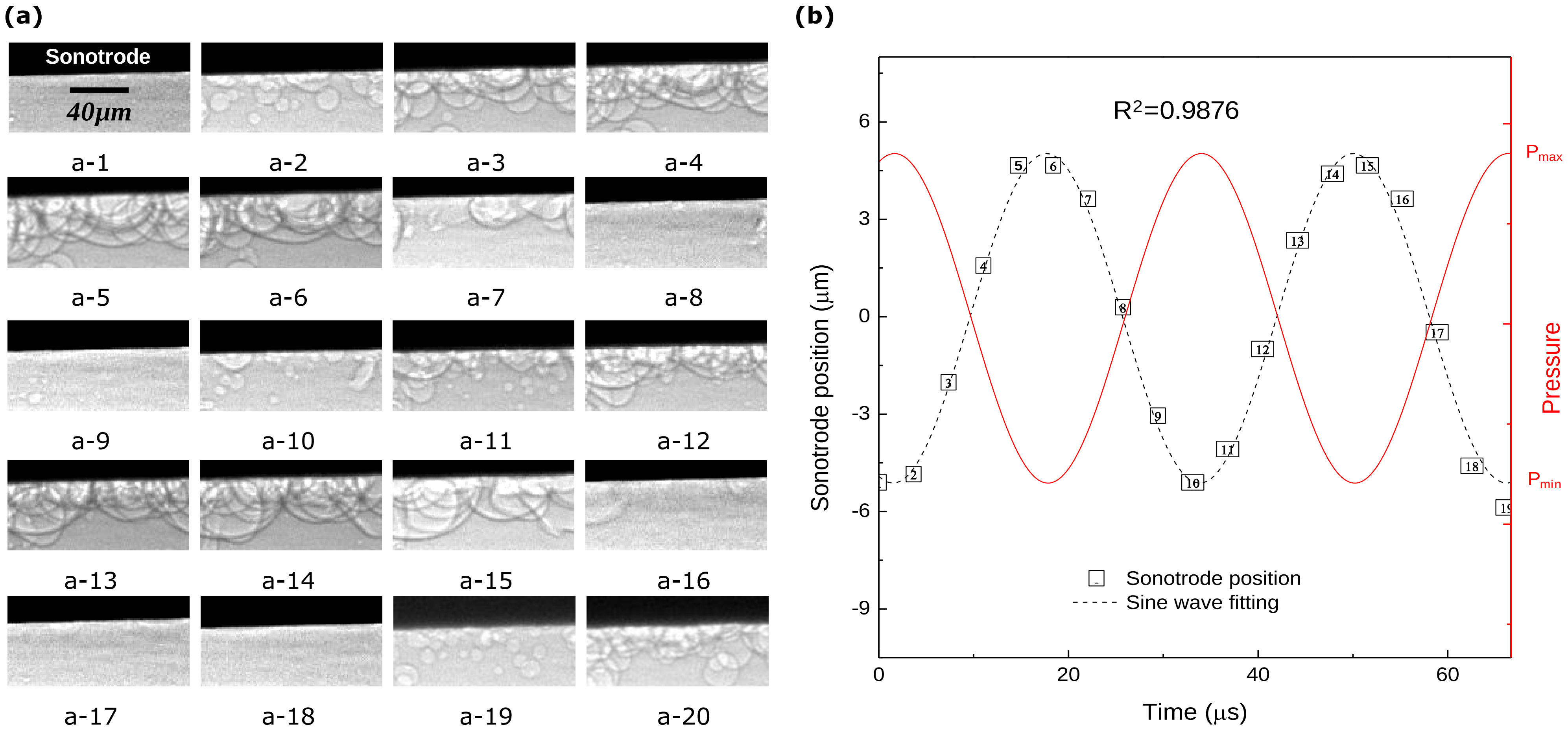

Fig. 4.1. *(a) Real time X-ray images captured in water using 271,554 fps, showing the up-and-down movement of the sonotrode tip. (b) The sonotrode positions measured from the images and fitted with a sine function; and the associated acoustic pressure wave.*

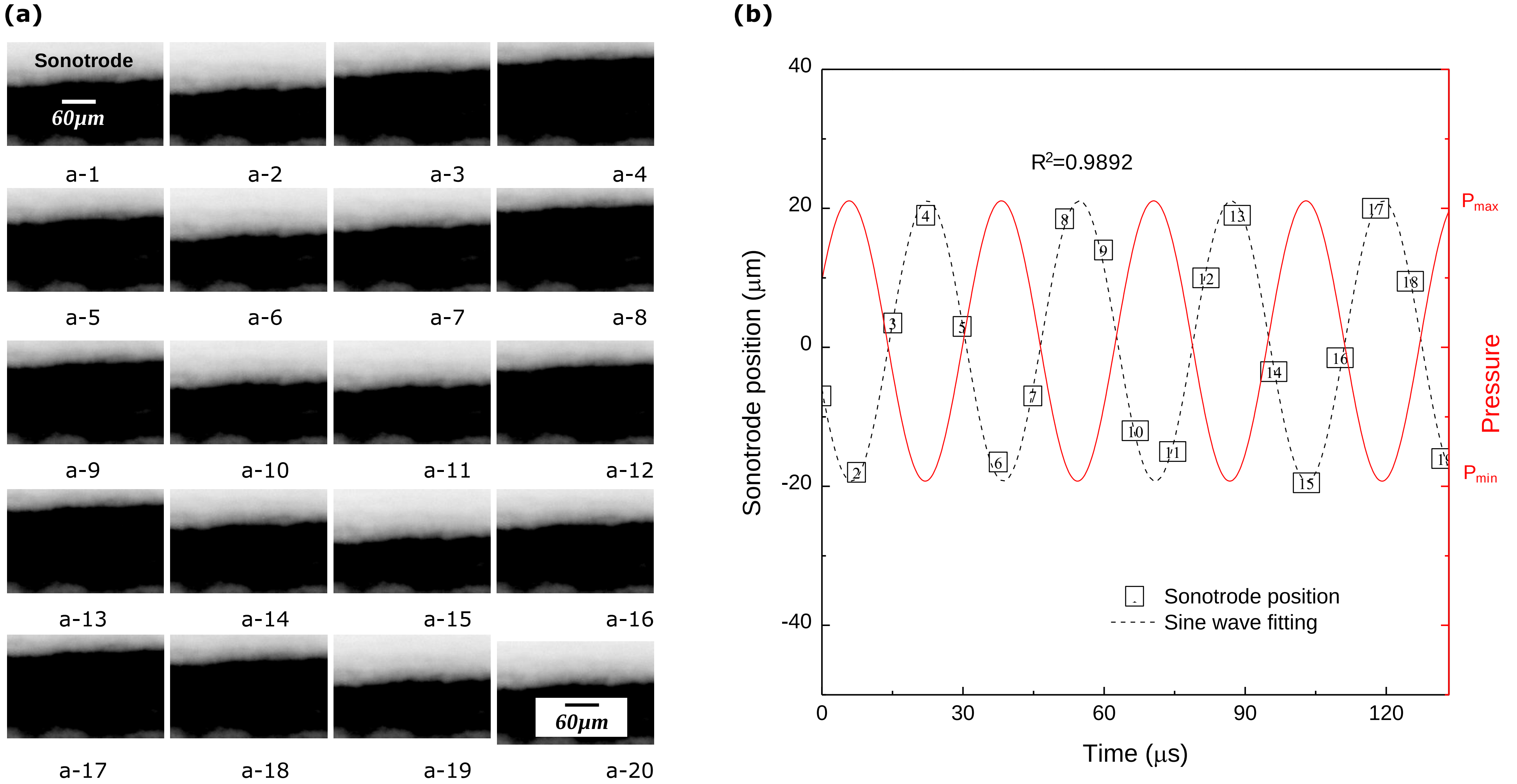

Fig. 4.2. *(a) X-ray images captured in Bi-8%Zn (700K) using 135,780 fps, showing the up-and-down movement of the sonotrode tip. (b) The sonotrode positions measured from the images and fitted with a sine function; and the associated acoustic pressure.*

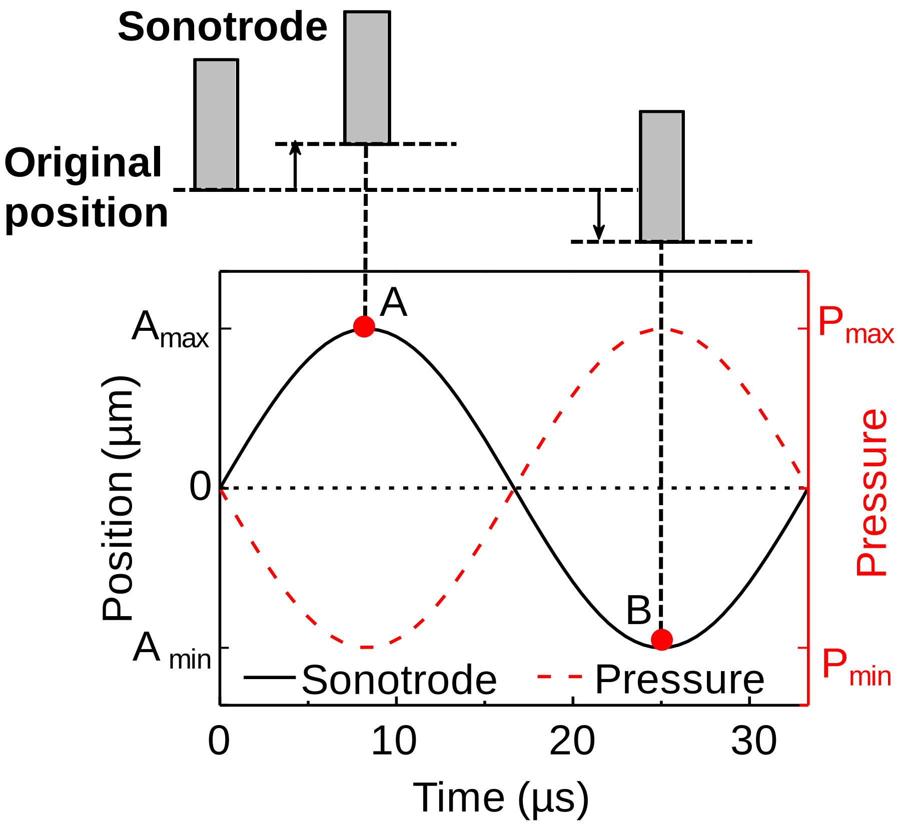

Fig. 4.3. *A sketch, showing the correlation between the sonotrode position and the resulting acoustic pressure at that position immediately below the sonotrode tip.*

From the 2nd to the 5th images (the 2nd to the 3rd for Bi-8%Zn), It can be seen that the nucleated bubbles grow during the half wave period when negative acoustic pressure is present because of the up-movement of the sonotrode. While a-6, b-6, and d-4 show that in the other half wave period when the positive acoustic pressure start to build up due to the down-movement of the sonotrode, the grown bubbles are compressed and imploded into a cluster of tiny bubbles, some of them disappearing (maybe due to the resolution limit) into the bulk liquid, and some of them observed to reattach to the sonotrode tip, acting as bubble nuclei for next cycle. Actually, the implosion of the grown bubbles creates many more number of tiny bubbles in the liquid than those started at the sonotrode surface. This is a very important phenomenon for the ultrasound induced bubbles and its mechanism will be further discussed in Chapter 7.

(a) In water, 271,554 fps

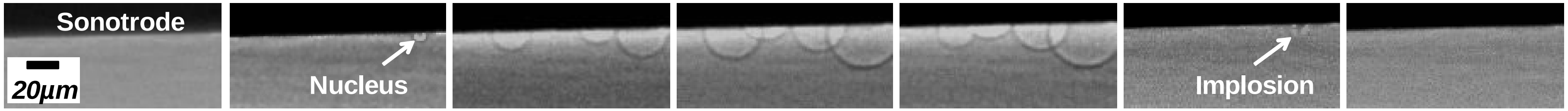

(a-1) 0 (a-2) 3.7 µs (a-3) 7.4 µs (a-4) 11.0 µs (a-5) 14.7 µs (a-6) 18.4 µs (a-7) 22.1 µs

(b) In Silicone oil, 271,554 fps

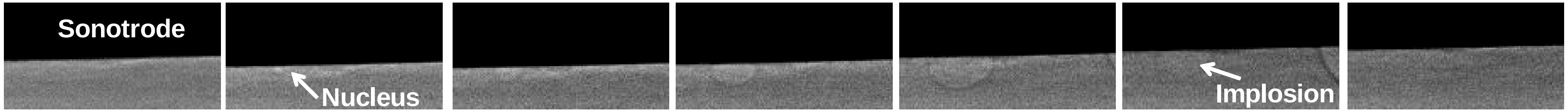

(b-1) 0 (b-2) 3.7 µs (b-3) 7.4 µs (b-4) 11.0 µs (b-5) 14.7 µs (b-6) 18.4 µs (b-7) 22.1 µs

(c) The sonotrode positions measured from the images showed in (a) and (b)

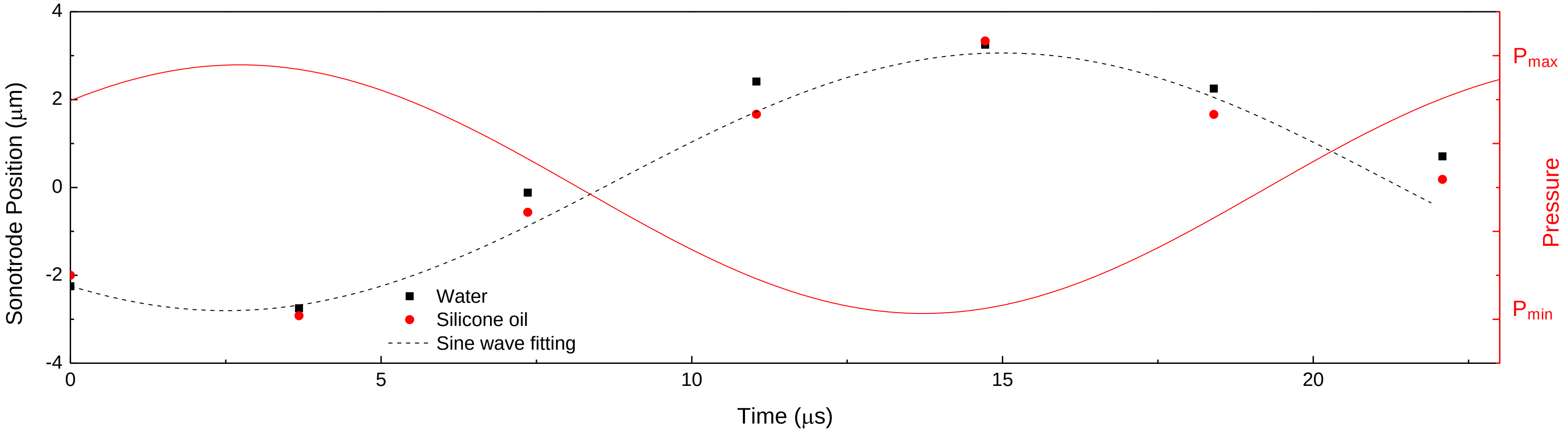

(d) In Bi-8%Zn, 135,780 fps

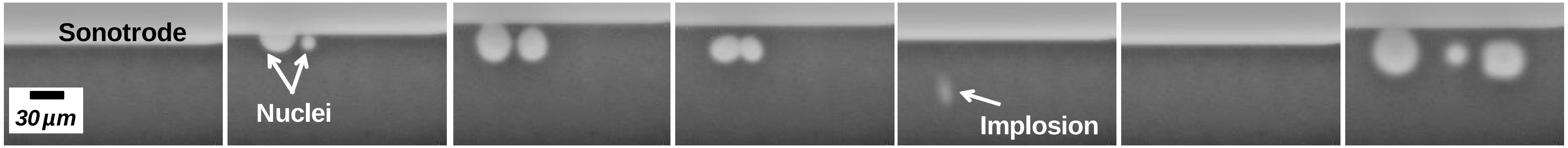

(d-1) 0 (d-2) 7.4 µs (d-3) 14.7 µs (d-4) 22.1 µs (d-5) 29.5 µs (d-6) 36.8 µs (d-7) 44.2 µs

(e) The sonotrode positions measured from the images showed in (d)

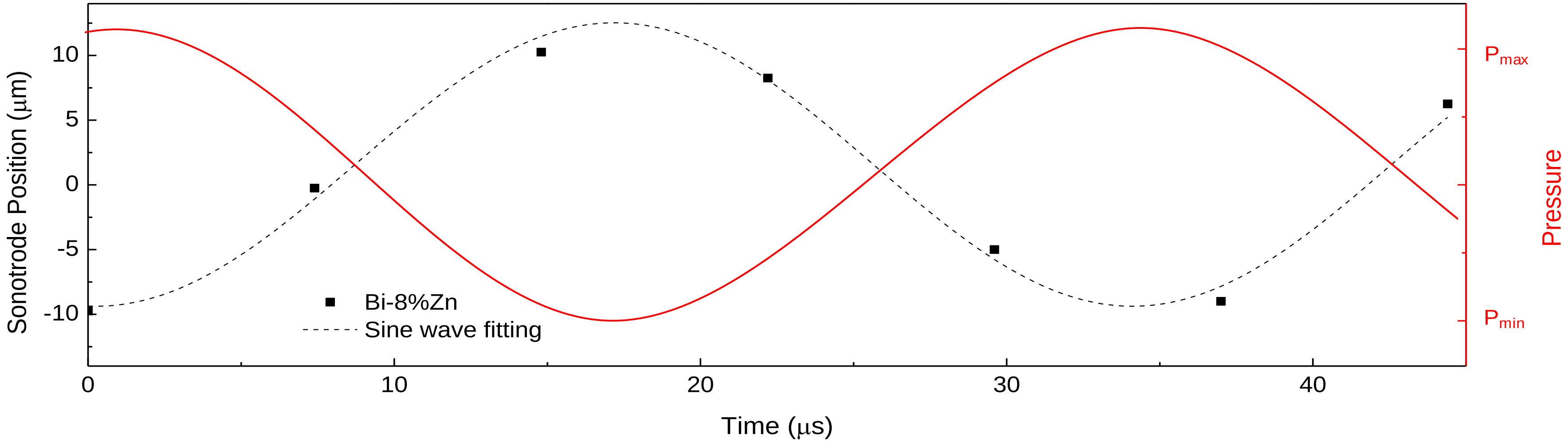

Fig. 4.4. *Three series of consecutive images, showing the nucleation, growth and implosion of ultrasonic bubbles immediately below the sonotrode tip in (a) water (271,554 fps), (b) silicone oil (271, 554 fps), and (d) Bi-8%Zn (135,781 fps), respectively. The sonotrode positions and corresponding pressure wave are shown in (c) for water and silicone oil, and (e) for Bi-8%Zn. The images were captured at 32-ID-B of APS, and the ultrasound power used is 20 W. The images are captured at the very start of ultrasound to purposely image the instants of bubble nucleation.*

4.3 Oscillation of ultrasonic bubbles

Fig. 4.4 indicates that, after nucleated, the bubbles grow near the sonotrode tip and behave very chaotically. Most of them cannot survive more than one wave period due to the high acoustic pressure at the region. However, at the location further below the sonotrode, for example ~2 mm away from the sonotrode tip, bubbles can often survive more than one wave period and oscillate cyclically under a relatively low acoustic pressure.

Fig. 4.5a, b, d shows the oscillating behaviour of a single bubble in water, silicone oil and Bi-8%Zn under the applied ultrasound of 20 W. The view fields are at the location ~4.7 mm (water), ~4.25 mm (silicone oil), and ~2.3 mm (Bi-8%Zn) below the sonotrode tip respectively. The images in water and silicone oil were taken using 135,780 fps and those in Bi-8%Zn using 5413 fps in order to track the movements of the bubbles in a relatively bigger view field. Apparently, the bubbles in all three cases oscillate cyclically under the influence of the cyclic acoustic pressures.

To quantify the oscillating behaviour, the radii of the bubbles are measured from the images showed in Fig. 4.5 a, b, d and plotted in c and e.

At 135, 780 fps, ~5 images were captured in a single wave period for the cases of water and silicone oil. Fig. 4.5a-c shows that, initially, bubbles with the radii of 4.5 μm (in water), and 6 μm (in silicone oil) grow in the first expansion cycle of the acoustic pressure wave period until reach ~11 μm and ~16 μm. Then the bubbles shrink in the subsequent compression cycle with the bubble radii decreasing to their initial sizes at the end of the wave period. Subsequently, similar phenomena repeat in the next wave period.

While in Bi-8%Zn, a relatively low acquisition rate, 5413 fps, was used and the interframe time is about 6 ultrasound wave periods. The images in Fig. 4.5d show that, although the bubble behaviour in a single wave period is not able to be captured at this acquisition rate. Over a long period of time, such as the ~50 wave periods in Fig. 4.5d, the steady-state oscillating behaviour of the bubble is clearly demonstrated with the bubble radii oscillate between ~7.5 μm and ~12 μm (Fig. 4.5e).

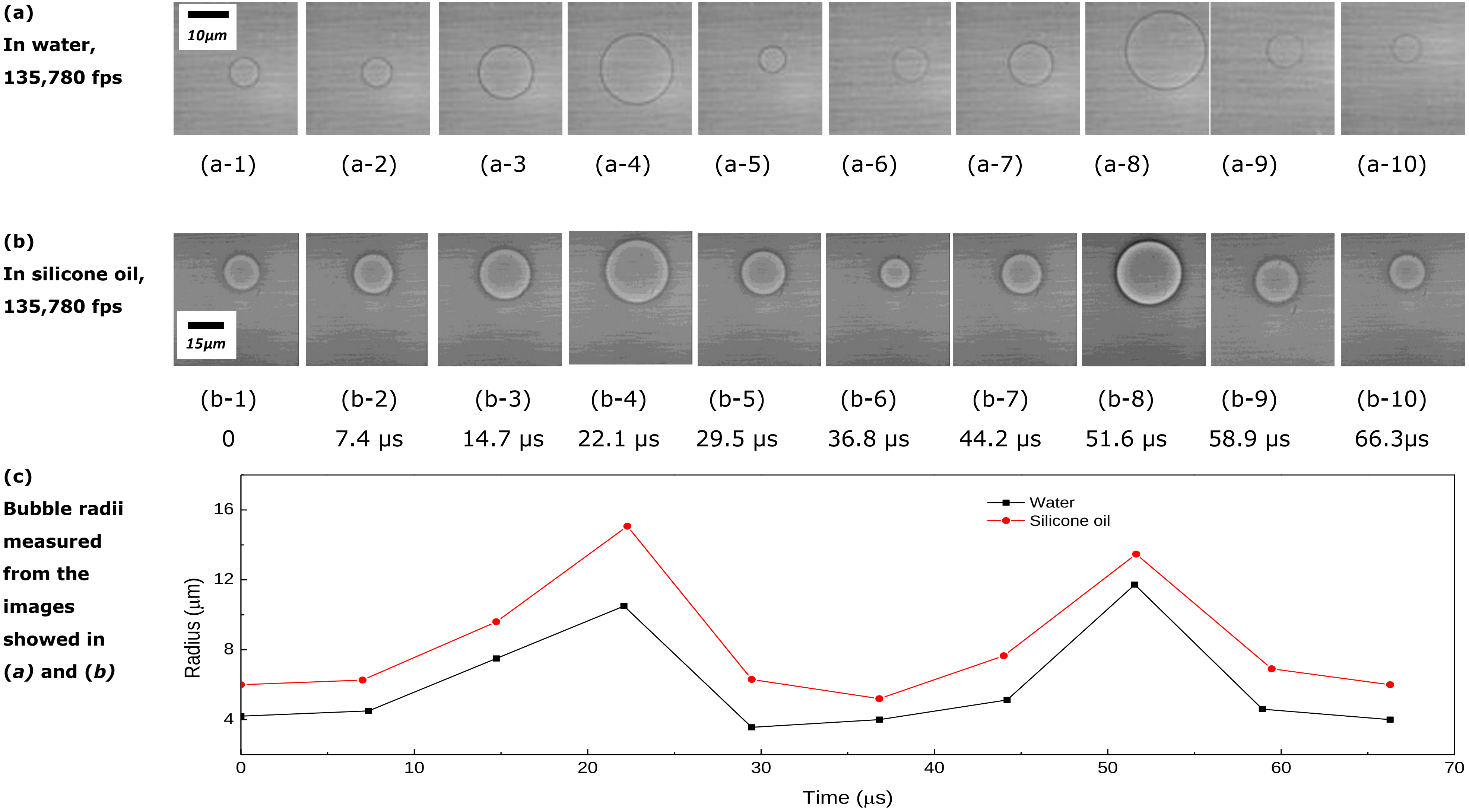
(a)
In water,
135,780 fps
10µm
(a-1)
(a-2)
(a-3
(a-4)
(a-5)
(a-6)
(a-7)
(a-8)
(a-9)
(a-10)
(b)
In silicone oil,
135,780 fps
15µm
(b-1)
(b-2)
(b-3)
(b-4)
(b-5)
(b-6)
(b-7)
(b-8)
(b-9)
(b-10)
0
7.4 µs
14.7 µs
22.1 µs
29.5 µs
36.8 µs
44.2 µs
51.6 µs
58.9 µs
66.3µs
(c)
Bubble radii
measured
from the
images
showed in
(a) and (b)
Water
Silicone oil
Radius (µm)
4
8
12
16
0
10
20
30
40
50
60
70
Time (µs)

(d) In liquid Bi-8%Zn, 5413 fps

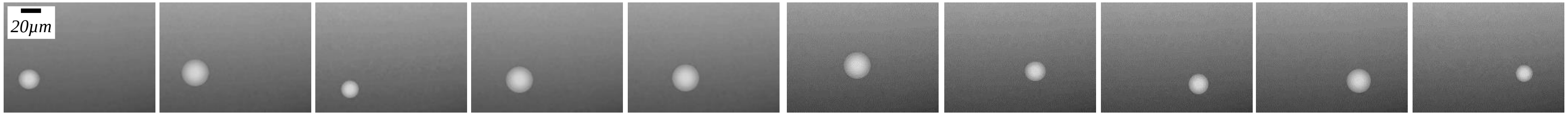

(d-1) 0 | (d-2) 185 μs | (d-3) 369 μs | (d-4) 554 μs | (d-5) 739 μs | (d-6) 924 μs | (d-7) 1108 μs | (d-8) 1293 μs | (d-9) 1478 μs | (d-10) 1663 μs

(e) The bubble radii measured from the images showed in (*d*)

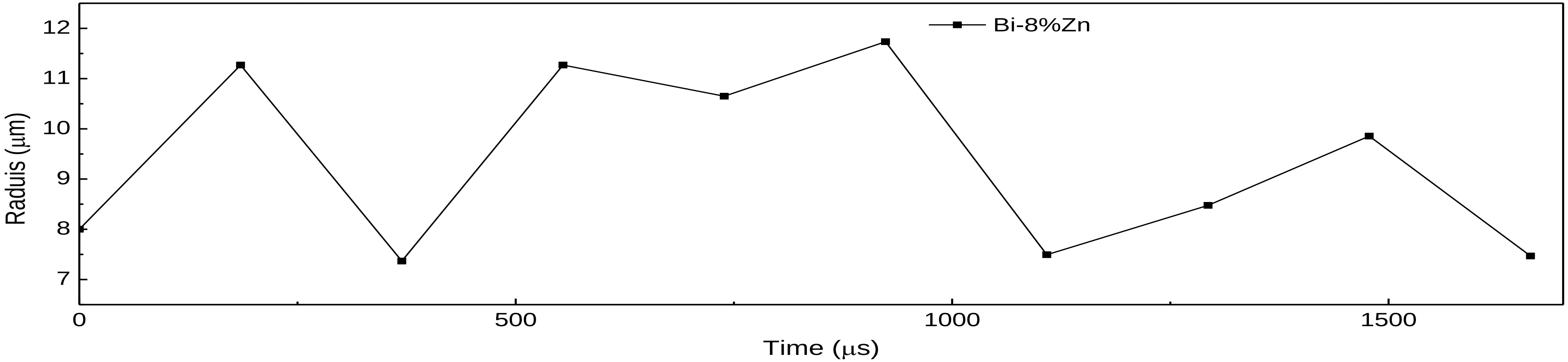

Fig. 4.5. *Typical X-ray images acquired at APS, showing that a single bubble oscillates in a quasi-steady manner (a) in water in the region ~4.7 mm below the sonotrode (an acoustic pressure of 0.118 MPa), (b) in silicone oil in the region ~4.25 mm below the sonotrode (0.125 MPa) using 135,780 fps, and (d) in Bi-8%Zn using 5413 fps (700K, ~2.3 mm below the sonotrode, 0.125 MPa). The bubble radii as a function of time measured from the images for (c) water and silicone oil; and (e) Bi-8%Zn.*

4.4 Implosion of ultrasonic bubbles

Images a-6, b-6 and d-5 in Fig. 4.4 have already demonstrated that the collapsing or implosion of the ultrasonic bubbles can be captured by the ultrafast X-ray imaging. Encouraged by the initial findings, we carried out a series of dedicated observations using the highest possible image acquisition rate at sector 32-ID-B of APS, and the observations were focused on the area immediately below the sonotrode tip in order to capture the highly dynamic event occurring during the implosion of the ultrasonic bubbles.

Fig. 4.6 shows three series of image sequences that contain a single bubble and its implosion in water (10 images in a single wave period), silicone oil and Bi-8%Zn alloy (at 700K, 10 images in 2 wave periods). The images were selected through painstaking image analyses from the real-time videos taken when the same sonotrode vibrating amplitude (A_m=5μm) was applied to each case, all the bubble implosions are immediately below the sonotrode with the ultrasound power set as 20 W. The acoustic pressure below the sonotrode tip can be calculated using the formula [5].

$$P_A = \rho\, C\, \omega\, A_m \tag{4.1}$$

where ρ is the density of the liquid, and C is the sound speed for the liquid, $\omega=2\pi f$ is the angular frequency, f is the frequency of ultrasound, and A_m is the vibrating amplitude of sonotrode tip.

Fig. 4.7a-c show the corresponding sonotrode positions measured from the images in Fig. 4.6a-c. The sonotrode up-and-down movement (indicated by the triangle markers) follows sine function with the fitting correlation coefficient of >0.95. The measured bubble radii (purple lines and circle markers) and the pressure waves calculated using Eq. 4.1 (red lines) for the three cases are also showed in Fig. 4.7a-c, respectively.

(a) In water, 271,554 fps

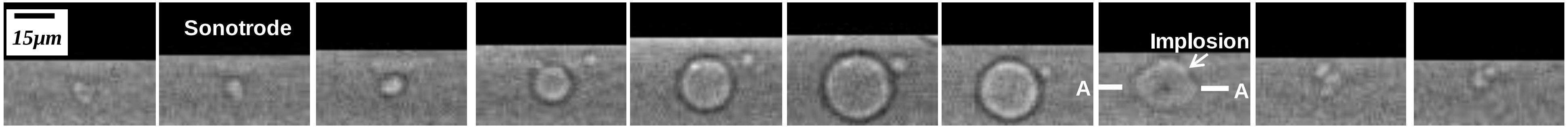

(a-1) (a-2) (a-3) (a-4) (a-5) (a-6) (a-7) (a-8) (a-9) (a-10)

0 3.7 μs 7.4 μs 11.0 μs 14.7 μs 18.4 μs 22.1 μs 25.8 μs 29.5 μs 33.2μs

(b) In silicone oil, 135,780 fps

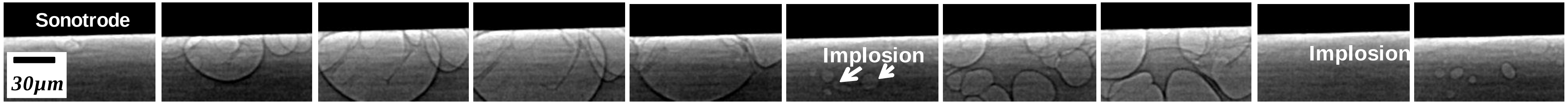

(b-1) (b-2) (b-3) (b-4) (b-5) (b-6) (b-7) (b-8) (b-9) (b-10)

(c) In Bi-8%Zn, 135,780 fps

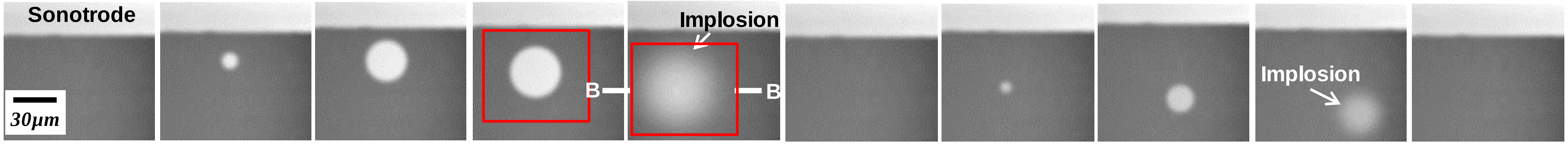

(c-1) (c-2) (c-3) (c-4) (c-5) (c-6) (c-7) (c-8) (c-9) (c-10)

0 7.4 μs 14.7 μs 22.1 μs 29.5 μs 36.8 μs 44.2 μs 51.6 μs 58.9 μs 66.3μs

Fig. 4.6. *Typical X-ray image sequences acquired at sector 32-ID-B of APS, showing the bubble implosions immediately below the sonotrode tip (a) in water using 271,554 fps, (b) in silicone oil and (c) Bi-8wt%Zn alloy (700K), both using 135,780 fps.*

.

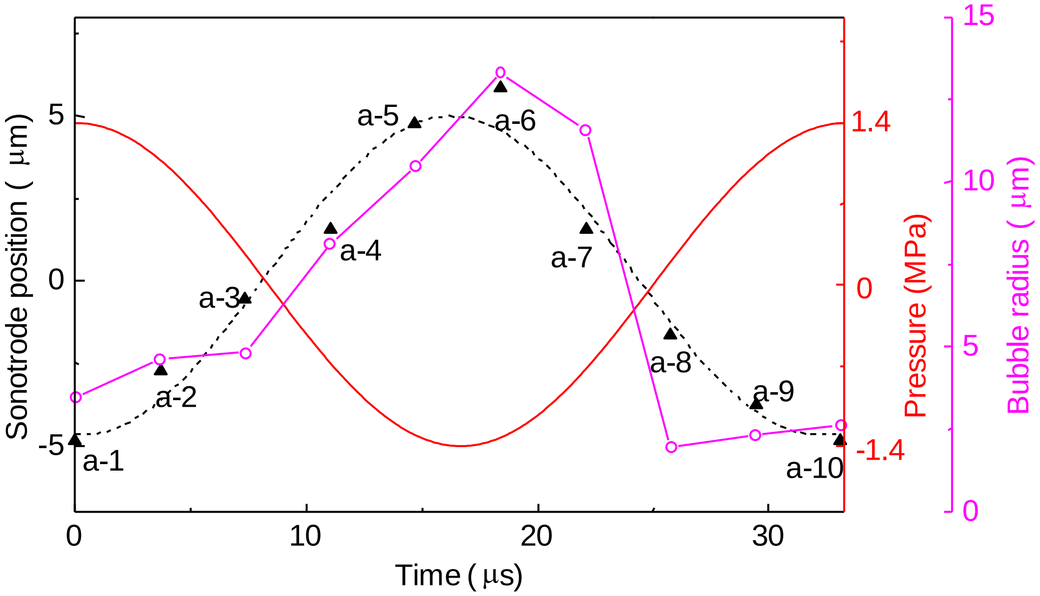

(a) Water

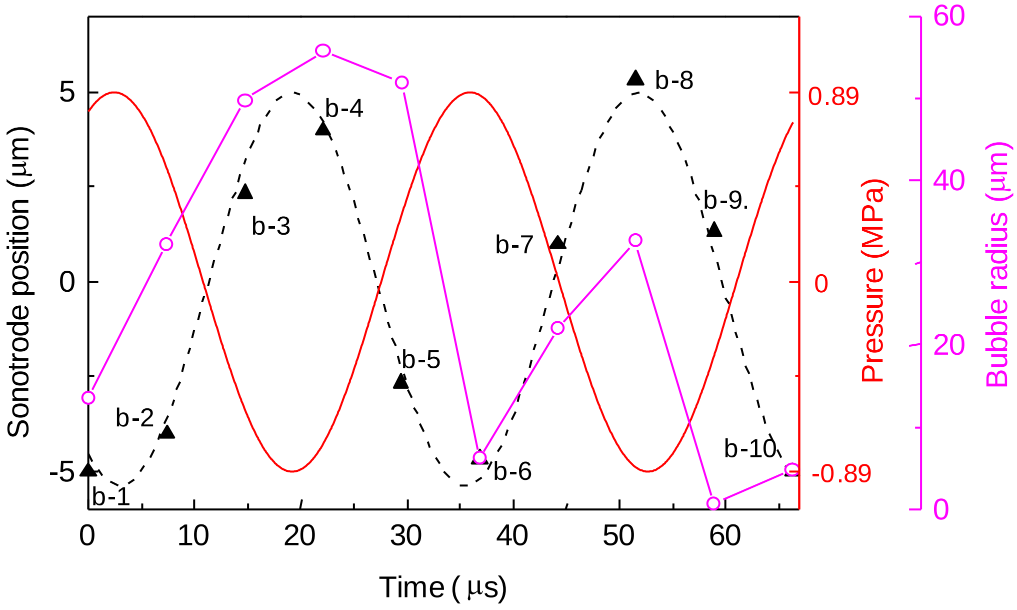

(b) Silicone oil

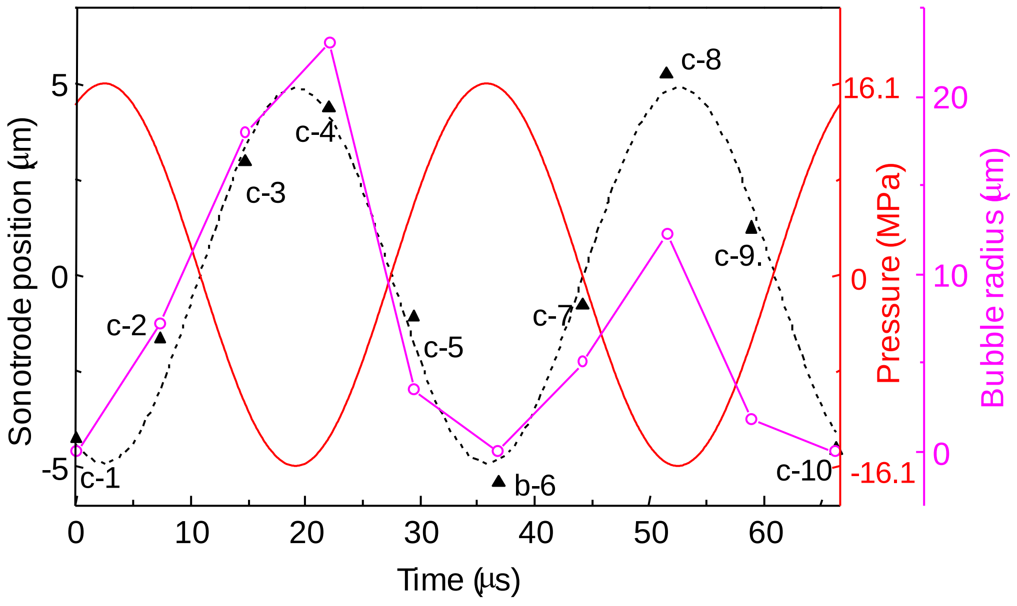

(c) Bi-8%Zn

Fig. 4.7. *The sonotrode positions are measured from the images showed in Fig. 4. 6a-c (marked by the triangle markers and the dotted line is the theoretical position calculated using a sine function) for (a) water, (b) silicone oil, and (c) liquid Bi-8%Zn. The corresponding acoustic pressures (red lines) are calculated using Eq. 4.1. The measured bubble radii oscillations (purple lines with circle markers) are also showed in each figure.*

4.4.1 Bubble implosion in water

Fig. 4.6a-1 shows that, initially, three tiny bubbles with radii of ~1.5 μm appeared at the location ~15 μm below the sonotrode tip. The imaging spatial resolution of 1 μm/pixel and the X-ray phase contrast is just able to resolve such tiny bubbles with parts of their boundaries clearly seen touching each other. The three tiny bubbles were actually the "bubble debris" left over immediately after the implosion of a big bubble in the previous image. Fig. 4.7a shows that, as the sonotrode moved upwards from a-1 to a-6 (the expansion cycle), and the acoustic pressure reduced from approximately a positive pressure of +1.4 MPa to a negative pressure of -1.4 MPa. The three tiny bubbles were found firstly to coalesce into a single bubble (Fig. 4.6a-2, 3), and then the single bubble became spherical (Fig. 4.6a-4), and continued to grow until the sonotrode reached the highest position at Fig. 4.4a-6.

Subsequently, the sonotrode started the downward movement (the compression cycle). The bubble was seen firstly compressed and the diameter decreased (Fig. 4.6a-7). In all images containing the spherical bubble (Fig. 4.6a-4 to a-7), a circular interface (the darker line delineating the bubble) is clearly showed in all cases.

In the next image, Fig. 4.6a-8 shows that the circular boundary became distorted and blurred, and a relative darker core was also found to appear near the centre of the bubble. The darker core can be seen more clearly from the grey value distribution along the line A-A, passing the darker core (Fig. 4.8c). The line A-A has 3 pixels in thickness, and the averaged grey values of the 3 pixels along the lines are used to minimise the effect of noise signals. Subsequently, 3 bubble debris appeared in Fig. 4.6a-9, similar to those showed in Fig. 4.6a-1. The 3 bubbles started to coalesce together (Fig. 4.6a-10), repeating the coalescence-expansion-compression-implosion cycle again. The evidence showed in Fig. 4.6a-8 and a-9 indicates that bubble implosion occurred between Fig. 4.6a-8 and a-9, and painstaking image analyses of many such videos confirmed that there is always a ‘darker core’ at or near the centre of the collapsing bubble with a distorted air-liquid interface radiating outwards (Fig. 4.6a-8).

4.4.2 Bubble implosion in silicone oil

Fig. 4.6b shows 10 consecutive images for the ultrasonic bubbles captured in silicone oil and the corresponding up-and-down movement of the sonotrode in two ultrasound periods. A bubble (an equivalent bubble radius of ~11 μm, because it is not spherical) was found to nucleate at the sonotrode tip (Fig. 4.6b-1). The bubble grew as the sonotrode moved up (from Fig. 4.6b-2 to b-4), reaching a maximum radius of ~52 μm (Fig. 4.6b-4). As the sonotrode moved down (Fig. 4.6b-5), the bubble is compressed and then imploded into a cluster of many small bubbles (Fig. 4.6b-6). The small bubbles were seen clearly to grow bigger in the subsequent two images before imploded again (Fig. 4.6b-9) with a similar cluster of small bubbles formed and seen more clearly in Fig. 4.6b-10. Clearly, bubble implosion is a more efficient process to create bubble nuclei for the next wave period.

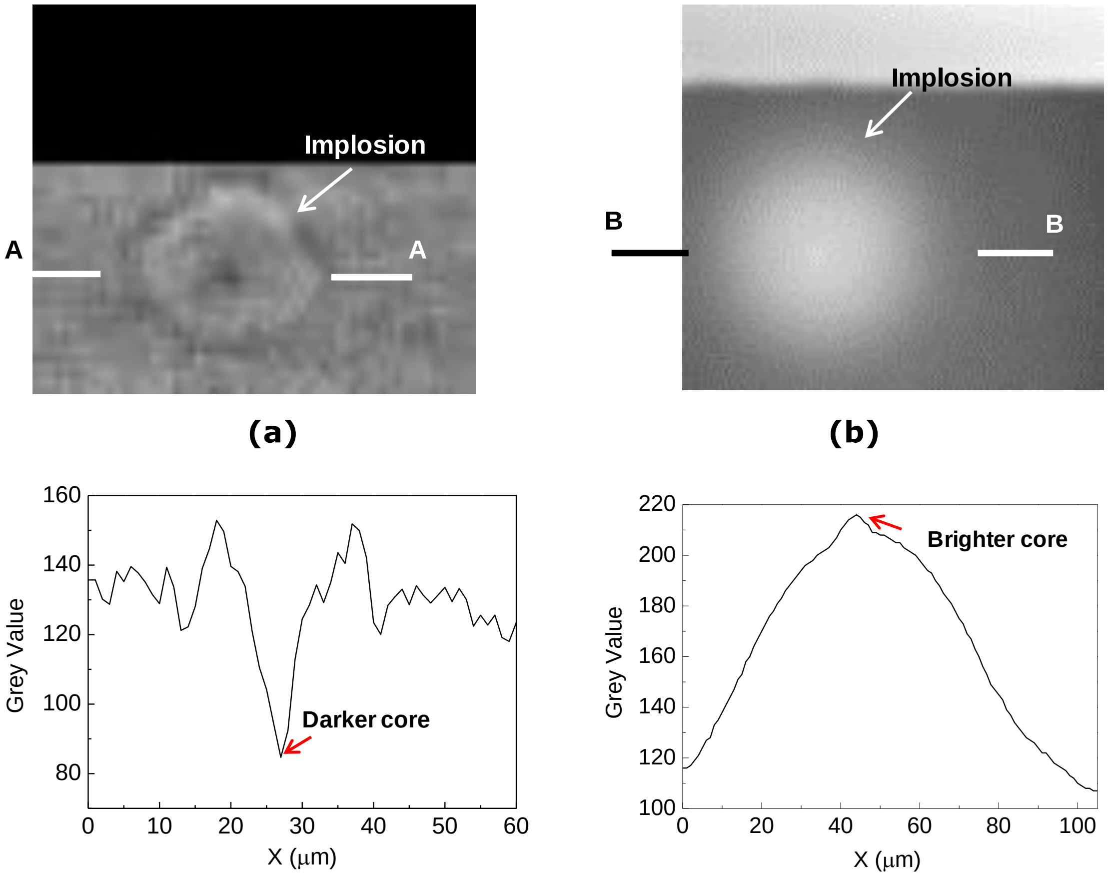

(a) **(b)**

(c) **(d)**

Fig. 4.8. *The enlarged images of (a) Fig. 4.6a-8 and (b) Fig. 4.6c-5, highlighting the bubble implosions in water and Bi-8%Zn. The grey value distributions along the lines (c) A-A in* ***(a)*** *and (d) B-B in* ***(b)****, respectively. Line A-A and B-B are 3 pixels lines, and the grey values are the averaged values for the 3 pixel lines.*

4.4.3 Bubble implosion in liquid metal

Fig. 4.6c shows 10 consecutive images for an ultrasonic bubble in liquid Bi-8%Zn and the corresponding up-and-down movement of the sonotrode in two ultrasound periods. A bubble with a radius of ~8 μm was found to appear in Fig. 4.6c-2, and grew to ~23 μm radius (Fig. 4.6c-4) in the expansion cycle before imploded with the generation of a spherical halo (Fig. 4.6c-5) after the sonotrode started to move down. The grey value distribution along the line B-B also shows that, there exists a small brighter core near the centre (Fig.

4.8d) of bubble. Similar expansion-implosion behaviour repeated in the next period as clearly shown from Fig. 4.6c-6 to c-10.

4.5 Coalescence of ultrasonic bubbles

As described in section 4.4, bubble implosion is a very efficient process to create new bubble nuclei. Subsequently, these bubble nuclei either grow individually (typically showed in Fig. 4.6b-7 to b-10 for silicone oil) or coalesce together (typically showed in Fig. 4.6a-9 to a-10 for water). The bubble coalescence process is a very important dynamic phenomenon for the ultrasonic bubbles and it is one of the main governing mechanisms to control the size of the bubbles and their distribution in the liquid. Through very detailed analyses, a series of typical images containing the bubble coalescence events are presented in this section to reveal the dynamics and mechanism of the bubble coalescence process. Fig. 4.9a-c shows the typical image sequences of bubble coalescence in water (~4.77mm below the sonotrode) and silicone oil (immediately below the sonotrode) captured at 271,554 fps, and that in liquid Bi-8%Zn (~2.34mm below the sonotrode, 700 K melt temperature) captured using 5413 fps. The ultrasound power is 20 W.

4.5.1 Bubble coalescence in water

Fig. 4.9a shows that, in water, two bubbles (marked 1 and 2 with the similar initial radii of ~10µm) expanded and approached to each other. They came in touch against each other (Fig. 4.9a-3) and the touched surfaces started to flatten and widen with a thin liquid film trapped in between (Fig. 4.9a-4). The touched surfaces started to break-up (Fig. 4.9a-5) at the point highlighted by the enlarged insert image. In Fig. 4.9a-6 (after 3.7 µs of the initial rupture of the liquid film between the bubbles), the two bubbles was seen to join together and form a new bubble, completing the coalescence process before suddenly imploded as showed in Fig. 4.9a-7.

4.5.2 Bubble coalescence in silicone oil

Fig. 4.9b-1 shows that, in silicone oil, there are very faint bubble nuclei below the sonotrode tip, which were generated from the implosion of previous bubbles. They grew bigger and bigger subsequently, and touched each other to create a liquid film interface in-between. The phase contrast from the X-ray imaging allows the liquid film to be “seen” clearly and it is a lens-shaped feature in the 2-D image projection (Fig. 4.9b-3).

(a) In water, 271,554 fps

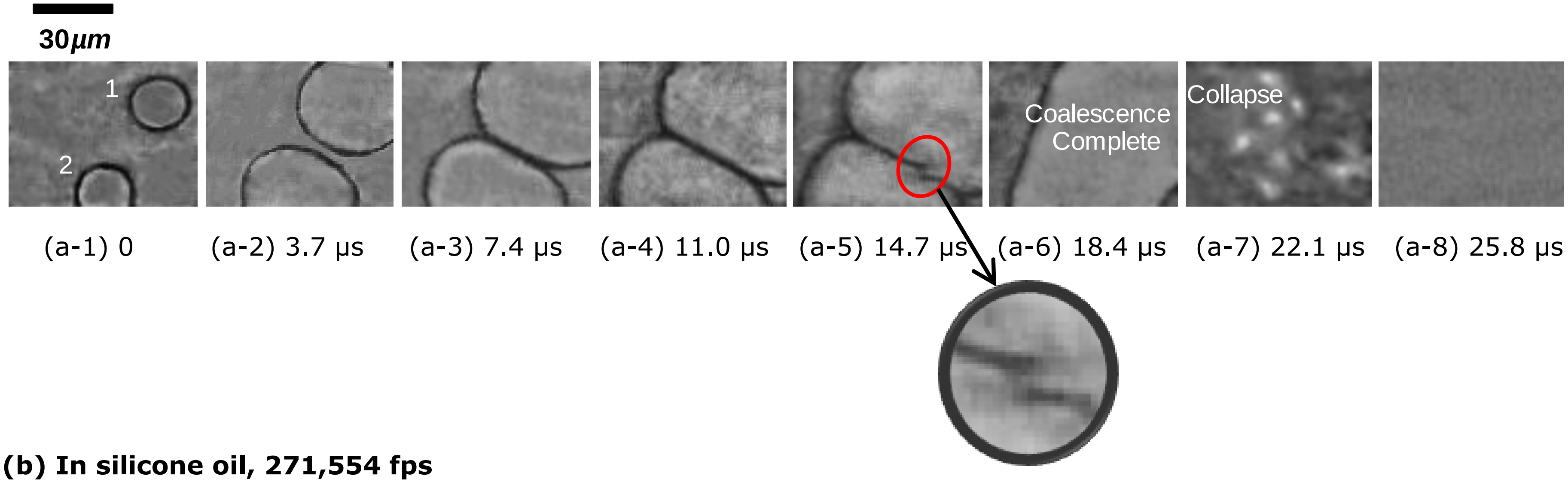

(a-1) 0 (a-2) 3.7 μs (a-3) 7.4 μs (a-4) 11.0 μs (a-5) 14.7 μs (a-6) 18.4 μs (a-7) 22.1 μs (a-8) 25.8 μs

(b) In silicone oil, 271,554 fps

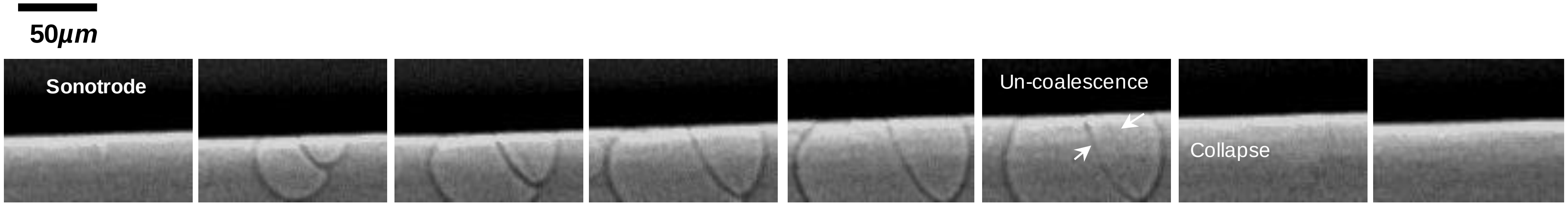

(b-1) 0 (b-2) 3.7 μs (b-3) 7.4 μs (b-4) 11.0 μs (b-5) 14.7 μs (b-6) 18.4 μs (b-7) 22.1 μs (b-8) 25.8 μs

(c) In Bi-8%Zn, 5413 fps

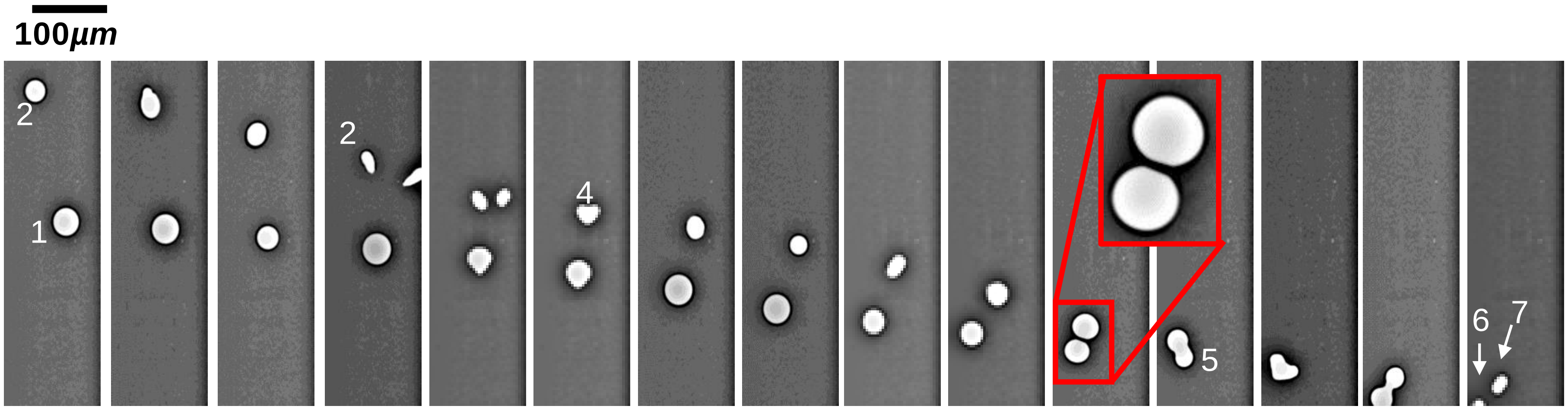

(c-1) 0
(c-2) 185 µs
(c-3) 396 µs
(c-4) 554 µs
(c-5) 739 µs
(c-6) 924 µs
(c-7) 1108 µs
(c-8) 1293 µs
(c-9) 1478 µs
(c-10) 1663 µs
(c-11) 1847 µs
(c-12) 2032 µs
(c-13) 2217 µs
(c-14) 2402 µs
(c-15) 2586 µs

Fig. 4.9. *Three typical image sequences, showing (a) the coalescence of two bubbles in water at the location ~4.77 mm below the sonotrode (271,554 fps). The insert is a zoom-in image to show in details how the liquid film ruptures. (b) the touching of two bubbles in silicone oil immediately below the sonotrode (271,554 fps), and (c) the coalescence and split of bubbles in Bi-8%Zn the location ~2.34 mm below the sonotrode (at 700K and 5413 fps). The ultrasound power is 20 W.*

During the expending half cycle (the up-movement of sonotrode from Fig. 4.9b-1 to b-6), the two bubbles grew continuously. While the liquid film in between was seen to grow too without rapture, indicating that the liquid trapped inside the liquid film is still there to separate the two bubbles. Therefore the coalescence is not completed (Fig. 4.9b-6). However, Fig. 4.9b-7 shows that, when the compression cycle started, both bubbles imploded under the acoustic pressure. It should be noted that the phase contrast from X-ray imaging allows the touching boundaries of the two bubbles to be clearly identified. The two bubbles showed in Fig. 4.9b-6 may be mistakenly recognised as a single coalescence bubble if a traditional visible light illumination is used.

4.5.3 Bubble coalescence in liquid metal

Fig. 4.9c shows two bubbles in liquid Bi-8%Zn captured at 700 K (marked 1 and 2). They oscillated and moved down with velocities of ~0.10 m/s and 0.17 m/s, respectively, and the 3rd bubble appeared at 0.55 ms. Bubble 2 and bubble 3 attracted each other, and became elliptical, and then joined to form a new bubble (bubble 4) with a radius of 20 μm. Bubble 4 and 1 moved close to each other, touched and formed a flat interface before joining together to create bubble 5 with an elliptical shape. However, the elliptical shaped bubble was not stable, split again under the cyclic pressure.

4.6 Bubble coalescence versus implosion

Due to the cyclic nature of the ultrasonic pressure field, the bubbles in the middle of performing coalescence maybe subject to the compression of the pressure field and implode before completing the coalescence process, resulting in non-symmetrical bubble debris.

Fig. 4.10a shows that, in water (consecutive images captured at 271,554 fps with ultrasound power of 20 W), two bubbles (marked a and b) approached to each other (Fig. 4.10a-2) and came in touch (Fig. 4.10a-3), and about to coalesce. But they were compressed (Fig. 4.10a-4) and then imploded (Fig. 4.10a-5) before completing the coalescence process, creating a micro-jet flow in the direction as the two arrows showed in Fig. 4.10a-4, similar to the result observed by Bremond, *et al*. [7]. The bubble nuclei (Fig. 4.10a-6) were formed at implosion along the microjet direction, Taking the rightest bubble nucleus (pointed by the right arrow in Fig. 4.10a-6) for example, its average velocity is calculated as ~10m/s (the velocity is calculated by its travel distance from the microjet position in Fig. 4.10a-5 to the current position in Fig. 4.10a-5 over the interframe time, 3.7 μs). Of course, at the instant of bubble implosion, the microjet should have much higher velocity.

Fig. 4.10b-1 to b-3 shows two bubbles (again marked a and b) touched and started to form a flat surface, however, before film drainage was completed, they were compressed (Fig. 4.10b-4) and then imploded (Fig. 4.10b-5), producing bubble nuclei as showed in Fig. 4.10b-5 and Fig. 4.10b-6. From the two adjacent images containing the bubble nuclei, the velocity of the bubble jet is calculated as ~4 m/s.

Fig. 4.10c shows that two bubbles (also marked a and b) completed the coalescence process and formed a new big bubble with irregular shape (pointed by the arrow in Fig. 4.10c-3). However, it imploded before recovering to be a spherical bubble, creating bubble nuclei with irregular pattern as shown in Fig. 4.10c-4. New bubbles grew from those bubble nuclei in the subsequent expansion cycle of the ultrasound wave.

Fig. 4.10d shows that two bubbles completed the coalescence process (Fig. 4.10d-1 and d-2) and recovered to become a spherical bubble and continue to expand (Fig. 4.10d-4 to Fig. 4.10d-5). The bubble imploded violently (Fig. 4.10d-6) with a bubble nucleus created at the original bubble centre, and the nucleus grew to be a single bubble subsequently, similar to those presented in the section **Section 4.4** for the implosion of a single bubble.

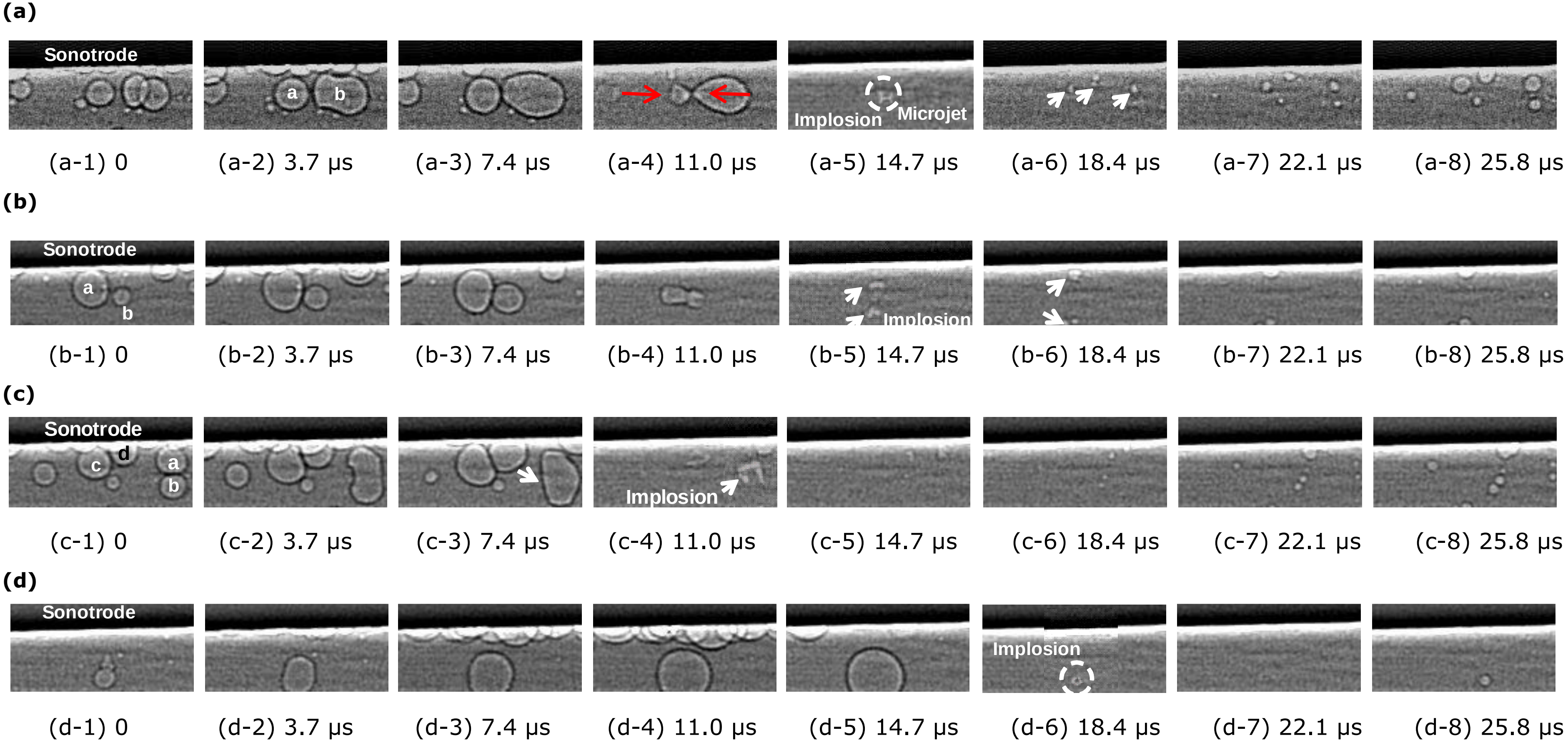

(a-1) 0 (a-2) 3.7 μs (a-3) 7.4 μs (a-4) 11.0 μs (a-5) 14.7 μs (a-6) 18.4 μs (a-7) 22.1 μs (a-8) 25.8 μs

(b-1) 0 (b-2) 3.7 μs (b-3) 7.4 μs (b-4) 11.0 μs (b-5) 14.7 μs (b-6) 18.4 μs (b-7) 22.1 μs (b-8) 25.8 μs

(c-1) 0 (c-2) 3.7 μs (c-3) 7.4 μs (c-4) 11.0 μs (c-5) 14.7 μs (c-6) 18.4 μs (c-7) 22.1 μs (c-8) 25.8 μs

(d-1) 0 (d-2) 3.7 μs (d-3) 7.4 μs (d-4) 11.0 μs (d-5) 14.7 μs (d-6) 18.4 μs (d-7) 22.1 μs (d-8) 25.8 μs

Fig. 4.10. *Bubble implosion at the different stages of bubble coalescence under the acoustic pressure in water (271,554 fps): (a) stage 1 - bubble approach and almost touch each other, (b) stage 2 - bubble touched and flattening interface occurs, (c) stage 3 - bubble coalesced and formed a irregular shape bubble, (d) stage 4 - bubble coalesced and formed a spherical bubble. The ultrasound power is 20W. The 4 stages of bubble coalescence are explained in details in Fig. 2.20. (128 x 64 μm)*

4.7 Bubble cloud

4.7.1 Bubble size distribution

The collective behaviour of bubbles, i.e. the bubble cloud, is actually one of the most important phenomena that have not been fully quantified in any previous research. To investigate the dynamic behaviour and the characteristics of bubble cloud, Low ultrasound power (20 W) and high image acquisition rate (135,780fps) were used first to capture as many as possible bubbles and used statistic method to quantify the characteristics of the bubbles in the compression and expansion cycle ultrasound wave periods.

Previously, researchers can only characterise bubble size distribution statistically in a long time duration, however, using the high frame rate, 5 images within a single wave period can be captured, and we have found that bubble sizes vary very differently in the compression cycle and expansion cycle, especially at highest negative pressure and positive pressure. Because the images captured are immediately below the sonotrode tip, the pressure phase can be derived from the sonotrode position by neglecting any phase delay or shift in the liquid (Fig. 4.3), that is, pressure reaches the highest positive (compression) value (P_{max}) when the sonotrode moves to the lowest position, but reaches the highest negative (expansion) value (P_{min}) when the sonotrode moves to the highest position.

Fig.4.11 shows the typical bubbles that were captured in water, silicone oil and liquid metal. For all cases, when the sonotrode tip moves to the lowest position (the highest acoustic pressure), the bubbles are much smaller (Fig. a, c, and e) than those (Fig. b, d, and f) found when the sonotrode tip is at the highest position (the lowest acoustic pressure).

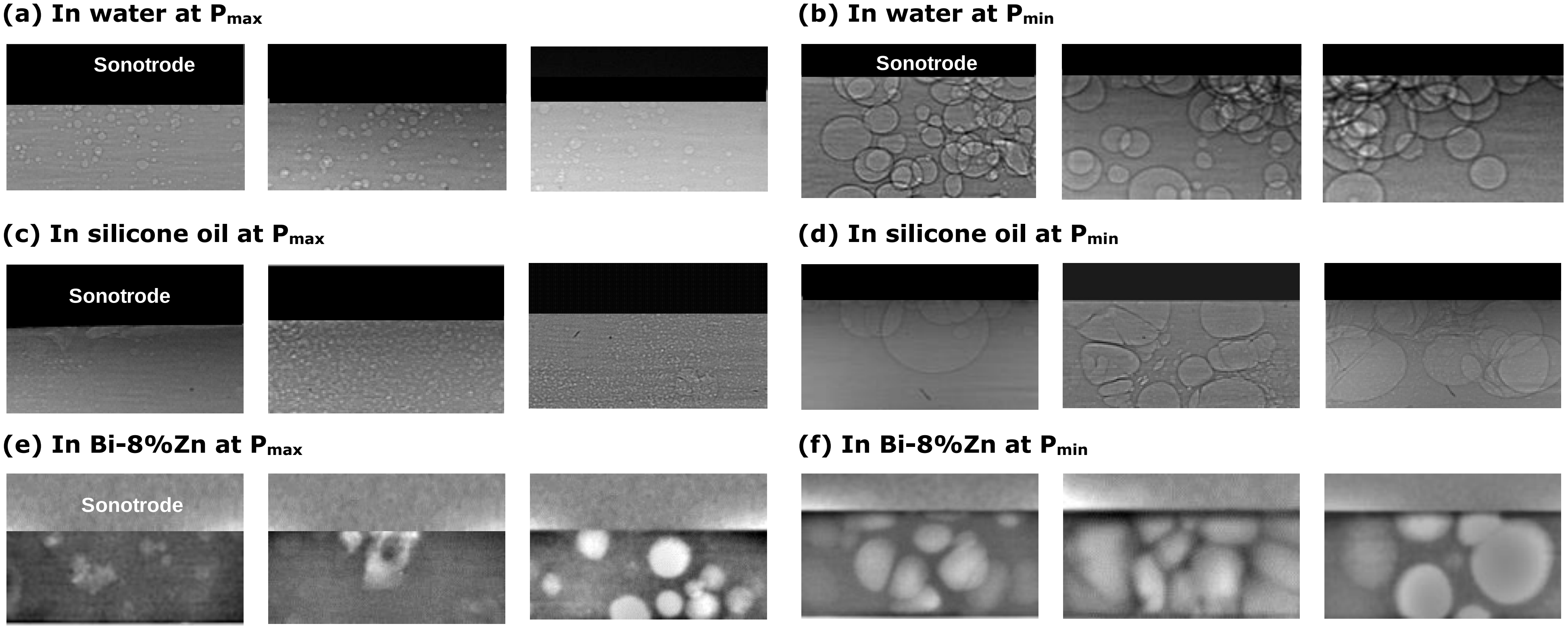

Fig.4.11. *Typical images of the ultrasonic bubbles captured immediately below the sonotrode tip when the sonotrode is at either the lowest position (highest pressure, P_{max}) or highest position (lowest pressure P_{min}) in (**a**, **b**) water, (**c**, **d**) silicone oil, and (**e**, **f**) liquid Bi-8%Zn (700K). The images were captured at 32-ID-B of APS, using 135,780 fps, and an ultrasound power of 20 W. The image size is 192 x 128 μm.*

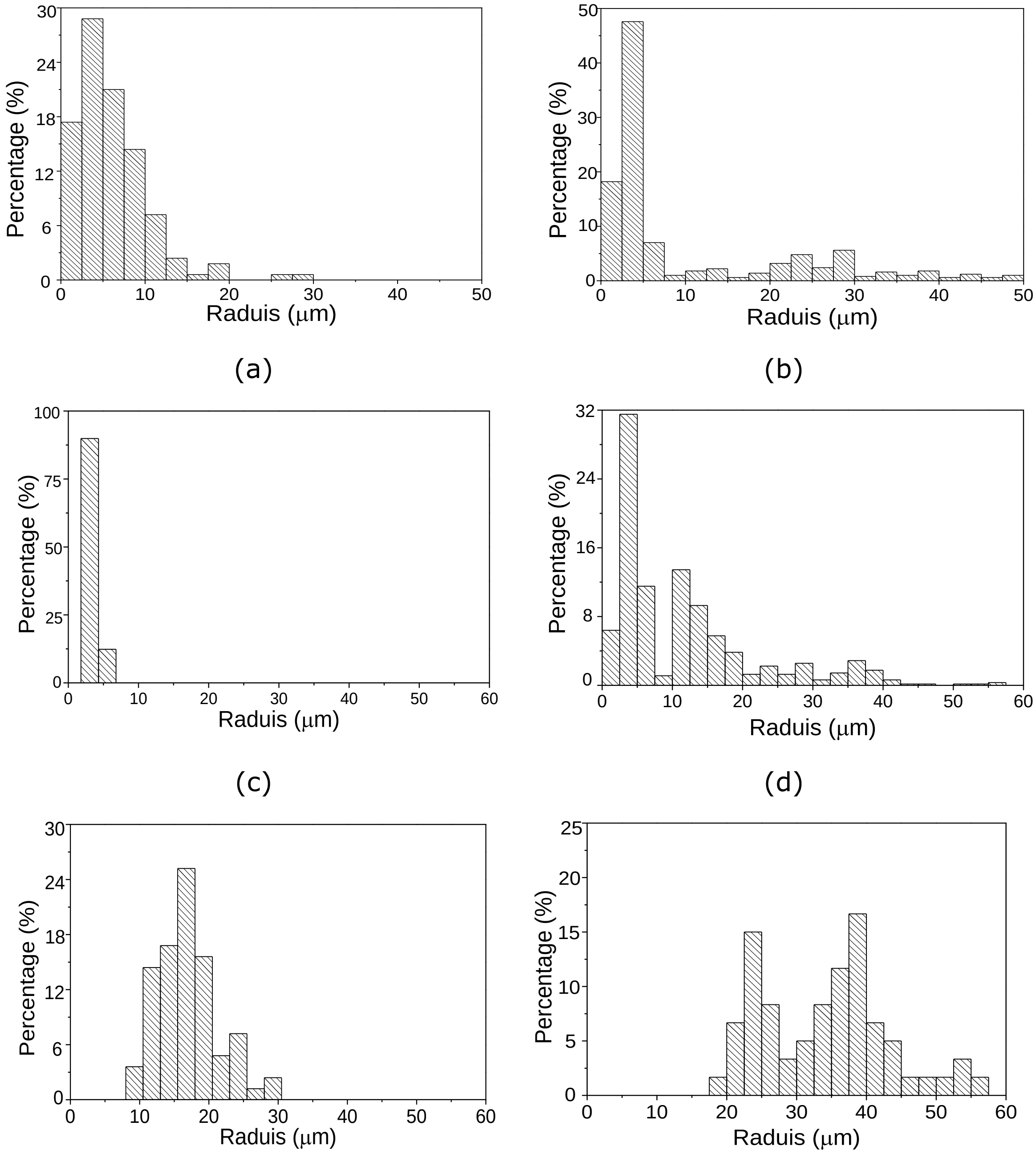

(a) (b)

(c) (d)

(e) (f)

Fig. 4.12. *Bubble size distribution when the sonotrode is at the lowest position (the highest acoustic pressure) and the highest position (the lowest acoustic pressure) in (a-b) water, (c-d) silicone oil, and (e-f) liquid Bi-8%Zn (700K). Each of the figures is calculated based on 100 images at the same condition. The typical images are showed in Fig. 4.11.*

Fig. 4.12a, c, and e show the percentage distributions of bubble radii for the highest acoustic pressure, and Fig. 4.12b, d and f show those at the lowest acoustic pressure. The calculation is based on the data gathered from 100 images at the same condition as typically showed in Fig. 4.11. The statistics shows that the majority of the bubble radii at the highest pressure are in the range of 2.5-15 μm for water, 5-7.5 μm for silicone oil, and 10-30 μm for Bi-8%Zn. At the lowest pressure, bubble radii become bigger and especially for the case of Bi-8%Zn (almost all bubbles are >20 μm). However, the large bubbles have a small percentage in the cases of water and silicone oil.

4.7.2 Bubble cloud and the cavitation zone

Using 5413 fps and a relatively big view field (1mm x 1mm), the collective behaviour of the bubble generated at the central region of the sonotorde can be captured. Fig. 4.13 shows some typical image sequences captured at 5413 fps using different diameter sontrode tips (Ø1 mm in water and silicone oil, Ø 0.5 in liquid Bi-8%Zn at 700K). For all cases, Fig. 4.13 show clearly the chaotic bubbles created below the sonotrode tip, i.e. the cavitation zone, which is mainly dependent on the size of the sonotrode tip and the ultrasound input power. At higher ultrasound input powers, the bubbles are stretched and distorted by the pressure field, and many layers of bubbles overlapped together, making it very difficult to see and separate any individual bubble from the bubble cloud. Hence a discrete approach to analyse the characteristics of the bubble cloud is no longer feasible. However, from the images, the region of the cavitation zone can still be clearly outlined as showed in Fig. 4.13.

Using a big view field (4.7 mm x 5.4 mm) and relatively slow acquisition rate (1500 fps) at I12 of DLS, We are able to capture the whole cavitation zone created below the sonotrode tip. Fig. 4.14 shows three typical snapshots of the bubble cloud extracted from a video sequence captured using an ultrasonic power of 60 W. It can be seen that, in the area immediately below the sonotrode tip, there is a bright region which contains many interconnected bubbles. However below this region (1.5 - 4 mm below the sonotrode tip), there are many individual bubbles spreading out in the field of view.

(a) In water, 5413 fps

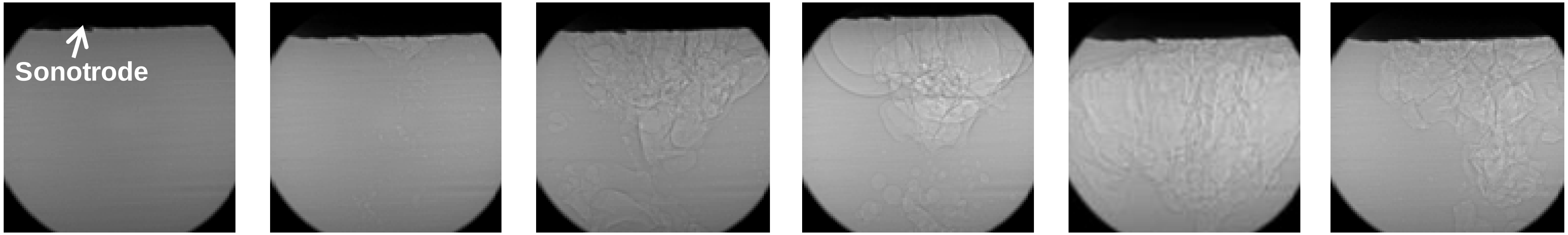

(a-1) 0 (a-2) 554 μs (a-3) 1108 μs (a-4) 1662 μs (a-5) 2216 μs (a-6)2770 μs

(b) In silicone oil, 5413 fps

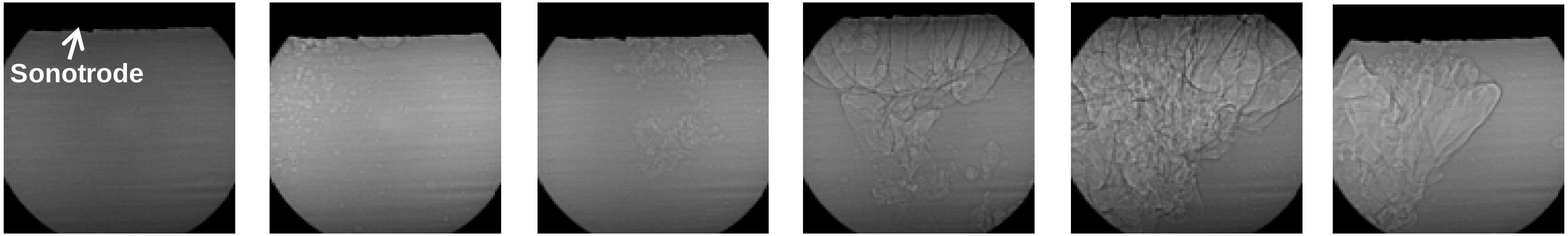

(b-1) 0 (b-2) 554 μs (b-3) 1108 μs (b-4) 1662 μs (b-5) 2216 μs (b-6) 2770 μs

(c) In Bi-8%Zn, 5413 fps

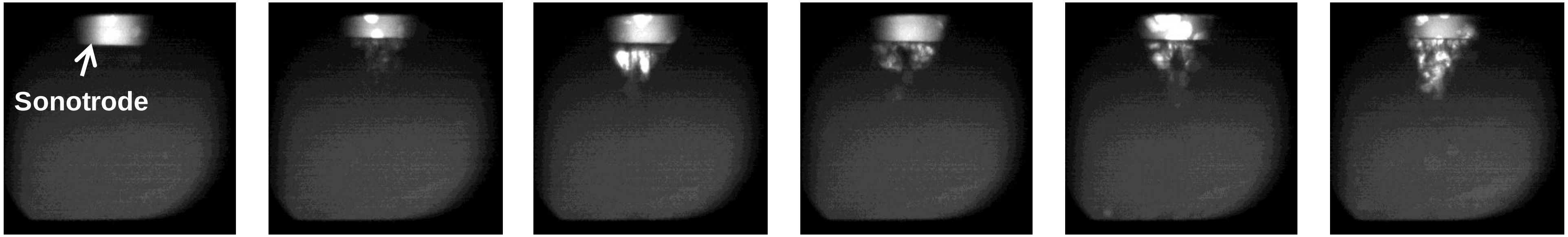

(c-1) 0 (c-2) 554 μs (c-3) 1108 μs (c-4) 1662 μs (c-5) 2216 μs (c-6) 2770 μs

Fig.4.13. *Typical images of the bubbles and cavitation zone immediately below the sonotrode tip in (a) water, (b) silicone oil, and (c) liquid Bi-8%Zn (700K). The images were captured at 32-ID-B of APS using 5413 fps. The ultrasound power was set at 100 W.*

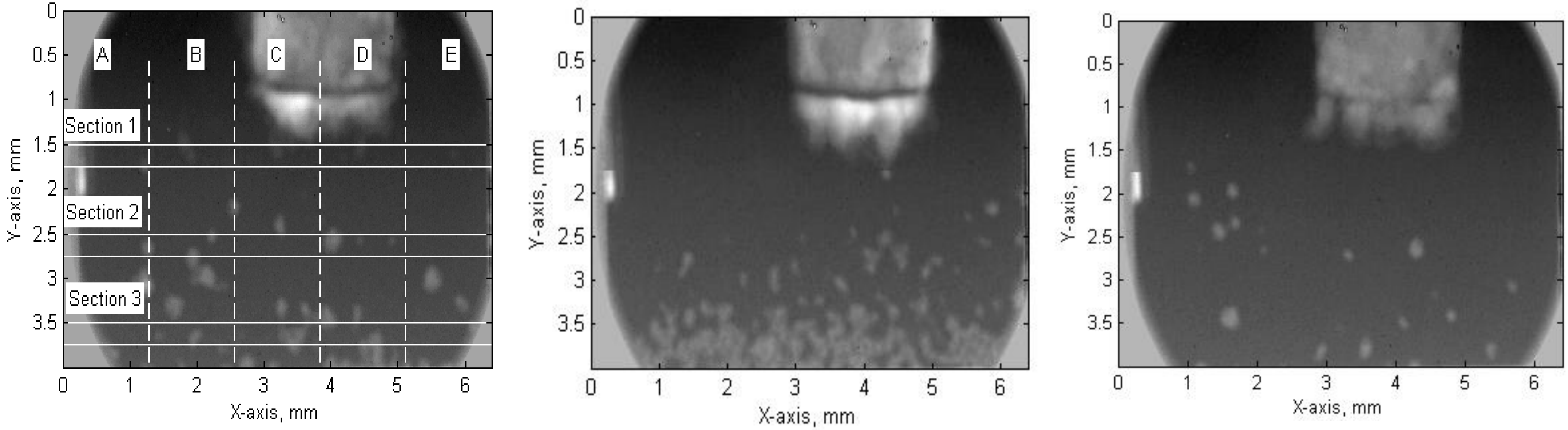

(a) **(b)** **(c)**

Fig. 4.14. *The X-ray images acquired using 2000 fps for the liquid Sn-30%Cu alloy at 948 K using an ultrasound power of 60 W, at (a)* t_0 *= 5 ms (b)* t_1 *= 25 ms (c)* t_2 *= 45 ms, showing the ultrasonic bubble cloud immediately below the sonotrode tip and the individual bubbles at the location 1.5 - 4 mm below the sonotrode tip.*

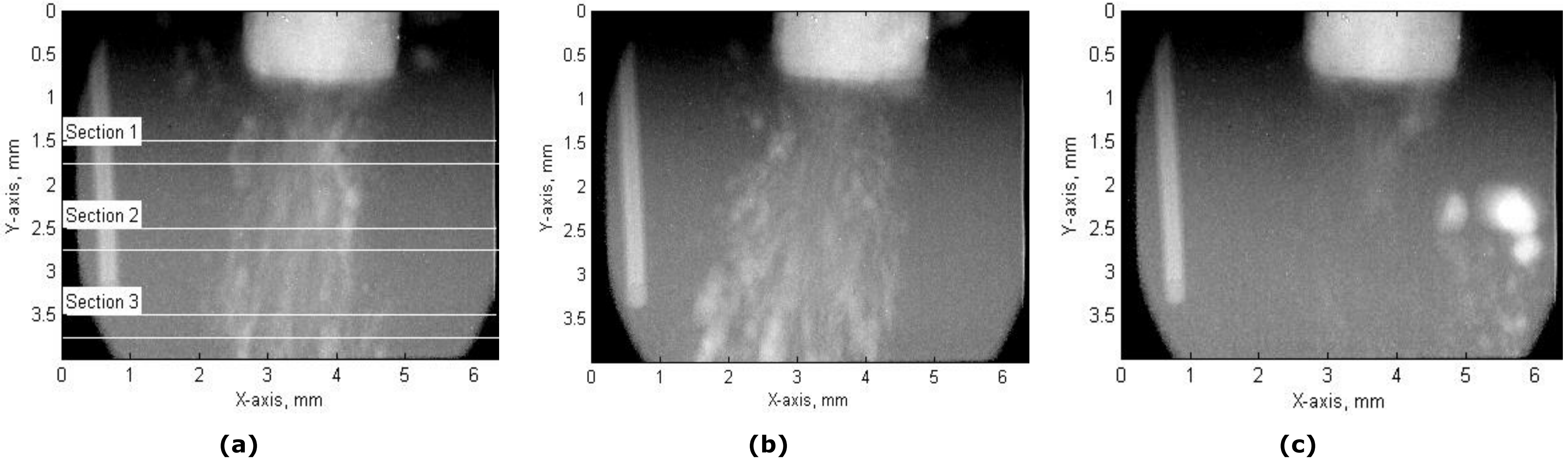

Fig. 4.15. *The X-ray images acquired using 2000 fps for the liquid Sn-30%Cu alloy at 948 K using an ultrasound power of 100 W, at (a)* t_0 *= 25 ms (b)* t_1 *= 35 ms (c)* t_2 *= 45 ms, showing the ultrasonic bubble cloud.*

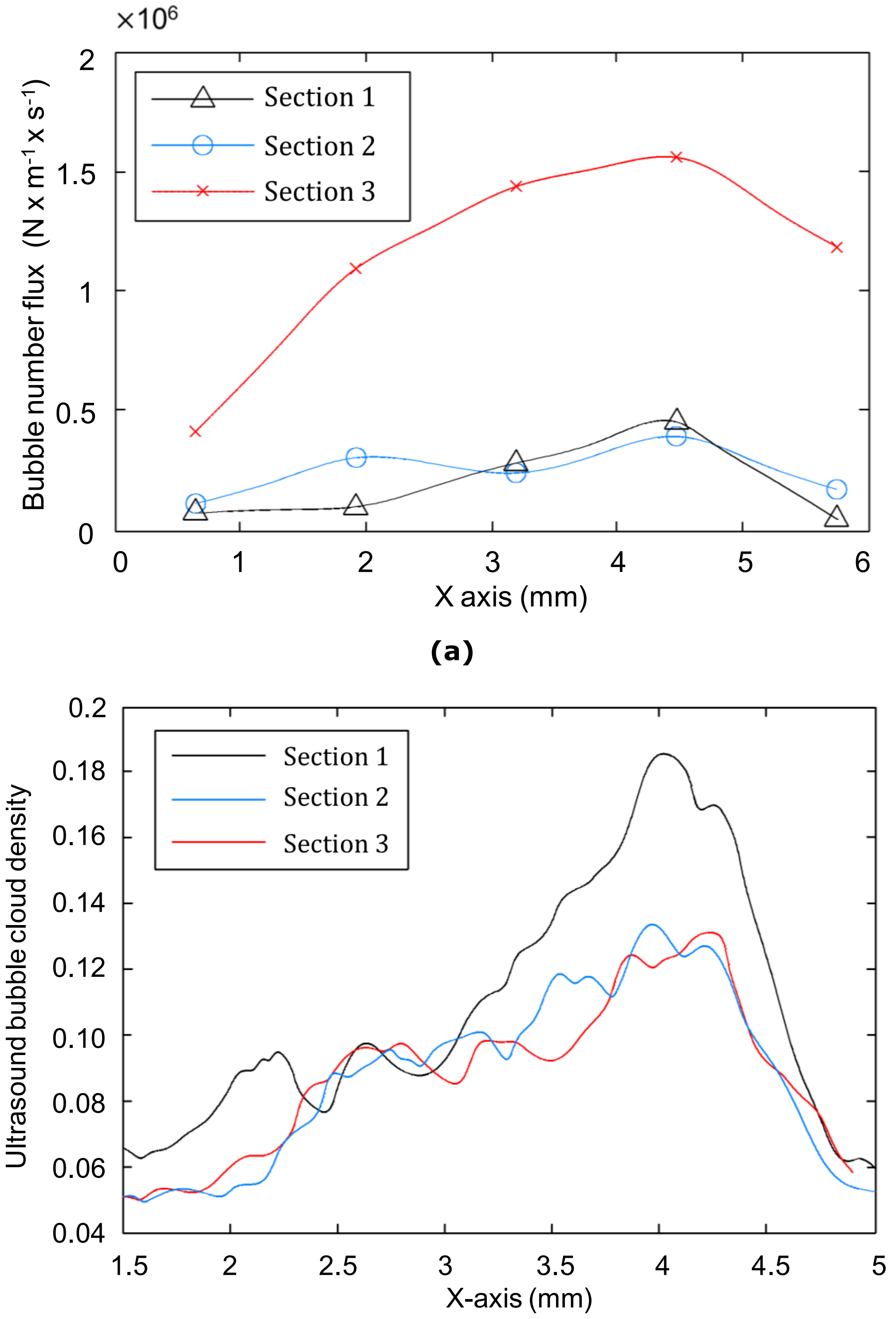

(a)

(b)

Fig. 4.16. *(a) The bubble number density for the section 1, 2 and 3 showed Fig. 4.14 (60 W), (b) the bubble cloud density for the section 1, 2 and 3 showed in Fig. 4.15 (100 W).*

Fig. 4.15 shows a cloud of bubbles captured at 100 W ultrasound power. Individual bubble cannot be clearly identified, instead, the bubbles seem to form a steam of interconnected bubble strings, indicating that, at 2000 fps, the individual bubbles moved too fast to be captured. However, at the location away from the sonotrode such as the right bottom corner of Fig. 4.15c where the acoustic pressure is much lower than the area immediately blow the sonotrode tip, big and individual bubble can still been seen.

Comparison between the images showed in Fig. 4.14 and Fig. 4.15, it is clearly seen that, at 60 W, especially at the region away from the sonotrode tip, the bubbles separated from each other clearly with a nearly spherical morphology. While those generated at 100 W were elongated and interconnected together to form a continuous bubble stream. To quantify the characteristics of the collective behaviour of the bubbles, *i.e.* the spatial distribution of the bubbles and bubble density, the numbers of bubbles passing though per unit length per unit time at a defined location are measured from each image. Fig. 4.14a shows the chosen sections, *i.e.* section 1, 2 and 3, and each section was divided into 5 areas, marked A, B, C, D, and E, with each sectional width of 1.25 mm. A total of 100 images were measured in this way to obtain sufficient statistic data and presented in Fig. 4.16a. It clearly shows that there is a larger population of bubbles passing through section 3. It also shows the maximum bubble flux occurred in the area C and D in Fig. 4.14a.

At 100 W, the interconnection of the bubbles makes it not accurate to measure them individually. However, the interconnected bubbles formed a nearly continuous bubble cloud and the distribution of the bubble cloud (or more accurately the density of the bubbles) passing through a sectional length can be measured by the grey value along that section. Therefore, the bubble density along the same sections 1, 2 and 3 were calculated from 20 images for the 100 W case and presented in Fig. 4.16b.

Before the calculation of grey value, the noise and background of the raw images were already removed by subtracting the background image. Therefore, the remained brightness was actually due to the ultrasound bubble cloud. By subtracting the background image (obtained from imaging the liquid metal only) from the flat field (without liquid metal), the difference in grey value was obtained and used as the baseline grey value. When bubble clouds were found in the sample, the grey value will be different to the grey value of the baseline. The ratio between the bubble cloud grey value and that of the baseline actually reflects the bubble density inside the sample. These ratios for the section 1, 2, and 3 for the case of 100 W were plotted in Fig. 4.16b.

Clearly although the data showed in Fig. 4.16a is the bubble number density, while in Fig. 4.16b, they are the bubble densities themselves, but the trend are very similar, indicating that the method we used, *i.e.* using the grey value to represent the bubble density, actually captures the essential characteristics of the bubble cloud distribution and flux behaviour.

4.8 Summary

Using the ultrafast synchrotron X-ray imaging facilities (up to 271,554 fps) at sector 32-ID-B of APS, the highly dynamic phenomena of ultrasonic bubbles, including the nucleation, oscillation, implosion, coalescence of individual bubble, and the collective behaviour of a group of bubbles, i.e. bubble cloud, were studied in great details. The key findings are:

- Bubble implosion is the most efficient mechanism for nucleating new bubbles.

- Bubbles can oscillate in a quasi-static manner for many wave periods in a relatively low acoustic pressure condition.

- Bubble coalescences behave very differently dependent on the properties of the liquids and the acoustic pressure during the different stage of coalescences.

- The bubble size distribution is strongly dependent on the acoustic pressure and the characteristics of the bubble cloud can be quantified by the bubble size distribution and the bubble flux.

Chapter 5: Bubble and acoustic flow interactions with solid particles

After two comprehensive imaging experiments at APS in 2011 and 2012 to study the highly dynamic behaviour of ultrasonic bubbles. The 2013 experiment at APS and the two experiments at DLS in 2013 and 2015 were focused on the interactions of ultrasonic bubbles and the acoustic flow with the solid particles in water and solid phases in liquid metals. A total of 610 videos were taken at ASP, while 222 were acquired at DLS as summarized in Table 5.1. This chapter describes the very typical videos and images acquired in those experiments and the key research findings accordingly.

Table 5.1. *A summary of the relevant experiments conducted at APS and DLS that produce the images presented in this chapter.*

Beamline	X-ray beam	Sample material	[1]S-D (mm)	Experimental Objectives	Number of videos
32-ID-B APS	White	Water	200	Bubble dynamics	97
		Water containing Ge particle	150	Bubble interact with particles	152
		Silicone oil	200	Bubble dynamic	57
		Sn-13%Bi	980	Bubble dynamic	120
		Bi-8%Zn	980	Bubble dynamics	184
I12 DLS	Mono-chromatic	Bi-8%Zn	900	Solidification process	20
		Sn-30%Cu		Microstructure	10
	White	Bi-8%Zn		[2]UST during solidification	155
		Sn-30%Cu		Bubble cloud	37

[1]S-D: Sample-to-detector distance [2]UST: ultrasound treatment

5.1 Microjet flow at bubble implosion

5.1.1 Microjet flow in water

Fig. 5.1 shows that a single bubble implodes in water with a microjet created. Due to the small view field at 271,554 fps, only half of the bubble is captured (Fig. 5.1a-1). At the instant of implosion, there is a microjet created, shooting downwards (Fig. 5.1a-2). In the next frame (3.7 µs later), the bubble was found to break up into a few bubble debris (Fig. 5.1a-3), then grew up and coalesced together (Fig. 5.1a-4). Similar phenomenon was reported by Ohl [17] in water and the microjet was captured using ~600,000 fps with its velocity estimated as ~150 m/s for the bubble radius bigger than 60 µm.

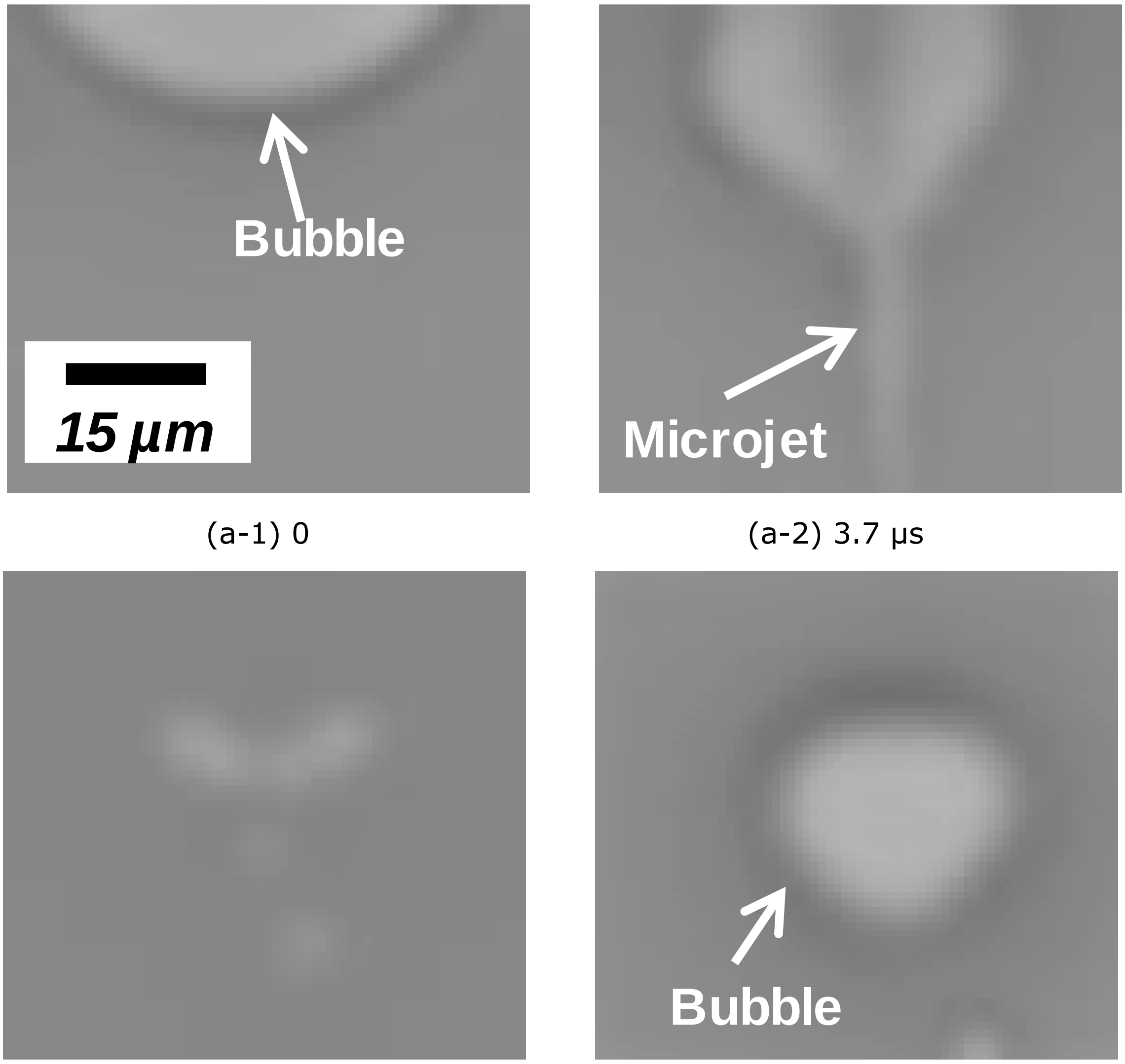

(a-1) 0

(a-2) 3.7 µs

(a-3) 7.4 µs

(a-4) 11.1 µs

Fig. 5.1. *X-ray images taken in water at APS using 271,554 fps, showing bubble implosion with a microjet created (a-2).*

5.1.2 Microjet flow in liquid metal

Fig. 5.2 shows five consecutive images of an ultrasonic bubble in liquid Bi-8%Zn (700K, 427°C) captured using 135,780 fps at APS. A single bubble appeared below the sonotrode tip at 0 s, and expanded as the sonotrode moved up until 14.8 μs. The bubble imploded when the sonotrode moved down at 22.2 μs, creating a microjet pointing towards the sonotrode tip before breaking up into a few bubble debris at 29.6 μs. Apparently, it is difficult to work out the actual velocity of the microjet observed in the liquid metals because the relative lower frame rate used in the X-ray imaging experiments.

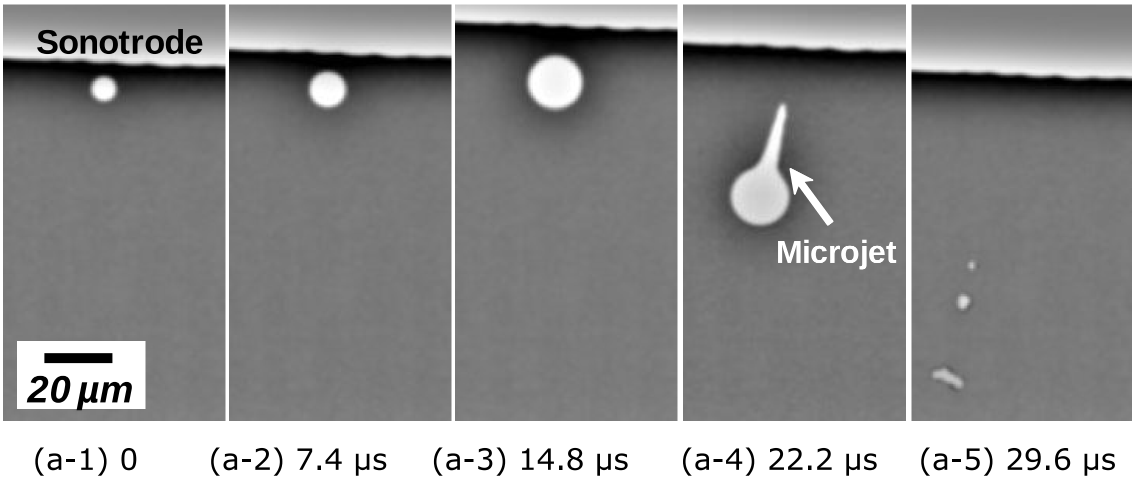

(a-1) 0 (a-2) 7.4 μs (a-3) 14.8 μs (a-4) 22.2 μs (a-5) 29.6 μs

Fig. 5.2. *Five consecutive images of Bi-8%Zn (~427 °C) captured at 32-ID-B of APS using 135,780 fps, showing the implosion of a bubble below the sonotrode tip with the creation of a microjet pointing towards the sonotrode tip.*

5.2 Bubble interaction with solid particles/phases

In order to investigate the interactions between ultrasonic bubbles and solid particles or phases, Germanium (Ge) particles (100 mesh particles with a concentration of 2 mg/ml) was added into water held inside a borosilicate tube (4.42 mm inner diameter, 5.65 mm outer diameter). Fig. 5.3 shows the experimental set-up on the specimen stage of the beamline 32-ID-B of APS. The sonotrode tip was inserted into the tube with the tip positioned at 4.95 mm above the inner bottom surface of the tube as highlighted in the circled and enlarged image.

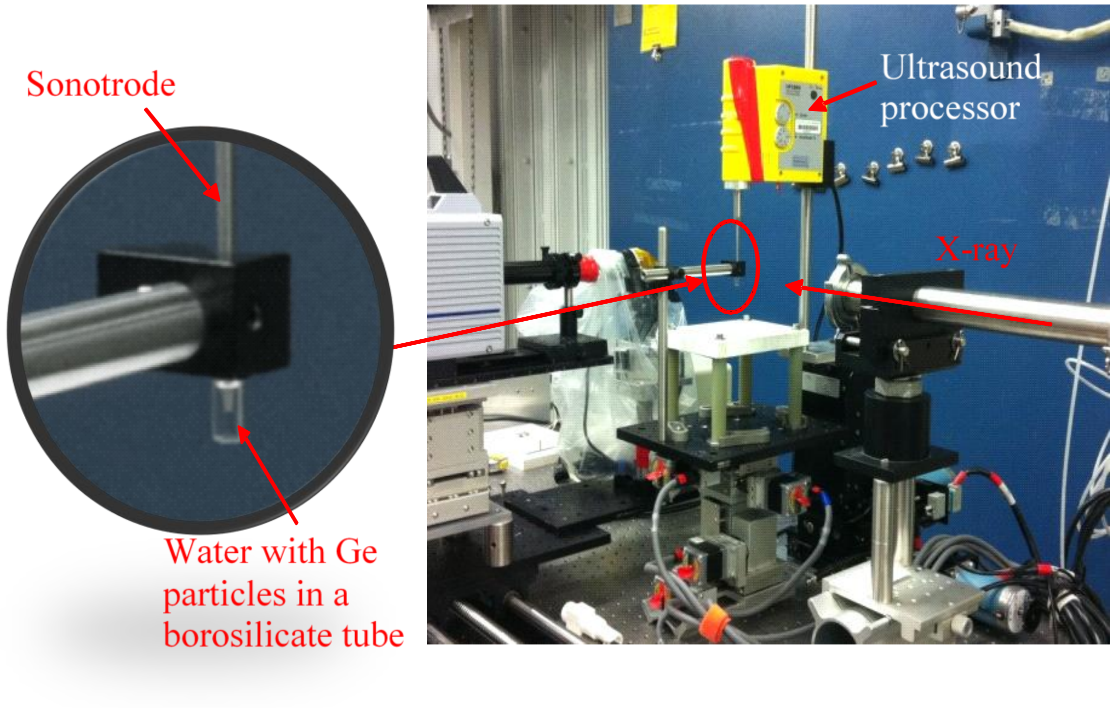

Fig. 5.3. *A Photo of the experimental set-up at APS, and the insert shows the enlarged view of the sonotrode tip and the borosilicate tube containing water mixed with Ge particles with the size of 100 mesh.*

5.2.1 The interaction of bubbles with Ge particles in water

Fig. 5.4 shows a typical series of images captured in water with Ge particles using the set-up showed in Fig. 5.3 at APS with 5413 fps. A bubble was seen to sit at the bottom of borosilicate tube (Fig. 5.4a-1) initially. After the ultrasound was turned on, the spherical bubble surface starts to be distorted (Fig. 5.4a-3) and to form a highly twisted surface morphology. Under the cyclic acoustic pressure, the twisted bubble continued to vibrate and stir the surround Ge particles sat at the bottom of the tube (from Fig. 5.4a-3.to a-10). During this process, the bubble was shown to undergo collapsing, splitting and rejoining with more and more mechanical actions on stirring up the Ge particles (from Fig. 5.4a-11 to a-15).

Fig. 5.5 is a series of X-ray images captured at 5413 fps, showing the motion of a cluster of ultrasonic bubbles and their interactions with the solid Ge particles (the black particles) sat at the bottom of the quartz tubes. The ultrasound power used was 100 W, and the images were taken at ~4.5 mm below the sonotrode tip. The red arrows point the direction of the bubbles' movement. Firstly, a single bubble appeared in Fig. 5.5a-2, moving downwards while oscillating (Fig. 5.5a-3) in responding to the ultrasonic wave. The bubble imploded at Fig. 5.5a-4 before hitting the Ge particles at the bottom in Fig. 5.5a-5. The Ge particles were disturbed by the imploded bubble (Fig. 5.5a-5), and a lot of more Ge particles were stirred up by the continuous arrivals of more bubbles from above (Fig. 5.5a-6 to a-15). It is very interesting to find that, under the cyclic ultrasonic pressure field, the ultrasonic bubbles are pushed downward with a velocity of ~2 m/s while at the same time the surround water and the Ge particles floating in the water do not move at all. The stirred up of the Ge particles are purely because of the bombardment of the imploding bubbles at the bottom, while the Ge particles not hit by the bubble do not move at all (Fig. 5.5a-5 to a-10). All evidence indicates that (1) the bubbles respond to the acoustic pressure field instantaneously and transfer the ultrasound energy into mechanical momentum for the movement. (2) The implosions of bubbles at an interface create microjet flow that can move micrometre size solid particles very effectively, and these are very different to the ultrasound enhanced acoustic flow as described in details in section 5.3.

5.2.2 The interaction of bubbles with Zn phases in Bi-8%Zn alloy

Fig. 5.6 is a typical image sequence, showing an ultrasonic bubble oscillating on top of a solid phase observed in the semi-solid Bi-8%Zn melt captured at APS using 5413 fps. A single bubble was found to attach onto a solid Zn phase at 0s. Under the cyclic acoustic pressure, the bubble kept oscillating and interacting with the solid Zn phase. Because a small ultrasound power of 20 W was used, the interaction between the bubble and solid phase was found to be quite weak. However, after only ~65 wave periods (Fig. 5.6a-13), a small piece (~20 μm) was seen to separate away from the original big piece and moved downwards (Fig. 5.6a-14 and a-15).

Fig. 5.7a-c show a series of image sequences captured at APS using 5413 fps at 0.5, 2.5, and 4.5 mm below the sonotrode tip (an ultrasound power of 20 W), respectively.

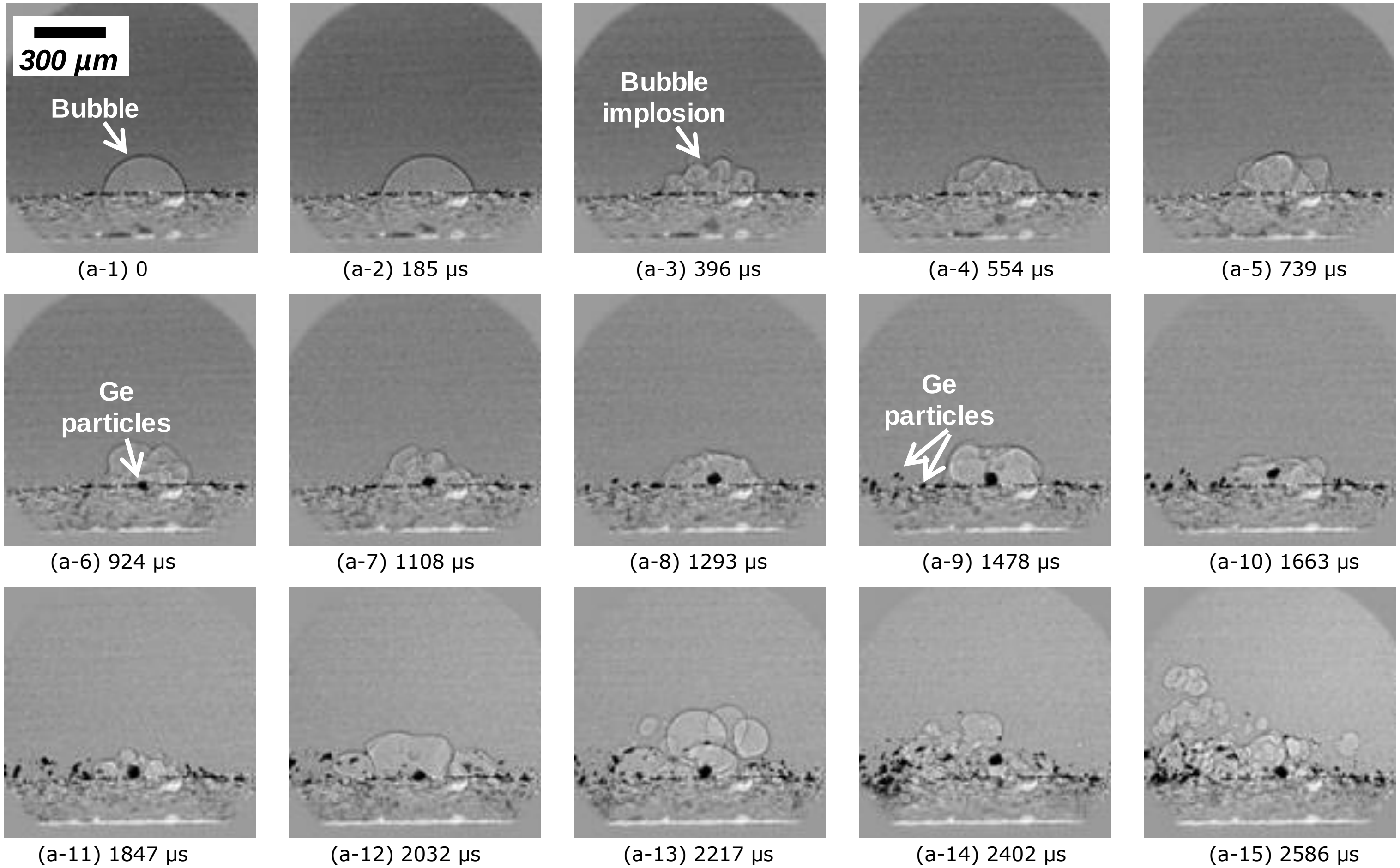

(a-1) 0 (a-2) 185 µs (a-3) 396 µs (a-4) 554 µs (a-5) 739 µs

(a-6) 924 µs (a-7) 1108 µs (a-8) 1293 µs (a-9) 1478 µs (a-10) 1663 µs

(a-11) 1847 µs (a-12) 2032 µs (a-13) 2217 µs (a-14) 2402 µs (a-15) 2586 µs

Fig. 5.4. *X-ray images captured in water at APS using 5413 fps, showing an ultrasonic bubble initially sit at the bottom of a borosilicate tube where the Ge (the black) particles were present, and its interaction with the Ge particles during and after implosion under an ultrasound power of 100 W. The image centre is ~4.5 mm below the sonotrode tip.*

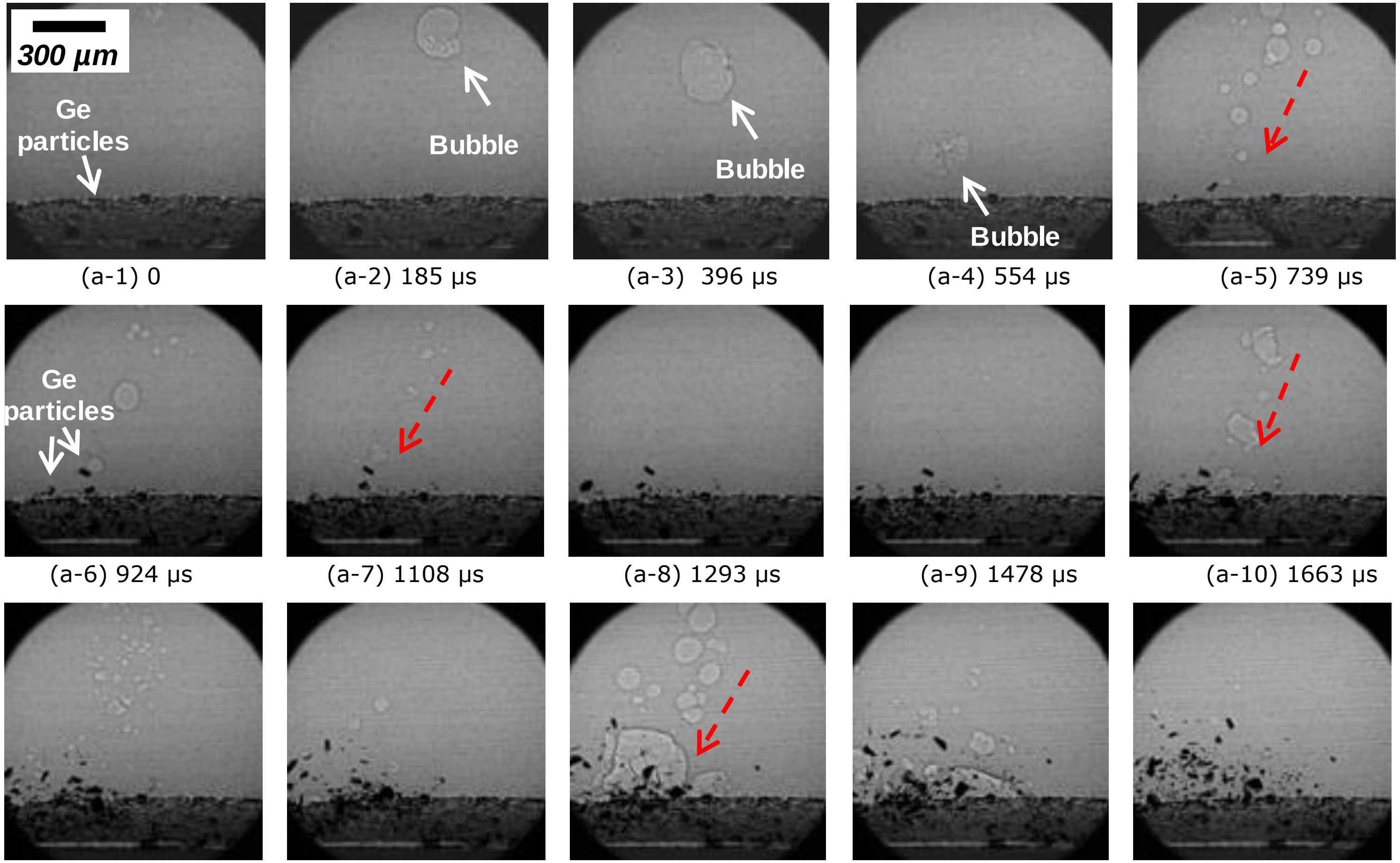

(a-1) 0 (a-2) 185 µs (a-3) 396 µs (a-4) 554 µs (a-5) 739 µs

(a-6) 924 µs (a-7) 1108 µs (a-8) 1293 µs (a-9) 1478 µs (a-10) 1663 µs

(a-11) 1847 µs (a-12) 2032 µs (a-13) 2217 µs (a-14) 2402 µs (a-15) 2586 µs

Fig. 5.5. *X-ray images captured in water at APS using 5413 fps, showing ultrasonic bubbles bombarding at the bottom surface of a borosilicate tube where Ge particles were present. The red dash lines mark the moving directions of the bubbles. The ultrasound power is 100W and the image centre is at about 4.5 mm below the sonotrode tip.*

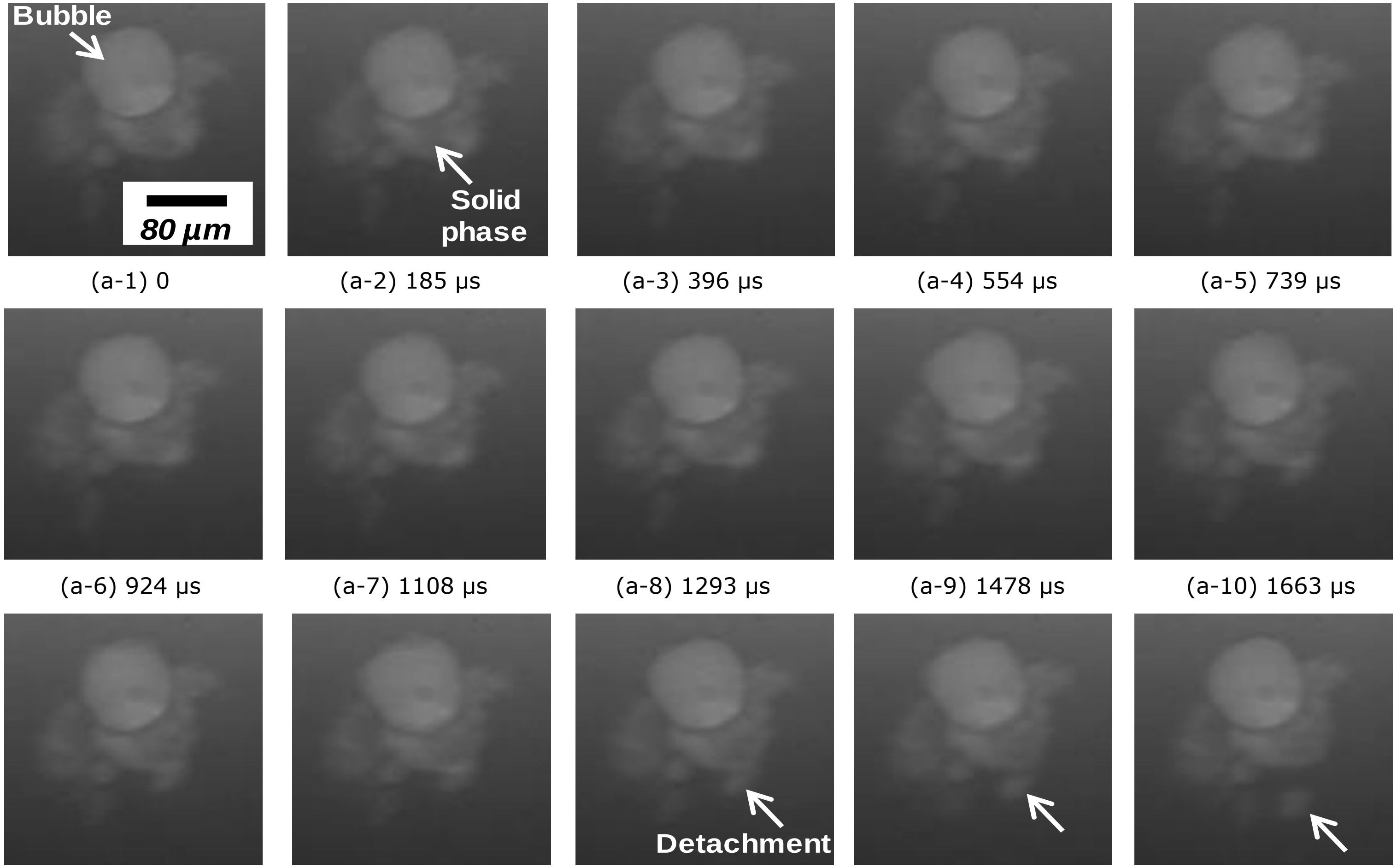

(a-1) 0 (a-2) 185 µs (a-3) 396 µs (a-4) 554 µs (a-5) 739 µs

(a-6) 924 µs (a-7) 1108 µs (a-8) 1293 µs (a-9) 1478 µs (a-10) 1663 µs

(a-11) 1847 µs (a-12) 2032 µs (a-13) 2217 µs (a-14) 2402 µs (a-15) 2586 µs

Fig. 5.6. *A typical X-ray image sequence captured at APS using 5413 fps, showing an ultrasonic bubble oscillating on top of a solid Zn phase observed in the semi-solid melt of a Bi-8%Zn alloy. The ultrasound power used is 20W.*

The melt temperatures measured at TC1, TC2 and TC3 were 650 K, 630K, 600K (377°C, 357°C, 327°C) respectively, indicating that the alloy was in a fully liquid state. A sonotrode with a tip diameter of ~ 0.5 mm and 20 W input power were used in the experiment to allow the dynamic behaviour of bubbles and particles surrounding the sonotrode tip to be imaged within the limited field of view, i.e. 1 mm × 1 mm at 5413 fps. Fig. 5.7a-1 shows that, although the alloy is in a liquid state, some solid Zn particles (marked by the arrows in Fig. 5.7a-1) formed around the sonotrode tip because of the relatively cold surface of the sonotrode tip. After applying ultrasound of 20 W, the Zn particles were "shaken" off the tip and flew downward together with any ultrasound bubbles as shown in Fig. 5.7a-2 to a-3). Due to the limited field of view (1 × 1 mm in this case), the behaviour of the bubbles and particles further away from the sonotrode tip were imaged separately using the identical melt conditions and ultrasound input power as that in Fig. 5.7a. The typical image sequences captured at 2.5 mm and 4.5 mm below the sonotrode tip are shown in Fig. 5.7b and c, respectively. The image sequences taken at the different distances away from the sonotrode tip allowed systematic and statistical datasets to be extracted from the images for studying quantitatively the dynamic behaviour of the bubbles, the particles and the enhanced metal flow under ultrasonic waves.

Firstly, the dynamic behaviour of an individual bubble and a particle were studied in detail by extracting 8 images that contained a typical bubble and a typical Zn particle at the same condition as those in Fig. 5.7b. The 8 selected images were enlarged and shown in Fig. 5.8a with the bubble circled and marked B, and the particle boxed and marked P. Using the in-house Matlab® code, the movement of B and P were tracked and their velocities were calculated and showed in Fig. 5.8b. Clearly, B moved in a zigzag manner, while P travelled in a straight line, and the calculated average velocity of B (0.26 m/s) was ~70% higher than that of P (0.15 m/s). These results indicate that the alternating acoustic pressure affects much more the movement of bubbles than that of the particle. Statistical analyses made on all the images and videos studied revealed that the trajectories of the particles were either a straight line (Fig. 5.8b), or slightly curved paths, further confirming that the particles are mainly dragged and moved by the flow of liquid metal, but not affected much by the alternating acoustic field. Hence the velocity of the particles calculated can be considered as the actual velocity of the liquid metal.

(a) X-ray images taken at 0.5 mm below the sonotrode tip (an ultrasound power of 20 W) in Bi-8%Zn, 5413 fps

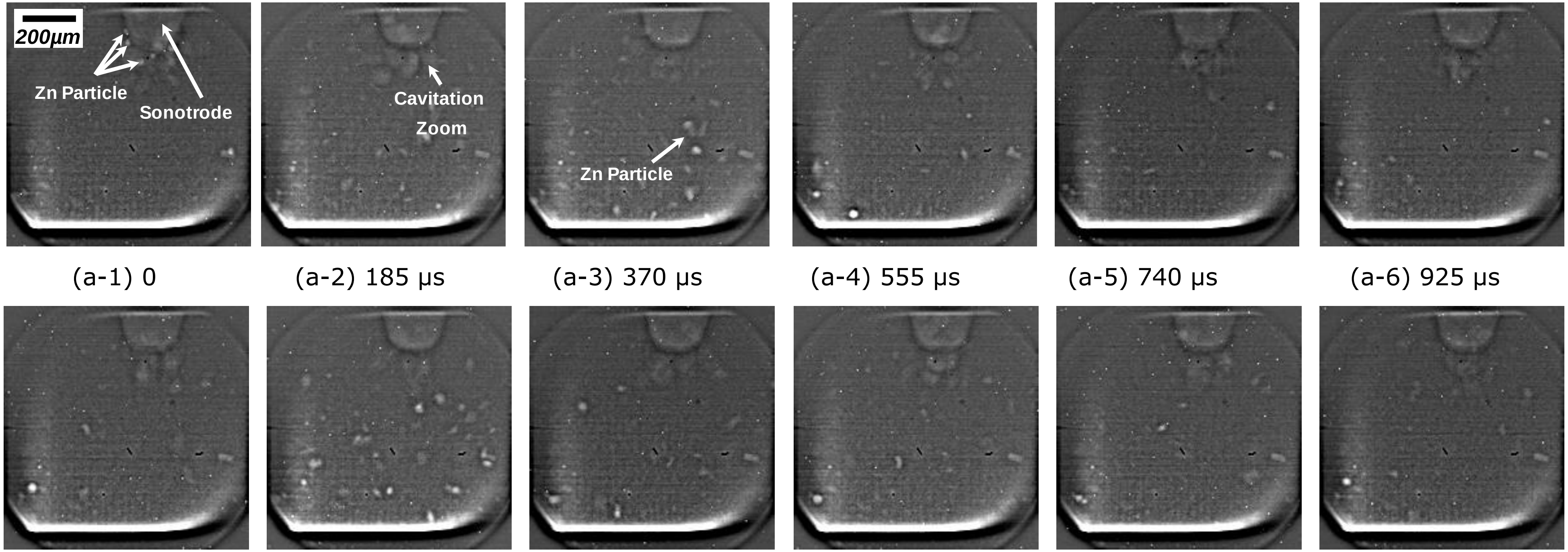

(a-1) 0 (a-2) 185 µs (a-3) 370 µs (a-4) 555 µs (a-5) 740 µs (a-6) 925 µs

(a-7) 1110 µs (a-8) 1295 µs (a-9) 1480 µs (a-10) 1665 µs (a-11) 1850 µs (a-12) 2035µs

(b) X-ray images taken at 2.5 mm below the sonotrode tip (an ultrasound power of 20 W) in Bi-8%Zn, 5413 fps

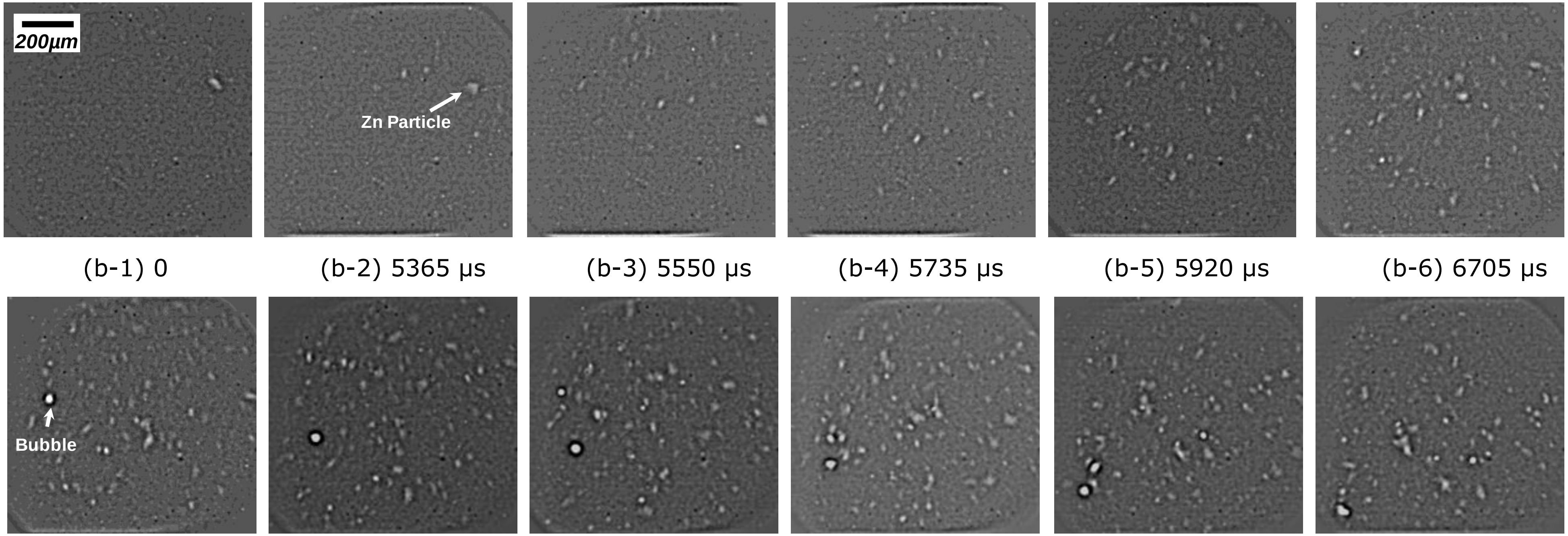

(b-1) 0 (b-2) 5365 μs (b-3) 5550 μs (b-4) 5735 μs (b-5) 5920 μs (b-6) 6705 μs

(b-7) 6290μs (b-8) 6475μs (b-9) 6660 μs (b-10) 6845 μs (b-11) 7030μs (b-12) 7215 μs

(c) X-ray images taken at 4.5 mm below the sonotrode tip (an ultrasound power of 20 W) in Bi-8%Zn, 5413 fps

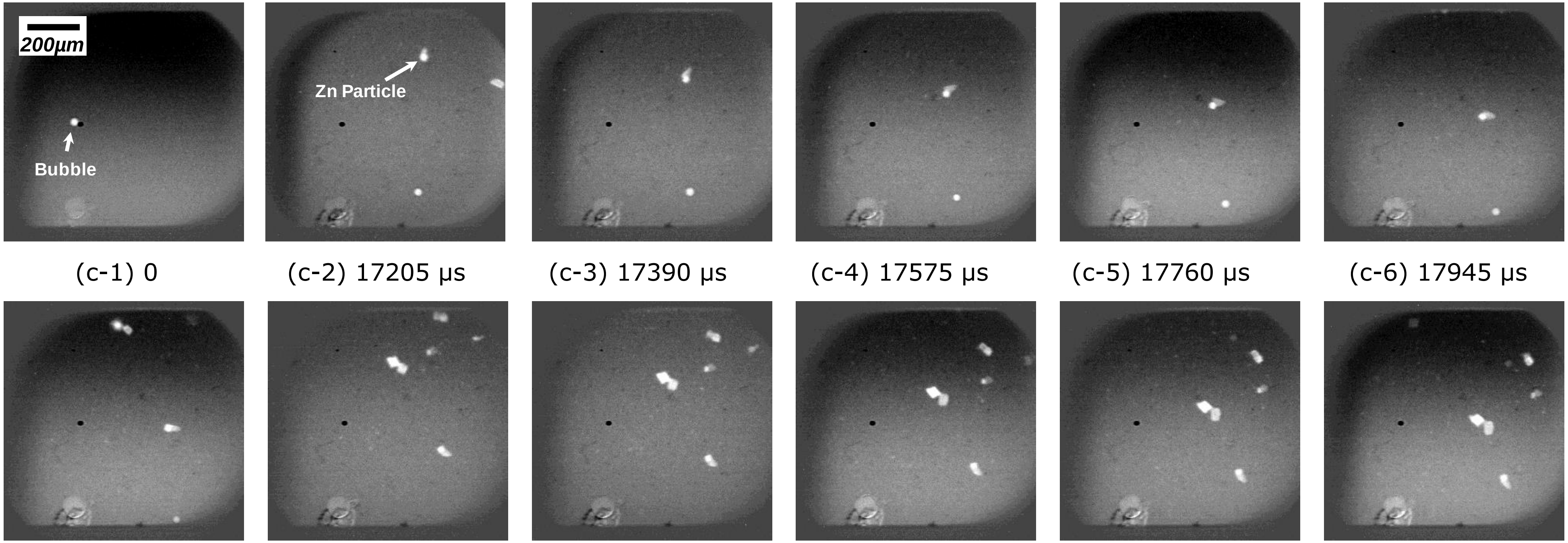

(c-1) 0 (c-2) 17205 µs (c-3) 17390 µs (c-4) 17575 µs (c-5) 17760 µs (c-6) 17945 µs

(c-7) 18130 µs (c-8) 18315 µs (c-9) 18500 µs (c-10) 18685 µs (c-11) 18870 µs (c-12) 19055 µs

Fig. 5.7. *A series of images captured in liquid Bi-8%Zn alloy with an ultrasound power of 20 W at APS using 5413fps. The images were taken at (a) 0.5 mm, (b) 2.5 mm and (c) 4.5 mm below the sonotrode tip, respectively.*

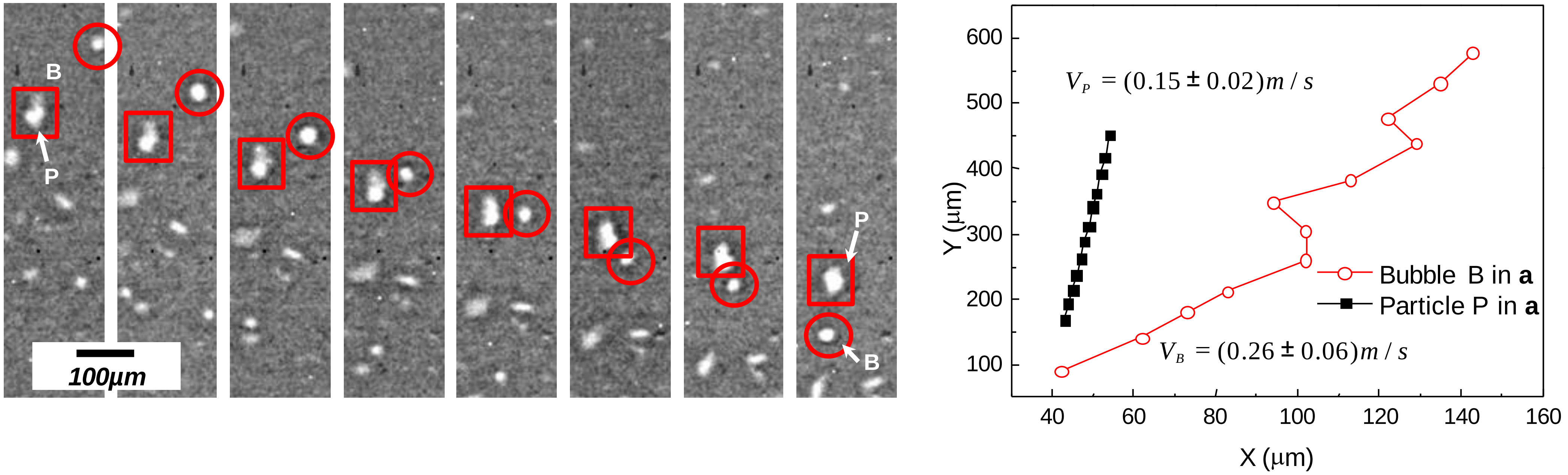

(a-1) 0 | (a-2) 185 μs | (a-3) 370 μs | (a-4) 555 μs | (a-5) 740 μs | (a-6) 925 μs | (a-7) 1110 μs | (a-8) 1295 μs

(a) **(b)**

Fig. 5.8. *(a) Eight typical images extracted from the image captured at 2.5 mm below the sonotrode tip, showing the locations of bubble B and particle P, and their trajectories were plotted in (b).*

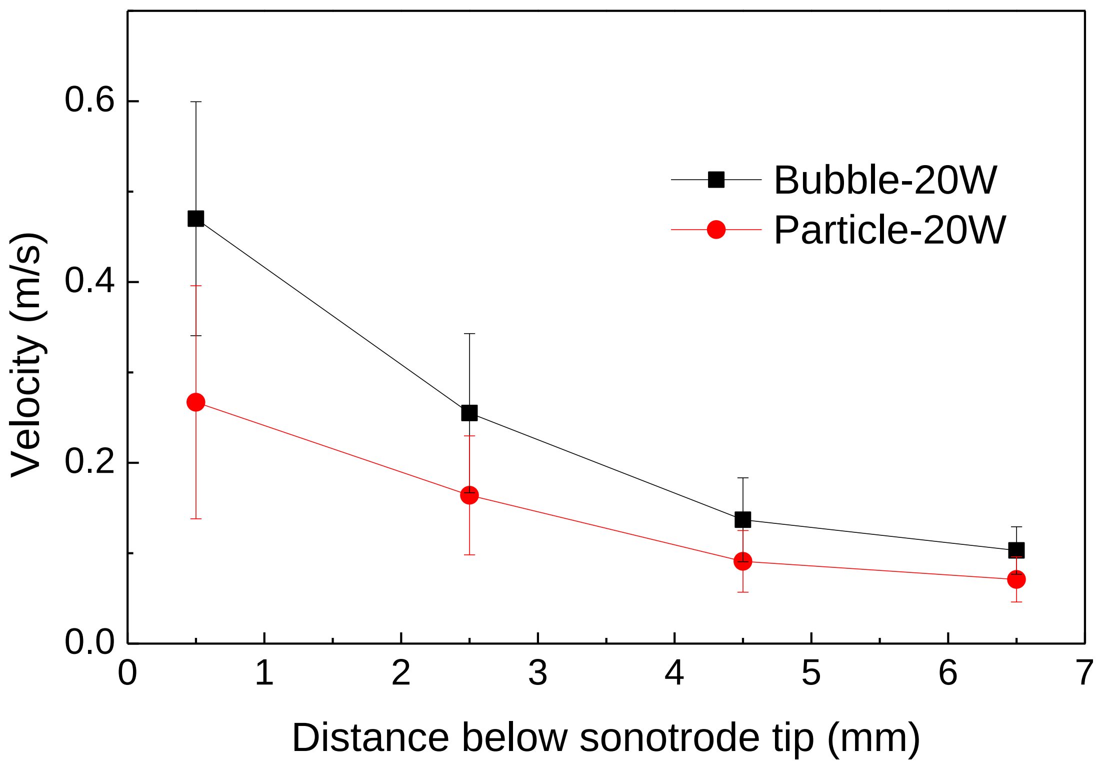

Fig. 5.9. *The velocities of particles and bubbles at different distances away from the sonotrode tip when the ultrasound input power of 20 W was applied. The error bar is the standard deviation of the measured dataset (> 20 particles and bubbles are measured for each point) in the field of view.*

Fig. 5.9 shows the calculated velocities for the particles and bubbles in the images (> 20 particles and bubbles were measured in each image) captured at different locations below the sonotrode tip with the ultrasound input powers of 20, respectively. At the position close to the sonotrode tip, the bubble velocity is 70 - 100% higher than the particle velocity, but the difference in velocity reduces gradually as it moves away from the sonotrode tip.

5.3 The effects of bubbles and acoustic flow on microstructures

5.3.1 The solidification microstructure of Bi-8%Zn

Three alloys, Bi-8%Zn, Sn-13%Bi and Sn-30%Cu alloys, selected for the real-time imaging studies. Fig 5.10 shows the typical real-time X-ray images obtained for each of them during the controlled solidification trials with the aim of selecting the best primary solid phases with the appropriate size and morphology for the imaging studies. It was found that Bi-8%Zn alloy has the primary Zn phase of needle shape with the average size of ~250 μm and the absorption contrast give a more clearly X-ray images compared to the other two cases. Hence Bi-8%Zn alloy was chosen for the subsequent studies.

Fig. 5.11 shows the primary Zn phases (white particles) formed during solidification. The area percentages of the Zn phase in the view field were measured from the real-time images showed in Fig. 5.12 captured under 53 keV monochromatic beam at DLS. The Zn phase in the Bi-8%Zn alloy is needle-shaped phase and grows as the temperature goes down. When the temperature is below 295 °C, the percentage of the solid Zn phase increases steeply and reaches 25% at 253°C. This percentage is higher than that calculated from the phase diagram using lever rule (Solid Zn phase occupies ~13.8% of the whole alloy at 254.5°C).

5.3.2 Control of the liquid-solid interface

Trial experiments were carried out first to carefully control the temperatures of the alloys and the temperature gradient in the thin channel area during solidification in order to form liquid-solid interface in the view field for imaging and to study the effects of the ultrasound bubbles and acoustic flow on the L-S interface. Fig. 5.13a shows typical temperature profiles of the Bi-8%Zn alloys measured during the controlled cooling process illuminated under the white beam. The cooling started at ~ 400 °C (TC1) with a cooling rate in all experiments controlled at ~ 0.2 °C/s. Relative stable temperatures can be normally achieved after 1500 s with ~47 °C difference between TC1 and TC3, giving a temperature gradient of ~5.2 °C/mm. Real-time X-ray images show that the solid phase formed during solidification is primary Zn particles (needle-shaped white particles, Fig. 5.12) and when TC3 reached at 245°C, TC2 will be normally at ~274°C. This temperature gradient allows a clear liquid-solid solidification front formed between TC 2 and TC3. The insert in Fig. 5.13a shows the sudden jump of temperature when the ultrasound was switched on, which will be discussed later. The white beam has an equivalent heating power of 0.028 W/mm^2 (calibrated for the experiment of Bi-8%Zn alloy). Hence when the beam is on, the temperatures jump ~1°C at TC2 and TC3 as shown in Fig. 5.13b.

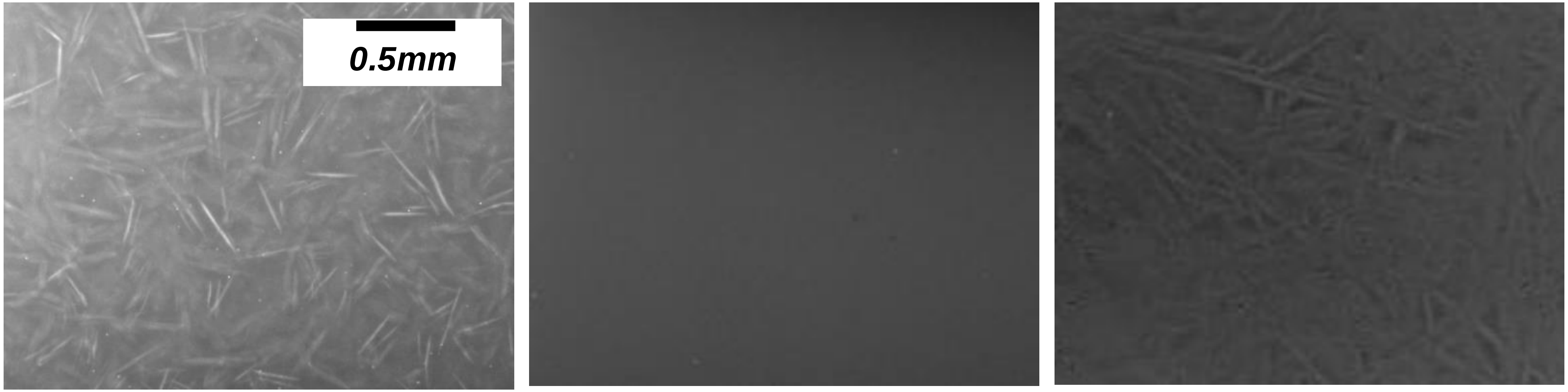

(a) **(b)** **(c)**

Fig. 5.10. *Typical synchrotron X-ray image for (a) Bi-8%Zn, (b) Sn-13%Bi and (c) Sn-30%Cu. The samples are double-side polished of a thickness of 0.3 mm.*

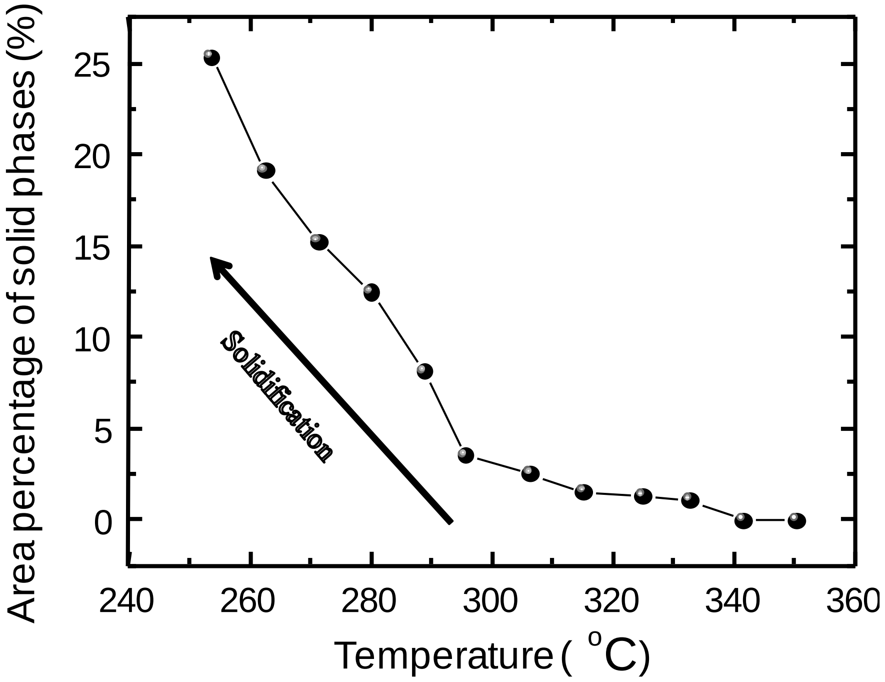

Fig. 5.11. *The area percentage of the solid Zn phase (white particles) at different temperatures during the solidification of Bi-8%Zn alloy in the thin channel region of the quartz tube.*

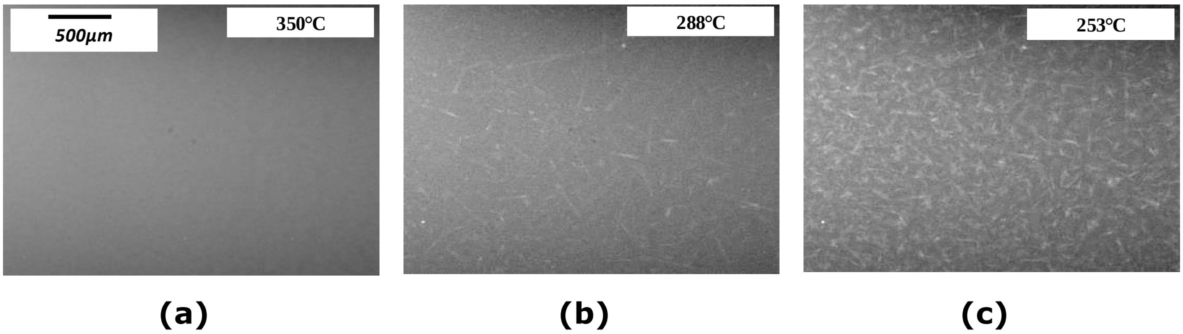

(a) **(b)** **(c)**

Fig. 5.12. *Real time X-ray images obtained using monochromatic beam of 53 KeV at DLS during the solidification of Bi-8%Zn at (a) 350 °C, (b) 288 °C and (c) 253 °C. The images are taken at 30 fps, with the exposure time of 0.3 ms.*

In order to investigate the influence of the white beam heating on the solidification of alloy, the solidification experiment without ultrasound was conducted first. The photos in Fig. 5.13c show that the heat from the white beam (10 minutes) has no obvious influence on the solidification front. Therefore, the effect of the white beam heating can be ignored. The procedure for achieving the temperature profiles showed in Fig. 5.13a was then used in all subsequent experiments of the Bi-8%Zn alloys.

5.3.3 Erosion of the liquid-solid (L-S) interface

Fig. 5.14 shows, at the ~5.5 mm below the sonotrode where is ~267°C, an ultrasound bubble appears at the L-S interface, and keeps pulsing on the top of the L-S interface, knocking out the primary Zn particles, and eroded into the solid phase. The detached particles are washed away by the streaming flow (in an anticlockwise direction) above the L-S interface and delivered to the bulk liquid. Please notice that there are also many detachments at the two shoulders of L-S interface which is washed away by the streaming flow. In order to find out the effect of the pulsing bubble and streaming flow on the L-S interface, two extreme conditions, that is, the erosion depth of the right shoulder of the L-S interface and the depth of the bubble "eating" into the L-S interface (by tracing the bottom of the bubble as the bubble-interface contact point as marked Fig. 5.14a-4) are measured, and the results are showed in Fig. 5.15a. It was found that the velocity of bubble eroding into the L-S interface is relatively constant at ~300 μm/s, without considering the fluctuation from 0.6 s to 1.2s which was caused by the movement of bubble in horizontal direction on the L-S interface. While the streaming flow caused erosion of L-S interface at ~200 μm/s. Hence the pulsing of the bubble definitely adds an extra contribution to the erosion of the L-S interface on top of the contribution from the acoustic flow.

Fig. 5.15b shows the bubble pressure and velocity at bubble wall calculated by using Gilmore Model (initial bubble radius is 60 μm, and ambient pressure is 0.24 MPa [42]), and they are ~50 MPa and ~30 m/s at their maximums within the 100 cycles of ultrasonic waves. The bubble pulsing to enhance the solid particle fragmentation at the L-S interface will be discussed in more details in Chapter 7.

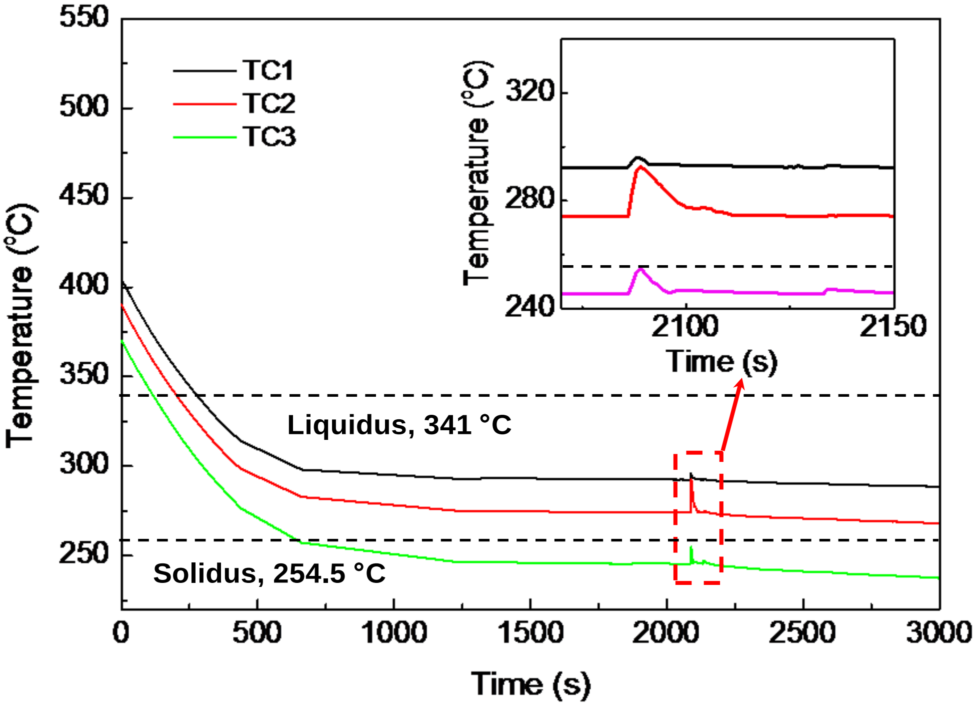
550
500
450
400
350
300
250
Temperature (°C)
0
500
1000
1500
2000
2500
3000
Time (s)
TC1
TC2
TC3
Liquidus, 341 °C
Solidus, 254.5 °C
320
280
240
Temperature (°C)
2100
2150
Time (s)

(a)

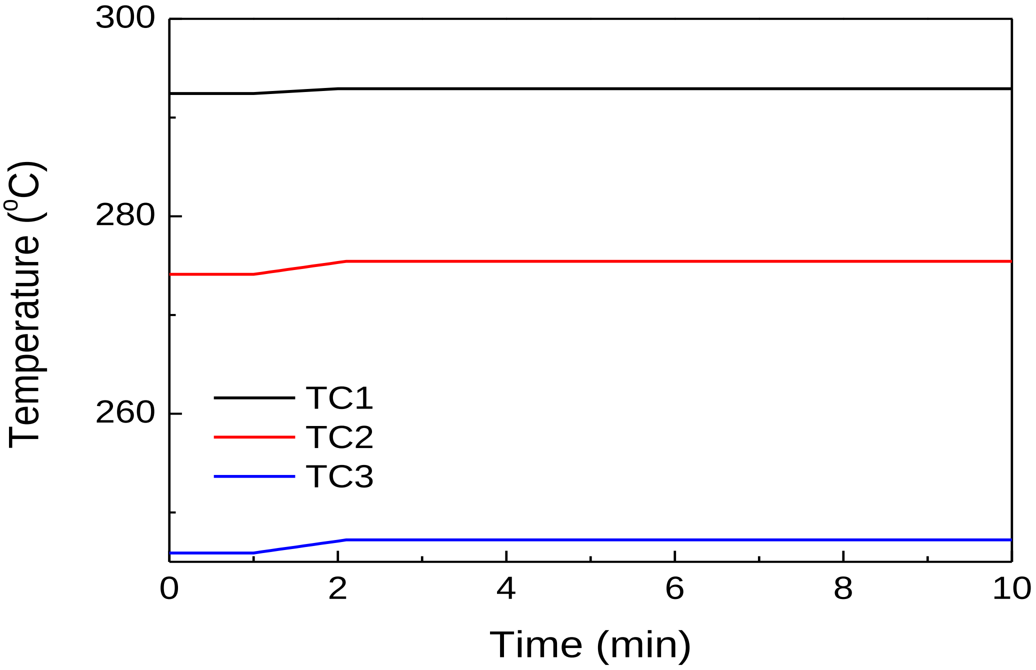
300
280
260
Temperature (^{o}C)
0
2
4
6
8
10
Time (min)
TC1
TC2
TC3

(b)

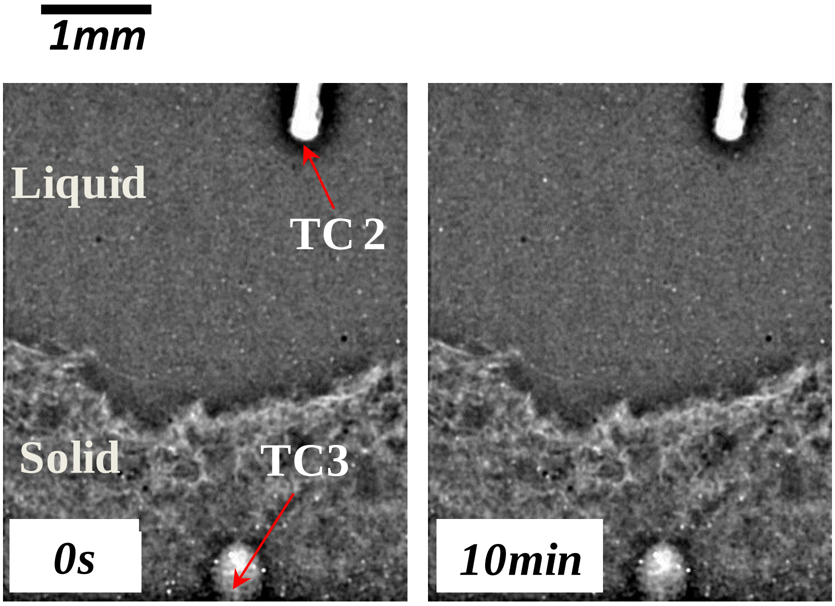

(c)

Fig. 5.13. *(a) The measured temperatures at locations TC1, TC2, and TC3 showing the cooling process and the insert shows the temperature jump when ultrasound is turned on. (b) The measured temperature at locations TC1, TC2, and TC3 when the white X-ray beam is on and (c) the solidification microstructure of Bi-8%Zn at 0 (left) and 10 minutes (right) after the white beam is turned on. (The images were captured at 1000 fps, with exposure time of 990 μs).*

5.3.4 Fragmentation of the solid phases

Fig. 5.16a shows the real-time fragmentation of a needle-shaped primary Zn phase caused by the joint effects of bubble pulsing and acoustic flow. A clear L-S interface was formed at the position of 5 mm below the sonotrode. The two bright columns are the “fingers” of the Al-20%Cu slot sample (250 μm thick) inserted into the thin channel (clearly shown in Fig. 3.9c). When the ultrasound (60 W) was switched on, a single bubble was seen to reach the L-S interface pulsing on the interface and on the right side of a needle-shaped ~200 μm long Zn phase (Fig. 5.16a-1). The bubble kept pulsing at the same position for ~50 ms (>1,500 cycles of ultrasonic waves), and then passed the Zn phase to the left. The long Zn was seen broken up after 55 ms of bubble pulsing on it (comparing the circled features in Fig. 5.16a-2 and Fig. 5.16a-3). The broken fragment was washed away by the streaming flow to the left, leaving a ~ 60 μm long part still embedded inside the solid phase below the L-S interface.

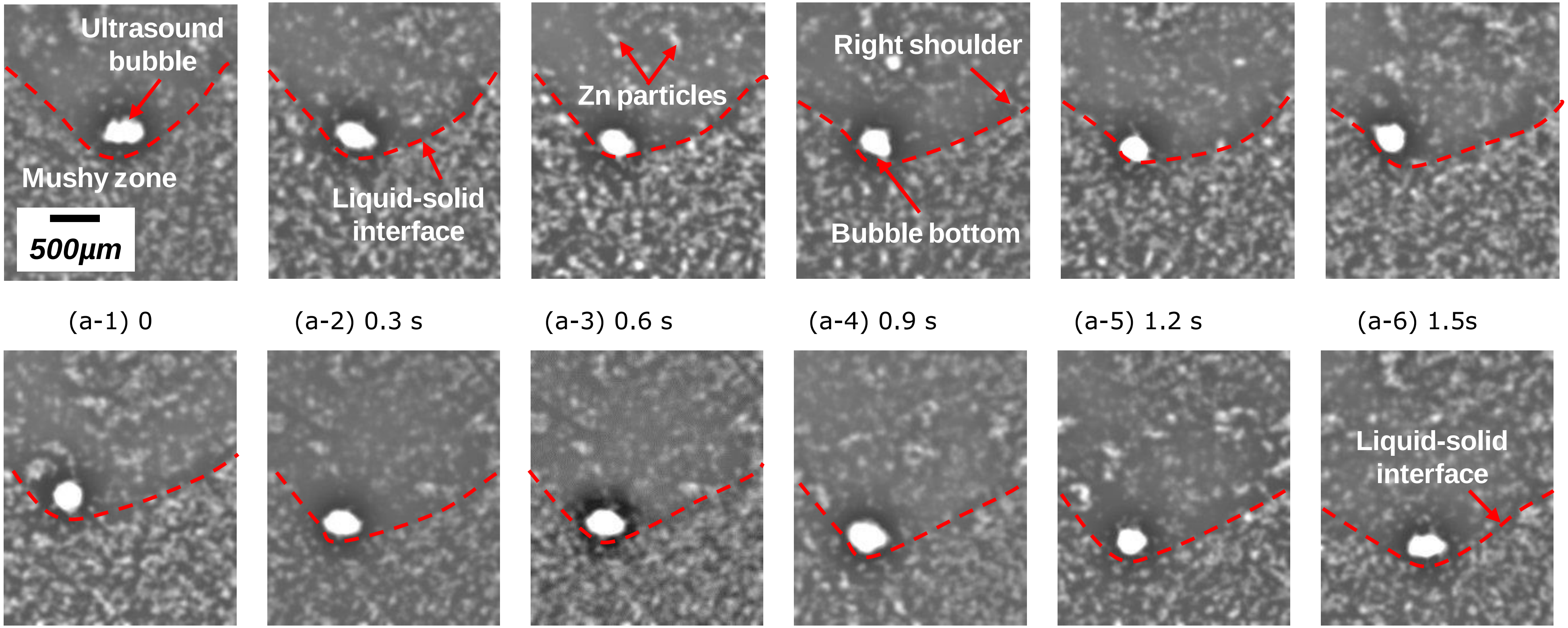

(a-1) 0 (a-2) 0.3 s (a-3) 0.6 s (a-4) 0.9 s (a-5) 1.2 s (a-6) 1.5s

(a-7) 1.8 s (a-8) 2.1 s (a-9) 2.4 s (a-10) 2.7.s (a-11) 3 s (a-12) 3.3s

Fig. 5.14. *Image sequence of a single ultrasonic bubble pulsing and eroding into an L-S interface found in Bi-8%Zn alloy captured at 1500 fps. (TC3 = 245°C, TC2 = 274°C before starting ultrasound). The center position of the image is ~5.5 mm below the sonotrode and ultrasound power used was 60 W.*

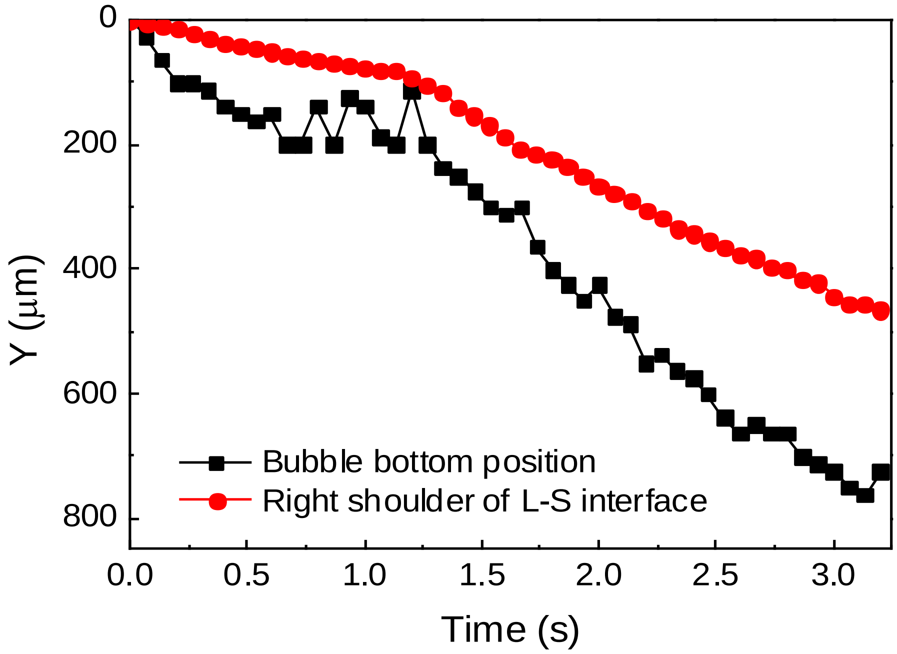
0
200
400
600
800
Y (µm)
0.0
0.5
1.0
1.5
2.0
2.5
3.0
Time (s)
Bubble bottom position
Right shoulder of L-S interface

(a)

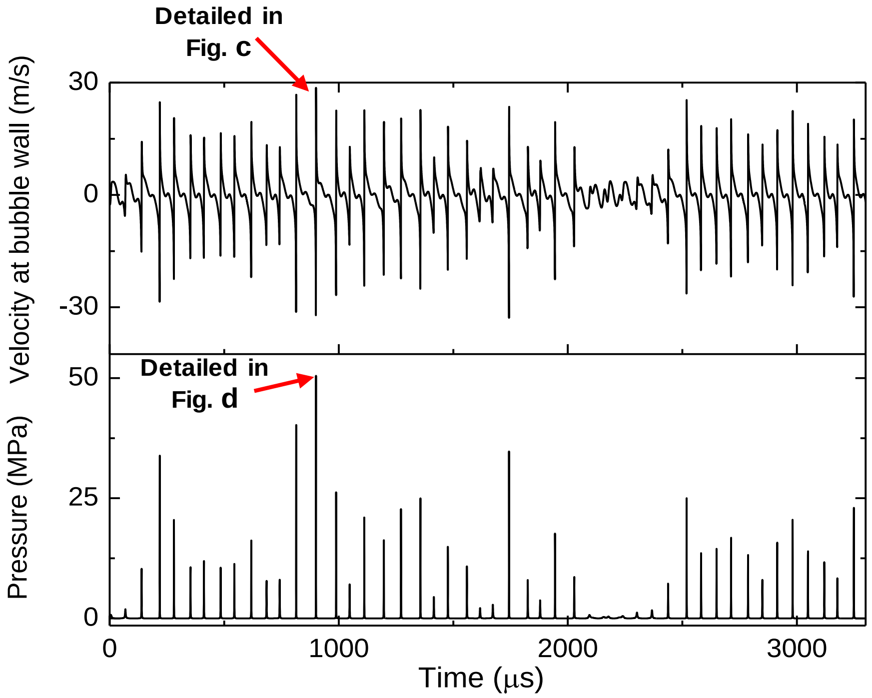
Detailed in
Fig. c
30
0
-30
Velocity at bubble wall (m/s)
Detailed in
Fig. d
50
25
0
Pressure (MPa)
0
1000
2000
3000
Time (µs)

(b)

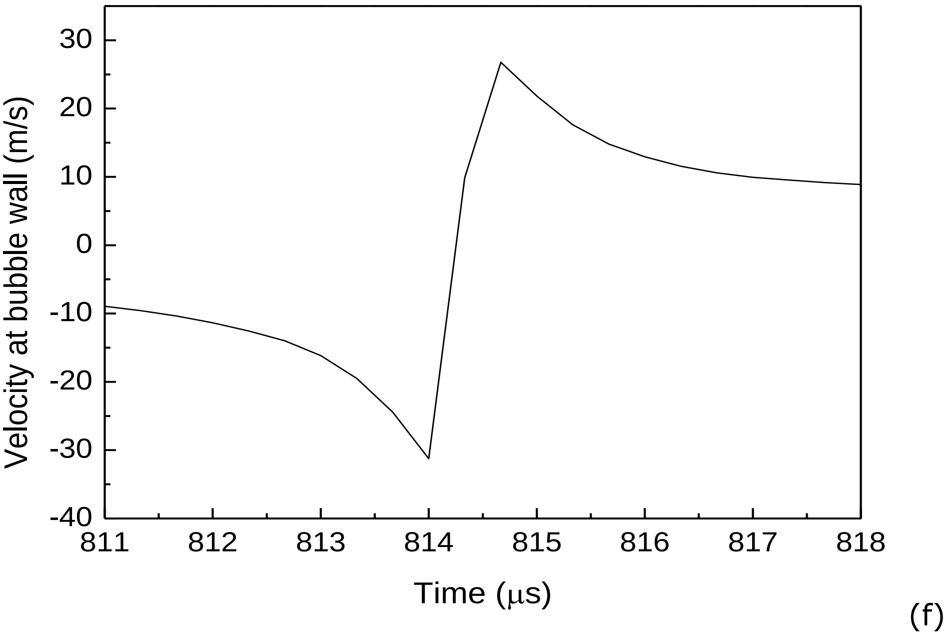

(c)

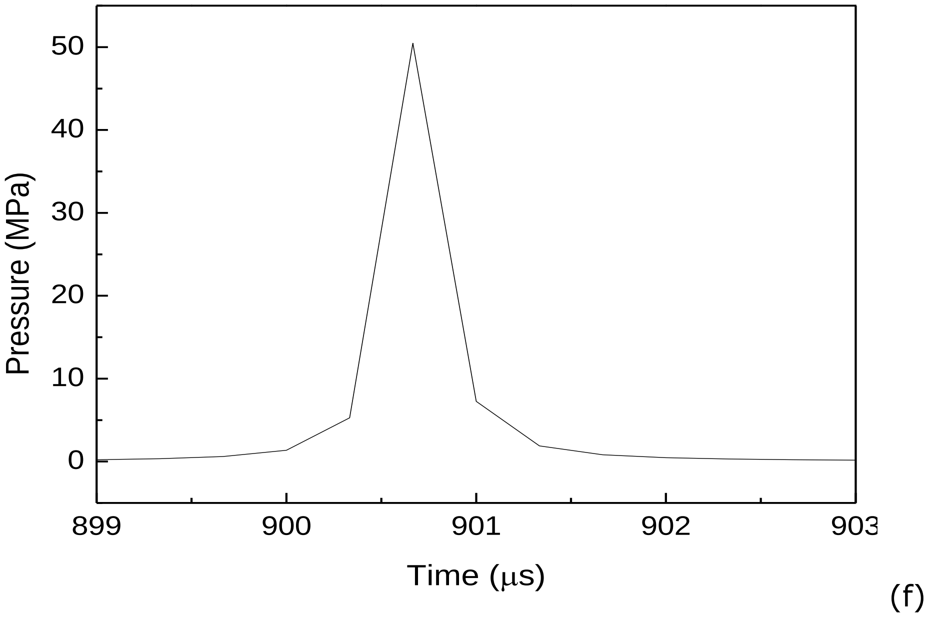

(d)

Fig. 5.15. *(a) Measurement of the depth caused by bubble eroding into the L-S interface (bubble bottom position) and the erosion depth of right shoulder of L-S interface purely due to the acoustic flow as a function of time, and (b) the pressure and velocity at bubble wall calculated by using Gilmore model (initial bubble radius is 60μm, and ambient pressure is 0.24 MPa), and the peak values are enlarged in (c) and (d).*

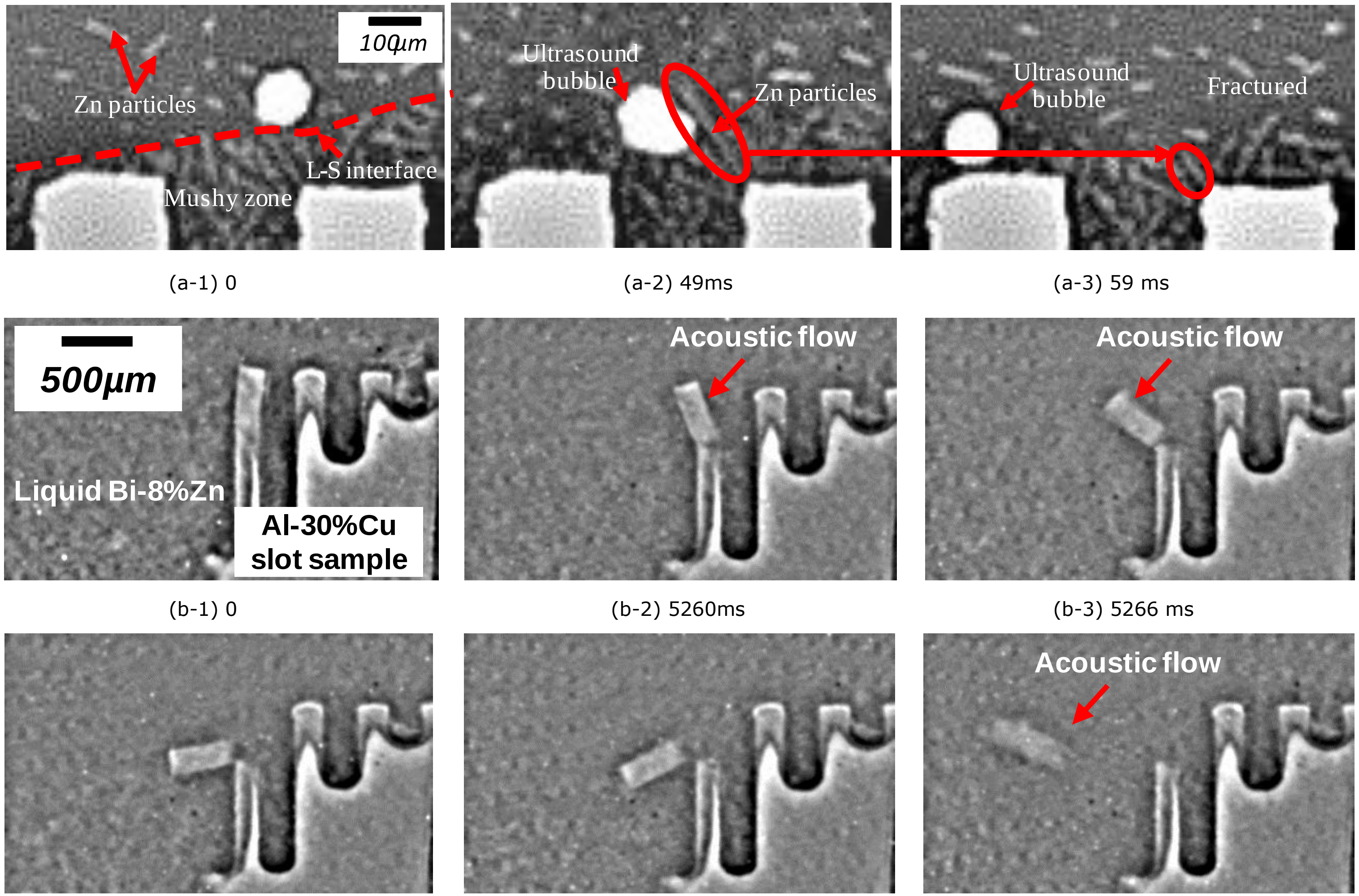

(a-1) 0 (a-2) 49ms (a-3) 59 ms

(b-1) 0 (b-2) 5260ms (b-3) 5266 ms

(b-4) 5261 ms (b-5) 5269 ms (b-6) 5272 ms

Fig. 5.16. *X-ray images (1500 fps, ultrasound power of 60 W, 5 mm below sonotrode), showing the fragmentation of (a) a needle-shaped Zn phase by a bubble and acoustic flow; and (b) a "finger" made by Al-20%Cu alloy. The temperature at the bubble position is ~270°C.*

In a similar experiment (liquid Bi-8%Zn inserted with a thin Al-20%Cu slot sample, 60 W ultrasound power), when imaging was focusing onto the thin “fingers” of the Al-20%Cu slot sample, it was found that one “finger” was bent after ~ 5.2 s ultrasonic treatment due to the acoustic flow, and then was broken up (Fig. 5.16b-5), and flowed away by the acoustic flow with the velocity calculated at ~1m/s (from Fig. 5.16b-5 to b-6). The detailed dimension of the Al-20%Cu slot sample is in **Appendix 3**.

Both cases provide very clear real-time evidences that the acoustic flow above the L-S interface play an important role in causing the fragmentation and detachment of solid particles. In order to clarify the influence of acoustic flow on the L-S interface under different ultrasound powers, in situ observations at the regions further away from the sonotrode tip (where bubbles are less likely to reach and survive) but still inside the thin channel were made.

Fig. 5.17 shows that different ultrasound powers were applied into liquid Bi-8%Zn during directional solidification to investigate the effects of acoustic flow on the solid Zn phases and liquid-solid interface. The images were captured at 1000 fps and the center position of the images is ~6 mm below the sonotrode tip which is between the TC2 and TC3. The temperatures at TC2 and TC3 before ultrasound are 274°C and 245°C, respectively. The ultrasound time is 2 s.

Fig. 5.13c already shows that, without ultrasound (0 W), no obvious detachment of solid Zn phases were found at the liquid-solid interface. At 20 W, Fig. 5.17a shows that with 2 s ultrasound applied, only the ‘loose’ particles on the L-S interface (marked by the white circle) were washed away by acoustic flow. The arrows show the direction of enhanced streaming flow obtained by tracking the trajectory of the Zn particles in the bulk liquid. The fluid flow is seen relatively symmetric to the sonotrode, and clockwise on the left and anti-clockwise on the right. When the power increase to 60 W, instead of washing off the individual particles, the streaming flow caused a ‘cleavage’ of a big cluster of solid Zn phase as showed in Fig. 5.17b, and the big cluster was broken up. Then some of them were washed away by the flow and carried back to the liquid region. The initial relatively flat L-S interface was changed significantly by the ultrasonic enhanced flow as indicated by the white dash-lines marked in Fig. 5.17b. At 100 W (Fig. 5.17c), the L-S interface was effectively destroyed by the ultrasonic flow and all the L-S interface in the view field collapsed after 1286 ms ultrasound processing, and the knock-off Zn particles from the interface were flowed back to the liquid region above.

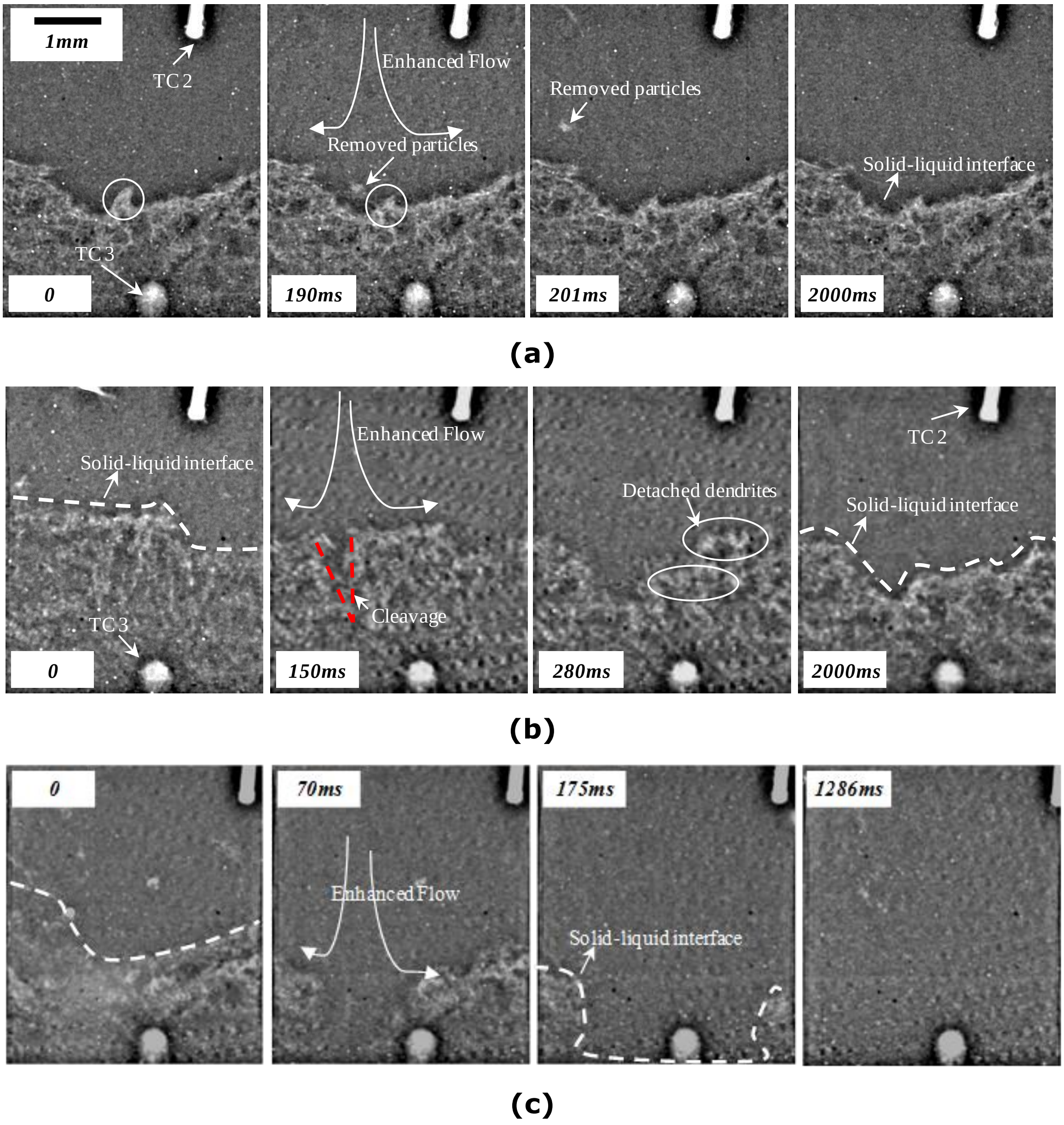

Fig. 5.17. *A series of images sequences of Bi-8%Zn, showing the effects of input ultrasound powers on the changes of the liquid-solid interface: (a) 20W, (b) 60W, (c) 100W.The temperatures of TC2 and TC3 are 274°C and 245°C respectively. The white arrows indicate the direction of ultrasound induced streaming flow and the movement of the Zn phases in the liquid (1000 fps, 990 μs exposure time). The center position of the image is about 5.5 mm below the sonotrode.*

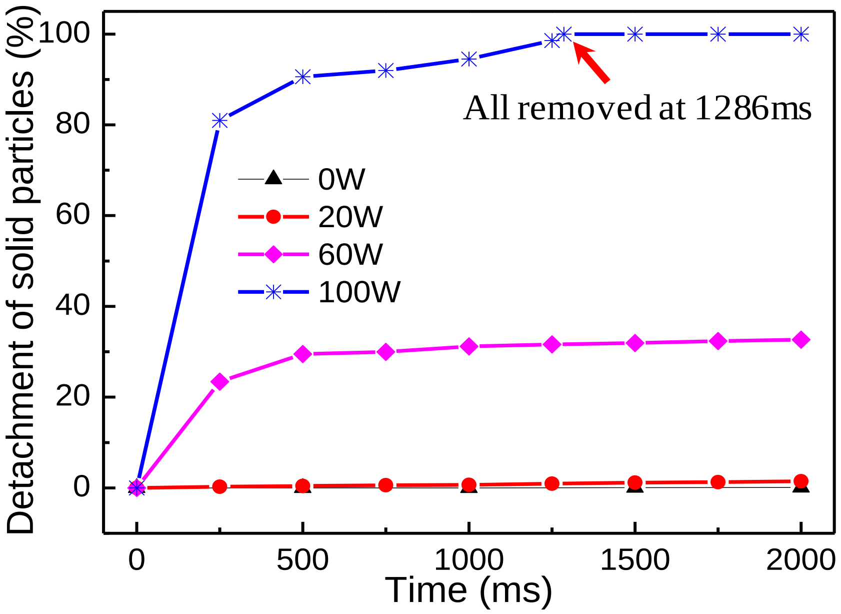

(a)

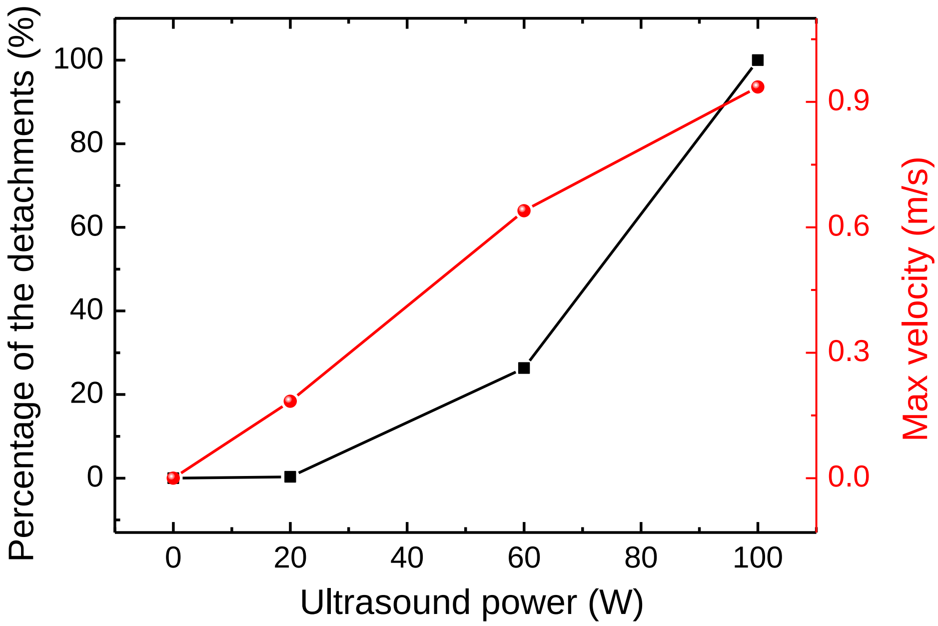

(b)

Fig. 5.18. *(a) Area percentage of the detached solid phases to the solid phases before the start of ultrasound as function of ultrasound processing time. (b) Final percentage of the detached solid phases after 2 s ultrasound processing and maximum velocity of solid particles in the view field as a function of ultrasound power measured from* ***Fig. 5.17****.*

Fig. 5.18a shows that, from the real-time images in Fig. 5.17, the area percentage of the detached solid phases (the area of detached solid phases divided by the original area of solid phases before the ultrasound is turned on) as a function of ultrasound processing time. The calculation was made by using an in-house Matlab® script, which can detect the L-S interface according to the grey value difference between solid and liquid. Fig. 5.18a shows that, at 20 W, there is no obvious detachment. At 60 W, the amount of detachment of Zn phase increase almost linearly with time before 250 ms, then slow down, and finally flatten out in the period of 500 – 2000 ms. The amount of detachment at 100 W ultrasound showed a similar trend as that at 60 W, i.e., 80% of the solid phases detached within the beginning 250 ms, and the detaching rate slow down after 250 ms, and all of the solid phase are destroyed under 100W after 1286 ms processing.

Fig. 5.18b shows the final area percentage of the detached solid phases and the maximum velocity of solid particles in the viewing field under different ultrasound power measured from Fig. 5.17. The position of solid phases (bright) above L-S interface, including the equaxied Zn particles in the liquid and deciduous particles or clusters. The measured velocity is calculated by the translation distance over the time interval of images (the particle velocity might be underestimated due to the neglect of the motion in the beam direction). From Fig. 5.18b, we can see that, at <20 W (the maximum particle velocity < 0.2 m/s), there are very a few Zn phase detached from the interface. With 2 s ultrasound processing time, the final detachment percentage of the solid Zn phases increase dramatically as the input power increase beyond 20 W (a particle velocity > 0.2m/s). All of the Zn solid phases were washed off from the L-S interface under 100 W before 2 s. The maximum velocity of solid particles increases as the increase of ultrasound power, reaching ~0.95 m/s at 100 W.

The velocity of Zn particles may not fully represents the velocity of streaming flow due to the inertia of the particles; the cavitation bubbles, although not appear at the depth of viewing field showed in Fig. 5.17, however, it will play an important role in terms of affecting the streaming flow as discussed before.

The velocity obtained in metallic alloy is much higher than those reported in water [120] and in transparent alloy [201]. The reason is that the intensity of the streaming effects is directly proportional to the ultrasonic momentum acquired by the liquid when it absorbs the wave energy; therefore, liquid metal absorbs more ultrasound wave energy due to its higher density and velocity of sound [38].

Thus, the ultrasound enhanced streaming flow is capable of fracturing and detaching the solid phase from the L-S interface (Fig.5.17). More importantly, many detached solid phases are observed to flow back into the top hotter liquid region by the acoustic streaming flow, and survive there for substantial period of time. Those surviving Zn phases will, at no doubt, act as embryonic grains for atoms in the liquid to grow upon. If in other alloy systems, no matter the surviving particles are grain refiners or embryonic grain themselves, they will enhance or promote very effectively the grain refinement of the solidifying alloys. This striking evidence indicates that the acoustic flow is one of the very important mechanisms for ultrasonic grain refinement in metallic alloys.

5.3.5 The effect of temperature

Fig. 19a shows the temperature increment ΔT (the maxium temperature during the ultrasound processing T_{MAX} minus the original temperature T_0 before ultrasound was turned on) of three thermocouples for the experiment results showed in Fig. 5.17 (with 2s ultrasound processing at the power of 20W, 60W and 100W). ΔT increases with the increase of ultrasound power, especially for the middle region, which is effective in reducing temperature difference between top and middle region. The temperature increment at top area most is probably due to the conversion from the acoustic energy to be the inner energy of the liquid alloy. However, comparing with the streaming flow induced temperature jump in the middle and bottom, this is relatively small because the hot liquid at the top will be pushed downwards by the streaming flow. The temperature at bottom area has little increment at 20 W and 60 W, but a steep jump at 100 W. Referring to the results in Fig. 5.17c, the steep temperature jump is actually caused by the acoustic flow delivering the hot fluid from the top to the bottom after the L-S interface was destroyed completely. More detailed temperature information is shown for the 60 W case in Fig. 5.19b. During the 2 s ultrasound (60W) processing, the temperature above the L-S interface was obviously homogenised, that is, the temperature gradient between TC1 and TC2 reduced from 4.07 °C/mm to 1.24 °C /mm. However, the high speed image sequence (Fig. 5.17b) and the measured data (Fig. 5.18a) show that majority of the Zn particles in the view field were detached or became loose within 250 ms after applying ultrasound during which there was hardly any obvious temperature increase (<2 °C) at the L-S interface region (TC 2 in Fig. 5.17b). Hence the hydrodynamic force induced by the acoustic flow plays a more dominant role than the temperature in dispersing and redistributing solid particles in the liquid metals.

Although the temperature induced re-melt is too slow to be the dominant factor in such short period, that is, 2 s ultrasound processing. Our experiments have found that it will become an important factor in long time ultrasound processing, for example, applying 20 W ultrasound for ~10s above the L-S interface.

When ultrasound is switched on temperature increase always occurs as the insert shown in Fig.5.13a. To investigate the effect on re-melt of the interface, ultrasound with a small power (20W) was applied for a relatively longer time, 10s (Fig. 5.20a). Consistent with the results showed in Fig. 5.17a, there are no obvious acoustic flows observed at ~6 mm below sonotrode. Any detached solid particles were seen to move slowly and straightly upwards without any interference from any acoustic flows. As the ultrasound processing continued, the temperature was obviously homogenized as showed in Fig. 5.20b, the top-middle (TC1 and TC2) temperature gradient reduced from 4.07°C/mm to almost 0, but the middle-bottom (TC2 and TC3) temperature gradient increased. There was about 15 °C increase at TC3, resulting in the detachment of solid particles from the L-S interface as Fig. 5.20b showed. As the temperatures increase in TC2 and TC3 during the ultrasound processing, more and more Zn phases are detached from the L-S interface. This temperature effect will be effective for more than 15 s, because even after 10 s ultrasound, Fig. 5.20b shows that the temperature maintained higher than that before ultrasound for a long time. By measuring the velocity of the erosion of L-S interface, the temperature induced re-melt was found to erode the interface in a seed of 50 μm/s. The detached Zn particles continued to move straight up with a speed of ~0.003 m/s due to buoyancy force, further confirming that the influence of the acoustic flow under this condition is trivial.

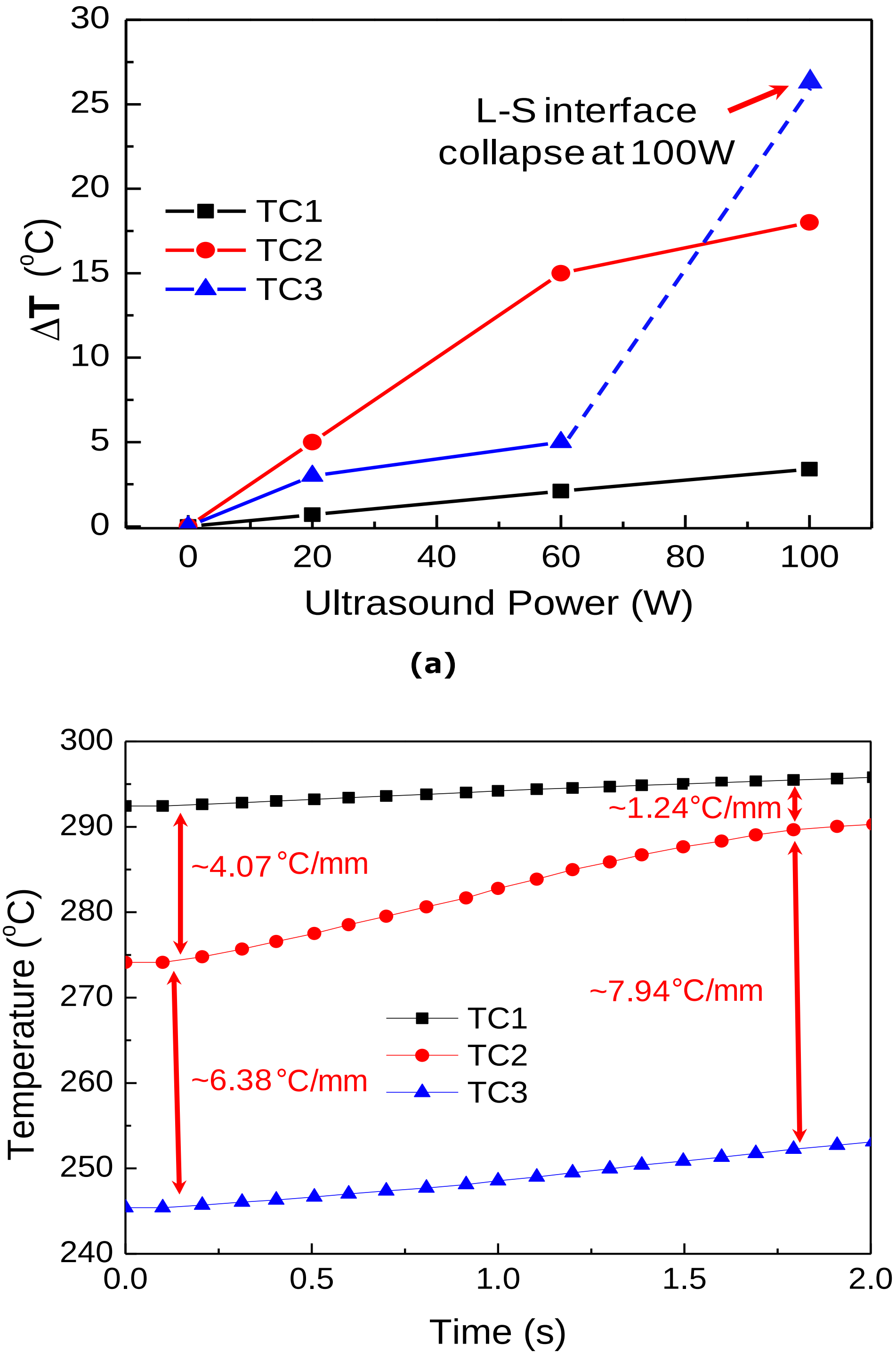

(a)

(b)

Fig. 5. 19. *(a) The temperature increment* ΔT *(*$\Delta T = T_{MAX} - T_0$*) of TC1, TC2, and TC3 as function of ultrasound power conresponding to the in situ observation in Fig. 5.17, and (b) temperature history after the ultrasound was switched on under the ultrasound power of 60W (real-time images shown in*

Fig. 5.17b).The positions of the thermocouples TC1, 2, 3 are shown in Fig. 3.17, that is, 4.5 mm between each thermocouple, and TC1 is 0.25 mm below the sonotrode.

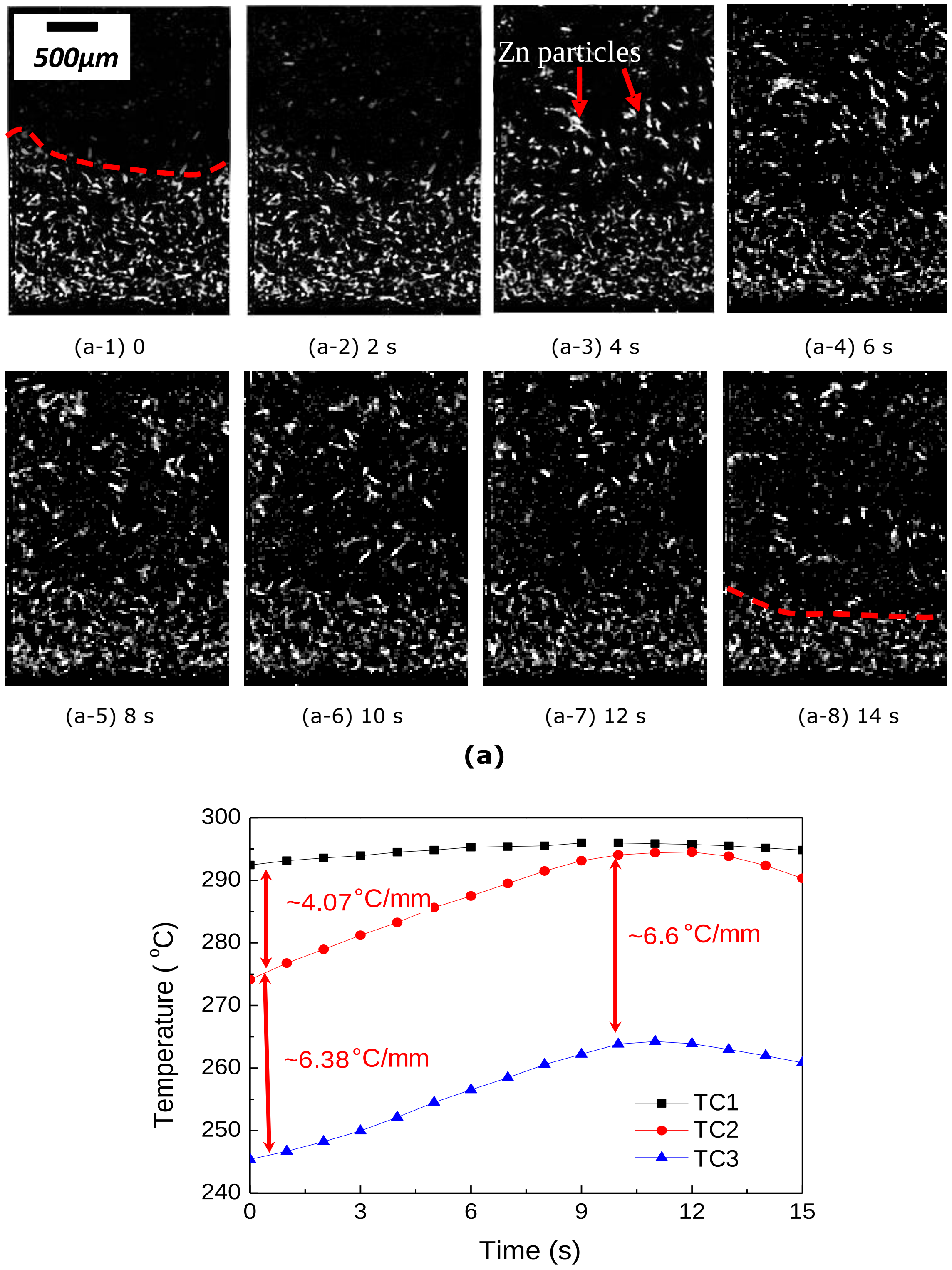

(a-1) 0 (a-2) 2 s (a-3) 4 s (a-4) 6 s

(a-5) 8 s (a-6) 10 s (a-7) 12 s (a-8) 14 s

(a)

(b)

Fig. 5.20. *(a) Image sequence of L-S interface for a Bi-8%Zn with 10 s ultrasound (20 W) processing. (b) The temperatures history at TC1, TC2, and TC3 with 10 s ultrasound processing corresponding to the real time images*

from (a-1 to a-8). The center position of the image is about 6 mm below the sonotrode, and TC2 is ~1 mm above the L-S interface at 0 s. The images were taken at 1000 fps and 990 μs exposure time.

5.4 Summary

The microjet flows at microscopic level are captured both in water and liquid metals. Systematic studies on the interactions between bubbles and acoustic flows indicate that bubble implosion and oscillation are very effective in stirring up solid particles in liquids. At liquid-solid interface, the energy and momentums coming from the imploding bubbles, oscillating bubbles and acoustic flows are sufficient to fracture solid phases, at microscopical level, ultrasonic bubbles are more energetic then acoustic flow in affecting the liquid-solid interface due to mainly the microjet flow effects.

Chapter 6: Modelling of acoustic pressure field and bubble dynamics

This chapter describes the modelling of the ultrasonic pressure field, the oscillation of ultrasonic bubbles in order to understand more quantitatively the dominant governing physics in controlling the dynamics of ultrasonic waves and ultrasonic bubbles in the different liquids studied.

6.1 Modelling of the acoustic pressure field

Fig. 3.17 in Chapter 3 shows that the ultrasonic waves were transmitted into the liquid held within the thin channel area via the vibration of the sonotrode tip set on top of the thin channel. To quantify the acoustic pressure field produced by the ultrasound transmitting through the liquid, finite element method and the commercial software, Comsol Multiphysics® were used to simulate the acoustic pressure distribution inside the liquid.

6.1.1 The governing equations

If assuming the ultrasound is a time harmonic vibration without the effect of cavitation, the cyclic ultrasonic pressure distribution in the liquid can be calculated using the Helmholtz equation [33, 42].

$$\frac{(\omega/C)^2}{\rho}P_a+\nabla\cdot\left(\frac{1}{\rho}\nabla P_a\right)=0 \tag{6.1}$$

where ρ and C are the density and sound speed of the liquid respectively. $\omega=2\pi f$ is the angular frequency and f is the frequency of sound wave.

P_a is the pressure source at the sonotrode tip, and in this case can be calculated by:

$$P_a=P_A\cos(\omega t) \tag{6.2}$$

$$P_A=\sqrt{2\rho CW/A} \tag{6.3}$$

where P_A is the pressure amplitude at the sonotrode tip surface. W is the ultrasound power, and A is the area of the ultrasound wave emitting surface (the 2 mm diameter tip has a wave emitting surface of 3.14×10^{-6}m^2).

6.1.2 The computational domain and mesh

The quartz sample container showed in Fig. 3.15 was modelled. The thin channel area has the dimension of 10 x 10 x 0.3 mm. By mimicking this geometry, the computational domain used in the modelling is shown in Fig. 6.1a, comprising of a cuboid of 10 mm (wide) x 20 mm (high) x 0.3 mm (thick). The domain is 10 mm higher than the thin channel itself which means that the liquid of 10 mm above the thin channel is considered in the simulation. The sonotrode is simulated by using another cuboid of 2 mm (wide) x 5 mm (high) x 0.3 mm (thick). Unstructured triangular mesh [202] was generated for the computational domain using the topology mesh function in Comsol Multiphysics. The mesh size is in the range from 0.042 to 0.237 mm as shown in Fig. 6.1a. The domain for the liquids was meshed using extra fine meshes, especially at the corners. The total number of mesh elements consists of 18354 domain elements, 8352 boundary elements, and 426 edge elements.

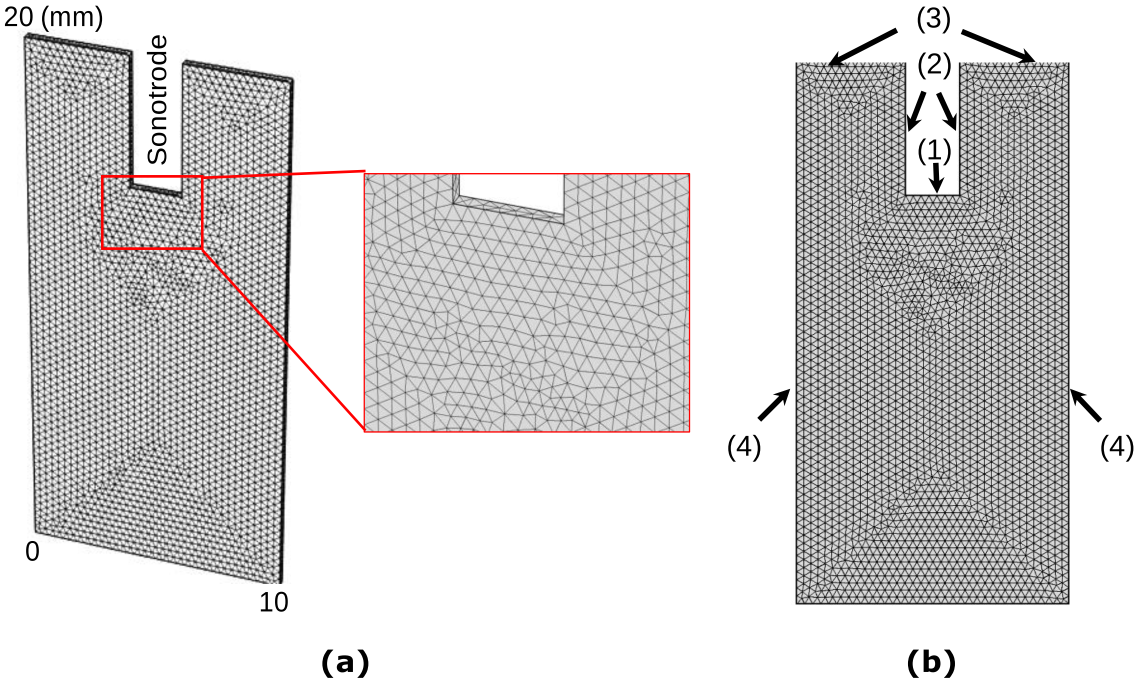

Fig. 6.1. *(a) A 3-D view of the computational domain and meshes for simulating the acoustic pressure. The insert shows the enlarged view of the mesh at the sonotrode tip. (b) A 2-D view of the domain, showing the boundaries with their conditions described in the text.*

6.1.3 The boundary and initial conditions

The boundary conditions were set as close as to the conditions used in the experiments:

(1) Boundary 1: this is the sonotrode tip, emitting ultrasonic waves into the liquid below. A pressure source $P_a = P_A cos(wt)$ is given at boundary 1, P_A is calculated from the imposed ultrasound input power (20-100W) and the area of the sonotrode tip, A (3.14×10^{-6}m^2).

(2) Boundary 2: this is the side surfaces of the sonotrode. Sound hard boundaries (zero normal derivative of pressure, $\partial P_a/\partial n=0$) are set at boundary 2.

(3) Boundary 3: this is the liquid top surface exposed to air. Sound soft boundaries ($P_a=0$) is set at Boundary 3.

(4) Boundary 4: this is the wall of the quartz container, a relative "soft glass" condition is set for Boundary 4 with the acoustic impedance $Z=\varrho^*c^*$, where ϱ^* and c^* are the density (2.203×10^3 kg m^{-3}) and sound velocity (5300 m s^{-1}) of quartz, respectively.

6.1.4 The material properties

Three materials, i.e. water, silicone oil, and Bi-8%Zn alloy were simulated using this model. The properties used in the simulation for the three materials and those of quartz container and sonotrode are listed in Table. 3.2.

Room temperature (20°C) was used for water and silicone oil. While for Bi-8%Zn, the measured temperature of 427°C was used, and its viscosity at 427°C was referenced from [199].

6.1.5 The modelled acoustic pressure distributions

Fig. 6.2 shows the simulated acoustic pressure distributions along the central line from the sonotrode tip downwards for the three different liquids with an input ultrasound power of 20 W. Immediately below the sonotrode tip surface, the acoustic pressure in Bi-8%Zn is 14.8 MPa, 3.4 times higher than that in water (4.35 MPa), and 4.3 times higher than that in silicone oil (3.46 MPa). However, it attenuates much faster, dropping to the same level as those in water and silicon oil at ~1.8 mm below. Apparently, the higher acoustic pressure at the wave emitting surface for Bi-8%Zn is because of the combined effect of higher density (9561 kg m^{-3}) and faster sound speed (1790 m s^{-1}). While the exponentially attenuation of the pressure is caused by mainly the higher density. Eq. 6.1 indicates that the heavy metal consumes the acoustic energy much faster than water and silicone oil do, and just ~1.8 mm away from the wave emitting surface, the acoustic pressure reached the same level as those in water and silicone oil. Fig. 6.2 also shows that, for all three cases, ~5 mm away from the wave emitting surface, the alternating acoustic pressures became very small.

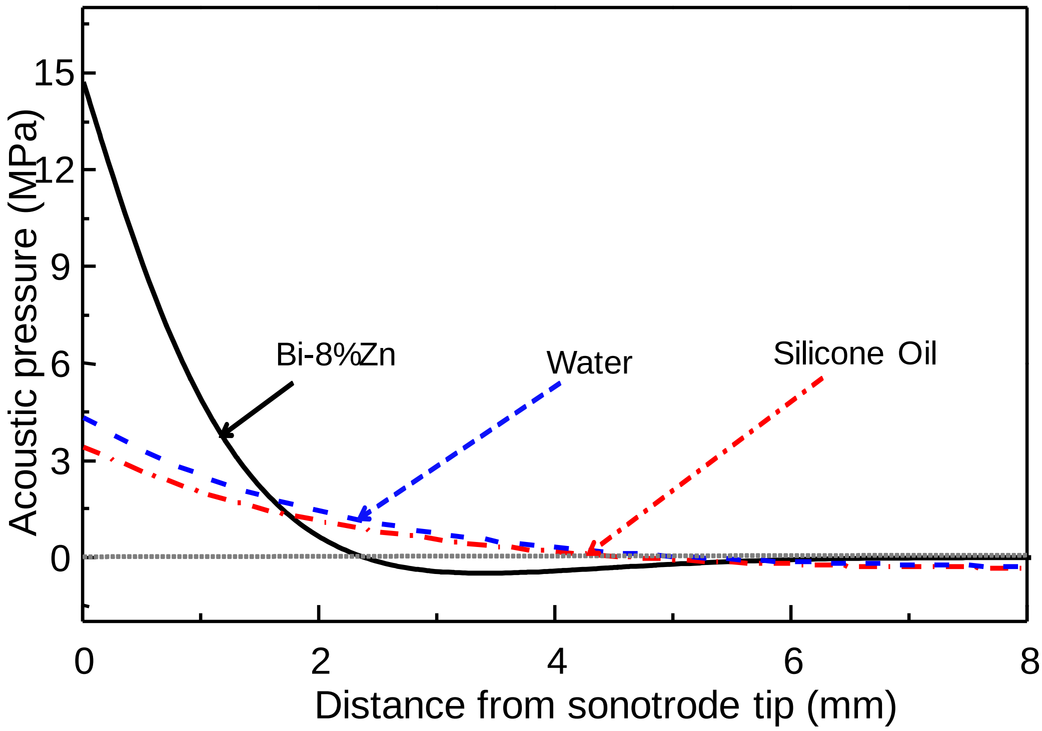

Fig. 6.2. *The acoustic pressure distributions below the sonotrode tip (along the central line of the geometry) in water, silicone oil and Bi-8%Zn, calculated by Helmholtz equation with an initial ultrasound power of 20 W.*

Fig. 6.3a shows the simulated acoustic pressure distributions along the central line in Bi-8%Zn for different ultrasound input powers (20 W, 40 W, 60 W, 80 W and 100 W respectively). For all cases, the acoustic pressures attenuate very fast and become very small 2 mm below the sonotrode tip.

Fig. 6.3b shows that, for different ultrasound powers, the acoustic pressure at the sonotrode tip is a cosine wave. The maximum acoustic pressures for different powers extracted from Fig. 6.3b (arrowed) are plotted in Fig. 6.4, with the inserts show the acoustic pressure distributions surrounding the sonotrode tip for different powers.

6.2 Modelling of the dynamics of ultrasonic bubbles

6.2.1 The governing equations

In this research, the classical Gilmore model [23] was used to simulate the dynamic evolution of the bubble radius for the three cases. The governing is:

$$\left(1-\frac{\dot{R}}{C}\right)R\ddot{R}+\frac{3}{2}\dot{\mathrm{R}}^2\left(1-\frac{\dot{\mathrm{R}}}{3\mathrm{C}}\right)=\left(1+\frac{\dot{R}}{C}\right)H+\frac{R\dot{R}}{C}\left(1-\frac{\dot{R}}{C}\right)\frac{dH}{dR} \qquad (6.4)$$

$$C^2=\frac{n(P+B)}{\rho}\left(\frac{P+B}{P_0+B}\right)^{-\frac{1}{n}} \qquad (6.5)$$

$$H=\frac{n}{n-1}\frac{(P_0+B)^{\frac{1}{n}}}{\rho}\left[(P+B)^{\frac{n-1}{n}}-(P_\infty+B)^{\frac{n-1}{n}}\right] \qquad (6.6)$$

$$P=\left(P_0+\frac{2\sigma}{R_0}\right)\left(\frac{R_0}{R}\right)^{3\gamma}-\frac{2\sigma}{R}-\frac{4\mu\dot{R}}{R} \qquad (6.7)$$

where R, P, H and C is the radius, pressure at the bubble wall, enthalpy and sound speed of the liquid, respectively; R_0 is the initial bubble radius, B and n are empirical constants that depend on the particular liquid, P_0 is the liquid ambient pressure at 1 atm and $P_\infty = P_0 + P_{ext}$ is the pressure at infinite distance from the bubble.

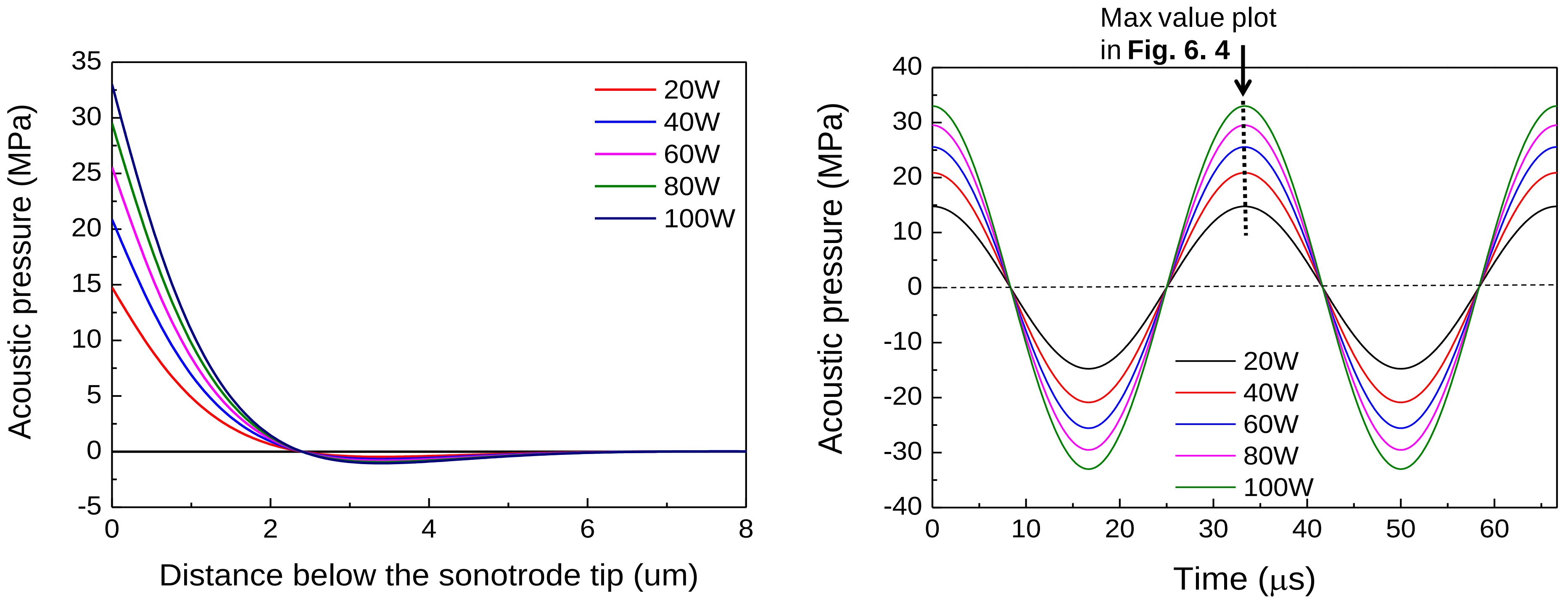

(a) **(b)**

Fig. 6.3. *(a) The acoustic pressure (at the maximum positive pressure) distribution below the sonotrode tip, and (b) the pressure at the sonotrod tip as a function of time for ultrasound powers of 20 W, 60 W, 80 W and 100 W in Bi-8%Zn.*

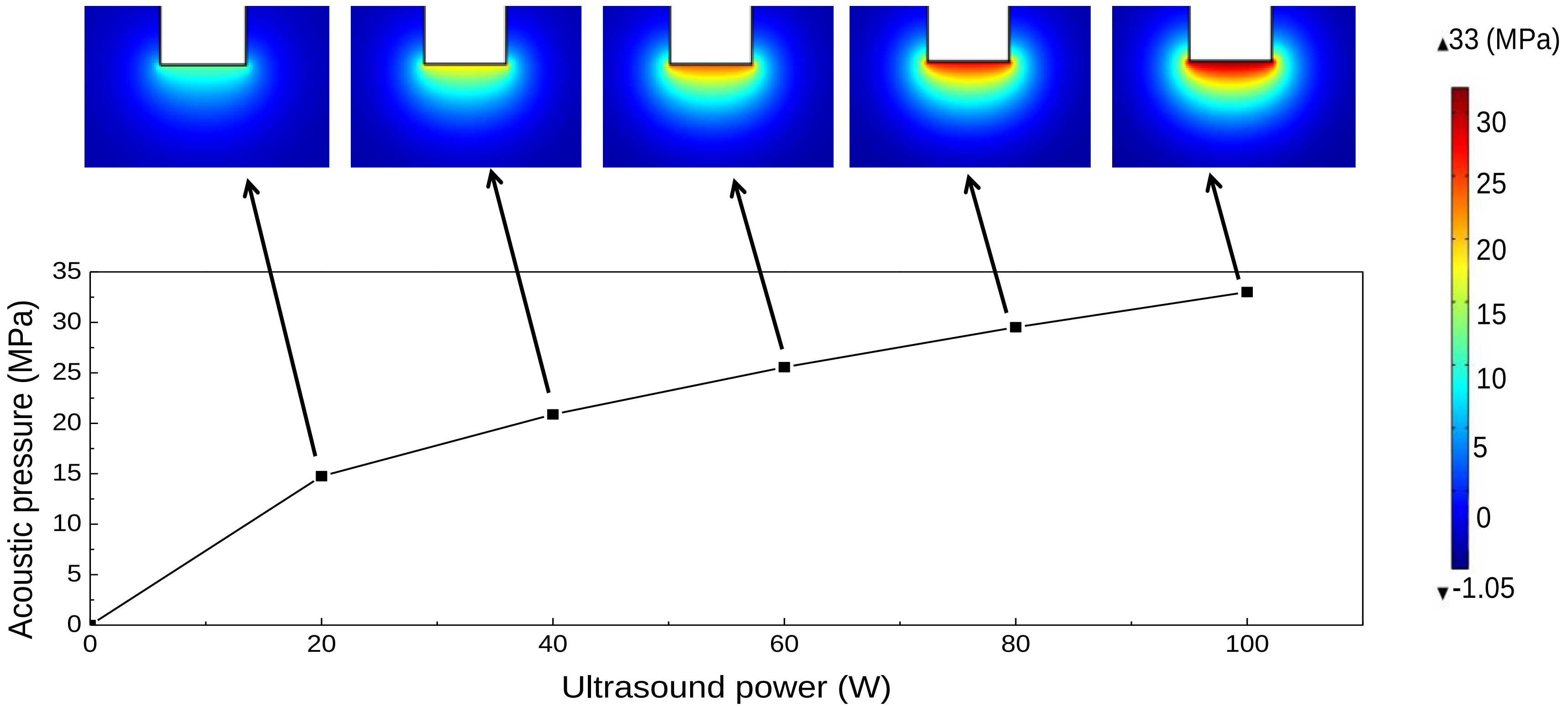

Fig. 6.4. *The acoustic pressure amplitude at the sonotrode tip in Bi-8%Zn for different ultrasound input powers. The inserts are corresponding 2-D colour maps of the acoustic pressure distribution at the middle plane of the sonotrode.*

Based on the acoustic pressure distributions simulated in the previous section, the external acoustic pressure P_{ext} for a bubble at a specific point can be calculated by:

$$p_{ext} = p\,cos(wt) \tag{6.8}$$

where p is the acoustic pressure amplitude at the location where the bubble is found.

6.2.2 Parameters used in the equations solving

The equation was solving in Comsol Multiphysics® using the model of Ordinary Deferential Equation (ODE). The accuracy of the calculation is down to 10^{-6}, and the time step is set as 3.33 x 10^{-9}s. By inputting the initial bubble radius (measured from the images) and the acoustic pressure amplitude at the location where the bubble is found (also from the X-ray images and calculated using Eq.6.1), and other parameters, such as the empirical constants B and n, density and viscosity of the liquid properties (all listed in Table 3.2), the bubble radius, velocity and pressure at the bubble wall can be calculated using Gilmore model.

6.2.3 The simulated bubble radii

Fig. 6.5a-c shows that the bubble radii measured from the images in Fig. 4.5a, b and d were compared with the calculated ones by using Gilmore model for the cases of water, silicone oil, and liquid Bi-8%Zn, respectively. An initial bubble radii of 4, 6, 8 μm based on experiment measurements, and pressure amplitude of 0.118, 0.125, 0.105 MPa at the bubble position were used in the Gilmore model for water, silicone oil and Bi-8%Zn. From Fig. 6.5a-c, we can see that in all the liquids, the measured and modelled bubble radii agree well when the same time intervals from the images (7.4 μs for water and silicone oil, and 0.185 ms for Bi-8%Zn) were used in the simulation. Fig. 6.5d-f shows that the velocity at the bubble wall simulated for the bubble showed in Fig. 4.5a, b and d. It was found that the Gilmore model predicts well the oscillation of quasi-steady bubbles.

Fig. 6.6 show a series of images acquired at 135,780 fps in a liquid Sn-13%Bi alloy (~2.65mm below the sonotrode tip) at 327°C and an acoustic pressure amplitude is calculates as 0.5 MPa. The dynamic expansion of the bubble and its sudden implosion (Fig. 6.6a-6) are clearly demonstrated. At implosion, the bubble boundary become blurring because of the pressure shockwave generated (as discussed in detail in Chapter 7) push the liquid away from the bubble wall. Using the Gilmore model again, the corresponding abrupt change in bubble radius and the velocity at the bubble wall are calculated and showed in Fig. 6.6b and c, respectively. Fig. 6.6b shows that the measured radii agree well with the simulation, and Fig. 6.6c shows that, at implosion, a velocity of the bubble wall is emitted in the range of 30 ~ 40 m/s.

6.4 Summary

Comparisons between the measured and simulated bubble radius indicate that the Gilmore model is capable of accurately simulating the quasi-static oscillations of spherical bubbles all liquids studied in this research.

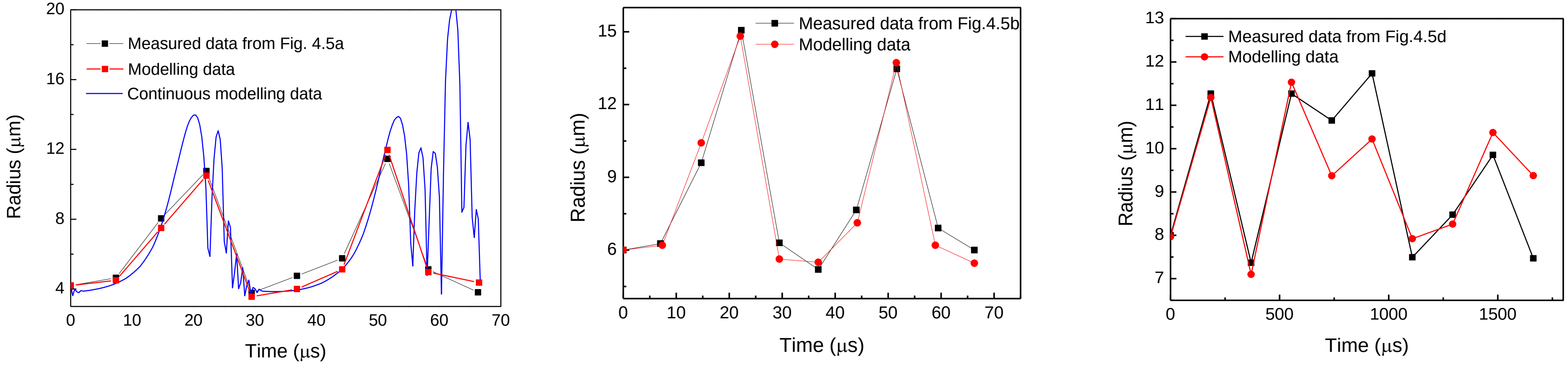

(a) water (b) Silicone oil (c) Bi-8%Zn

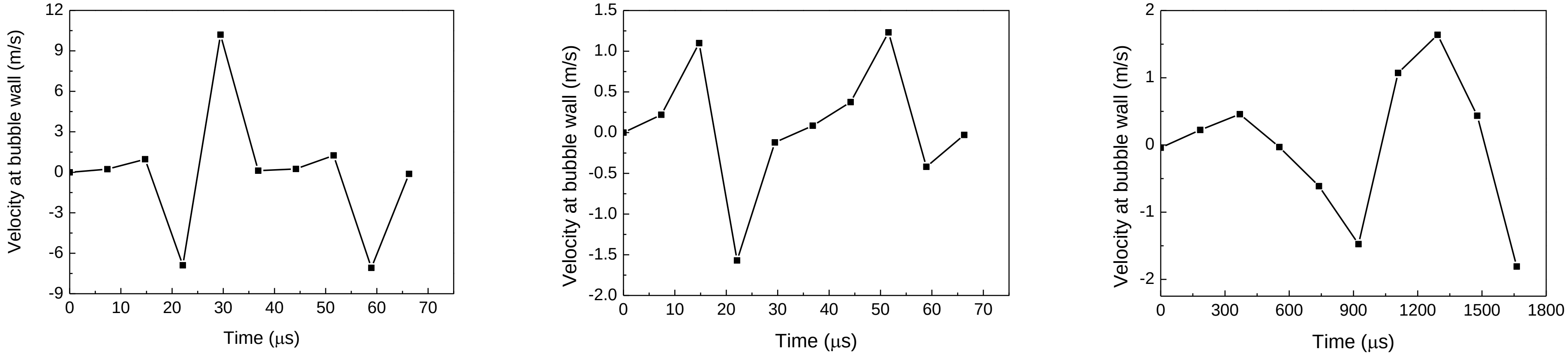

(d) water (e) Silicone oil (f) Bi-8%Zn

Fig. 6.5. *(a-c) Bubble radii measured from the image sequence in* ***Fig. 4.5*** *and comparison with the calculated bubble radii using Gilmore model (the initial radius = 4, 6, 8 μm, pressure amplitude= 0.118, 0.125, 0.105 MPa) for water, silicone oil and Bi-8%Zn, respectively and (d-f) the velocities at the bubble wall calculated using the Gilmore model and the same time step as the images showed in* ***Fig. 4.5****.*

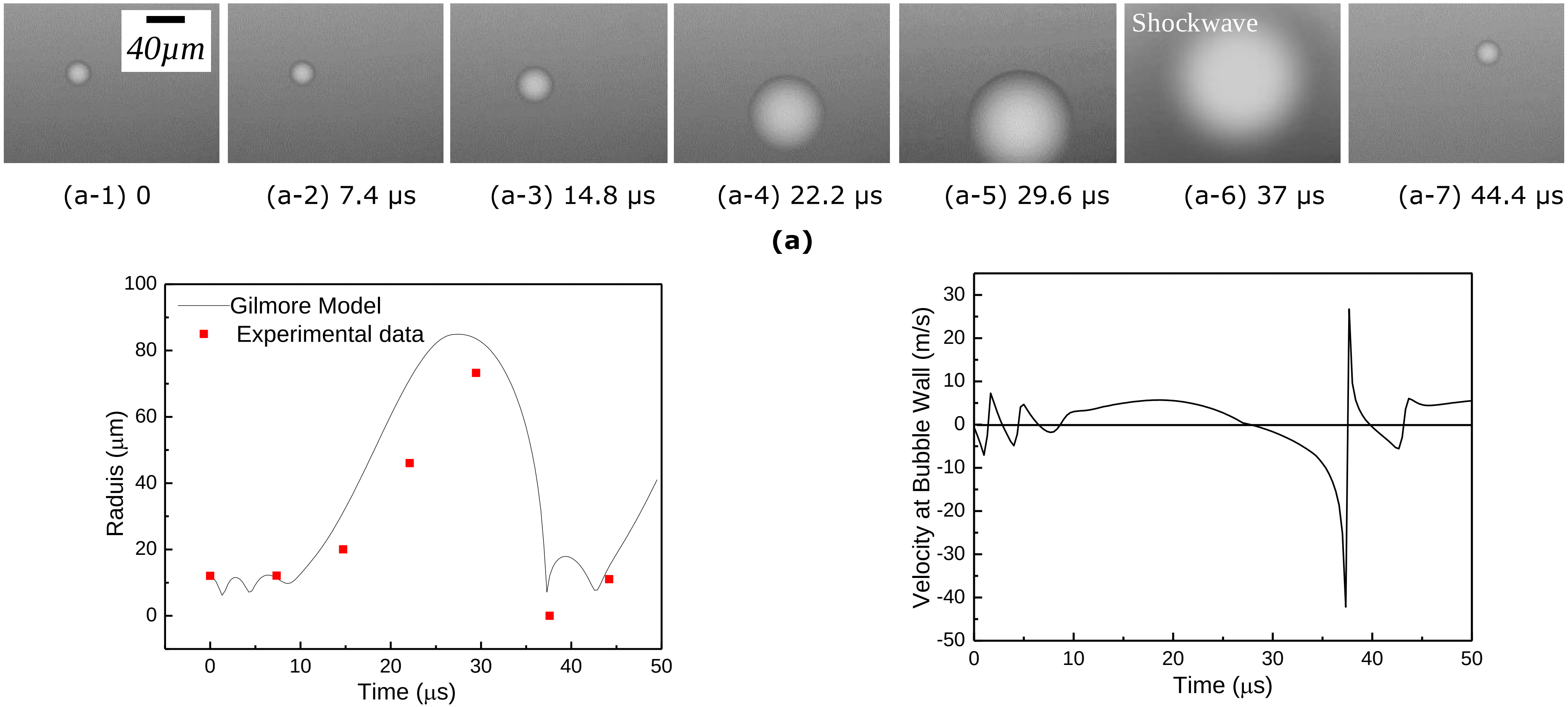

(a-1) 0 (a-2) 7.4 μs (a-3) 14.8 μs (a-4) 22.2 μs (a-5) 29.6 μs (a-6) 37 μs (a-7) 44.4 μs

(a)

(b) **(c)**

Fig. 6.6. *(a) A series of images, showing the expansion and implosion of a single bubble in a Sn-13%Bi alloy (327°C) captured at 135,780 fps ~2.65 mm below the sonotrode tip (time interval of 7.36 μs); (b) the simulated abrupt change of the bubble radius before and at implosion, and (c) the abrupt change of velocity at the bubble wall at implosion, emitting a shockwave.*

Chapter 7: Discussion

The large number of real-time X-ray images and simulation results presented in chapter 4, 5 and 6 contain a large amount of novel information concerning the dynamics of ultrasound bubbles in water, silicone oil and liquid metals. Majority of them are revealed for the first time, especially for the case of liquid metals because of the uses of the ultrafast X-ray imaging.

In this chapter, the novelties of the research, the key new findings and discoveries are discussed by comparing the experimental results with the numerical modelling in this research and those published in the open literatures by other researchers in the past. The significance on new knowledge creation and scientific contribution to the advance of the research in this very important field are highlighted in this chapter.

7.1. The novelty of the experimental apparatus

Real-time imaging of the highly dynamic events of ultrasound bubbles in liquids, especially for the case of liquid metals, is not a trivial task. A systematic design and experimental trials were carried out in the past four years to design and manufacture the suitable experimental apparatus and the corresponding control and synchronisation systems for the research. Through a steady and progressive improvement, and many iterations of experimental trials as described in chapter 3, a very advanced experimental apparatus has been successfully designed, manufactured and commissioned for this research and used to acquire many thousands of images data in the four past years. The key novelties of the designed apparatus are firstly discussed here:

7.1.1 The special sample containers and furnace

As detailed described in Chapter 3, the sample container is the key element in the in situ solidification studies of liquid metals. It needs to have sufficient volume to hold the sufficient quantity of liquid metals to allow ultrasound to be applied into the melt, and have a large enough X-ray window to allow a sufficient number of ultrasound bubbles to pass through that window for the in situ imaging studies. Initially, Duratec and Marco materials were chosen because they are machinable ceramics and can be machined into the designed geometry as showed in Fig. 3.4 without difficulty to realise the designed functions. They can be also made as a tiny casting mould and used repeatedly. The experimental trials made in the first two experiments at APS in 2011 and 2012 indicated that the Duratec and Marco moulds performed well during the solidification experiments, and reasonable good quality X-ray images were obtained using the two types of mould as typically showed in Fig. 3.6 and 3.7. However, the non-uniform background on the X-ray images due to the Duratc and Marco mould causes problems in analysing the bubbles captured, especially difficult in differentiating clearly the boundaries of the bubbles (Fig. 3.7). With such smeared bubble boundaries, it is virtually impossible to study the details of bubble implosion and bubble coalescence events.

Encouraged by the success of the designed geometry for the sample containers, we then searched for other materials that have a very low X-ray absorption properties in order to achieve a clear and uniform background on the X-ray images, while at the same time can withstand the high temperature. Apparently, quartz is one such material because it has very low X-ray absorption coefficient as showed in Fig. 3.5, and its soft temperature is around 1660 °C [203]. The difficulty is to make a quartz into the similar geometry as showed Fig. 3.9a. Through many rounds of discussion with a glass specialist, Ms. Julia Malle at the Glass Workshop at our University and many trials subsequently, the special quartz containers as showed in Fig. 3.15 were made successfully and X-ray images (Fig. 3.9b) with very clear background were then acquired in the experimental trials at APS. Other materials such as thin sheets of carbon [34-37], boronitride [182], and alumina [181] were all used in the in situ solidification experiments conducted by other researchers in the past. However, those sheet materials are more difficult to be manufactured into the specially designed geometry as showed in Fig. 3.9a. Hence, such quartz containers were used in all subsequent experiments to contain liquid metals. In addition, the thickness of the thin channel for the X-ray window area is set at 0.3 ~0.35 mm thick to allow the ultrasound bubbles to pass freely into the thin channel as confirmed again by the experimental trials at APS (Fig. 3.6b). In this way, the bubble to be studied will not be restricted very much by the thin channel geometry, especially at very high image acquisition rate where the bubbles just have a chance to travel a few micrometres apart. The 0.3 mm thickness is also thin enough to allow sufficient X-ray flux to pass through the metal samples (Fig. 3.5b and 3.11) to form images with good contrast.

Most of the previous in situ imaging studies of solidification microstructures used a sample of 0.1~0.2 mm thick [37] which is too thin for any ultrasonic bubble to pass through as confirmed by Fig. 3.6. While others used 1 mm [182] and 2 mm [181] thick samples to image ultrasound bubbles in Al-Cu alloys, which will have many overlapped bubbles in the view field, having much less chance to pick up the information from the individual bubble.

For the furnace, a jigsaw type design was used as showed in Fig. 3.14. There are 6 plates of ceramic-Duratec 750 (Fig. 3.14), each holding one or two cartridge heaters. The can be easily assembled around the sample container after the focus of the X-ray beam on the sample is made. This flexibility is very important for the in situ experiment because the focus of X-ray can be more easily carried out without the obscure of the furnace surround the samples.

In addition, the breakdown of any cartridge heater can be promptly replaced without wasting the precious beam time during the X-ray imaging experiments. By changing the position of the sample containers relative to the cartridge heater, different temperature gradients can be achieved for the melt held inside the quartz container. For example, Fig. 5.14, Fig. 5.16, and Fig. 5.17 show that, by using an appropriate thermal gradient, a clear L-S interface can be formed in the view field for imaging.

7.1.2 The beamlines and integration with the apparatus

As mentioned, the beamline in 32-ID-B was a specially designed beamline with the advantages of ultrafast imaging by synchronising the camera, shutter, and X-ray beam using a Stanford DG535 delay generator fed with the radio-frequency signal from the storage ring. A relay system which can be synchronized with the beamline was also designed and made to control switch on/off of the ultrasound relative to that of the X-ray beam, camera, and shutter. Fig. 7.1 shows that, the X-ray and camera is on at t_1, and at the same time, the shutter is started to open, and it takes 5 ms (at t_2) to reach the fully open position. The ultrasound is switched on at t_3 after the shutter is fully opened. The ultrasound is then switched off at t_4 before the shutter start to close at t_5, so the full ultrasound processing procedure (t_4-t_3) can be imaged. Finally, the shutter is fully closed at t_6, and at the same time, the camera and X-ray is off. By setting the time Δt_1, Δt_2, and ultrasound processing duration t_4-t_3, the entire process of ultrasound processing of the sample can be captured in the video.

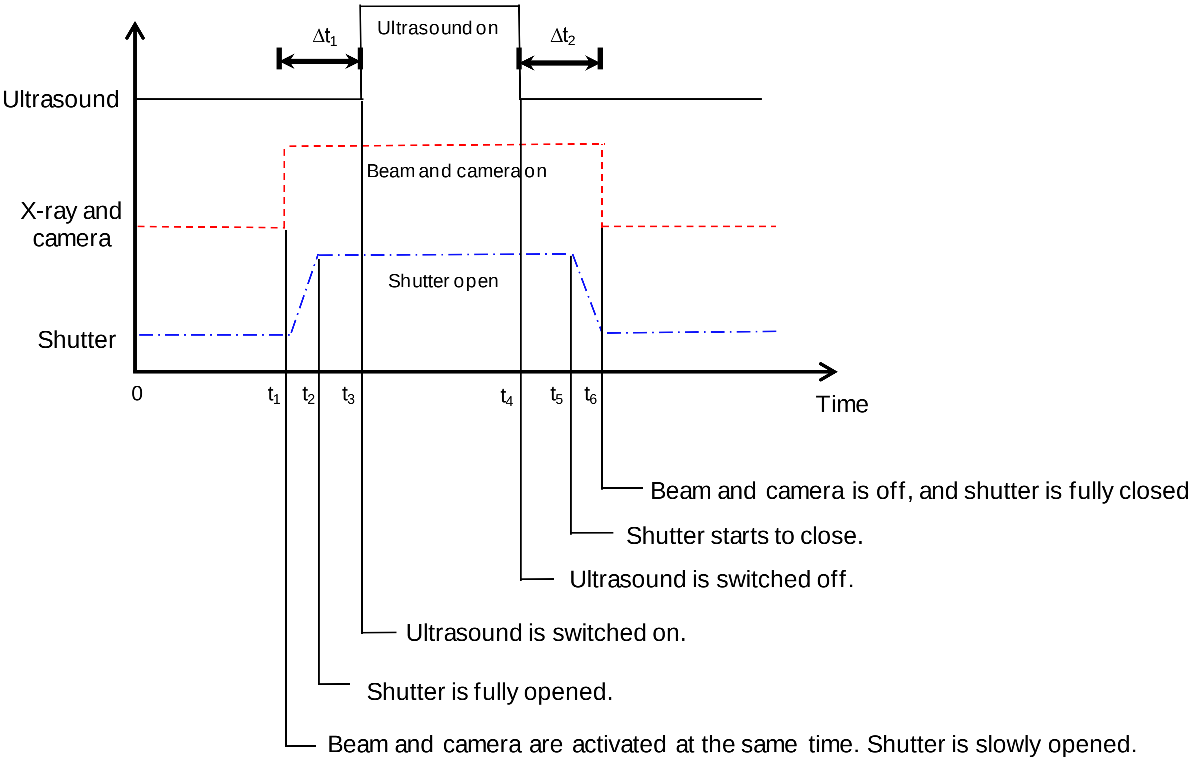

Fig. 7.1. *A schematic, showing the time sequence for the ultrasound, X-ray, camera, and shutter during the experiments.*

The hybrid operation mode of APS provides the brightest synchrotron X-rays in the west hemisphere and sector 32-ID-B is the dedicated beamline for ultrafast X-ray imaging research, for example, the impact of bullets onto materials. The combining advantages of the ultrafast X-ray imaging capability and dedicated ultrasound solidification experimental apparatus developed by Dr Mi's group make it possible for us to investigate the highly dynamic behaviour of the ultrasound bubbles in liquids, especially in the cases of liquid metals which have never been achieved at such fast speed, i.e. 271,554 fps before.

Although I12 of DLS cannot achieve such high image acquisition rate, its flexible lenses system allows us to study the phenomena in a relatively large field of view, such as bubble cloud and ultrasound enhanced acoustic flow. Led by Dr Mi, a total of 68 shifts (22.5 days) of synchrotron X-ray beam time have been awarded by APS and DLS for studying the fundamentals of ultrasound processing of materials with the emphasis on metal alloys.

I am one of the key researchers who have played an important role in conducting the in situ experiments, and analysing the huge amount of images obtained. The key findings and the contributions I made are documented here as the essential materials for my PhD thesis.

7.2 Novel information concerning bubble dynamics

7.2.1 Bubble nucleation

The ultrafast X-ray images clearly illustrates that ultrasonic bubbles are easily nucleated at the solid-liquid interface because any voids on the side of the solid surface can accommodate tiny air bubbles that act as the nuclei. The small bubbles showed in Fig. 4.4a-2, b-2 and d-2 provide the strong evidence for this argument. Although bubble nuclei are often well below 1 μm [3], it is logically to assume that the small bubbles showed in Fig. 4.4a-2, b-2 and d-2 are actually growing out the even smaller bubble nuclei that cannot be seen in the 1st images due to the limit of 1 μm/pixel spatial resolution. However, the number of bubbles nucleated by this mechanism is constrained by the limited number of sites on the solid-liquid interface for nucleation.

In addition, bubble coalescence and any subsequent collapsing or implosion is another important mechanism for creating new bubbles whatever big or small.

Of course, all the above mechanisms are governed by the acoustic field created by the ultrasonic waves which differ hugely depending on the distance away from the source of the ultrasound (the sonotrode) and its amplitude. For example, Fig. 4.13-4.15 and 5.5 show that the bubble clusters were pushed downwards due to the primary Bjerknes force [54] and fluid flow [120] in the pressure field into the bulk liquid far away from the sonotrode. These bubbles imploded or split to form new bubbles. Fig. 7.2 shows another typical example where a group of bubbles were pushed downwards and spread into the bulk liquid.

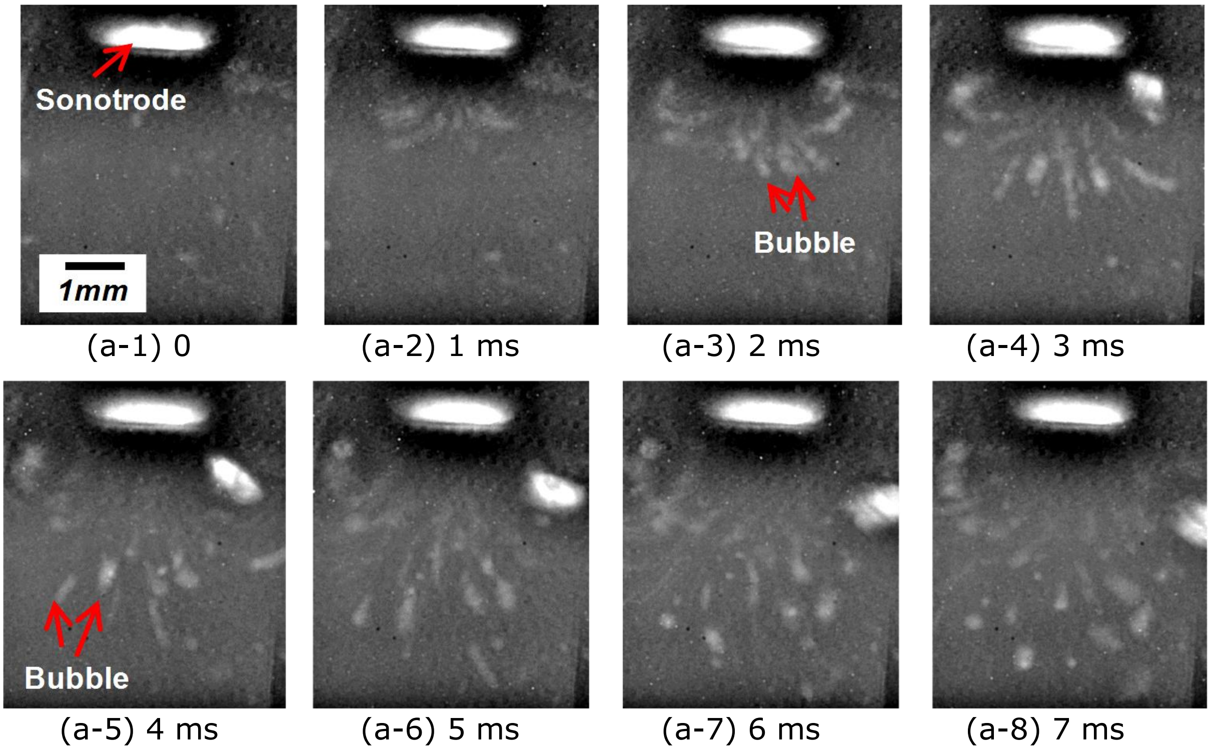

(a-1) 0 (a-2) 1 ms (a-3) 2 ms (a-4) 3 ms

(a-5) 4 ms (a-6) 5 ms (a-7) 6 ms (a-8) 7 ms

Fig. 7.2. *Image sequences of bubbles emitted from the sonotrode tip in Bi-8%Zn alloys. The temperature is 427°C at TC1 and images are captured at 1000 fps with an exposure time of 990 μs at DLS.*

Comparing the ultrasound amplitudes showed in Fig. 4.4c and e, it is also interesting to find that, in water and silicone oil, bubbles were found to be nucleated when the sonotrodes vibrate with an amplitude of ~3 μm; while in Bi-8%Zn, the amplitude is ~10 μm, indicating that the bubble nucleation in water and silicone oil need less energy than those in Bi-8%Zn due to the high surface tension of the metallic alloys [3].

7.2.2 Bubble oscillation

Fig. 6.5a-c shows, in water, silicone oil, and Bi-8%Zn, the measured bubble radii agree well with the calculated bubble radii at the experimental conditions. For the transparent liquids (water and silicone oil in this study) many researchers have shown that the bubble radii match well with Gilmore model. In this and that published in [38], it shows that the dynamic oscillation of a quasi-steady ultrasonic bubble in liquid metal can also be predicted well using Gilmore model. Hence, all variables simulated in the bubble oscillation, including the bubble radius, pressure and velocity at bubble wall can be used with much confidence on helping to interpret the phenomena observed from the experiments. The bubble ambient pressure used in Gilmore model was calculated by using the Helmholtz equations.

Of course, the properties of the liquids, such as density and sound speed, are the dominant parameters in determining the acoustic pressure distribution in the liquids (Eq. 6.1-6.3). Bi-8%Zn has a much higher density and faster sound speed than water and silicone oil, the pressure amplitude at sonotrode tip is much higher than both water and silicone oil. However, it also attenuates faster in Bi-8%Zn because more acoustic energy is dissipated to overcome the relatively big inertia of the metal during the wave propagation.

As discussed in the bubble nucleation part, the bubbles that are nucleated and growing near the sonotrode tip behave very chaotic and cannot survive more than one wave period due to the high acoustic pressure at the region adjacent to the sonotrode tip. However, at the location further below the sonotrode, for example, ~2 mm away from the sonotrode tip, some bubbles (Fig.4.5) were shown to survive more wave periods and its size oscillated in responding to the modest acoustic pressure.

Although the bubbles in different liquids respond to the pressure in the same manner, that is, bubble is compressed when pressure increases and expanded when pressure decreases, the bubble size, velocity and pressure at the bubble wall are different because they strongly depend on the acoustic pressure and properties of the fluid properties, including surface tension, viscosity, density and sound speed. Fig.7.3 shows, using the same initial bubble radius and the same pressure amplitude for water, silicone oil, and Bi-8%Zn. The bubble in silicone oil and water behave similarly, while the bubble radius in Bi-8%Zn is smaller mainly because the surface tension of the Bi-8%Zn is higher, resisting the expanding of the bubble.

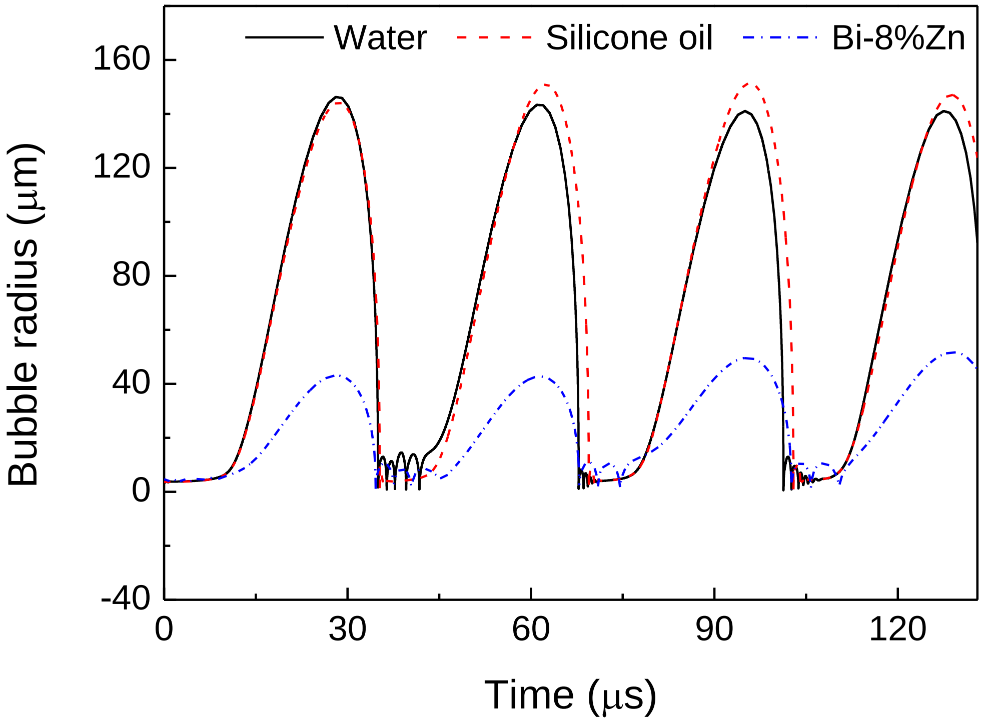

Fig.7.3. *Bubble radius evolution versus the time under an ultrasound in water, silicone oil and Bi-8%Zn. The same initial bubble radius of* R_0 *=5 μM is used for the three liquids, and the pressure amplitude is* p_a *= 0.3 MPa.*

The effect of the acoustic pressure on the bubble oscillation have been studied and discussed by Kurz and Geisler [204]. As the driving force of bubble oscillation, the pressure amplitude affect the life time and maximum size of the bubble, because the pressure difference between the bubble inside and outside determines the speed of the bubble increase and the bubble collapses when the surface tension cannot balance the pressure difference. The initial bubble radius is also very important for the bubble oscillation, as the bubble might be bigger than the resonant size to the acoustic pressure, which lead to a highly instable bubble interface under the acoustic pressure as the example showed in Fig. 5.4a-3 to a-7.

7.2.3 Bubble implosion

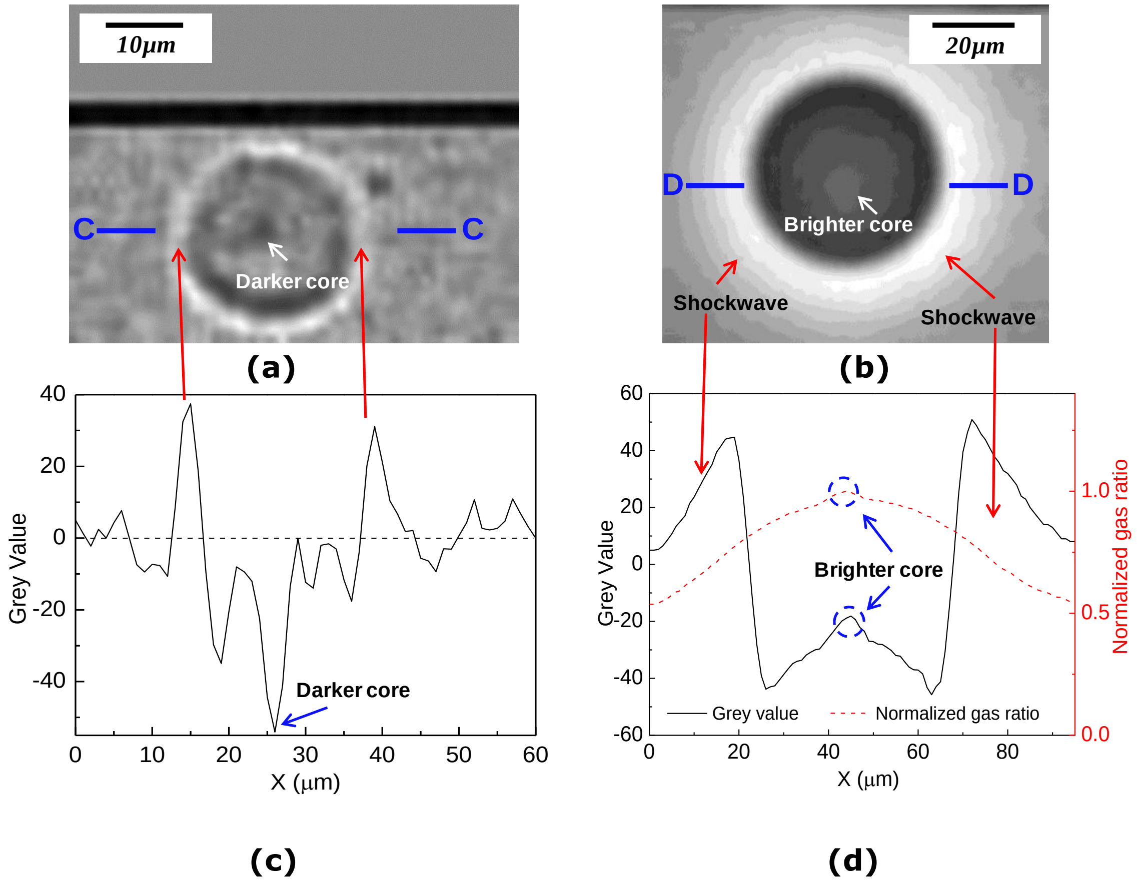

Fig. 7.4. *(a) The images obtained by subtracting Fig. 4.6a-7 from a-8. (b) The image by subtracting the squared area in Fig. 4.6c-4 from that in c-5. The averaged grey values along (c) the marked line C-C in* ***(a)*** *and (d) D-D in* ***(b)****, respectively.*

Compared the bubble implosion phenomena in the three liquids, the implosion(s) of the non-spherical bubble(s) in silicone oil is not as violent as those spherical bubbles in water and liquid Bi-8%Zn, and shockwave was not observed in silicone oil. However, the bubble (nuclei) multiplication induced by bubble implosion is very clearly demonstrated in silicone oil (Fig. 4.6b). The bubble implosions with a darker core in water and brighter core in liquid Bi-8%Zn are very interesting, thus to further reveal and analyze this phenomenon, the imploding bubbles were subtracted by the bubbles in the previous images, i.e. Fig. 4.6a-8 minus a-7 for water, and the marked area in Fig. 4.6c-5 minus that in c-4 for liquid Bi-8%Zn. The image subtraction operations were made by firstly finding the X and Y coordinates of the bubble centre for each image, and then positioning the centres of the two bubbles together for the subtraction. In this way, any changes occurred at implosion are highlighted. The resulting images are showed in Fig. 7.4a and b, with the grey values along line C-C in Fig. 7.4a and line D-D in Fig. 7.4b plotted in c and d, respectively. The darker core in water and brighter core in the liquid Bi-8%Zn are delineated clearly by the different grey values in the central region after the image subtraction operations (Fig. 7.4c and d), and they are estimated as 1 μm and 3.5 μm in radius respectively.

By using the grey value distribution along the shock wave, the ratio of the grey value is normalized by taking the grey value along the centreline of imploding bubble as plotted in Fig. 7.4d. This different grey value along the image is most probably because some of the gases from the bubble were diffused outwards and mixed with the liquid metal, thus lead to a less dense material (brighter). This can be confirmed by the ratio curve because the grey (gas) ratio in the centre is higher than the outwards.

From the images of bubble implosion in different liquid, actually the darker core and brighter core in the central region of the imploding bubbles are the compressed hot gas cores occurred at the instant of implosion as argued in many papers concerning the studies of bubble physics [16, 205]. It is darker in water because the contrast due to refraction is ~10 times bigger than that due to absorption between air and water, while it is brighter in metal because the contrast due to refraction is less than 1/15 of that due to absorption between air and Bi-8%Zn at the experimental condition.

Many publications concerning the studies of bubble physics [16, 87, 205] have argued that there exist a hot gas core in the central region of the bubble at implosion, and it is therefore logically to assume that the darker core (Fig. 4.6a-8) and brighter core (Fig. 4.6c-5) captured in the X-ray images are actually the hot gas cores for the two cases studied. It appears as a darker core in water, but a brighter core in liquid Bi-8%Zn. The reason is that, in water (see the grey value distributions in Fig. 7.5), the X-ray phase contrast (PC) provides the dominant contrast for the X-ray image, and PC occurs at the bubble boundary. The darker core (Fig. 4.6a-8) has a very similar grey value to that of the bubble boundary (Fig. 4.6a-7), and this evidence indicates that the darker core is most likely the hot gas core generated at bubble implosion.

Although the interframe time in the water case is 3.68 μs, the actual imaging temporal resolution is 500 ns, because the 8-electron long bunch generates an X-ray pulse with the duration of 500 ns, and the information captured is actually the highly dynamic event occurred during the 500 ns. The steep change of the grey value in the central region of the bubble in Fig. 4.6a-8 (comparing to that of the bubble in Fig. 4.6a-7) also indicates that a shock wave is radiating outwards from the darker core. By viewing all the X-ray videos acquired, it is very interesting to find that, in a single wave period, one such image frame that contains the highly transient information at implosion can be always captured. In the case of liquid Bi-8%Zn, the absorption contrast (AC) is dominant and provides the contrast for the X-ray images, while the PC across the bubble boundary is very small and therefore can be ignored (Fig. 7.5b). Furthermore, the grey value in Fig. 4.8d for the imploding bubble shows that there exists a small peak at the centre of the bubble (a brighter core of ~3.5 μm in radius). This means that the brighter core contains less dense material, and it is logically to assume that the brighter core is also the hot gas core formed at bubble implosion.

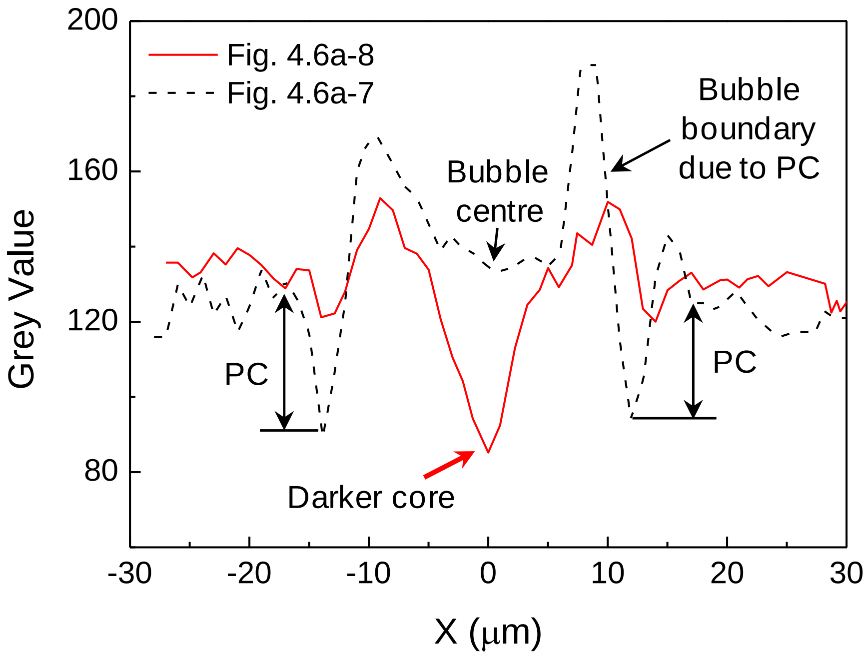

(a)

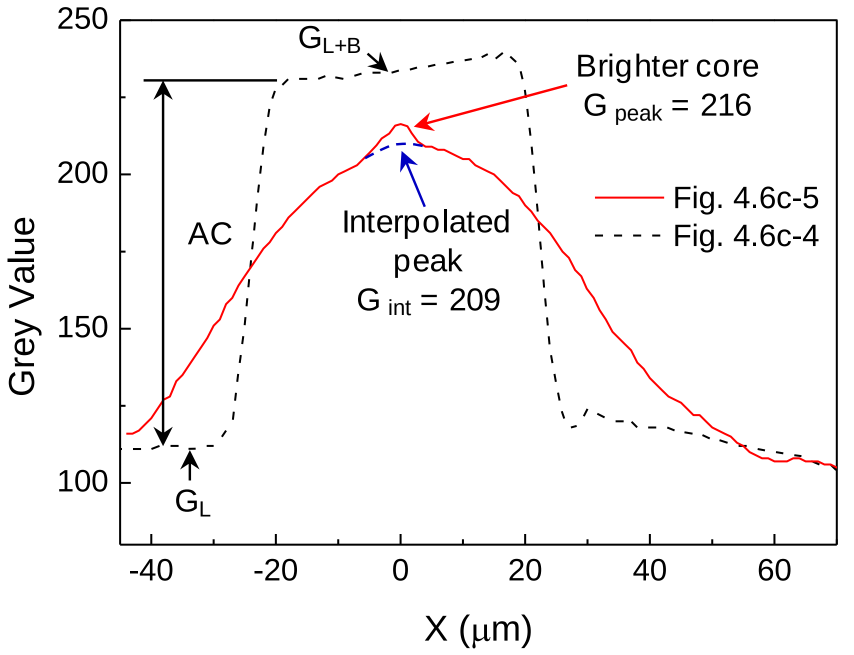

(b)

Fig.7.5. *The grey value distributions along the lines passing through the centres of the bubbles showed in (a)* ***Fig.4.6a-7*** *and* ***a-8****; and (b) those in* ***Fig. 4.6c-4*** *and* ***c-5****.*

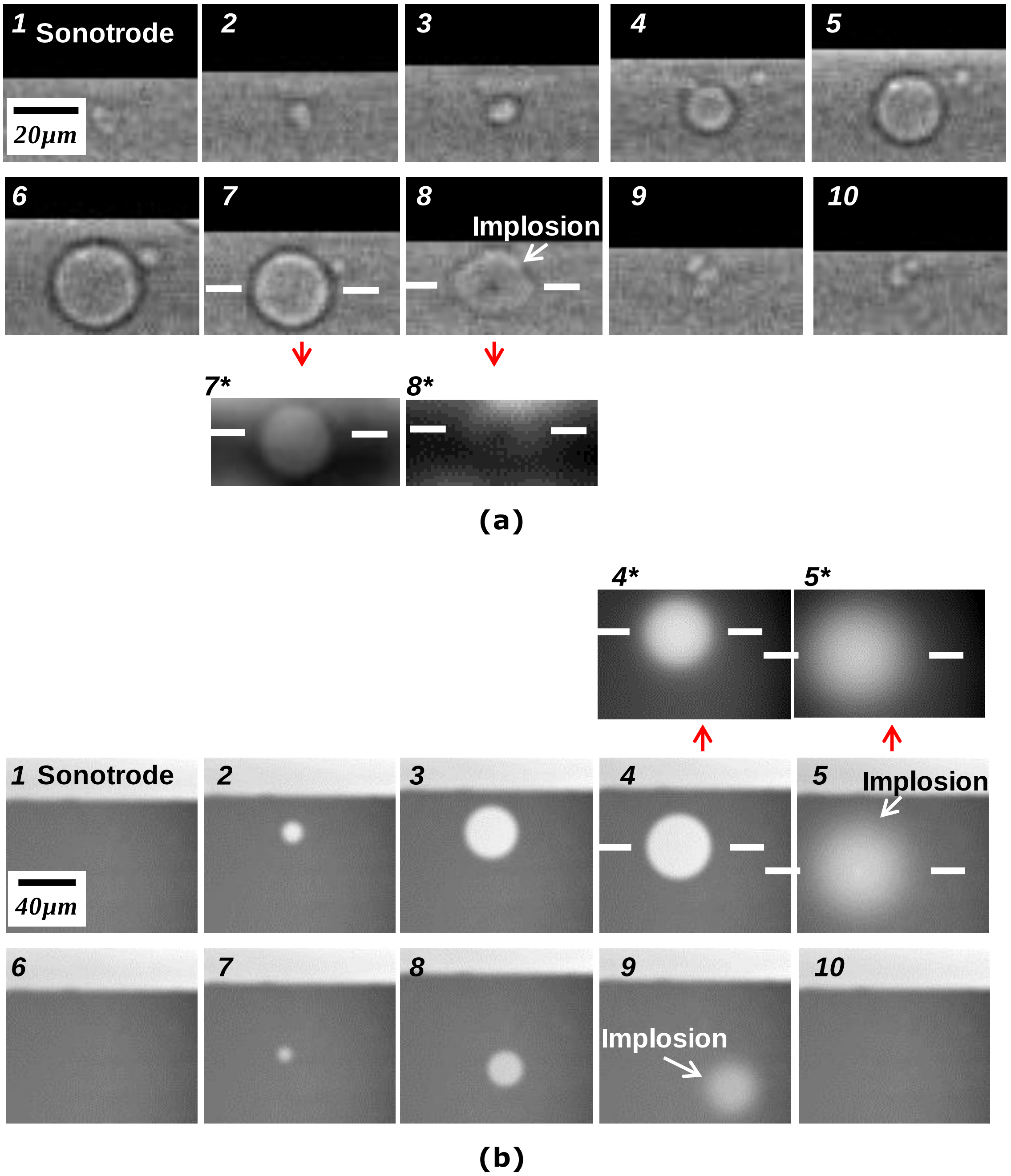

Fig. 7.6. *(a) and (b) The consecutive images acquired in water in 1 wave period (271,554 fps, interframe time is 3.68 μs), and those in liquid Bi-8%Zn at 700K in 2 wave periods (135,781 fps, interframe time is 7.36 μs). Bubble implosion in water is showed in image* ***a-8****; and that in liquid Bi-8%Zn is showed in* ***b-5*** *and* ***b-9*** *respectively. The inserts in a and b are the phase retrieved images based on* ***a-7****,* ***a-8****,* ***b-4*** *and* ***b-5*** *by using 7.7 keV (the first harmonic) for water and 30.5 keV (the fourth harmonic) for liquid metal.*

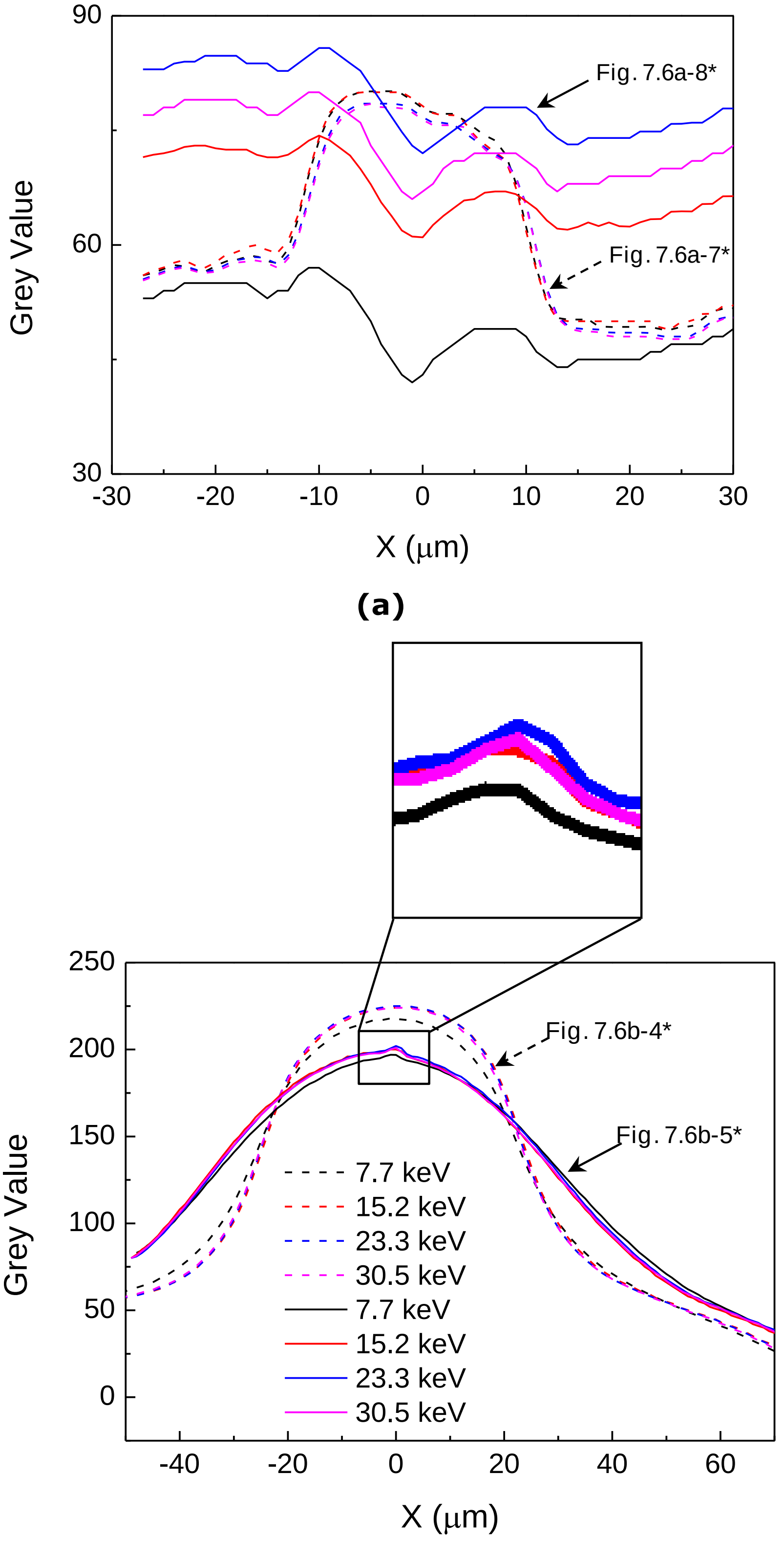

(a)

(b)

Fig.7.7. *The grey value distributions along the lines the phase retrieved images (a) in water and (b)in Bi-8%Zn under different X-ray harmonic energy* (7.7, 15.2, 23.3, 30.5 keV).

This is further approved by using ANKAphase (a software for single-distance phase retrieval from inline X-ray phase-contrast radiographs [206]), and by using the experimental parameters, including the sample to detector distance , that is 200mm and 980mm for water and liquid metal), and X-ray energy range. The first four harmonic energy (7.7, 15.2, 23.3, 30.5 keV) were used to test the energy effect on the phase retrieval results, and with those energies, the corresponding rarefaction parameters, that is, delta/beta ratio at such X-ray energy are 256, 1040, 2100, and 2410 for water and 7.81, 9.16, 13.2, 18.6 for Bi-8%Zn [207, 208], respectively. An averaged stabiliser value 0.5 was used to partially compensate the image blurring introduced by the single-distance phase-retrieval. The process pixel size is defined by using the image resolution, 1 μm/pixel. To avoid the inference of the interface of the sonotrode with liquid, the sonotrode was cropped off from the images (Fig.7.6a and b) and left with only the liquid with bubble. The cropped images were processed by using this technique and the results images are showed in the inserts of Fig.7.6a and b, which are the images before implosion and at implosion.

We can see that after phase retrieval, the bubble interfaces are smeared and the bubbles before implosion are displayed as a integrate object caused by the absorption contrast (Fig.7.6a-7* and Fig.7.6b-4*). The grey value distributions along the bubble centre after phase retrieve (white lines marked in the inserts of Fig. 7.6a and b) under different X-ray energy are showed in Fig. 7.7a and b, respectively. We can see that the bubble at implosion after phase retrieve is not as integrate as that before implosion, however, cores near the bubble centre is still can be detected although the contrasts of the cores are reduced after phase retrieve and come with the same regulation with different X-ray energy. This indicates that the dark core or the bright core exist due to different X-ray absorption coefficient, that is density of the gas.

To analyse the density, pressure, and temperature of the brighter core at bubble implosion is on processing, so it will not discuss in this thesis.

7.2.4 Bubble coalescence and interactions

Fig. 7.8a-b shows that the bubble boundaries are very clear because of the phase contrast effect. The overlapped area (arrowed) is brighter than either of the bubbles, while there is no such bright area, but just a darker interface when the bubbles are just in contact (arrowed). Hence whether the bubbles are just in contact or being overlapped can be clearly identified which is a very important for the study of bubble coalescence. Fig. 4.9 shows that in the different liquids, the bubble coalescence events are different, e.g. the bubble lifetime and the coalescence time.

For the coalescence time, the classical bubbles coalescence theories [89, 93] argue that, after two bubbles touching each other, the thin liquid film that is trapped between the two touching boundaries need to be drained out in order to complete bubble coalescence. The time needed to complete the liquid film drainage is the dominant parameter in governing bubble coalescence time as it is much longer compared to the time needed for film rupture. The time of film drainage is determined by the physical properties of the liquid such as surface tension, viscosity, and environmental conditions such as temperature, pressure [93].

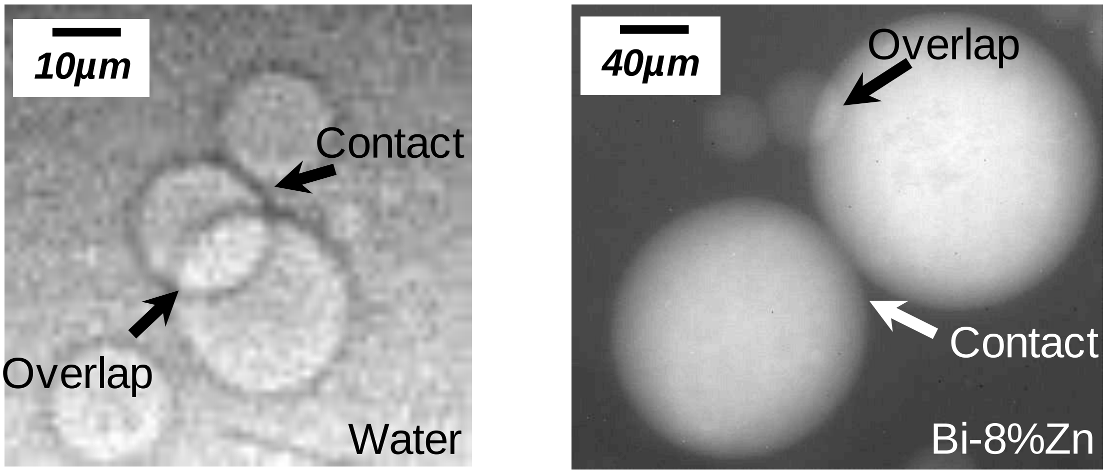

(a) **(b)**

Fig. 7.8. *Typical X-ray images, showing the contacted or overlapped bubble boundaries (a) in water, and (b) in liquid Bi-8%Zn. The phase-contrast allows the overlapped surface to be clearly identified.*

Thus, in this session, the film drainage times for different liquids by using both experimental data and the two classical models are calculated and discussed. Two models, namely no-slip interface (Eq. 2.31, as detailed in Chapter 2) and free interface model (Eq. 2.33), were used to calculate the film drainage times for bubble coalescence.

The mean bubble radius R_e is defined as:

$$\frac{2}{R_e} = \frac{1}{R_1} + \frac{1}{R_2} \tag{7.1}$$

Eq. 2.31 and Eq. 2.33 can be transformed into:

No-slip (the drainage flow is considered as laminar flow):

$$t_d \approx \frac{3\eta}{8\sigma h_c^2}(R_f^2 R_e) \tag{7.2}$$

Free interface (the drainage flow is considered as plug flow):

$$t_d \approx \sqrt{\frac{\rho}{16\sigma}} log\left(\frac{h_i}{h_c}\right)(R_f^2 R_e)^{\frac{1}{2}} \tag{7.3}$$

Where R_1 and R_2 are the radii of the two touching bubbles, R_f is the radius of the trapped liquid film (Fig. 2.14), η and σ are viscosity and surface tension of liquid, respectively. h_c is the critical thickness, i.e. the mean thickness of the film at the instant of its rupture, and is set at 20nm according to [105]. h_i is the initial thickness of liquid film, and $\frac{h_i}{h_c} \approx 100$ referred from [21].

As R_f is also determined by the bubble radius, in this way, we can use $\mathrm{R_f^2 R_e}$ which represents the size of the bubbles at coalescence, as the single variable and the results can be analyzed as below.

From Eq. 7.2 and 7.3 we can see that the drainage time of No-slip interface case is proportional to $\mathrm{R_f^2 R_e}$, while the drainage time of free interface case is proportional to $(\mathrm{R_f^2R_e})^{\frac{1}{2}}$. By using the parameters listed in Table 3.2 for each liquid, we can obtain the theoretical drainage time for both liquid, as the lines showed in Fig. 7.9a, including the free interface for water, Bi-8%Zn, and no-slip interface for Bi-8%Zn and silicone oil.

Also, for the experimental results, *R_f* and Re can be measured or calculated by Eq. 7.1 from the images captured immediately before the coalescence, as well as the corresponding drainage time by count the duration when two bubbles start to touch each other until the completion of the coalescence. The error of the measured drainage time is half of the interframe time, i.e., 92.4 μs for liquid metal and 1.8 μs for water.

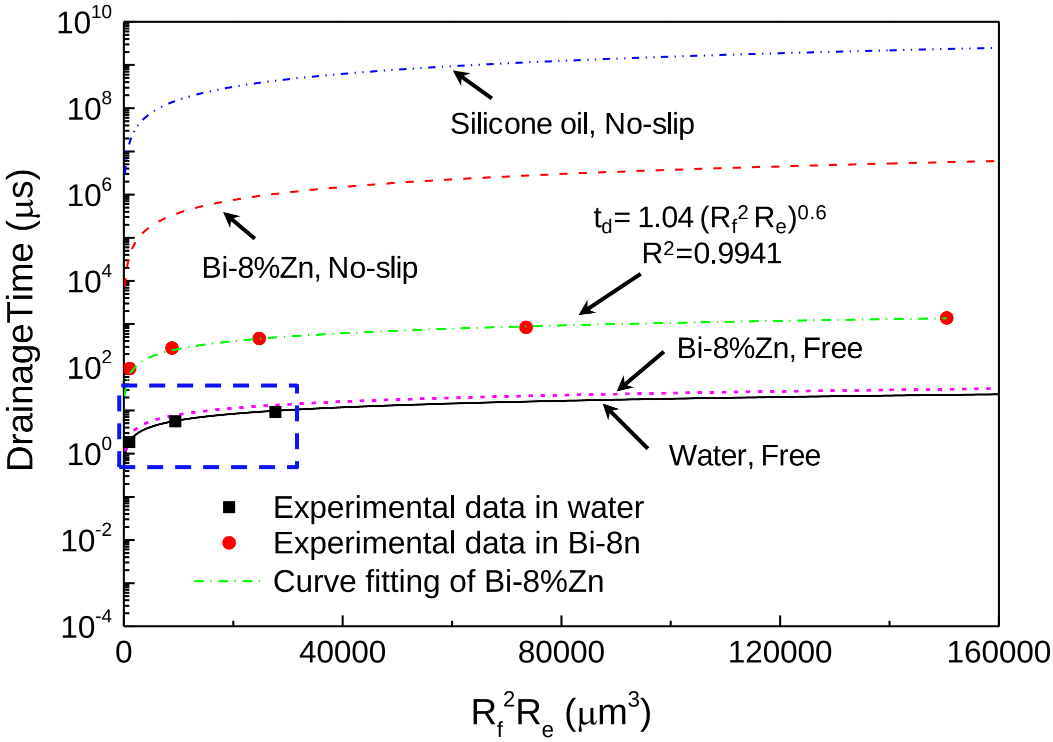

(a)

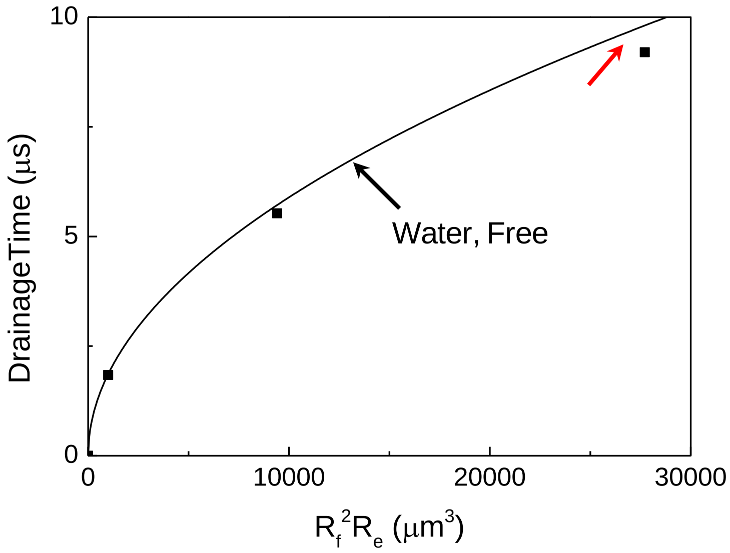

(b)

Figure 7.9. *(a) A comparison of the calculated film drainage time with experimental measurement. The error of the experimental data is half of the interframe time (92.4 μs for liquid metal and 1.8 μs for water), and (b) the enlarged graph of the squared area in* ***a****, showing the detailed differences between the measured and the calculated data.*

Both calculated and measured results are plotted in Fig. 7.9a as a function of $R_f^2R_e$. We can see that, in water, the measured film drainage time agrees well with the calculation using the free interface model which also agreed with the previous findings [21, 89, 95]. However, for the case of liquid Bi-8%Zn, neither of the calculations by Eq. 7.2 or Eq. 7.3 matched the measured time from the images. The measured time is in between the predictions made by Eq. 7.2 and Eq. 7.3.

For silicone oil, as there is no coalescence event observed (not coalescence before collapse), so the drainage time of silicone oil more likely follows the no-slip interface model (the free interface model results of silicone oil is very close to those of water).

Eq. 7.2 shows that the drainage time is directly proportional to surface tension, but inversely proportional to viscosity. Generally, higher surface tension causes stronger resistance to the deformation of bubbles, leading to the formation of smaller area of liquid film, and therefore shorter time to drain it out. Apparently, higher viscosity leads to more difficulties in "flowing out" (draining) the residual liquid, and therefore more time is needed for reaching the critical thickness, which is the prerequisite for film rupture and bubble coalescence.

Furthermore, we used power law ($t_d = aR^b$) to fit the measured time for Bi-8%Zn, and it was found out that $t_d = 1.04\,(\mathrm{R_f^2 R_e})^{1.6}$ give the best fitting with the correlation coefficient of 0.9941.

Using Eq.7.2, the prediction for Bi-8%Zn would be ~2 orders of magnitude longer than the measured time. Fundamentally, Reynolds equation [98] is based on the assumption of perfect tangential immobility and plane-parallel configuration of the interfaces. However, it was found, in reality, the boundary of two touching bubbles, especially for the case of high temperature liquid metal, are not perfectly flat and parallel [93]. Fig. 2.14 show that, at micrometer level, the touching boundary is a combination of low frequency hydrodynamic surface wave plus high frequency thermal perturbation [93]. Hence the critical thickness h_c has three components:

$$h_c = A_{sw} + A_{tp} + h_t \tag{7.13}$$

where A_{sw} and A_{tp} are the amplitude of surface wave and thermal perturbation, respectively, and h_t is the thickness of the film at the thinnest position (Fig. 2.14) where is the location for film rupture to start.

The wave length and amplitude of thermal perturbations is much less than those of hydrodynamic surface wave, but the thermal perturbation at the thinnest part of the liquid film will be the dominant factor for the film rupture. For the small gas bubble (micrometer range), the initial thermal perturbation is of the order of $\sqrt{\frac{kT}{\sigma}}$, where k is Boltzmann's constant and T is the absolute temperature. For liquid Bi-8%Zn at 700K, calculation using the data of surface tension versus temperature in pure Bi [200] show that the thermal perturbation at 700K is about 75% higher than that at room temperature (from 0.1nm to 0.175nm), and greatly enhancing the possibility of film rupture before it reaches the critical thickness.

Moreover, under the influence of 30 kHz ultrasonic wave, the hydrodynamic surface wave is greatly amplified in terms of amplitude and frequency, enhancing very effectively the ‘pumping’ action of this travelling surface wave and the thinning of the liquid film.

This is proved by the observation in water, as showed in Fig. 7.9b, the measured drainage time is lower than water of free interface case, and this difference become bigger when the bubble size increase, which is 6.6% difference at the last point (as the red arrow in Fig. 7.9b). The bubbles in liquid metal are bigger than water, so the ultrasound effect on the bubble coalescence in liquid metal will be more significant.

The results suggests that in the applications of ultrasound induced bubble calescence, e.g. the ultrasonic degassing of Al alloys, the fluid properties, such as increasing temperature or reducing viscosity [200] can be utilised to increase thermal perturbation of the contacting bubble surface to reduce the drainage time, thus enhancing the rate for bubble coalescence.

Fig. 7.10 shows the bubble radii measured from Fig. 4.9c during the process of bubble coalescence with the bubble radii of bubble 1 simulated by using Gilmore model. The calculated radius of bubble 1 (using an initial bubble radius of R_0=25μm, and pressure at the bubble wall P=0.05MPa), agree quite well with the experimental results before 1 ms (the dash line inside the square); However, after 1 ms, exactly when the bubble 2 and 3 coalesced and approached to bubble1, the oscillation of bubble 1 doesn’t follow the Gilmore model any more. This may be due to, during bubble coalescence, the bubbles do not respond well to the acoustic wave when a third bubble is present nearby. This information is very important for understanding the collective behaviour of ultrasonic bubbles [209].

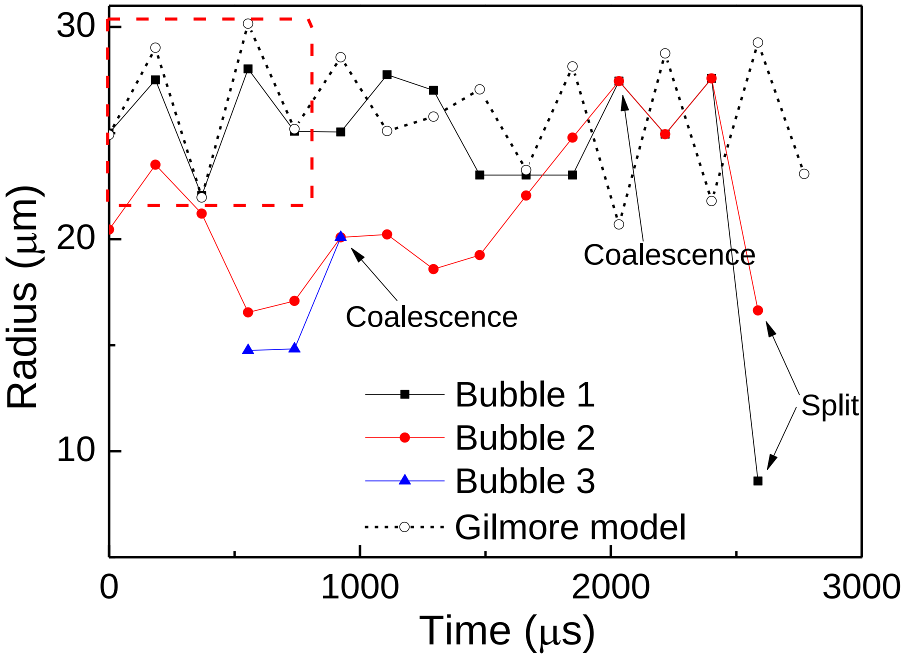

Fig. 7.10. *Bubble radii in Bi-8%Zn, measured from* ***Fig. 4.9c.*** *The calculated bubble radii using Gilmore model are superimposed.*

Fig. 4.10 showed schematically the interaction of the close or touched bubbles at different coalescence stage. When the two bubbles are close but not touch, due to their small distance and strongly nonlinear oscillation they experience a shape distortion upon interaction, similar to the case of bubble–solid-boundary interaction. Thus closely spaced bubbles have interaction scenarios similar to bubble collapse in the vicinity of a solid boundary as observed and discussed by Lauterborn et al [72] and Testud-Giovanneschi et al [210]. The X-ray images in this research show that when two bubble are touched with a flat surface formed, the pressure has to emit into the direction perpendicular to the flatten surface as shown in Fig. 4.10. Hence microjets shooting out perpendicular to the touching bubble surface which are really interesting.

The very typical experimental results in Fig.4.10 and the sketch in Fig. 7.11 indicate that, (1) when the bubble collapse at stage 1 (touch or almost touch), the bubble will shoot microjet to each other, and the new bubbles are distributing almost in a line along the direction of microjet; (2) when the bubble collapse at stage 2 (flat surface formed in-between), the nuclei are shot out perpendicularly to the bubbles centreline and if the nuclei are close enough, then they will coalesced and finally lead to a single bubble on each side; (3) when the bubble collapse at stage 3 (coalesced and form a irregular shape), due to the bubble size difference, the bubble nuclei are formed in a arc shape, and most of the nuclei are generated near the side of bigger bubble; (4) when the bubble collapse at the 4th stage (coalesced and recover to be a spherical shape), the nuclei are located in a the centre of the bubble, and very close to each other, as a result, they will coalesce and form a single bubble.

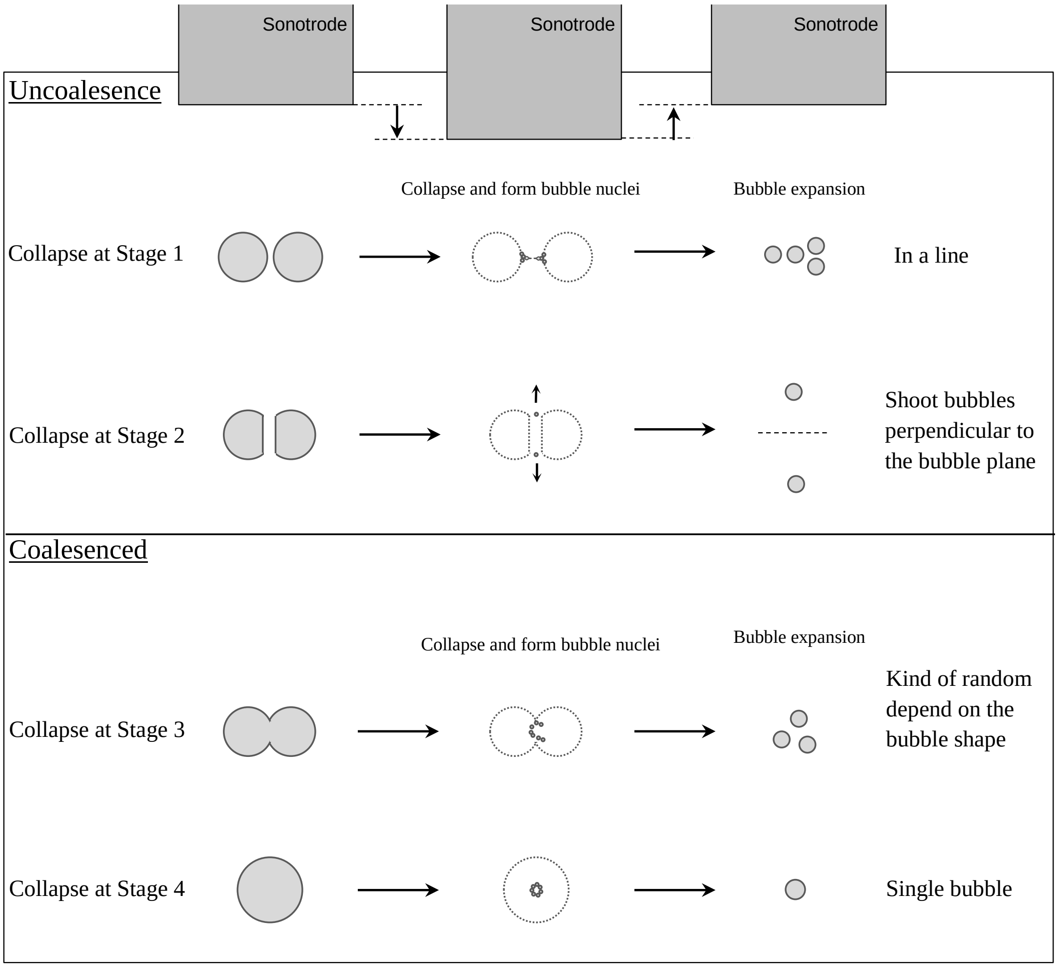

Fig. 7.11. *Schematic diagram, showing 4 scenarios of bubble collapsing at the different coalescence stage.*

7.2.5 Bubble clouds

As discussed in Chapter 2, many researchers studied the bubble structure under the acoustic pressure field, i.e. steamer, filament, cone shape, etc. [112]

Fig. 4.13 shows the typical bubble clouds formed at the sonotrode tip in all three liquids. Similar phenomena were observed by Zhen [211], and Moussatov [112]. The acoustic pressure distribution plays an important role in the bubble structure, as the bubbles formed near the sonotrode tip are pushed away, and undergo attractive and repulsive Bjerknes forces caused by the pressure fluctuation and strongly nonlinear oscillations of the bubbles. Although macrostructure of the cone shaped bubble cloud remains remarkably stable, the bubbles at micro level is highly dynamic.

The bubble flux and its density in metallic alloy were quantified as showed in Fig. 4.14-4.16, and they are related to the acoustic pressure and acoustic stream. The bubbles movement in the acoustic field is mainly dominated by the fluid flow and pressure gradient as further verified by the comparison of bubble flux and density under different ultrasound power in Fig. 4.14 and 4.15, that is, the higher, the ultrasound power, the higher, the fluid velocity (Fig. 5.18b).

Previously presented works focused on the bubble size distribution statistically in a long time duration, however, in our research, with the advantages of the high frame rate, we can capture about 5 images within a single wave period, and we have found that bubble sizes vary hugely in the compression cycle and expansion cycle, especially at the highest negative pressure and positive pressure. Because the images captured are immediately below the sonotrode tip, the pressure phase can be derived from the sonotrode position by neglecting phase delay as the sketch showed in Fig. 4.3, that is, the pressure reach the biggest positive (compression) value when the sonotrode moves to the lowest position, and reach the biggest negative (expansion) value when the sonotrode moves to the highest position.

Fig. 4.12 shows the distributions of bubble radii when sonotrode at the lowest and highest positions in different liquids. When the sonotrode comes to the highest position, bubble radii become bigger and especially for the cases of Bi-8%Zn (almost all the bubbles are > 20μm) as the pressure near the sonotrode reduce and reach the lowest when the sonotrode at the highest position.

By knowing the single and double bubbles behaviour under ultrasound, the collective behaviour can be explained well. The large sized bubbles have a small percentage in the cases of water and silicone oil, as they might be generated because of the coalescence of the small bubbles, and due to the low surface tension, the big bubbles are tend to collapse and generate a huge amount of bubble nuclei and tiny bubbles (less than 5μm). Less small bubbles in liquid metal because the higher surface tension and large pressure due to its density and sound speed, the bubbles can grow quickly and largely. The viscosity affects apparently the bubble coalescence in silicone oil and liquid metal as confirmed by the different bubble coalescence time measured. These certainly influence the collective bubble size distribution. For example, in silicone oil, the higher percentage of small bubble (0~5μm) may be due to the difficulty in coalescence because of its high viscosity.

7.3 Ultrasonic bubbles and acoustic flow in semisolid metallic alloy

7.3.1 Bubble interaction with solid phases

Microjet flows at bubble implosion were captupred in water at 271,554 fps (Fig. 5.1), and, for the first time, in liquid Bi-8%Zn at 135,780 fps (Fig. 5.2). According to Lauterborn and Ohl [17, 18], the velocity of the micorjet in water was estimated at ~150 m/s for the bubble radius bigger than 60 μm. Due to the lower frame rate used in our experiment, the obtained average velocity (~5.37 m/s calculated from Fig. 5.2a-4 and a-5) of the microjet in the interframe time of 7.4 μs far too low than that found in [17].

The oscillating bubbles (Fig. 5.4 and 5.5) respond to the acoustic pressure faster than the particles and fluid flow especially in Fig. 5.5. Hence the momentum difference can stir up the solid particles or phases. In liquid Bi-8%Zn, the oscillation of the bubble on a free solid phase is capable of fracturing it within a few tens of wave periods (Fig. 5.6). The implosion is more effective in bombarding the solid particles (Fig. 5.5).

Fig. 5.7 and 5.8 show the acoustic flow including bubbles, Zn particles, move together downwards in a radiation pattern from the sonotrode tip. As further away from the sonotrode tip, the radiation front becomes larger as showed in Fig.5.7a-b while the velocities of the bubbles, particles and fluid are reduced as showed in Fig.5.9. Similar phenomenon was also observed by using the PIV in water and discussed [120, 212].

Under ultrasound, bubbles are moving faster than the particles especially at the position near the sonotrode. This is because both of the bubbles and particles are subjected to the acoustic pressure and fluid field, due to the less mass, the bubbles are easier to be motivated than particles. However, as the distance below the sonotrode tip increase, the driven force, the pressure gradient and fluid velocity, of the motions of bubbles and particles are dissipated apparently as we discussed before, thus under the buoyancy, the velocity of bubbles and particles are very similar.

7.3.2 Bubble interaction with liquid-solid interface

The experimental results show that bubbles are capable of fracturing (Fig. 5.16a) and detaching (Fig. 5.14 and Fig. 5.16a) the solid phases from the L-S interface, and all of the detachments and fragments are delivered to the bulk liquid by the fluid flow. The mechanism of the fragmentation and detachment are:

Firstly, microflows [213] and pressure [38] are generated in the vicinity of a bubble. At the presence of solid particles or L-S interface, the pressure and microflow are directed towards the particles, leading to the fragmentation or detachment of the solid particles [214]. Also, bubble oscillation on the solid particles might not be as violent as bubble implosion, but oscillating bubble can pulse on the particles for hundreds of wave cycles (Fig. 4.5), likely to cause fatigue of the solid phase and the break up (Fig. 5.14) and for the transparent alloy described in [33].

Fig. 5.15b shows the bubble pressure and velocity at bubble wall calculated by using Gilmore Model (initial bubble radius is 60μm, and ambient pressure is 0.24 MPa), which is more than 50 MPa within 100 cycles of ultrasound waves. According to the method proposed by Frost and Ashby, the yield strength σ_y at the melting point can be estimated as [31],

$$\sigma_y = 10^{-3} \cdot E(T) \tag{7.3}$$

$$E(T) = E_{300}\left(1 + B \cdot \left(\frac{T-300}{T_m}\right)\right) \tag{7.4}$$

where *E(T)* is the elastic modulus at an absolute temperature *T*, E_{300} is the modulus at 300 K, and T_m is the absolute melting temperature. We obtained the yield strength of Zn particles at 550K is about 56.15 MPa. Thus, the pressure induced by the bubble might not able to fracture the primary phase directly, but a fatigue effect (as Fig. 5.14 and 5.16a shown) may work, when the bubble keep oscillating on the surface of particles for thousands of cycles.

Secondly, as the previous research reported, the solidification process will trap some solute-rich liquid between the particles or dendrites [37, 160], the oscillation of bubble at the L-S interface, by diluting the liquid trapped in the solid phases, and uniform it with the bulk liquid, thinning the root of solid particles so that enhances the detachment [31, 171, 215]. This mechanism was detailed discussed in [171].

Thirdly, apart from the fatigue effect of the oscillating bubble on the particle, the bubble implosion (the irregular shape of the bubble in Fig. 5.14 and 5.16a) will also play an important role in fracturing process. Due to the limitation of the acquisition rate in such a big viewing field (Fig. 5.14 and 5.16a), we cannot capture the bubble implosion; however, our research from APS has captured the clear morphology of bubble implosion in the liquid Bi-8%Zn at 135,780fps as showed in Fig. 4.6c with a shockwave emitted, and in Fig. 5.2 with a microjet flow shooting towards the boundary (sonotrode). The shockwave in Fig. 4.6c-5 can affect the area about 1 times bigger than the bubble showed in Fig. 4.6c-4. As discussed in bubble implosion section in this chapter, the pressure of the bubble implosion results in a pressure up to 59,156 bar in the bubble centre, although this pressure will damp out fast with increase of the distance away from the bubble centre, it will be definitely affect the structure at L-S interface. Also, the microjet towards the interface (Fig. 5.2) at bubble implosion will also contribute to the fracture and detachment of solid phases at L-S interface.

7.3.3 Effect of acoustic flow on the L-S interface during solidification

Fig. 5.16 shows the 60W power ultrasound induces a considerable strong convection in the semisolid Bi-8%Zn (~270°C) and fracture a ~250 μm thick Al-20%Cu slot sample (cantilever beam) at position about 5 mm below the sonotrode (image centre position) within few tens of millisecond. It has no doubt that this strong convection is the dominant factor to break Al-20%Cu cantilever beam, accelerating it to be ~1 m/s within 3 ms.

The velocity obtained in metallic alloy is much higher than those reported in water [120] and in transparent alloy. The reason is that the intensity of the streaming effects is directly proportional to the ultrasonic momentum acquired by the liquid when it absorbs the wave energy; therefore, liquid metal absorbs more ultrasound wave energy due to its higher density and velocity of sound [38].

Thus, the ultrasound enhanced fluid flow is capable of fracturing and detaching the solid phase from the L-S interface (Fig.5.17). More importantly, we have observed many detached solid Zn phases were delivered back into the top hotter liquid region by the acoustic streaming flow but survive there for substantial period of time (Fig. 5.7). Those surviving Zn phases certainly will act as embryonic grains for atoms in the liquid to grow upon, enhancing and promoting very effectively the grain refinement of the solidifying alloys. This striking evidence indicates that the acoustic streaming flow is one of the very important mechanisms for ultrasonic grain refinement in metallic alloys.

Fig. 5.18a shows that, during 2 s ultrasound processing, almost 80% of the detachment occurred within the first 250 ms.[201] This is because the fluid flow induced hydrodynamic force destroyed the L-S interface very effectively (Fig. 5.17b-c). However much less detachments occurred after 500 ms. As showed in Fig. 5.19b, the ultrasound can cause an obvious temperature increase and reduce the temperature gradient of the liquid alloy (the temperature gradient has been more than 2 times reduced between TC1 and TC2).

From the video captured, the detachment and fracturing of the solid phase at L-S interface are mainly because of the hydrodynamic force from the fluid flow. However, the hot liquid that was pushed from the top to the bottom will cause an increase of the temperature at the L-S interface, and re-melt the solid phases as the ultrasound continued. This is another mechanism which is discussed in detail in the following section.

7.3.4 The coupled effects of fluid flow and temperature

Fig. 5.20 shows that the temperature increase generated by the applied ultrasound is also capable of detaching the Zn particles from the L-S interface. This temperature increase is mainly due to 3 mechanisms: firstly, the energy from the ultrasonic vibration is absorbed by the liquid metal and converts to the inner energy of the metal alloy; secondly, the implosion of ultrasonic bubbles; and finally, those liquid of high temperature on the top near the sonotrode zone is pushed down by the acoustic flow to the colder zone below, which is the most important mechanism for the re-melt of the solid particles at the L-S interface.

By measuring the velocity of the erosion of L-S interface, the temperature induced re-melt in our experiment was found to be able to erode the interface at ~50 μm/s, which is one sixth of the efficiency of the ultrasonic bubble showed in Fig. 5.14.

7.4 Summary

The novel findings from the ultrafast X-ray imaging experiments are discussed in details in this chapter, including the prove of the existence of the gas core at bubble implosion, the time for bubble coalescence, and the interaction of ultrasonic bubbles and acoustic flow with solid particles and phases, as well as their coupled effects on the liquid-solid interface.

Chapter 8: Conclusions and Future works

8.1 Conclusions

A very comprehensive experimental and modelling research have been carried out to study the highly dynamic behaviour of ultrasonic bubbles and acoustic flows in water, silicone oil, and Bi-8%Zn alloy in different conditions. The key conclusions of this thesis are:

- A novel in situ ultrasound experimental apparatus was successfully built and used for this research. It is particularly useful for in situ studying metal alloy solidification under ultrasonic waves using the most advanced synchrotron X-ray beamline, such as 32-ID-B at APS and I12 at DLS.

- For bubble implosion: For the first time, bubble implosion in liquid metal was captured in real-time and in situ. In both water and liquid Bi-8%Zn, gas cores were found in the bubble centre at implosion. Phase retrieval was used to prove the existence of the gas core at bubble implosion.

- For bubble oscillations at quasi-steady state condition, the measured bubble radii oscillations agree well with the predictions made by Gilmore model for all liquids studied in this research.

- For bubble coalescence, the time needed for water can be predicted using the free interface model, while that for liquid Bi-8%Zn cannot be predicted using either the no-slip or the free interface model. A new power law model is developed and the prediction made using this new model agrees well with the experiments.

- For bubble cloud, bubble size distributions at two extreme pressure phases were found for water, silicone oil and liquid metals. The bubble flux in liquid metal, a Sn-30%Cu alloy, was presented.

- For the first time, real-time experimental evidences in metal alloys were presented, showing that the ultrasonic bubbles and the acoustic flows are capable of fracturing and detaching the solid phases from the liquid-solid interface.

- The temperature increase caused by the applied ultrasound in Bi-8%Zn during solidification is capable of detaching the solid Zn phases from the liquid-solid interface. However, it is a slower effect compared to that caused by the acoustic pressure field.

- Ultrasound power is a dominant factor in governing the interactions between ultrasonic bubbles, acoustic flows and liquid-solid interface. In addition, quantitative information about ultrasound powers versus the efficiency of the coupled effects of bubbles, acoustic flows and temperatures on the liquid-solid interface erosion has been provided.

8.2 Future works

It will be valuable to study other alloy systems using the developed in situ ultrasound experiment devices, especially for those having different solidification phases and structures. Also, the study of collective behaviour of bubble cloud which have a direct relevance to industrial scale-up applications will be the focus of our research in the next step.

References

[1] J. D. Achenbach and O. K. Parikh, "Ultrasonic Detection of Nonlinear Mechanical Behavior of Adhesive Bonds," *Review of Progress in Quantitative Nondestructive Evaluation,* vol. 10B, pp. 1837-1844, 1991.

[2] H. R. Mayer, H. Lipowsky, M. Papakyriacou, R. Rösch, A. Stich, and S. Stanzl-tschegg, "Application of ultrasound for fatigue testing of lightweight alloys," *Fatigue & Fracture of Engineering Materials & Structures,* vol. 22, pp. 591-599, 1999.

[3] D. G. Shchukin, E. Skorb, V. Belova, and H. Möhwald, "Ultrasonic cavitation at solid surfaces," *Advanced Materials,* vol. 23, pp. 1922-1934, 2011.

[4] J.Campbell, "Effects of vibration during solidification," *International Materials Reviews,* vol. 26, pp. 77-108, 1981.

[5] G. I. Eskin and D. G. Eskin, *Ultrasonic Treatment of Light Alloy Melts*, 2nd ed. Boca Raton: CRC Press, 2015.

[6] W. Lauterborn and T. Kurz, "Physics of bubble oscillations," *Reports on Progress in Physics,* vol. 73, pp. 1-88, 2010.

[7] N. Bremond, M. Arora, S. M. Dammer, and D. Lohse, "Interaction of cavitation bubbles on a wall," *Physics of Fluids,* vol. 18, pp. 1-11, 2006.

[8] K. S. Suslick and D. J. Flannigan, "Inside a collapsing bubble: sonoluminescence and the conditions during cavitation," *Annual Review of Physical Chemistry,* vol. 59, pp. 659-683, 2008.

[9] K. S. Suslick, D. A. Hammerton, and R. E. Cline, "Sonochemical hot spot," *Journal of the American Chemical Society,* vol. 108, pp. 5641-5642, 1986.

[10] J. Holzfuss, M. Rüggeberg, and A. Billo, "Shock Wave Emissions of a Sonoluminescing Bubble," *Physical Review Letters,* vol. 81, pp. 5434-5437, 1998.

[11] T. J. Mason, "Ultrasound in synthetic organic chemistry," *Chemical Society Reviews,* vol. 26, pp. 443-451, 1997.

[12] Y. M. Wang, B. Judkewitz, C. A. DiMarzio, and C. Yang, "Deep-tissue focal fluorescence imaging with digitally time-reversed ultrasound-encoded light," *Nature Communications,* vol. 3, pp. 928-935, 2012.

[13] J. Giles, "Ultrasound scans accused of disrupting brain development," *Nature,* vol. 431, pp. 1026-1026, 2004.

[14] P. Prentice, A. Cuschieri, K. Dholakia, M. Prausnitz, and P. Campbell, "Membrane disruption by optically controlled microbubble cavitation," *Nature Physics,* vol. 1, pp. 107-110, 2005.

[15] M. L. Calvisi, O. Lindau, J. R. Blake, and A. J. Szeri, "Shape stability and violent collapse of microbubbles in acoustic traveling waves," *Physics of Fluids* vol. 19, pp. 1-15, 2007.

[16] D. J. Flannigan and K. S. Suslick, "Plasma formation and temperature measurement during single-bubble cavitation," *Nature,* vol. 434, pp. 52-55, 2005.

[17] C. D. Ohl and R. Ikink, "Shock-Wave-Induced Jetting of Micron-Size Bubbles," *Physical Review Letters,* vol. 90, p. 214502, 2003.

[18] W. Lauterborn and C. D. Ohl, "Cavitation bubble dynamics," *Ultrasonics Sonochemistry,* vol. 4, pp. 65-75, 1997.

[19] P. C. Duineveld, "Bouncing and coalescence of two bubbles in pure water," in *IUTAM Symposium on Waves in Liquid/Gas and Liquid/Vapour Two-Phase Systems*, 1995, pp. 151-160.

[20] M. Qian and A. Ramirez, "An approach to assessing ultrasonic attenuation in molten magnesium alloys," *Journal of Applied Physics,* vol. 105, pp. 013538.1 - 013538.6, 2009.

[21] M. Postema, P. Marmottant, C. T. Lancee, S. Hilgenfeldt, and N. de Jong, "Ultrasound-induced microbubble coalescence," *Ultrasound in Medicine & Biology,* vol. 30, pp. 1337-1344, 2004.

[22] D. J. May, J. S. Allen, and K. W. Ferrara, "Dynamics and fragmentation of thick-shelled microbubbles," *IEEE Trans Ultrasonics Ferroelectrics and Frequency Control,* vol. 49, pp. 1400-1410, 2002.

[23] F. R. Gilmore, "The growth or collapse of a spherical bubble in a viscous compressible liquid," California Institute of Technology, Pasadena,California, USA. 1952.

[24] M. Dhainaut and S. T. Johansen, "Literature study on observations and experiments on coalescence and breakup of bubbles and drops," *SINTEF Report,* vol. 24, pp. 1-64, 2002.

[25] F. Helmchen and W. Denk, "Deep tissue two-photon microscopy," *Nature Methods,* vol. 2, pp. 932-940, 2005.

[26] E. G. van Putten, D. Akbulut, J. Bertolotti, W. L. Vos, A. Lagendijk, and A. P. Mosk, "Scattering lens resolves sub-100 nm structures with visible light," *Physical Review Letters,* vol. 106, p. 193905, 2011.

[27] I. M. Vellekoop and A. P. Mosk, "Universal optimal transmission of light through disordered materials," *Physical Review Letters,* vol. 101, p. 120601, 2008.

[28] P. C. F. Tischer, M. R. Sierakowski, H. Westfahl Jr, and C. A. Tischer, "Nanostructural reorganization of bacterial cellulose by ultrasonic treatment," *Biomacromolecules,* vol. 11, pp. 1217-1224, 2010.

[29] Y. Huang, L. Liu, J. Qiu, and L. Shao, "Influence of ultrasonic treatment on the characteristics of epoxy resin and the interfacial property of its carbon fiber composites," *Composites science and technology,* vol. 62, pp. 2153-2159, 2002.

[30] T. V. Atamanenko, D. G. Eskin, L. Zhang, and L. Katgerman, "Criteria of Grain Refinement Induced by Ultrasonic Melt Treatment of Aluminum Alloys Containing Zr and Ti," *Metallurgical and Materials Transactions A,* vol. 41, pp. 2056-2066, 2010.

[31] J. Pilling and A. Hellawell, "Mechanical deformation of dendrites by fluid flow," *Metallurgical and Materials Transactions A,* vol. 27, pp. 229-232, 1996.

[32] G. M. Swallowe, J. E. Field, C. S. Rees, and A. Duckworth, "A photographic study of the effect of ultrasound on solidification," *Acta Metallurgica,* vol. 37, pp. 961-967, 1989.

[33] D. Shu, B. Sun, J. Mi, and P. Grant, "A High-Speed Imaging and Modeling Study of Dendrite Fragmentation Caused by Ultrasonic Cavitation," *Metallurgical and Materials Transactions A,* vol. 43, pp. 3755-3766, 2012.

[34] R. H. Mathiesen, L. Arnberg, K. Ramsoskar, T. Weitkamp, C. Rau, and A. Snigirev, "Time-resolved x-ray imaging of aluminum alloy solidification processes," *Metallurgical and Materials Transactions B,* vol. 33, pp. 613-623, 2002.

[35] R. H. Mathiesen and L. Arnberg, "X-ray radiography observations of columnar dendritic growth and constitutional undercooling in an Al–30wt%Cu alloy," *Acta Materialia,* vol. 53, pp. 947-956, 2005.

[36] R. H. Mathiesen, L. Arnberg, Y. Li, V. Meier, P. L. Schaffer, I. Snigireva, A. Snigirev, and A. K. Dahle, "X-Ray Videomicroscopy Studies of

Eutectic Al-Si Solidification in Al-Si-Cu," *Metallurgical and Materials Transactions A,* vol. 42, pp. 170-180, 2011.

[37] R. H. Mathiesen, L. Arnberg, F. Mo, T. Weitkamp, and A. Snigirev, "Time Resolved X-Ray Imaging of Dendritic Growth in Binary Alloys," *Physical Review Letters,* vol. 83, pp. 5062-5065, 1999.

[38] T. L. Lee, J. C. Khong, K. Fezzaa, and J. Mi, "Ultrafast X-ray imaging and modelling of ultrasonic cavitations in liquid metal," *Materials Science Forum,* vol. 765, pp. 190-194, 2013.

[39] L. E. Kinsler, A. R. Frey, A. B. Coppens, and J. V. Sanders, *Fundamentals of acoustics*, 4th ed.: Wiley-VCH, 1999.

[40] Wikipedia. (http://en.wikipedia.org/wiki/File:Ultrasound_range_diagram.svg).

[41] G. I. Eskin, *Ultrasonic Treatment of Light Alloy Melts*, 1st ed. Amsterdam, Netherlands Gordon and Breach Science, 1998.

[42] J. Mi, D. Tan, and T. L. Lee, "In Situ Synchrotron X-ray Study of Ultrasound Cavitation and Its Effect on Solidification Microstructures," *Metallurgical and Materials Transactions B,* vol. 46, pp. 1615-1619, 2014/12/11 2015.

[43] F. R. Young, *Cavitation*, 1st ed.: World Scientific, 1999.

[44] J. I. Thornycroft and S. W. Barnaby, "Torpedo-boat destroyers (including appendix and plate back of volume)," in *Minutes of the Proceedings*, 1895, pp. 51-69.

[45] L. Rayleigh, "VIII. On the pressure developed in a liquid during the collapse of a spherical cavity," *The London, Edinburgh, and Dublin Philosophical Magazine and Journal of Science,* vol. 34, pp. 94-98, 1917.

[46] R. W. Boyle, "Cavitation in the propagation of sound," *Transactions of the Royal Society of Canada,* vol. 16, pp. 157-161, 1922.

[47] R. W. Boyle, G. B. Taylor, and D. K. Froman, "Cavitation in the Track of an Ultrasonic Beam," *Phys. Rev.(II),* vol. 27, p. 518, 1929.

[48] S. Balibar and F. Caupin, "Metastable liquids," *Journal of Physics: Condensed Matter,* vol. 15, p. 75, 2003.

[49] R. J. Speedy, "Limiting forms of the thermodynamic divergences at the conjectured stability limits in superheated and supercooled water," *The Journal of Physical Chemistry,* vol. 86, pp. 3002-3005, 1982.

[50] M. C. D’Antonio and P. G. Debenedetti, "Loss of tensile strength in liquids without property discontinuities: A thermodynamic analysis," *The Journal of Chemical Physics,* vol. 86, pp. 2229-2235, 1987.

[51] C. E. Brennen, *Cavitation and bubble dynamics*: Cambridge University Press, 2013.

[52] F. Caupin and E. Herbert, "Cavitation in water: a review," *Comptes Rendus Physique,* vol. 7, pp. 1000-1017, 2006.

[53] G. Bjoern, "Cavitation in focused ultrasound," Doctoral dissertation, University of Dundee, 2013.

[54] R. Mettin, "From a single bubble to bubble structures in acoustic cavitation," in *Oscillations, Waves and Interactions*, 2007, pp. 171-198.

[55] D. J. Fisher and W. Kurz, *Fundamentals of solidification*. Aedermannsdorf, Switzerland: Trans Tech Publications Ltd, 1986.

[56] S. C. Mossop, "The freezing of supercooled water," in *Proceedings of the Physical Society. Section B*, 1955, pp. 193-208.

[57] D. Turnbull, "Phase changes," *Solid state physics,* vol. 3, pp. 225-306, 1956.

[58] H. Flynn, "Physics of acoustic cavitation in liquids," *Physical Acoustics,* vol. 1, pp. 57-172, 1964.

[59] H. Nanjo, A. Shima, and T. Tsujino, "Formation of damage pits by cavitation in a polymer solution," *Nature,* vol. 320, pp. 516-517, 1986.

[60] C. Brennen, *Cavitation and bubble dynamics*. United Kingdom: Oxford University Press, 1995.

[61] T. J. Matula, "Inertial cavitation and single–bubble sonoluminescence," *Philosophical Transactions of the Royal Society of London. Series A: Mathematical, Physical and Engineering Sciences,* vol. 357, pp. 225-249, 1999.

[62] K. Weninger, B. Barber, and S. Putterman, "Pulsed Mie scattering measurements of the collapse of a sonoluminescing bubble," *Physical Review Letters,* vol. 78, p. 1799, 1997.

[63] M. S. Plesset and A. Prosperetti, "Bubble dynamics and cavitation," *Annual Review of Fluid Mechanics,* vol. 9, pp. 145-185, 1977.

[64] W. Lauterborn, "Numerical investigation of nonlinear oscillations of gas bubbles in liquids," *The Journal of the Acoustical Society of America,* vol. 59, pp. 283-293, 1976.

[65] R. Löfstedt, B. P. Barber, and S. J. Putterman, "Toward a hydrodynamic theory of sonoluminescence," *Physics of Fluids A: Fluid Dynamics (1989-1993),* vol. 5, pp. 2911-2928, 1993.

[66] J. B. Keller and M. Miksis, "Bubble oscillations of large amplitude," *The Journal of the Acoustical Society of America,* vol. 68, pp. 628-633, 1980.

[67] U. Parlitz, V. Englisch, C. Scheffczyk, and W. Lauterborn, "Bifurcation structure of bubble oscillators," *The Journal of the Acoustical Society of America,* vol. 88, pp. 1061-1077, 1990.

[68] A. Prosperetti and A. Lezzi, "Bubble dynamics in a compressible liquid. Part 1. First-order theory," *Journal of Fluid Mechanics,* vol. 168, pp. 457-478, 1986.

[69] A. Lezzi and A. Prosperetti, "Bubble dynamics in a compressible liquid. Part 2. Second-order theory," *Journal of Fluid Mechanics,* vol. 185, pp. 289-321, 1987.

[70] R. Geisler, *Untersuchungen zur laserinduzierten Kavitation mit Nanosekunden-und Femtosekundenlasern*: Universit tsverlag Gˆttingen, 2004 (Ref from [1]).

[71] W. Lauterborn and H. Bolle, "Experimental investigations of cavitation-bubble collapse in the neighbourhood of a solid boundary," *Journal of Fluid Mechanics,* vol. 72, pp. 391-399, 1975.

[72] W. Lauterborn, T. Kurz, R. Mettin, and C. D. Ohl, "Experimental and theoretical bubble dynamics," *Advances in chemical physics,* vol. 110, pp. 295-380, 1999.

[73] Y. Tian, J. A. Ketterling, and R. E. Apfel, "Direct observation of microbubble oscillations," *The Journal of the Acoustical Society of America,* vol. 100, pp. 3976-3978, 1996.

[74] K. S. Suslick and G. J. Price, "Applications of ultrasound to materials chemistry," *Annual Review of Materials Science,* vol. 29, pp. 295-326, 1999.

[75] L. A. Crum and R. A. Roy, "Sonoluminescence," *Science,* vol. 266, pp. 233-234, 1994.

[76] T. Prozorov, R. Prozorov, and K. S. Suslick, "High velocity interparticle collisions driven by ultrasound," *Journal of the American Chemical Society,* vol. 126, pp. 13890-13891, 2004.

[77] N. C. Eddingsaas and K. S. Suslick, "Intense mechanoluminescence and gas phase reactions from the sonication of an organic slurry," *Journal of the American Chemical Society,* vol. 129, pp. 6718-6719, 2007.

[78] C. D. Ohl, T. Kurz, R. Geisler, O. Lindau, and W. Lauterborn, "Bubble dynamics, shock waves and sonoluminescence," vol. 357, pp. 269-94, 1999.

[79] W. Lauterborn and C. D. Ohl, "Cavitation bubble dynamics," *Ultrasonics Sonochemistry,* vol. 4, pp. 65-75, 1997.

[80] W. Lauterborn, "Kavitation durch laserlicht," Doctoral dissertation, 1974.

[81] E. A. Brujan, C. D. Ohl, W. Lauterborn, and A. Philipp, "Dynamics of laser-induced cavitation bubbles in polymer solutions," *Acta Acustica united with Acustica,* vol. 82, pp. 423-430, 1996.

[82] Y. Tomita and A. Shima, "High-speed photographic observations of laser-induced cavitation bubbles in water," *Acta Acustica united with Acustica,* vol. 71, pp. 161-171, 1990.

[83] A. Shima, Y. Tomita, D. Gibson, and J. Blake, "The growth and collapse of cavitation bubbles near composite surfaces," *Journal of Fluid Mechanics,* vol. 203, pp. 199-214, 1989.

[84] M. S. Plesset and R. B. Chapman, "Collapse of an initially spherical vapour cavity in the neighbourhood of a solid boundary," *Journal of Fluid Mechanics,* vol. 47, pp. 283-290, 1971.

[85] J. C. Isselin, A. P. Alloncle, and M. Autric, "On laser induced single bubble near a solid boundary: contribution to the understanding of erosion phenomena," *Journal of Applied Physics,* vol. 84, pp. 5766-5771, 1998.

[86] S. Shaw, e. Y. Jin, W. Schiffers, and D. Emmony, "The interaction of a single laser‐generated cavity in water with a solid surface," *The Journal of the Acoustical Society of America,* vol. 99, pp. 2811-2824, 1996.

[87] K. S. Suslick, W. B. McNamara, and Y. Didenko, "Hot spot conditions during multi-bubble cavitation," in *Sonochemistry and Sonoluminescence*, 1st ed: Springer, 1999, pp. 191-204.

[88] A. Henglein, "Physicochemical properties of small metal particles in solution:" microelectrode" reactions, chemisorption, composite metal particles, and the atom-to-metal transition," *The Journal of Physical Chemistry,* vol. 97, pp. 5457-5471, 1993.

[89] R. V. Chaudhari and H. Hofmann, "Coalescence of gas bubbles in liquids," *Reviews in Chemical Engineering,* vol. 10, pp. 131-190, 1994.

[90] P. A. Ramachandran and R. V. Chaudhari, *Three-phase catalytic reactors* vol. 2: Gordon & Breach Science Pub, 1983.

[91] L. K. Doraiswamy and M. M. Sharma, *Heterogeneous reactions: analysis, examples, and reactor design* vol. 1: Wiley, 1984.

[92] G. Marrucci, "A theory of coalescence," *Chemical Engineering Science,* vol. 24, pp. 975-985, 1969.

[93] A. Sharma and E. Ruckenstein, "Critical thickness and lifetimes of foams and emulsions: Role of surface wave-induced thinning," *Journal of Colloid and Interface Science,* vol. 119, pp. 14-29, 1987.

[94] A. Vrij, "Possible mechanism for the spontaneous rupture of thin, free liquid films," *Discussions of the Faraday Society,* vol. 42, pp. 23-33, 1966.

[95] A. K. Chesters and G. Hofman, "Bubble coalescence in pure liquids," in *Mechanics and Physics of Bubbles in Liquids*, 1st ed: Springer Netherlands, 1982, pp. 353-361.

[96] C. Y. Lin and J. Slattery, "Thinning of a liquid film as a small drop or bubble approaches a fluid–fluid interface," *AIChE Journal,* vol. 28, pp. 786-792, 1982.

[97] E. Klaseboer, J. P. Chevaillier, C. Gourdon, and O. Masbernat, "Film drainage between colliding drops at constant approach velocity: experiments and modeling," *Journal of Colloid and Interface Science,* vol. 229, pp. 274-285, 2000.

[98] O. Reynolds, "On the Theory of Lubrication and Its Application to Mr. Beauchamp Tower's Experiments, Including an Experimental Determination of the Viscosity of Olive Oil," *Philosophical Transactions of the Royal Society of London,* vol. 177, pp. 157-234, 1886.

[99] J. Lee, T. Tuziuti, K. Yasui, S. Kentish, F. Grieser, M. Ashokkumar, and Y. Iida, "Influence of Surface-Active Solutes on the Coalescence, Clustering, and Fragmentation of Acoustic Bubbles Confined in a Microspace," *The Journal of Physical Chemistry C,* vol. 111, pp. 19015-19023, 2007.

[100] T. Tuziuti, K. Yasui, J. Lee, T. Kozuka, A. Towata, and Y. Iida, "Influence of surface active solute on ultrasonic waveform distortion in liquid containing air bubbles," *Journal of Physical Chemistry A,* vol. 113, pp. 8893-8900, 2009.

[101] P. A. Kralchevsky, K. D. Danov, and I. B. Ivanov, "Thin Liquid Film Physics," in *Foams: Theory, Measurements and Applications*, R. K. Prud'homme and S. A. Khan, Eds., ed New York: Marcel Dekker, Inc., 1995, pp. 1-97.

[102] A. Sheludko, "Thin liquid films," *Advances in Colloid and Interface Science,* vol. 1, pp. 391-464, 1967.

[103] L. van Wijngaarden, "The mean rise velocity of pairwise-interacting bubbles in liquid " *Journal of Fluid Mechanics,* vol. 251, pp. PP 55-78, 1993.

[104] R. D. Kirkpatrick and M. J. Lockett, "The influence of approach velocity on bubble coalescence," *Chemical Engineering Science,* vol. 29, pp. 2363-2373, 1974.

[105] J. Angarska, B. Dimitrova, K. Danov, P. Kralchevsky, K. Ananthapadmanabhan, and A. Lips, "Detection of the hydrophobic surface force in foam films by measurements of the critical thickness of the film rupture," *Langmuir,* vol. 20, pp. 1799-1806, 2004.

[106] D. Dekée, P. J. Carreau, and J. Mordarski, "Bubble velocity and coalescence in viscoelastic liquids," *Chemical Engineering Science,* vol. 41, pp. 2273-2283, 1986.

[107] B. Jingliang, L. Xipeng, and D. M. Christopher, "Effects of bubble coalescence dynamics on heat flux distributions under bubbles," *AIChE Journal,* vol. 59, pp. 1735-1745, 2013.

[108] Y. Shah, B. G. Kelkar, S. Godbole, and W. D. Deckwer, "Design parameters estimations for bubble column reactors," *AIChE Journal,* vol. 28, pp. 353-379, 1982.

[109] G. I. Eskin, "Ultrasonic treatment of molten aluminum," *Metallurgiya, Moscow,* 1988.

[110] G. I. Eskin, "Ultrasonic treatment of molten aluminum," *Metallurgiya, Moscow,* 1965.

[111] B. Dubus, C. Vanhille, C. Campos-Pozuelo, and C. Granger, "On the physical origin of conical bubble structure under an ultrasonic horn," *Ultrasonics Sonochemistry,* vol. 17, pp. 810-818, 2010.

[112] A. Moussatov, C. Granger, and B. Dubus, "Cone-like bubble formation in ultrasonic cavitation field," *Ultrasonics Sonochemistry,* vol. 10, pp. 191-195, 2003.

[113] R. Mettin, I. Akhatov, U. Parlitz, C. D. Ohl, and W. Lauterborn, "Bjerknes forces between small cavitation bubbles in a strong acoustic field," *Physical Review E,* vol. 56, pp. 2924-2931, 1997.

[114] R. Mettin, "Bubble structures in acoustic cavitation," *Bubble and Particle Dynamics in Acoustic Fields: Modern Trends and Applications,* pp. 1-36, 2005.

[115] S. Fogler and K. Lund, "Acoustically augmented diffusional transport," *Journal of the Acoustical Society of America,* vol. 53, pp. 59-64, 1973.

[116] V. Frenkel, R. Gurka, A. Liberzon, U. Shavit, and E. Kimmel, "Preliminary investigations of ultrasound induced acoustic streaming using particle image velocimetry," *Ultrasonics,* vol. 39, pp. 153-156, 2001.

[117] L. D. Rozenberg, *High-intensity ultrasonic fields*: Plenum Publishing Corporation, 1971.

[118] O. Dahlem, J. Reisse, and V. Halloin, "The radially vibrating horn: a scaling-up possibility for sonochemical reactions," *Chemical Engineering Science,* vol. 54, pp. 2829-2838, 1999.

[119] A. Kumar, T. Kumaresan, A. B. Pandit, and J. B. Joshi, "Characterization of flow phenomena induced by ultrasonic horn," *Chemical Engineering Science,* vol. 61, pp. 7410-7420, 2006.

[120] M. C. Schenker, M. J. B. M. Pourquié, D. G. Eskin, and B. J. Boersma, "PIV quantification of the flow induced by an ultrasonic horn and numerical modeling of the flow and related processing times," *Ultrasonics Sonochemistry,* vol. 20, pp. 502-509, 2013.

[121] Y. Ishiwata, S. Komarov, and Y. Takeda, "Investigation of Acoustic Streaming in Aluminum Melts Exposed to High - Intensity Ultrasonic Irradiation," in *ICAA13: 13th International Conference on Aluminum Alloys*, 2012, pp. 183-188.

[122] A. P. Panov, "Ultrasonic cleaning of high-precision parts.," *Ultrasonic cleaning of high-precision parts.,* 1984.

[123] P. M. Kanthale, P. R. Gogate, A. B. Pandit, and A. M. Wilhelm, "Mapping of an ultrasonic horn: link primary and secondary effects of ultrasound," *Ultrasonics Sonochemistry,* vol. 10, pp. 331-335, 2003.

[124] O. V. Abramov, Y. S. Astashkin, and V. S. Stepanov, "On acoustic flows in melts," *Akust. Zh.,* vol. 25, pp. 180-186, 1979.

[125] S. Luther, R. Mettin, P. Koch, and W. Lauterborn, "Observation of acoustic cavitation bubbles at 2250 frames per second," *Ultrasonics Sonochemistry,* vol. 8, pp. 159-162, 2001.

[126] F. Burdin, N. A. Tsochatzidis, P. Guiraud, A. M. Wilhelm, and H. Delmas, "Characterisation of the acoustic cavitation cloud by two laser techniques," *Ultrasonics Sonochemistry,* vol. 6, pp. 43-51, 1999.

[127] K. S. Suslick, D. J. Casadonte, M. L. Green, and M. E. Thompson, "Effects of high intensity ultrasound on inorganic solids," *Ultrasonics,* vol. 25, pp. 56-59, 1987.

[128] K. S. Suslick, S.-B. Choe, A. A. Cichowlas, and M. W. Grinstaff, "Sonochemical synthesis of amorphous iron," *Nature,* vol. 353, pp. 414-416, 1991.

[129] H. Xu, Q. Han, and T. T. Meek, "Effects of ultrasonic vibration on degassing of aluminum alloys," *Materials Science and Engineering: A,* vol. 473, pp. 96-104, 2008.

[130] N. Alba-Baena, T. Pabel, N. Villa-Sierra, and D. G. Eskin, "Effect of ultrasonic melt treatment on degassing and structure of aluminium alloys," in *Materials Science Forum*, 2013, pp. 271-275.

[131] G. I. Eskin, "Cavitation mechanism of ultrasonic melt degassing," *Ultrasonics Sonochemistry,* vol. 2, pp. S137-S141, 1995.

[132] H. Xu, X. Jian, T. T. Meek, and Q. Han, "Degassing of molten aluminum A356 alloy using ultrasonic vibration," *Materials Letters,* vol. 58, pp. 3669-3673, 2004.

[133] E. O. Hall, "The deformation and ageing of mild steel: II Characteristics of the Lüders deformation," in *Proceedings of the Physical Society. Section B*, 1951, pp. 742-749.

[134] N. J. Petch, "The cleavage strength of polycrystals," *Journal of the Iron and Steel Institute,* vol. 174, pp. 25-28, 1953.

[135] X. Jian, H. Xu, T. T. Meek, and Q. Han, "Effect of power ultrasound on solidification of aluminum A356 alloy," *Materials Letters,* vol. 59, pp. 190-193, 2005.

[136] G. I. Eskin, "Improvement of the structure and properties of ingots and worked aluminum alloy semifinished products by melt ultrasonic treatment in a cavitation regime," *Metallurgist,* vol. 54, pp. 505-513, 2010.

[137] G. I. Eskin and D. G. Eskin, "Production of natural and synthesized aluminum-based composite materials with the aid of ultrasonic (cavitation) treatment of the melt," *Ultrasonics Sonochemistry,* vol. 10, pp. 297-301, 2003.

[138] T. V. Atamanenko, D. G. Eskin, M. Sluiter, and L. Katgerman, "On the mechanism of grain refinement in Al–Zr–Ti alloys," *Journal of Alloys and Compounds,* vol. 509, pp. 57-60, 2011.

[139] M. Khosro Aghayani and B. Niroumand, "Effects of ultrasonic treatment on microstructure and tensile strength of AZ91 magnesium alloy," *Journal of Alloys and Compounds,* vol. 509, pp. 114-122, 2011.

[140] H. Chen, Z. Li, Z. Wu, and Z. Zhang, "A novel route to prepare and characterize Sn–Bi nanoparticles," *Journal of Alloys and Compounds,* vol. 394, pp. 282-285, 2005.

[141] O. V. Abramov, "Action of high intensity ultrasound on solidifying metal," *Ultrasonics,* vol. 25, pp. 73-82, 1987.

[142] L. Zhang, D. G. Eskin, and L. Katgerman, "Influence of ultrasonic melt treatment on the formation of primary intermetallics and related grain refinement in aluminum alloys," *Journal of Materials Science,* vol. 46, pp. 5252-5259, 2011.

[143] X. Jian, T. T. Meek, and Q. Han, "Refinement of eutectic silicon phase of aluminum A356 alloy using high-intensity ultrasonic vibration," *Scripta Materialia,* vol. 54, pp. 893-896, 2006.

[144] R. Hickling, "Nucleation of Freezing by Cavity Collapse and its Relation to Cavitation Damage," *Nature,* vol. 206, pp. 915-917, 1965.

[145] J. D. Hunt and K. A. Jackson, "Nucleation of Solid in an Undercooled Liquid by Cavitation," *Journal of Applied Physics,* vol. 37, pp. 254-257, 1966.

[146] B. Chalmers, *Liquids: Structures, Properties, SolidInteractions*, 1st ed. Amsterdam: Elsevier, 1965.

[147] R. Chow, R. Blindt, R. Chivers, and M. Povey, "A study on the primary and secondary nucleation of ice by power ultrasound," *Ultrasonics,* vol. 43, pp. 227-230, 2005.

[148] T. V. Atamanenko, "Cavitation-aided grain refinement in aluminium alloys," Doctoral dissertation, Delft University of Technology, 2010.

[149] S. Komarov, Y. Ishiwata, and I. Mikhailov, "Industrial Application of Ultrasonic Vibrations to Improve the Structure of Al-Si Hypereutectic

Alloys: Potential and Limitations," *Metallurgical and Materials Transactions A,* vol. 46, pp. 2876-2883, 2015.

[150] V. Bojarevics, G. S. Djambazov, and K. A. Pericleous, "Contactless Ultrasound Generation in a Crucible," *Metallurgical and Materials Transactions A,* vol. 46, pp. 2884-2892, 2015.

[151] K. Jackson, R. Doremus, B. Roberts, and D. Turnbull, *Growth and perfection of crystals*. New York: Wiley, 1958.

[152] K. Jackson and J. Hunt, "Transparent compounds that freeze like metals," *Acta Metallurgica,* vol. 13, pp. 1212-1215, 1965.

[153] R. Trivedi, S. A. David, M. A. Eshelman, J. M. Vitek, S. S. Babu, T. Hong, and T. DebRoy, "In situ observations of weld pool solidification using transparent metal-analog systems," *Journal of Applied Physics,* vol. 93, pp. 4885-4895, 2003.

[154] C. Beckermann and C. Y. Wang, "Equiaxed dendritic solidification with convection: Part III. Comparisons with NH4Cl-H2O experiments," *Metallurgical and Materials Transactions A,* vol. 27, pp. 2784-2795, 1996/09/01 1996.

[155] R. Chow, R. Blindt, A. Kamp, P. Grocutt, and R. Chivers, "The microscopic visualisation of the sonocrystallisation of ice using a novel ultrasonic cold stage," *Ultrasonics Sonochemistry,* vol. 11, pp. 245-250, 2004.

[156] O. V. Abramov, "Crystallization of metals in ultrasonic field," *Metallurgiya, Moscow,* vol. 256, 1972.

[157] M. C. Flemings, "Solidification processing," *Metallurgical transactions,* vol. 5, pp. 2121-2134, 1974.

[158] K. Jackson, J. Hunt, D. Uhlmann, and T. Seward, "On origin of equiaxed zone in castings," *Transactions of the Metallurgical Society of AIME,* vol. 236, p. 149, 1966.

[159] T. Z. Kattamis, J. Coughlin, and M. C. Flemings, "Influence of coarsening on dendrite arm spacing of aluminum-copper alloys," *Transactions of the Metallurgical Society of AIME,* vol. 239, pp. 1504-1511, 1967.

[160] D. Ruvalcaba, R. H. Mathiesen, D. G. Eskin, L. Arnberg, and L. Katgerman, "In situ observations of dendritic fragmentation due to local solute-enrichment during directional solidification of an aluminum alloy," *Acta Materialia,* vol. 55, pp. 4287-4292, 2007.

[161] E. L. Cussler, *Diffusion: Mass Transfer in Fluid Systems* 2nd ed. New York: Cambridge University Press, 1997.

[162] R. S. B. Reddi, S. Kant, U. S. Rai, and R. N. Rai, "Crystallization, thermal, phase diagram and microstructural studies of organic analog of metal–nonmetal monotectic alloy: 4-Bromochlorobenzene–succinonitrile," *Journal of Crystal Growth,* vol. 312, pp. 95-99, 2009.

[163] A. Robinson, "History of synchrotron radiation," Ernest Orlando Lawrence Berkeley National Lab., Advanced Light Source, CA (US)2001.

[164] J. Als-Nielsen and D. McMorrow, "Elements of Modern X-ray Physics," ed. London, UK: A John Wiley & Sons, Ltd Publication, 2011.

[165] G. T. Herman, *Fundamentals of computerized tomography: image reconstruction from projections*: Springer Science & Business Media, 2009.

[166] "National Institute of Standards and Technology (NIST) Physical Measurement Laboratory, http://www.nist.gov/pml/data/xraytrans/index.cfm."

[167] *Diamond Light Source,* *http://diamondlifeblog.tumblr.com/post/92147428772/what-is-diamond-light-source*.

[168] *Advanced Photon Source, Overview,* *http://www.aps.anl.gov/About/APS_Overview/loms_beamlines.html*.

[169] *M. Drakopoulos, http://www.diamond.ac.uk/Beamlines/Engineering-and-Environment/I12/applications.html*.

[170] *http://www.spring8.or.jp/en/about_us/whats_sr/sp8_features/*.

[171] E. Liotti, A. Lui, R. Vincent, S. Kumar, Z. Guo, T. Connolley, I. P. Dolbnya, M. Hart, L. Arnberg, R. H. Mathiesen, and P. S. Grant, "A synchrotron X-ray radiography study of dendrite fragmentation induced by a pulsed electromagnetic field in an Al–15Cu alloy," *Acta Materialia,* vol. 70, pp. 228-239, 2014.

[172] D. Tan, T. L. Lee, J. C. Khong, T. Connolley, K. Fezzaa, and J. Mi, "High-Speed Synchrotron X-ray Imaging Studies of the Ultrasound Shockwave and Enhanced Flow during Metal Solidification Processes," *Metallurgical and Materials Transactions A,* vol. 46, pp. 2851-2861, 2015/03/31 2015.

[173] D. Calloway, "Beer-Lambert Law," *Journal of Chemical Education,* vol. 74, p. 744, 1997.

[174] S. Seltzer. *X-ray Mass Attenuation Coefficients,* *http://physics.nist.gov/PhysRefData/XrayMassCoef/tab3.html (accessed 25 July 2014)*.

[175] H. Yasuda, T. Nagira, M. Yoshiya, N. Nakatsuka, A. Sugiyama, K. Uesugi, and K. Umetani, "Development of X-ray imaging for observing solidification of carbon steels," *ISIJ international,* vol. 51, pp. 402-408, 2011.

[176] F. Offi, S. Iacobucci, L. Petaccia, S. Gorovikov, P. Vilmercati, A. Rizzo, A. Ruocco, A. Goldoni, G. Stefani, and G. Panaccione, "The attenuation length of low energy electrons in Yb," *Journal of Physics: Condensed Matter,* vol. 22, p. 305002, 2010.

[177] K. Fezzaa and Y. Wang, "Ultrafast x-ray phase-contrast imaging of the initial coalescence phase of two water droplets," *Physical Review Letters,* vol. 100, pp. 13-16, 2008.

[178] T. Weitkamp, "XWFP: an x-ray wavefront propagation software package for the IDL computer language," 2004, pp. 181-189.

[179] B. Cai, S. Karagadde, L. Yuan, T. J. Marrow, T. Connolley, and P. D. Lee, "In situ synchrotron tomographic quantification of granular and intragranular deformation during semi-solid compression of an equiaxed dendritic Al–Cu alloy," *Acta Materialia,* vol. 76, pp. 371-380, 2014.

[180] T. Wang, J. Xu, T. Xiao, H. Xie, J. Li, T. Li, and Z. Cao, "Evolution of dendrite morphology of a binary alloy under an applied electric current: an in situ observation," *Physical Review E,* vol. 81, p. 042601, 2010.

[181] H. Huang, D. Shu, Y. Fu, J. Wang, and B. Sun, "Synchrotron radiation X-ray imaging of cavitation bubbles in Al–Cu alloy melt," *Ultrasonics Sonochemistry,* vol. 21, pp. 1275-1278, 2014.

[182] W. Xu, I. Tzanakis, P. Srirangam, S. Terzi, W. U. Mirihanage, D. G. Eskin, R. H. Mathiesen, A. P. Horsfield, and P. D. Lee, "In situ synchrotron radiography of ultrasound cavitation in a molten Al-10Cu alloy," in *TMS 2015 Supplemental Proceedings*, 2015, pp. 61-66.

[183] Y. Yu and J. Wang, "Beam hardening-respecting flat field correction of digital X-ray detectors," in *Image Processing (ICIP), 19th IEEE International Conference*, 2012, pp. 2085-2088.

[184] Y. Xie, L. Chen, and U. G. Hofmann, "Reduction of periodic noise in Fourier domain optical coherence tomography images by frequency domain filtering," *Biomedical Engineering,* vol. 57, pp. 830-832, 2012.

[185] Y. Wang, X. Liu, K.-S. Im, W.-K. Lee, J. Wang, K. Fezzaa, D. L. S. Hung, and J. R. Winkelman, "Ultrafast X-ray study of dense-liquid-jet flow dynamics using structure-tracking velocimetry," *Nature Physics,* vol. 4, pp. 305-309, 2008.

[186] R. Boll, D. Anielski, C. Bostedt, J. Bozek, L. Christensen, R. Coffee, S. De, P. Decleva, S. Epp, B. Erk, L. Foucar, F. Krasniqi, J. Küpper, A. Rouzée, B. Rudek, A. Rudenko, S. Schorb, H. Stapelfeldt, M. Stener, S. Stern, S. Techert, S. Trippel, M. Vrakking, J. Ullrich, and D. Rolles, "Femtosecond photoelectron diffraction on laser-aligned molecules: Towards time-resolved imaging of molecular structure," *Physical Review A,* vol. 88, p. 061402, 2013.

[187] D. Milathianaki, S. Boutet, G. J. Williams, A. Higginbotham, D. Ratner, A. E. Gleason, M. Messerschmidt, M. M. Seibert, D. C. Swift, P. Hering, J. Robinson, W. E. White, and J. S. Wark, "Femtosecond Visualization of Lattice Dynamics in Shock-Compressed Matter," *Science,* vol. 342, pp. 220-223, 2013.

[188] *X-Ray Attenuation Length,* *http://henke.lbl.gov/optical_constants/atten2.html*.

[189] *National Institute of Standards and Technology (NIST),* *http://physics.nist.gov/PhysRefData/XrayMassCoef/chap2.html*.

[190] K. Yoshida, S. Kitagawa, K. Mitose, and K. Susai, "Development of Cu-Sn Alloy Plating with Superior Excellent Sliding Characteristics and Corrosion Resistance," *Furukawa Review,* vol. 40, pp. 8-11, 2011.

[191] W. Pu, X. He, J. Ren, C. Wan, and C. Jiang, "Electrodeposition of Sn–Cu alloy anodes for lithium batteries," *Electrochimica Acta,* vol. 50, pp. 4140-4145, 2005.

[192] T. B. Massalski and H. Okamoto, *Binary Alloy Phase Diagrams*, 2nd ed. USA: Materials Park, Ohio: ASM International, 1990.

[193] J. Vizdal, M. H. Braga, A. Kroupa, K. W. Richter, D. Soares, L. F. Malheiros, and J. Ferreira, "Thermodynamic assessment of the Bi–Sn–Zn System," *Calphad,* vol. 31, pp. 438-448, 2007.

[194] *National Institute of Standards and Technology (NIST) phase diagram database, http://www.nist.gov/srd/nist31.cfm*.

[195] J. Campbell, *Casting*, 1st ed. Oxford: Butterworth- Heinemann Ltd, 1991.

[196] J. Campbell, "An overview of the effects of bifilms on the structure and properties of cast alloys," *Metallurgical and Materials Transactions B,* vol. 37, pp. 857-863, 2006.

[197] R. Gopalan and N. K. Prabhu, "Oxide bifilms in aluminium alloy castings – a review," *Materials Science and Technology,* vol. 27, pp. 1757-1769, 2011.

[198] J. Campbell, "Counter Gravity Casting," in *Advances in the Science and Engineering of Casting Solidification*, 1st ed: John Wiley & Sons, Inc., 2015, pp. 355-362.

[199] L. C. Prasad and R. K. Jha, "Surface tension and viscosity of Sn-based binary liquid alloys," *physica status solidi (a),* vol. 202, pp. 2709-2719, 2005.

[200] B. J. Keene, "Review of data for the surface tension of pure metals," *International Materials Reviews,* vol. 38, pp. 157-192 1993.

[201] O. V. Abramov, *Ultrasound in liquid and solid metals*, 1st ed.: CRC press, 1994.

[202] J. Tu, G. H. Yeoh, and C. Liu, *Computational fluid dynamics: a practical approach*: Butterworth-Heinemann, Oxford, 2007.

[203] *Heraeus Quartz America LLC,* http://heraeus-quarzglas.com/media/webmedia_local/downloads/broschrenbm/BM_Quartz_Glass_Tubes_EN.pdf.

[204] T. Kurz, D. Kröninger, R. Geisler, and W. Lauterborn, "Optic cavitation in an ultrasonic field," *Physical Review E,* vol. 74, p. 066307, 2006.

[205] D. J. Flannigan and K. S. Suslick, "Inertially confined plasma in an imploding bubble," *Nature Physics,* vol. 6, pp. 598-601, 2010.

[206] T. Weitkamp, D. Haas, D. Wegrzynek, and A. Rack, "ANKAphase: software for single-distance phase retrieval from inline X-ray phase-contrast radiographs," *Journal of synchrotron radiation,* vol. 18, pp. 617-629, 2011.

[207] *The center for X-ray optics,* http://henke.lbl.gov/optical_constants/.

[208] B. L. Henke, E. M. Gullikson, and J. C. Davis, "X-ray interactions: photoabsorption, scattering, transmission, and reflection at E= 50-30,000 eV, Z= 1-92," *Atomic data and nuclear data tables,* vol. 54, pp. 181-342, 1993.

[209] J. Lee, M. Ashokkumar, S. Kentish, and F. Grieser, "Determination of the Size Distribution of Sonoluminescence Bubbles in a Pulsed Acoustic Field," *Journal of the American Chemical Society,* vol. 127, pp. 16810-16811, 2005.

[210] P. Testud‐Giovanneschi, A. Alloncle, and D. Dufresne, "Collective effects of cavitation: Experimental study of bubble‐bubble and bubble‐shock wave interactions," *Journal of Applied Physics,* vol. 67, pp. 3560-3564, 1990.

[211] Z. Xu, M. Raghavan, T. L. Hall, C. Chang, M. A. Mycek, J. B. Fowlkes, and C. Cain, "High speed imaging of bubble clouds generated in pulsed ultrasound cavitational therapy-histotripsy," *Ultrasonics, Ferroelectrics, and Frequency Control, IEEE Transactions on,* vol. 54, pp. 2091-2101, 2007.

[212] J. L. Laborde, A. Hita, J. P. Caltagirone, and A. Gerard, "Fluid dynamics phenomena induced by power ultrasounds," *Ultrasonics,* vol. 38, pp. 297-300, 2000.

[213] L. K. Zarembo, *Power ultrasonic fields,* , 1st ed. Nauka, Moscow: Russian Federation, 1968.

[214] D. Tan and J. Mi, "High speed imaging study of the dynamics of ultrasonic bubbles at a liquid-solid interface," *Materials Science Forum,* vol. 765, pp. 230–234, 2013.

[215] I. Steinbach, "Pattern formation in constrained dendritic growth with solutal buoyancy," *Acta Materialia,* vol. 57, pp. 2640-2645, 2009.

Appendices

Appendix 1: Design of the sample container

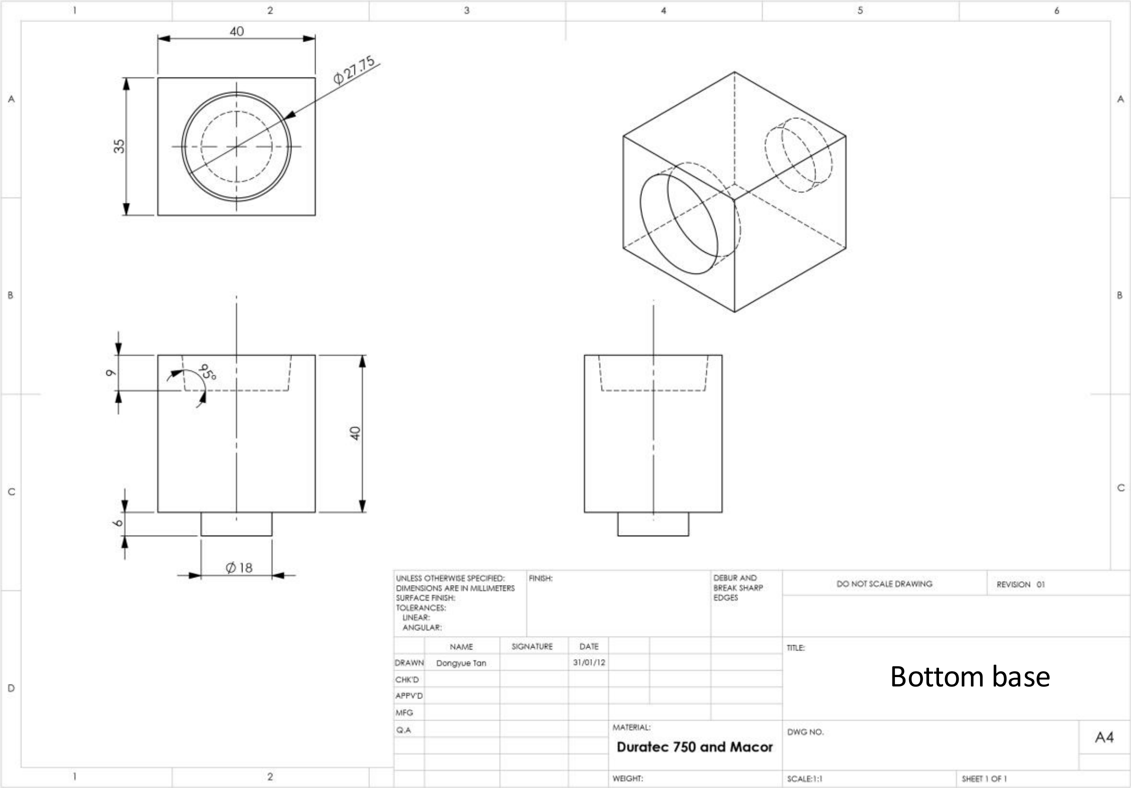

Bottom base

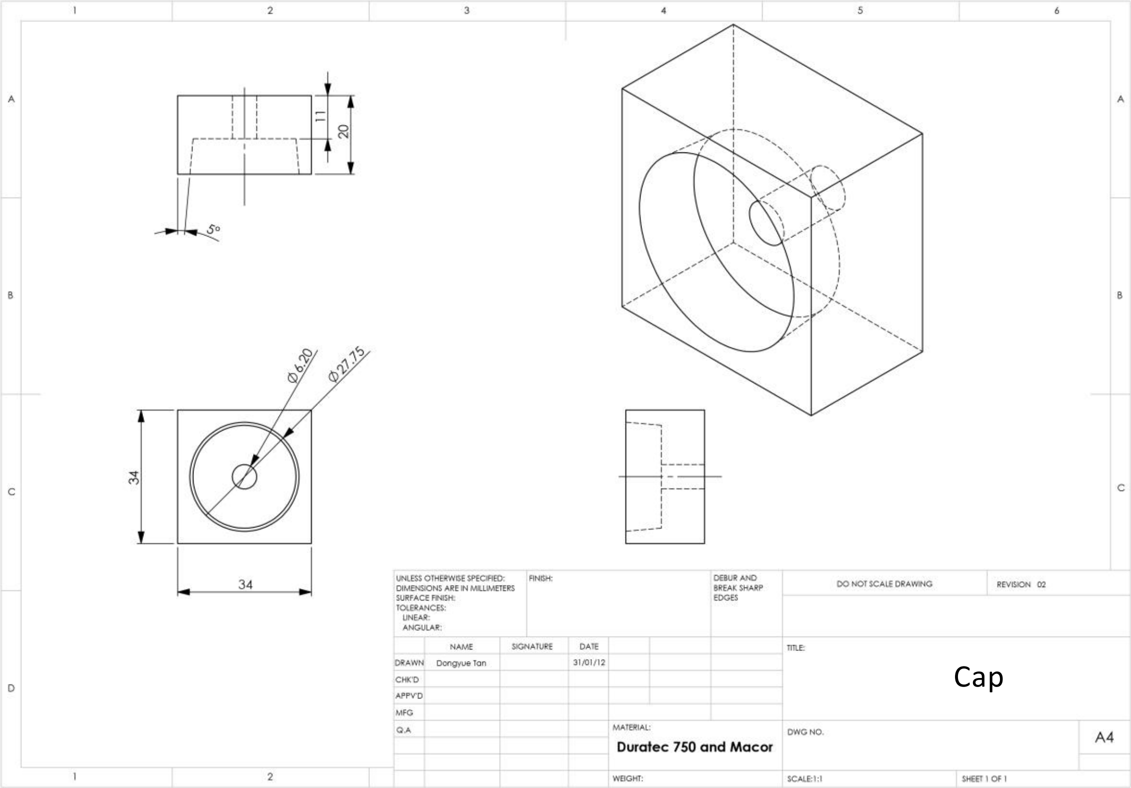

Cap

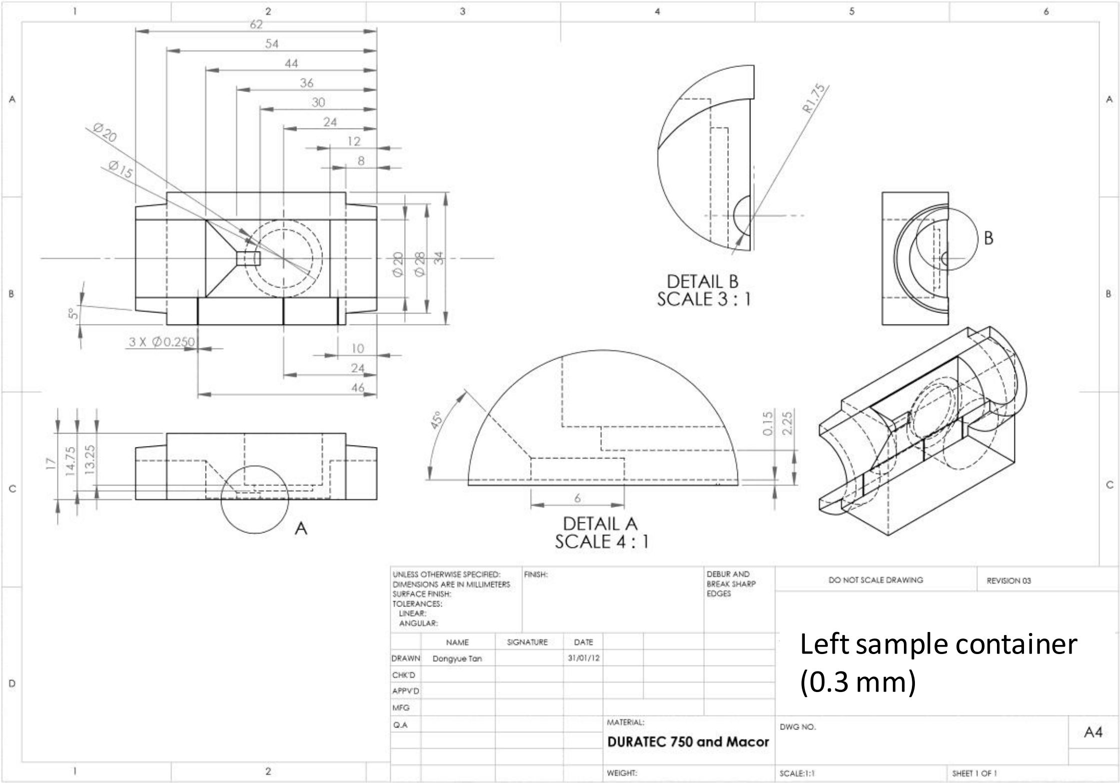

Left sample container (0.3 mm)

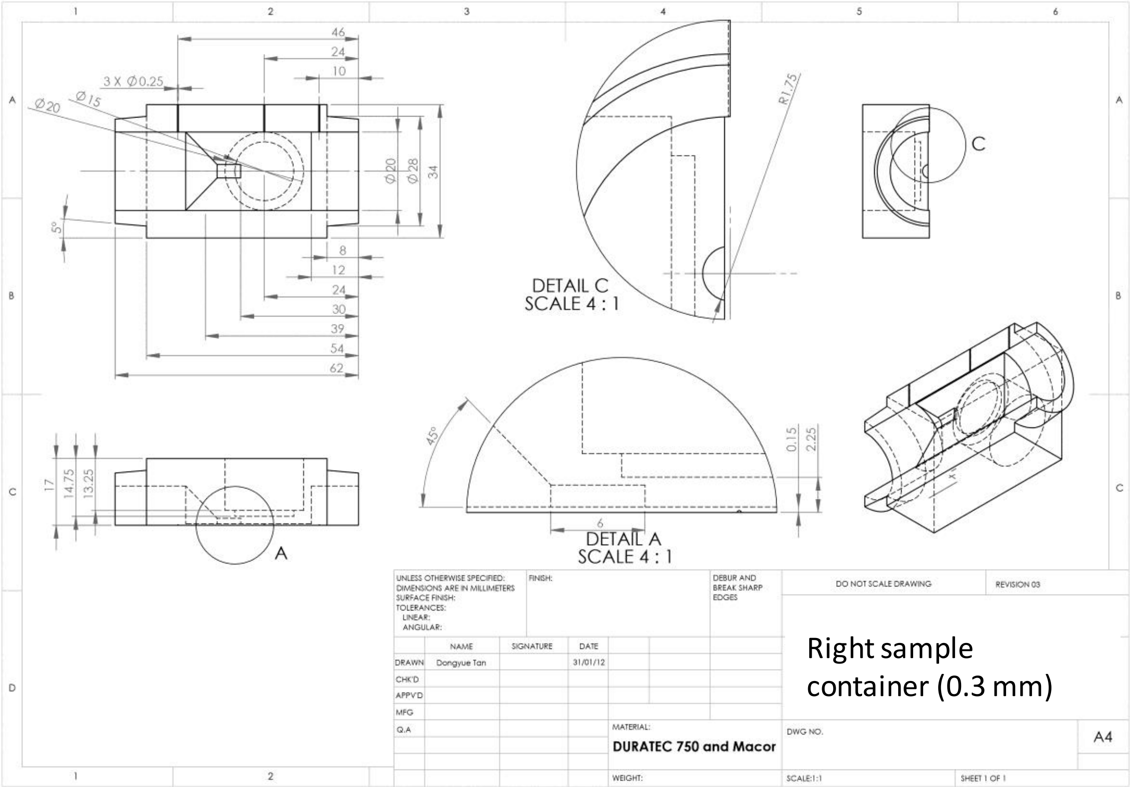

Right sample container (0.3 mm)

Appendix 2: Design of the Furnace

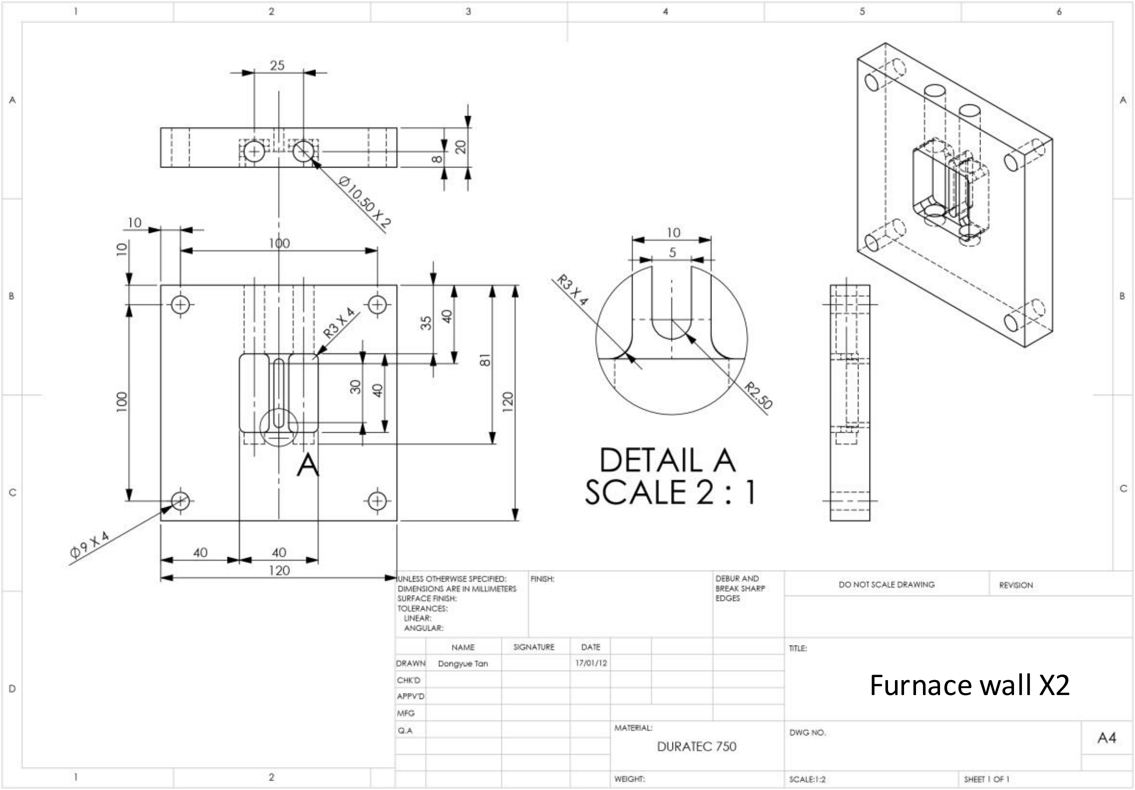

Furnace wall

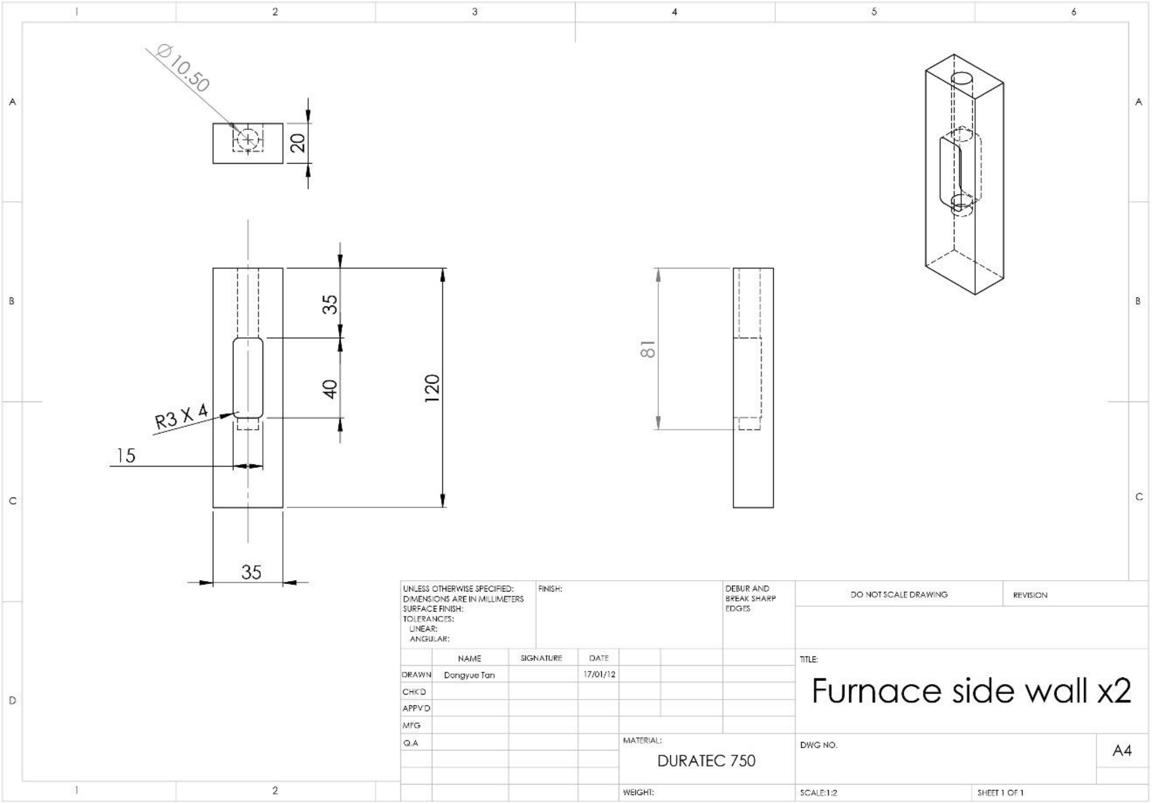

Furnace side wall

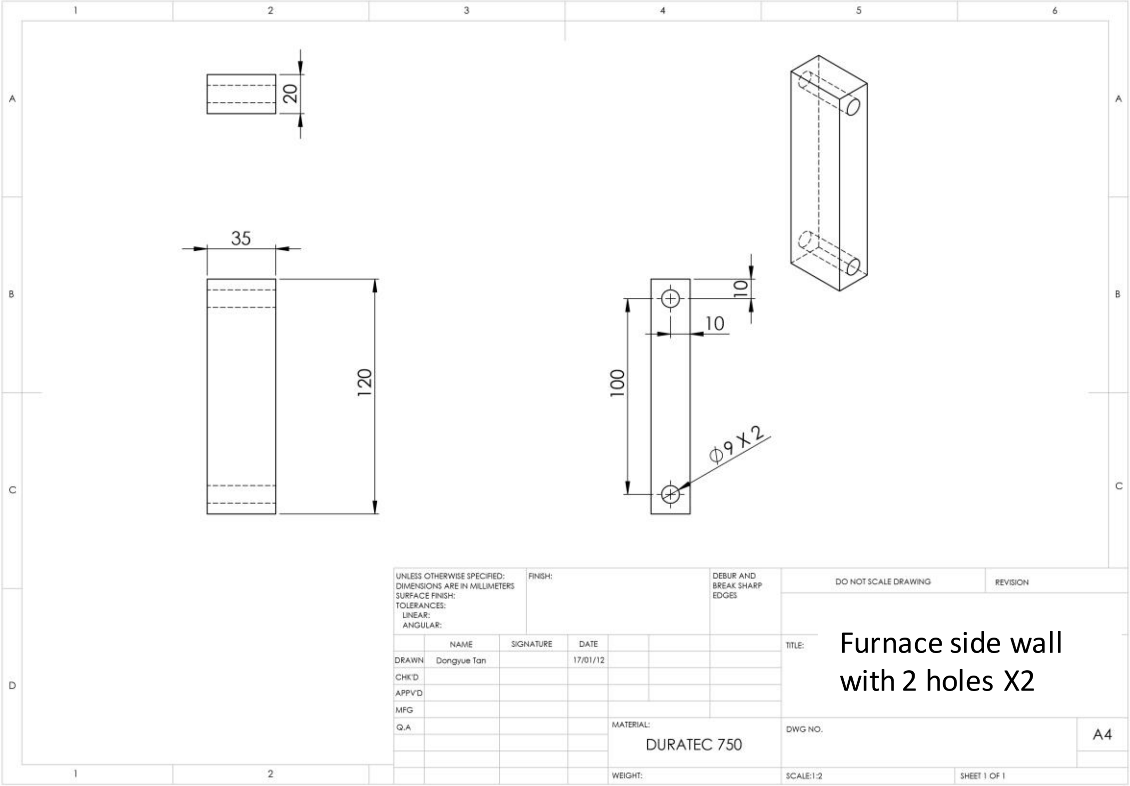

Furnace side wall with 2 holes

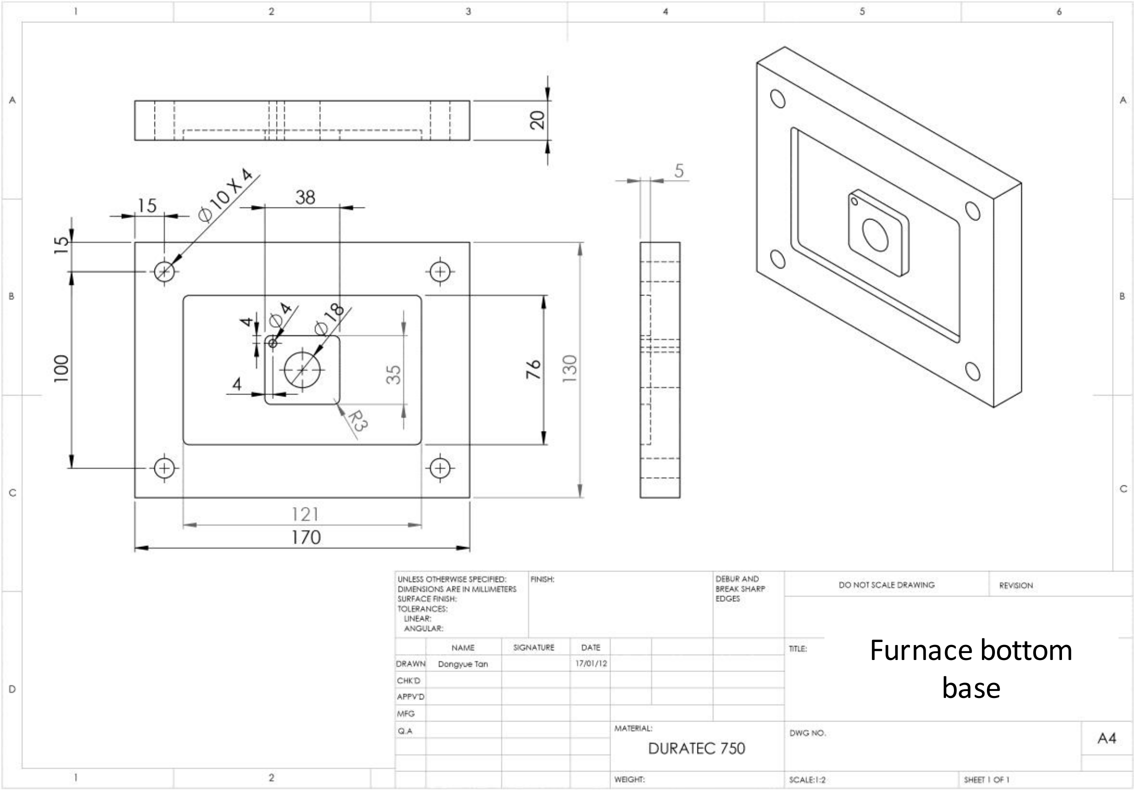

Furnace bottom base

Appendix 3: Al-20%Cu slot sample design

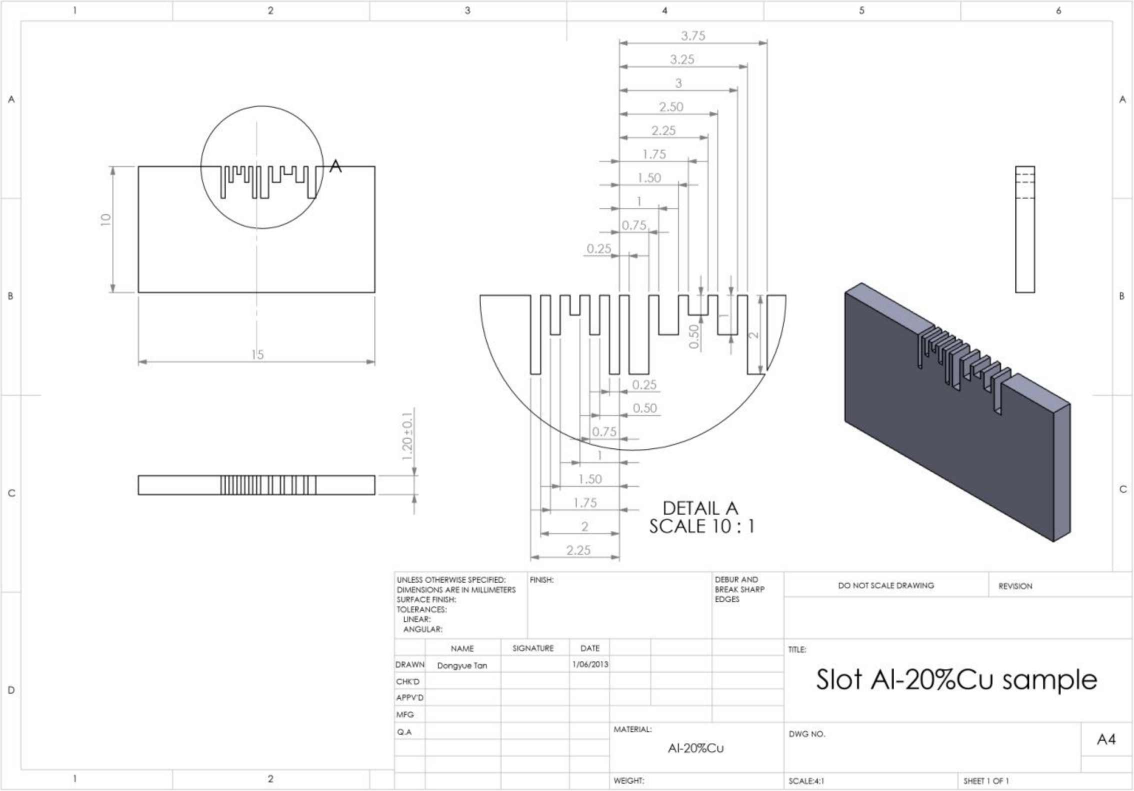

UNLESS OTHERWISE SPECIFIED:
DIMENSIONS ARE IN MILLIMETERS
SURFACE FINISH:
TOLERANCES:
LINEAR:
ANGULAR:

FINISH:

DEBUR AND BREAK SHARP EDGES

DO NOT SCALE DRAWING

REVISION

	NAME	SIGNATURE	DATE
DRAWN	Dongyue Tan		1/06/2013
CHK'D			
APPV'D			
MFG			
Q.A			

TITLE: Slot Al-20%Cu sample

MATERIAL: Al-20%Cu

DWG NO.

A4

WEIGHT:

SCALE:4:1

SHEET 1 OF 1

Appendix 4: Matlab code for image processing and analysis

A: Code of particle and bubble position finding and trajectory in liquid metal

```
clear all

% In put the image sequence into Matlab

 x = which('name of the files');
dirOutput = dir([fileparts(x) filesep 'file name_100*.tif']);

 fileNames = {dirOutput.name};
numFrames = numel(fileNames);
I = imread(fileNames{1});

% Binary the image sequence
 for k = 1:numFrames
    Newimage1{k,1}= imread(fileNames{1,k});
    Ix=Newimage1{k,1};
    BW = im2bw(Ix,0.5);
    BW2 = im2uint8(BW);

% Change the colour
    BW2=~BW2;
    BW2 = bwareaopen(BW2, 4);
    BW3{k,1}=BW2;

 end

for k = 1:numFrames
    Ix=Newimage1{k,1};
% Fill image holes
    BW4 = imfill(BW3{k,1},'holes');
% Find the centre position of the particles
    s = regionprops(BW4, 'centroid');
    centroids{k} = cat(1, s.Centroid);
```

```
    c{k} = struct2cell(s);
    imshow(Ix);
    hold(imgca,'on');
    plot(imgca, centroids{k}(:,1), centroids{k}(:,2), 'ro','MarkerFaceColor', 'r',
'MarkerSize',3);
    hold(imgca,'off');
    saveas(imgca,sprintf('Processed Image # %d.tif',k));

end
```

B: Code of bubble position and size finding in water and silicone oil

```
clear all

% In put the image sequence into Matlab
x = which('name of the file');
dirOutput = dir([fileparts(x) filesep 'name of the file_100*.jpg']);
 fileNames = {dirOutput.name};
numFrames = numel(fileNames);
I = imread(fileNames{1});

% Analyze the single layer of the grey value matrix (for the greyscale images)
 for k = 1:5
    Newimage{k,1}= imread(fileNames{1,k});
    Ix=Newimage{k,1};

% Find the centre position, radius and index of the bubbles
    [centers, radii, metric] = imfindcircles(Ix,[2 10], 'sensitivity', 0.90);
    sz=size(centers,1);
    centersstrong{k,1} = centers(1:sz,:);
    radiistrong{k,1} = radii(1:sz);
    metricstrong{k,1} = metric(1:sz);
    dataoutput{k,1} = cat(2,radiistrong{k,1},centersstrong{k,1});
    figure;
    imshow(Ix);
    hold on;

%Highlight the selected bubbles to check the accuracy of the results
     viscircles(centersstrong{k,1}, radiistrong{k,1},'edgecolor','k');
     hold on;
     plot(centersstrong{k,1}(:,1),centersstrong{k,1}(:,2),'yx','color',2);
     hold off;

end
```